INVESTIGATION ON THE NATURAL CIRCULATION CHARACTERISTICS OF A MOLTEN SALT LOOP

By

JAYARAJ

ENGG 01201104003

Bhabha Atomic Research Centre, Mumbai

A thesis submitted to the

Board of Studies in Engineering Sciences

In partial fulfillment of requirements

for the Degree of

DOCTOR OF PHILOSOPHY

of

HOMI BHABHA NATIONAL INSTITUTE

January, 2017

Homi Bhabha National Institute

Recommendations of the Viva Voce Committee

As members of the Viva Voce Committee, we certify that we have read the dissertation prepared by Mr. Jayaraj entitled "Investigation on the natural circulation characteristics of a molten salt loop" and recommend that it may be accepted as fulfilling the thesis requirement for the award of Degree of Doctor of Philosophy.

Chairman – Dr. P. K. Vijayan	**Date:** 18/1/17
Guide / Convener – Dr. N. K. Maheshwari	**Date:** 18/1/17
Co-guide - Dr. P. Satyamurthy	**Date:** 18/1/17
Examiner – Prof. R. P. Vedula	**Date:** 18/1/17
Member 1- Dr. K. Velusamy	**Date:** 18/1/2017
Member 2 – Dr. A. K. Nayak	**Date:** 18/1/17
Member 3- Prof. Atul Sharma	**Date:** 18/1/17
The Technology Advisor – Dr. A. M. Vaidya	**Date:** 18/01/2017

Final approval and acceptance of this thesis is contingent upon the candidate's submission of the final copies of the thesis to HBNI.

I/We hereby certify that I/we have read this thesis prepared under my/our direction and recommend that it may be accepted as fulfilling the thesis requirement.

Date: 18/1/17

Place: Mumbai

The Technology Advisor **Co-guide** **Guide**

STATEMENT BY AUTHOR

This dissertation has been submitted in partial fulfillment of requirements for an advanced degree at Homi Bhabha National Institute (HBNI) and is deposited in the Library to be made available to borrowers under rules of the HBNI.

Brief quotations from this dissertation are allowable without special permission, provided that accurate acknowledgement of source is made. Requests for permission for extended quotation from or reproduction of this manuscript in whole or in part may be granted by the Competent Authority of HBNI when in his or her judgment the proposed use of the material is in the interests of scholarship. In all other instances, however, permission must be obtained from the author.

Jayaraj

DECLARATION

I, hereby declare that the investigation presented in the thesis has been carried out by me. The work is original and has not been submitted earlier as a whole or in part for a degree / diploma at this or any other Institution / University.

Jayaraj

DEDICATIONS

I dedicate this thesis to my beloved family and my teachers.

ACKNOWLEDGEMENTS

I would like to express my sincere gratitude to my guide **Dr. N. K. Maheshwari** for the guidance and encouragement to work to the best of my abilities. His knowledge, insightfulness and consistent care for the best output have been great assets without which research would not have been possible. I would also like to thank my co-gudie **Dr. P. Satyamurthy** for the constant encouragement and help in CFD tool. I would also like to thank my technical advisor **Dr. A. M. Vaidya** for the guidance and encouragement throughout this research work. I am very much thankful to him for his knowledge share in CFD and careful proof-reading of manuscript.

I am indebted to the chairman (**Dr. P. K. Vijayan**) and other members of doctoral committee for their valuable comments and suggestions during the review presentations, oral general comprehensive examinations and pre-synopsis viva-voce. My sincere thanks to *Shri. A. K. Srivastava, Shri. Praveen Rai* and *Shri. B. M. Lingade* their support and encouragement during this research work. I would like to express my sincere thanks to *Shri. Vikas Jain, Shri. P. Haldar, Dr. Manish Sharma, Dr. Naveen Kumar, Shri. S. K. Bhatia, Shri. M. T. Kamble, Shri. Inder Kumar, Shri. A. Borgohain, Shri. Anuj Kansal, Shri. Avinash Moharana* and *Shri. Ganesh Kumawat* for their support and encouragement.

I am thankful to the Management, Principal and all the staff members of SDM College of Engineering & Technology Dharwad, for their encouragement to complete my PhD.

I am thankful to all my friends of BARC, specially *Shri. Mohit Sharma, Shri. Y. Vidyasagar, Ms. Archana. V, Mr. Suresh Sahu, Mr. Sunil Kumar, Mr. Nitendra Singh, Mr.*

Abhishek Chinchole, Ms. Sapna Singh, Mr. Ashwini Kumar, Ms. Paridhi Goel, Mr. Vinay Karnam and *all the staff of RED* for their support and encouragement.

I am extremely grateful to my father *Shri. Yallappa Kudariyawar* and my mother *Smt. Gouravva Kudariyawar* for their encouragement and support throughout the entire tenure of my education. I am grateful to my sister *Smt. Prabhavati,* my brother-in-law *Shri. MarutiKumar* and his family members for their support and blessings. Last but not least, I am grateful to my wife *Smt. Roopashree,* my lovely daughter *Prerana,* my son *Siddesh* and all my family members for their moral support and blessings.

Jayaraj

List of Publications from present research work

International Journals

1. Jayaraj Yallappa Kudariyawar, Abhijeet Mohan Vaidya, Naresh Kumar Maheshwari and Polepalle Satyamurthy, Computational study of instabilities in a rectangular natural circulation loop using 3D CFD simulation, **International journal of Thermal Sciences**, 101 (2016), 193-206. http://dx.doi.org/10.1016/j.ijthermalsci.2015.11.003

2. Jayaraj Yallappa Kudariyawar, Abhishek Kumar Srivastava, Abhijeet Mohan Vaidya, Naresh Kumar Maheshwari and Polepalle Satyamurthy, Computational and Experimental Investigation of Steady state and Transient Characteristics of Molten Salt Natural Circulation Loop, **Applied Thermal Engineering,** 99 (2016), 560-571, http://dx.doi.org/doi:10.1016/j.applthermaleng.2015.12.114

3. A. K. Srivastava, Jayaraj Y. Kudariyawar, A. Borgohain, N. K. Maheshwari and P. K. Vijayan, Experimental and theoretical studies on the natural circulation behaviour of molten salt, **Applied Thermal Engineering,** 98 (2016), 513-521. http://dx.doi.org/doi:10.1016/j.applthermaleng.2015.12.065

4. J. Y. Kudariyawar, A. M. Vaidya, N. K. Maheshwari, P. Satyamurthy and A. K. Srivastava, Estimating Steady state and Transient characteristics of Molten Salt Natural Circulation Loop using CFD, **KERNTECHNIK** 80 (1) (2015), 20-31. DOI 10.3139/124.110478

5. Jayaraj Yallappa Kudariyawar, Abhijeet Mohan Vaidya, Naresh Kumar Maheshwari, Polepalle Satyamurthy, Abhishek Kumar Srivastava and Babulu Mohan Lingade, Investigation on heat transfer behaviour of molten salt natural circulation loop using numerical simulations, **Journal of Nuclear Energy Science and Power Generation Technology**, 5:5 (2016), DOI: 10.4172/2325-9809.1000165

International Conferences

1. Jayaraj Yallappa Kudariyawar, A. M. Vaidya, N. K. Maheshwari and P.K.Vijayan, Steady State Characteristics and Flow Initiation Transients of Molten Salt Natural Circulation Loop, In the Proceedings of the Conference on Molten Salt Nuclear Technology (CMSNT), 199-203, January 9-11, 2013, BARC, Mumbai.

2. Jayaraj Y Kudariyawar, A. M. Vaidya, N. K. Maheshwari, P. Satyamurthy and P. K. Vijayan, Computation of flow transients in molten salt natural circulation loop using PHOENICS, In the Proceedings of 22nd National and 11th International ISHMT-ASME Heat and Mass Transfer Conference, Paper Number HMTC1300640, December 28-31, 2013, IIT Kharagpur, India

3. Jayaraj Y Kudariyawar, A. M. Vaidya, N. K. Maheshwari and P. Satyamurthy, Computational study of flow in rectangular natural circulation loop using 1D and 3D simulations, In the Proceedings of 5th International and 41st National Conference on Fluid Mechanics (FMFP-2014), Paper Number – 155, December 12-14, 2014, IIT Kanpur, India.

4. Jayaraj Y Kudariyawar, A. M. Vaidya, N. K. Maheshwari and P. Satyamurthy, Steady state and Transient Heat Transfer on Molten Salt Natural Circulation Loop, In the Proceedings of 6th International and 43rd National Conference on Fluid Mechanics and Fluid Power (FMFP-2016), Paper ID – 77, December 15-17, 2016, MNNIT Allahabad, India.

National conferences

1. Jayaraj Yallappa Kudariyawar, Abhijeeth Mohan Vaidya, N. K. Maheshwari and P. K. Vijayan, "3D CFD Simulation of molten salt natural circulation loop", In the Proceedings of 39th national conference on Fluid Mechanics and Fluid Power, NCFMFP2012-101, December 13-15, 2012, SVNIT Surat.

2. Jayaraj Y Kudariyawar, A. M. Vaidya, N. K. Maheshwari and P. Satyamurthy, "Investigation of flow and heat transfer characteristics of molten nitrate salt in a pipe using CFD simulations", In the Proceedings of National conference on Thorium: Present status and future directions, December 22-24, 2014, BARC Mumbai, India.

Jayaraj

SYNOPSIS

High Temperature Reactors (HTR) and solar thermal power plants use molten salts as a coolant/heat transfer fluid. Molten salts have comparatively low melting point and high boiling point at low pressure. This is highly desirable because a high temperature system can be designed without increasing system pressure. Hence design and operation of molten salt based system gets simplified. Natural circulation of molten salt is being preferred in some systems like solar thermal power plant or molten salt fast breeder reactor. Such systems can be studied with the help of a natural circulation loop.

Natural circulation loops are representative of primary heat transport system of nuclear reactor and other facilities working on natural circulation flow. Natural circulation phenomenon has been used in many engineering applications such as, solar water heaters, transformer cooling, geothermal power extraction, cooling of internal combustion engines, gas turbine blades, computer cooling and nuclear reactor cores. A Natural Circulation Loop (NCL) consists of a heater and cooler connected by piping. The heater is placed at lower elevation than the cooler. As a consequence of the heat flux, the heated part of the fluid becomes lighter and rises up, while the cooler part becomes denser and drops down due to gravity. These combined effects establish natural circulation of fluid in the loop. Thus, the motive force for the flow in NCL is generated simply because of the presence of the heat source and heat sink, without need of any external force. The absence of moving/rotating parts to generate the motive force for flow makes it less prone to failures. Also maintenance and operating costs are reduced. Hence the heat removal/transfer by natural circulation system takes the most attention. In view of this, molten salt natural circulation loop has been installed to study heat transfer capability of molten salt and also to understand the steady state and transient thermal-hydraulic behaviour of molten salt natural circulation loop.

Experimental and computational investigations of natural circulation loop with water are published previously. These available experimental data are used to validate the CFD model and also to understand the thermal-hydraulic behaviour of natural circulation loop working with water. Hence, the rectangular natural circulation loop working with water is also simulated using 3D CFD software. The CFD results are compared with available experimental data and correlations to validate the CFD models. The promising results obtained from CFD simulation are used to explain the reason behind the uni-directional and bi-directional oscillations occurs in the horizontal cooler and horizontal heater configurations of the natural circulation loop. This is one of the novel contributions of this thesis.

Transient 3D CFD simulation of the molten salt natural circulation loop is carried out. The experimental data generated on molten salt natural circulation loop are used to validate the CFD model, whereas the computed data are useful to know the design parameter of molten salt reactor and also for solar power plant. Various transient computational studies such as (i) flow initiation transients, (ii) power rising from steady state transients, (iii) power step back transients, (iv) heater trip transients and (v) loss of heat sink transients are performed to understand the thermal-hydraulic behavior of the loop at different operating conditions and various orientations of heater and cooler. Further, the heat transfer study on molten salt natural circulation loop has been carried out. The steady state heat transfer characteristics shows good match with Boelter's mixed convection correlation. Effect of developing length on heat transfer has been studied. The transient unsteady heat transfer characteristics are also studied and the unique heat transfer characteristic in the oscillatory flow has been explained in the thesis.

CONTENTS

SYNOPSIS i

CONTENTS iii

LIST OF FIGURES viii

LIST OF TABLES xvii

NOMENCLATURE xviii

CHAPTER 1 INTRODUCTION 1

1.1 Introduction 1

1.2 Natural Circulation Loop 3

1.3 Molten salt as a coolant 5

1.4 Objective of present work 6

1.5 Accomplishment of present project 10

1.6 Organization of the thesis 11

1.7 Closure 13

CHAPTER 2 REVIEW OF LITERATURE 14

2.1 Molten salts 14

2.1.1 Thermo-physical properties of molten salts 15

2.1.2 Molten salts applications 19

2.2 Natural circulation systems 25

2.2.1 Experimental studies on natural circulation loop 26

2.2.2 Theoretical studies on natural circulation loop 30

2.3 Heat transfer characteristics of molten salt natural circulation loop 36

2.4 Summary and Discussion on literature review 37

CHAPTER 3 EXPERIMENTAL STUDIES ON MOLTEN SALT NATURAL CIRCULATION LOOP 41

3.1 Introduction 41

3.2 Description of the loop 42

3.3 Materials used in nitrate salt environment 46

3.4 Design of various components 47

3.4.1 Main loop 47

3.4.2 Melt tank 47

3.4.3 Expansion tank 47

3.5 Blower 48

3.6 Various heaters used in the loop 48

3.7 Instrumentation for the loop 48

3.7.1 Pressure measurement 49

3.7.2 Level measurement 49

3.7.3 Temperature measurement 50

3.7.4 Control valves, PRVs and RVs 50

3.8 Experimental procedure 51

3.9 Experimental Results and Discussions 52

3.9.1 Steady state tests 53

3.9.2 Transient tests 56

3.10 Closure 69

CHAPTER 4 STEADY STATE AND TRANSIENT CHARACTERISTICS OF NATURAL CIRCULATION LOOP WORKING WITH WATER 70

4.1 Introduction 70

4.2 Loop description 72

4.3 CFD simulation 73

4.3.1 Computational domain and mesh 73

4.3.2 Formulation and numerical settings 75

4.4 Mesh and time step independence 80

4.5 Steady state characteristics 83

4.6 Transient characteristics 88

4.6.1 Flow initiation transient in VHHC configuration 88

4.6.2 Flow initiation transient in VHVC configuration 91

4.6.3 Flow initiation transient of HHHC configuration 94

4.6.4 Flow initiation transients in HHVC configuration 100

4.7 Explanation of uni/bi-directional oscillations in HHHC configuration at low and high powers 105

4.7.1 Uni-directional oscillations at low power 105

4.7.2 Bi-directional oscillations at high power 108

4.7.3 Oscillatory behaviour of temperature at different locations 111

4.7.4 Oscillatory behaviour of temperature difference across heater 112

4.8 Power raising transients 114

4.9 Power step back transient 115

4.10 Closure 117

CHAPTER 5 3D CFD SIMULATION OF MOLTEN SALT NATURAL CIRCULATION LOOP 119

5.1 Introduction 119

5.2 CFD model of molten salt natural circulation loop 120

5.2.1 Computational domain 120

5.2.2 Mesh 120

5.2.3 Governing equations and numerical parameters 121

5.2.4 Thermo-physical properties of primary and secondary fluids 121

5.2.5 Boundary conditions 123

5.2.6 Initial conditions 124

5.3 Mesh independence study 124

5.4 Time step independence study 128

5.5 Results and Discussions 132

5.5.1 Steady state characteristics 132

5.5.2 Loop operating limits 138

5.5.3 Transient simulations 139

5.6 Closure 171

CHAPTER 6 HEAT TRANSFER CHARACTERISTICS OF MOLTEN SALT NATURAL CIRCULATION LOOP 172

6.1 Introduction 172

6.2 Computational study of vertical pipe flow 173

6.3 Steady state characteristics of MSNCL 177

6.4 Comparison of computed heat transfer characteristics in the MSNCL with that in the half loop 180

6.5 Heat transfer characteristics in half loop of MSNCL at high Reynolds number flow condition 183

6.6 Heat transfer characteristics in the unsteady oscillatory flow condition 186

6.7 Closure 195

CHAPTER 7 SUMMARY, CONCLUSIONS AND SCOPE FOR FUTURE WORK 196

7.1 Introduction 196

7.2 Studies on NCL working with water 196

7.3 Studies on molten salt natural circulation loop 198

7.4 Scope for future work 200

REFERENCES 201

LIST OF FIGURES

Figure 1.1: Schematic diagram of rectangular natural circulation loop....................................3

Figure 2.1: Density variation of molten salt (mixture of $NaNO_3$+KNO_3 in 60:40 by weight) with temperature..16

Figure 2.2: Variation of Specific heat of molten salt (mixture of $NaNO_3$+KNO_3 in 60:40 by weight) with temperature..17

Figure 2.3: Variation of dynamic viscosity of molten salt (mixture of $NaNO_3$+KNO_3 in 60:40 by weight) with temperature...18

Figure 2.4: Variation of thermal conductivity of molten salt (mixture of $NaNO_3$+KNO_3 in 60:40 by weight) with temperature...19

Figure 3.1: Schematic diagram of molten salt natural circulation loop (MSNCL) 43

Figure 3.2: Photograph of MSNCL experimental facility 44

Figure 3.3 Flow sheet (P&ID) of MSNCL 45

Figure 3.4: Experimental data obtained at steady state condition achieved by MSNCL at different heater powers 54

Figure 3.5: Variation of experimental steady state Reynolds number with non-dimensional parameter $\left(Gr_m / N_G\right)$..56

Figure 3.7: Experimental observation of transient variation of temperature at different location in PRSS transient of 1500 W to 1600 W 59

Figure 3.8: Experimental observation of transient variation of temperature at different location in PRSS transient of 1600 W to 1700 W 60

Figure 3.9: Experimental observation of transient variation of temperature at different location in PRSS transient of 1800 W to 2000 W 61

Figure 3.10: Transient variation of temperature at different location in power step back transient of 2000 W to 1800 W by experimental observation 62
Figure 3.11: Transient variation of temperature at different location in power step back transient of 1800 W to 1600 W by experimental observation 63
Figure 3.12: Transient variation of temperature at different location in power step back transient of 1600 W to 1400 W by experimental observation 63
Figure 3.13: Transient variation of temperature at different location in power step back transient of 1400 W to 1200 W by experimental observation 64
Figure 3.14: Transient variation of temperature at different location in loss of heat sink transient of 1200 W by experimental observation 66
Figure 3.15: Transient variation of temperature at different location in loss of heat sink transient of 1500 W by experimental observation 67
Figure 3.16: Transient variation of temperature at different location in Power trip transient of 2000 W by experimental observation 69
Figure 4.1: Schematic diagram of water loop (Vijayan et al., 2001) 71
Figure 4.2 Cross-sectional view of cooler section 74
Figure 4.3: Mesh generated for the computational domain 75
Figure 4.4: Mesh independence study 82
Figure 4.5: Time step independence study 82
Figure 4.6: Steady state characteristics of VHVC configuration; Comparison of computed result with experimental data and correlations 86
Figure 4.7: Steady state characteristics of VHVC configuration; Comparison of computed result with experimental data and correlations. 87
Figure 4.8: Comparison of computed transient variation of pressure drop with time in VHHC configuration at 232 W 90

Figure 4.9: Comparison of computed transient variation of pressure drop with time in VHHC configuration at 368 W 90

Figure 4.10: Computed transient variation of $\Delta P_{bottom\ leg}$ in VHVC configuration at 105 W .. 91

Figure 4.11: Temperature fields in central vertical plane at different instants of an oscillatory cycle for VHVC configuration at 105 W; (A) 25 s, (B) 100 s, (C) 150 s, (D) 200 s, (E) 225 s, (F) 300 s 93

Figure 4.12: Transient variation of ΔP in HHHC configuration at 120 W; Comparison of computed results with experimental data. 95

Figure 4.13: Transient variation of ΔP in HHHC configuration at 220 W; Comparison of computed results with experimental data 96

Figure 4.14: Predicted transient variation of $\Delta P_{across\ bottom\ leg}$ at 450 W HHHC configuration 96

Figure 4.15: Comparison of computed transient ($\Delta P_{across\ bottom\ leg}$ with time) obtained from laminar model with experimental data for 120 W HHHC configuration 97

Figure 4.16: Comparison of computed transient ($\Delta P_{across\ bottom\ leg}$ with time) obtained from laminar model with experimental data for 220 W HHHC configuration 97

Figure 4.17: Temperature contour and vector representation in a cross-sectional plane (a) at heater (b) at cooler in HHHC configuration 99

Figure 4.18: Comparison of computed transients ($\Delta P_{across\ bottom\ leg}$ with time) obtained from Standard k-ε turbulence and low-Re k-ε turbulence models with experimental data for 220 W HHHC configuration 99

Figure 4.19: Comparison of computed transients ($\Delta P_{bottom\ leg}$ with time) obtained from Standard k-ε turbulence and low-Re k-ε turbulence models with experimental data for 120 W HHHC configuration 100

Figure 4.20: Transient variation of $\Delta P_{bottom\ leg}$ for HHVC configuration at 257 W 101

Figure 4.21: Comparison of computed transients ($\Delta P_{bottom\ leg}$ with time) obtained from Standard k-ε turbulence and low-Re k-ε turbulence models with experimental data for 257 W HHVC configuration 102

Figure 4.22: Temperature contours at different time instants in 257 W HHVC (mentioned temperature is in Kelvin) 104

Figure 4.23: Enlarged portion of flow initiation transient for HHHC at 120 W showing one cycle of unidirectional oscillation 106

Figure 4.24: Temperature contours at various time instants of an oscillatory cycle for HHHC configuration at 120W 107

Figure 4.25: Enlarged portion of flow initiation transient for HHHC at 450 W showing one cycle of bi-directional oscillation 108

Figure 4.26: Temperature field in central vertical plane at different time instances for HHHC at 450W 110

Figure 4.27: Predicted transient variation of Temperature at different locations in 120 W HHHC configuration 111

Figure 4.28: Predicted transient variation of Temperature at different locations in 450 W HHHC configuration 112

Figure 4.29: Predicted transient variation of ΔT across heater at 120 W HHHC configuration 113

Figure 4.30: Predicted transient variation of ΔT across heater at 450 W HHHC configuration 113

Figure 4.31: Computed transient variation of $\Delta P_{bottom\ leg}$ during power raising from 220 W to 450 W in HHHC configuration 114

Figure 4.32: Prediction of transient variation in power step back from 220 W heater power to 120 W heater power in HHHC configuration 115

Figure 4.33: Prediction of transient variation in power step back from 220 W heater power to 45 W heater power in HHHC configuration......................................116

Figure 5.1: Mesh adopted in the CFD model (a) mesh in a vertical plane, (b) mesh at cooler outlet cross-section, and (c) mesh in the primary fluid cross-section 121

Figure 5.2: Velocity variation at heater inlet using different mesh size in radial direction...125

Figure 5.3: Velocity variation at heater outlet using different mesh size in radial direction.126

Figure 5.4: Velocity variation at left leg using different mesh size in axial direction...........126

Figure 5.5: Temperature variation at left leg using different mesh size in axial direction....127

Figure 5.6: Schematic diagram of pipe flow problem 128

Figure 5.7: Comparison of computed axial velocity profile with the velocity profile obtained from analytical expression in a laminar pipe flow problem 128

Figure 5.8: Transient variation of temperature at heater inlet 129

Figure 5.9: Transient variation of temperature at heater outlet 130

Figure 5.10: Transient variation of velocity at heater inlet..130

Figure 5.11: Transient variation of velocity at heater outlet...131

Figure 5.12: Transient variation of heater outlet temperature with different time steps in the sudden power trip of 2000 W steady state condition of VHHC configuration..132

Figure 5.13: Comparison of computed steady state temperature at different locations in the loop with corresponding temperature observed in experiment...................134

Figure 5.16: Comparison of computed steady state Reynolds number with different correlations and experimental data of VHHC configuration............................137

Figure 5.17: Comparison of computed steady state Reynolds number with different correlations and experimental data of HHVC configuration............................138

Figure 5.18: Transient variation of computed $\Delta T_{across\ heater}$ and mass flow rate in 1000 W VHVC configuration 141

Figure 5.19: Transient variation of computed $\Delta T_{across\ heater}$ and mass flow rate in 2000 W VHVC configuration 141

Figure 5.20: Computed transient variation of mass flow rate in 2000 W VHVC configuration..142

Figure 5.21: Temperature contours at different time instants in 2000 W VHVC configuration..143

Figure 5.22: Comparison of computed transient variation of mass flow rate in VHVC configuration for different heater powers 144

Figure 5.23: Computed flow initiation transient of 1200 W heater power VHHC configuration..146

Figure 5.24: Computed transient variation of ΔT across heater and mass flow rate in 2000 W VHHC configuration...146

Figure 5.25: Computed transient variation of heater outlet temperature in 2000 W VHHC configuration..147

Figure 5.26: Transient variation of computed $\Delta T_{across\ heater}$ and mass flow rate in 1200 W HHVC configuration 148

Figure 5.27: Transient variation of computed $\Delta T_{across\ heater}$ and mass flow rate in 2000 W HHVC configuration 148

Figure 5.28: Computed transient variation of mass flow rate in 2000 W HHVC configuration..149

Figure 5.29: Temperature contours at different time instants in 2000 W HHVC configuration..151

Figure 5.30: Comparison of computed transient variation of mass flow rate in HHVC configuration for different heater power 152

Figure 5.31: Computed transient variation of mass flow rate in 1000 W HHHC configuration..153

Figure 5.32: Comparison of computed transient variation of $\Delta T_{across\ heater}$ with mass flow rate in 1000 W HHHC configuration 153

Figure 5.33: Comparison of computed transient variation of $\Delta T_{across\ heater}$ with mass flow rate in 1800 W HHHC configuration 154

Figure 5.34: Enlarged portion of transient variation of mass flow rate in 1000 W HHHC configuration..156

Figure 5.35: Temperature contours of central vertical plane of 1000 W HHHC configuration at different time instants..157

Figure 5.36: Comparison of experimental and computational data of PRSS transient in VHHC configuration at 1200 W to 1500 W...159

Figure 5.37: Comparison of experimental and computational data of PRSS transient in VHHC configuration at 1500 W to 1600 W...159

Figure 5.38: Comparison of experimental and computational data of PRSS transient in VHHC configuration at 1600 W to 1700 W...160

Figure 5.39: Comparison of experimental and computational data of PRSS transients in VHHC configuration at 1800 W to 2000 W...160

Figure 5.40: Power step back transient: 2000 W to 1800 W in VHHC configuration 162

Figure 5.41: Comparison of Power step back transient: 1800 W to 1600 W in VHHC configuration..162

Figure 5.42: Comparison of Power step back transient: 1600 W to 1400 W in VHHC configuration..163

Figure 5.43: Transient variation of temperature at heater outlet and cooler inlet during power trip transient; Comparison of experimental data with CFD models (with and without expansion tank) 164
Figure 5.44: Temperature contour at the steady state condition of 2000 W VHHC configuration..167
Figure 5.45: Comparison of computed transient variation of temperature at different locations with experimental data during the power trip of 2000 W VHHC configuration..168
Figure 5.46: Comparison of predicted computational data with experimental data in the transient study of loss of heat sink at 1200 W heater power VHHC configuration..169
Figure 5.47: Comparison of predicted computational data with experimental data in the transient study of loss of heat sink at 1500 W heater power VHHC configuration..170
Figure 5.48: Transient variation of mass flow rate, maximum, minimum and average temperature of the loop during loss of heat sink at 1500 W VHHC 170
Figure 6.1: Schematic diagram of vertical pipe and half loop..174
Figure 6.2: Comparison of computed local Nusselt number with correlations for (a) Re=500 and (b) Re=1000 176
Figure 6.3: Comparison of computed local Nusselt number with correlations for (a) Re=1500 and (b) Re=2000 177
Figure 6.4: Temperature contour at heater section in 1200 W VHHC 178
Figure 6.5: Variation of wall temperature and bulk fluid temperature at heater in 1200 W VHHC..179
Figure 6.6: Comparison of computed Nusselt number with correlations 179

Figure 6.7: Schematic diagram of half loop..180

Figure 6.8: Comparison of computed local Nusselt number obtained in full loop of MSNCL with that in half loop at a heater power of 1200 W 181

Figure 6.9: Comparison of computed local Nusselt number obtained in full loop of MSNCL with that in half loop at a heater power of 2000 W 182

Figure 6.10: Comparison of computed velocity profile at heater inlet of 1200 W VHHC with the fully developed velocity profile by analytical expression...................183

Figure 6.11: Comparison of computed local Nusselt number at different Reynolds number in half loop with and without consideration of gravity term................185

Figure 6.12: Nusselt number of molten salt at turbulent region in half loop.........................186

Figure 6.13: Transient variation of mass flow rate for 1800 W HHHC configuration..........187

Figure 6.14: Enlarged portion of transient variation of mass flow rate for 1800 W HHHC configuration...188

Figure 6.15: Temperature contours of central vertical plane of 1800 W HHHC configuration at different time instants...190

Figure 6.16: Cross-sectional plane situated at the middle of the heater 191

Figure 6.17: Temperature contours of the cross-sectional plane at (a) 160 s, (B) 190 s,(C) 205 s, (D) 210 s, (E) 215 s, (F) 220 s, (G) 235 s, and (H) 260 s. 192

Figure 6.18: Transient variation of mass flow rate in the loop and local Nu in the cross-sectional plane at the middle of the heater section 193

Figure 6.19: Comparison of transient variation of loop mass flow rate, local Nu, local surface temperature, local bulk temperature and local temperature difference.194

LIST OF TABLES

Table 2.1: Different applications and types of molten salts in nuclear reactors [David Samuel, (2009)] 20

Table 2.2: ORNL MSR systems and key features (David Samuel, 2009)....................22

Table 2.3: Operational solar thermal facilities with molten salt as thermal energy storage system (Kurvi et al. 2013) 24

Table 3.1: Material used to construct the MSNCL....................46

Table 3.2: Test matrix for experiments in MSNCL....................53

Table 4.1: Constants used in Eq. 4.13....................85

Table 5.1: Constants used to evaluate the thermo-physical properties of solar salt [Nissen (1982), Ferrie et al., (2008)] 122

Table 5.2: Thermo-physical properties of solar salt (at 300^{o}C) obtained from Eq. 5.1....................123

NOMENCLATURE

A	flow area (m^2)
a	constant
a_i	dimensionless flow area, A_i/A_r
b	constant
c	constant
C	constant in Eq. (2)
C_p	specific heat (J kg^{-1} K^{-1})
D	Hydraulic diameter, m
d	constant
d_i	dimensionless hydraulic diameter, D_i/D_r
E	total energy (W)
exp	exponential
g	gravitational acceleration (m s^{-2})
Gr	Grashoff number
Gr_m	modified Grashoff number (Eq. 2)
Gz	Greatz number
H	loop height (m)
k	turbulent kinetic energy
K	thermal conductivity (W m^{-1} K^{-1})
L	length, m
N	total number of pipe segments
N_G	dimensionless parameter
Nu	Nusselt number
Pr	Prandtl number
p	pressure (Pa)

Q	total heat input (W)
q”	heat flux (W m^{-2})
r	constant in Eq. (2)
Ra	Rayleigh number
Re	Reynolds number
T	temperature (K)
T_0	reference temperature (K)
t	time (s)
v	velocity (m s^{-1})
$\dot{m}$	mass flow rate (kg s^{-1})
x	distance from entrance (m)
ΔP	Pressure difference (mm of water column)
ΔT	temperature difference (K)
Δz	centre line elevation difference between cooler and heater, (m)

Greek Symbols

ρ	density of fluid (kg m^{-3})
ρ_0	reference density (kg m^{-3})
β	thermal expansion co-efficient (K^{-1})
μ	dynamic viscosity (Ns m^{-2})
υ	kinematic viscosity (m^2 s^{-1})
ε	turbulent dissipation rate

Subscripts

avg	average

b	bulk
CFD	Computational Fluid Dynamics
ci	cooler inlet
co	cooler outlet
cs	cross-sectional plane
eff	effective
expt	experiment
h	heater
hi	heater inlet
ho	heater outlet
i	i^{th} segment
max	maximum
min	minimum
r	reference value
s	surface
ss	steady state
t	turbulent
w	wall

Abbreviations

AHTR	Advanced High Temperature Reactor
CAREM	Central Argentina de Elementos Modulares
CI	Cooler Inlet
CFD	Computational Fluid Dynamics
CLOP	Complete Loss Of Power
CO	Cooler Outlet

cP	centiPoise (1 mPa-s=10^{-3} Pa.s)
CSP	Concentrating Solar Power
CV	Control Valve
DACS	Data Acquisition and Control System
Expt	Experiment
HI	Heater Inlet
HHHC	Horizontal Heater Horizontal Cooler
HHVC	Horizontal Heater Vertical Cooler
HO	Heater Outlet
HTGR	High Temperature Gas cooled Reactor
HTR	High Temperature Reactor
ID	Internal Diameter
LBE	Lead Bismuth Eutectic
LES	Large Eddy Simulation
LFR	Lead-cooled Fast Reactor
MASLWR	Multi-Application Small Light Water Reactor
mPa	milliPascal (=10^{-3} Pa)
MSFBR	Molten Salt Fast Breeder Reactor
MSNCL	Molten Salt Natural Circulation Loop
MSR	Molten Salt Reactor
MW	Mega Watt
NB	Nominal Bore
NCL	Natural Circulation Loop
NGNP	Next Generation Nuclear Plant
NHI	Nuclear Hydrogen Initiative

NITI	National Institution for Transforming India
ORNL	Oak Ridge National Laboratory
PHWR	Pressurised Heavy Water Reactor
PRSS	Power Raising from Steady State
PRV	Pressure Regulating Valve
PWR	Pressurised light Water Reactor
RV	Relief Valve
SFR	Sodium-cooled Fast Reactor
SS	Stainless Steel
SSTAR	Small, Sealed, Transportable, Autonomous Reactor
STAR-LM	The Secure, Transportable, Autonomous Reactor-Liquid Metal variant
STP	Standard Temperature and Pressure
VHHC	Vertical Heater Horizontal Cooler
VHTR	Very High Temperature gas cooled Reactor
VHVC	Vertical Heater Vertical Cooler
VVER	Vodo-Vodyanoi Energetichesky Reaktor; Water-Water Power Reactor

CHAPTER 1

INTRODUCTION

1.1 Introduction

India is the fourth largest energy consuming nation in the world after China, Russia and United States, according to a report released by U.S. Energy Information and Administration in April 2013. According to the NITI Ayoga report (2015), the overall power installed capacity in India will increase from 193 GW in the year 2011-12 to 562 GW in the year 2030. In this, share from renewable energy in the year 2030 would be 170 GW, that is almost 32% of the overall power capacity. Given India's growing energy demands and limited domestic fossil fuel reserves, the country has ambitious plans to expand its renewable and nuclear power industries.

Utilization of solar power is one of the options to expand renewable energy. Sunlight can be converted into electricity by using photovoltaic (PV) cells or solar thermal power plant. In solar thermal power plant, power is generated by concentrating solar rays on a receiver to generate high pressure steam which is used to drive a steam turbine and generator to finally produce electricity. But the sunlight is an intermittent resource whose intensity is subject to planetary rotation, orbit and atmospheric effects associated with weather conditions. This leads to the unavailability of sunlight during night time and during cloudy weather conditions. This drawback can be taken care in solar power plants by using heat storage medium. This is the distinct advantage of solar thermal power plants compared with other renewable energies, such as wind, tidal and the solar energy from PV cells. This method of heat storage is relatively cheap. Storing electricity is much more expensive than storing thermal energy.

Molten salts are used as heat transfer and heat storage media in solar thermal power plants, because molten salts exhibit high boiling point at low pressure. Molten nitrate salts and fluoride salts are useful for high temperature applications. Many of the parabolic solar trough plant projects, such as La Florida Bdajoz, Andasol-1 Granada, Andasol-2 Granada, Extresol-1, Ciudad Real, Manchasol-2 are from spain and Archimede Sicily of Italy have used molten nitrate salt as heat storage medium (Kuravi et al., 2013). Recent development of 768 KWe (approximately) solar power tower system at Bhabha Atomic Research Centre (BARC) is based on natural circulation of molten nitrate salt (Jaiswal et al., 2011). Apart from solar thermal power plant, molten salt is also useful in high temperature nuclear reactors. The development of 600 MWth high temperature nuclear reactor (Duler and Sinha, 2008), cooled by natural circulation of fluoride salt and capable of supplying process heat at high temperature is in progress to facilitate hydrogen production by splitting water. Fast breeder reactor working with molten salt coolants is also being designed (Borghoain et al., 2015). Both forced circulation and natural circulation of molten salt coolant has been evaluated for this reactor. It is observed that molten salt is increasingly being used in various applications as given above. These systems are also increasingly using passive cooling by molten salt. Beside these, natural circulation mode of heat transfer is the only way to remove the decay heat in case of accidental conditions of nuclear reactor. Many other systems employing molten salt are described in Chapter 2 of this thesis.

It is important to estimate heat removal capacity of molten salt in natural circulation condition. Hence, it is required to study the thermal-hydraulic behaviour of molten salt in a natural circulation. Such a study is performed in a natural circulation loop. Natural circulation loop is the representative of primary heat transport system of nuclear reactor having passive cooling system. The following sections contain detailed information about natural circulation loop, molten salts and their suitability for heat transfer applications. The objective of present research work is then explained in detail.

1.2 Natural Circulation Loop

Natural Circulation Loop (NCL) consists of a heater at lower elevation and cooler at higher elevation. Heater and cooler are connected by piping as shown in Fig. 1.1. At a time only one heater and one cooler is operated. In NCL, heat is supplied in the heater. As the consequence of the heat flux, the heated part of the fluid becomes lighter and rises up and reaches cooler. In the cooler, heat is rejected to secondary coolant. The cooled fluid becomes denser and drops down due to gravity. These combined effects establish natural circulation of the fluid in the loop. Thus, the motive force for the flow in NCL is generated simply because of the presence of the heat source and heat sink, without need of any external force. If the heat addition in source and heat removal in sink is maintained, a steady state is expected to be achieved. In a steady state, the heat absorbed by fluid at the source gets fully rejected at the sink.

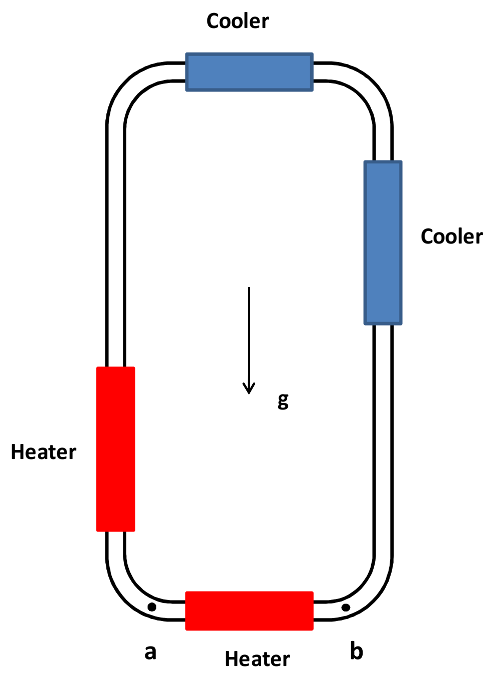

Figure 1.1: Schematic diagram of rectangular natural circulation loop

It is possible to operate a NCL in four different configurations. These are (i) Vertical Heater Vertical Cooler (VHVC), (ii) Vertical Heater Horizontal Cooler (VHHC), (iii) Horizontal Heater Vertical Cooler (HHVC) and (iv) Horizontal Heater Horizontal Cooler (HHHC) configuration. For HHHC configuration, the generation of flow in NCL due to heating (in heater) and cooling (in cooler) can be explained as below.

Assuming flow is established in anti-clockwise direction, following analysis can be done. Under steady state condition, right vertical leg gets filled with hot fluid, left vertical leg gets filled with cold fluid. We assign a density of ρ_h to the vertical leg filled with hot fluid and ρ_c to the other vertical leg containing cold fluid. Now we can obtain the hydrostatic pressure, P_a and P_b at the locations 'a' and 'b' located at the extremes of the bottom horizontal leg (Fig.1) as:

$$P_a = \rho_c g H \tag{1.1}$$

$$P_b = \rho_h g H \tag{1.2}$$

Where H is the loop height and g is the acceleration due to gravity. Clearly, since $\rho_c > \rho_h$, $P_a > P_b$ leading to a pressure difference between locations 'a' and 'b'. At steady state, the driving buoyancy force is balanced by the frictional forces.

It is easy to note that the induced flow rate can be increased by increasing the loop height and the density difference between the two vertical legs. Enhancing the loop flow area reduces the hydraulic resistance which increases the flow rate. This discussion on Eq. 1.1 and 1.2 is just to explain how a natural circulation is formed in the loop due to differing densities leading to differential pressure and eventually a circulation, as long as heater and cooler are kept active. These equations are not used for analysis or generating any results.

The absence of moving/rotating parts to generate the motive force for flow makes a natural circulation loop less prone to failures. Also maintenance and operating costs are reduced. Due to this, natural circulation loops find several engineering applications in conventional as well as nuclear industries. Notable among these are solar water heaters, transformer cooling, geothermal power extraction, cooling of internal combustion engines, gas turbine blades, computer cooling and nuclear reactor cores. In view of this, the detailed study of natural circulation loop has to be carried out.

A natural circulation loop is representative of primary heat transport system of a nuclear reactor in following way. The heater represents core of the nuclear reactor in which fission heat is generated. Cooler represent heat exchanger in a nuclear reactor in which heat from primary coolant is removed. In different types of nuclear reactors, the locations of the heat source (core) and the heat sink (steam generator) are different. For example, PHWRs (Pressurised Heavy Water Reactors) have horizontal core and vertical steam generators, PWRs (Pressurised light Water Reactors) have vertical core and vertical steam generator and VVERs (Vodo-Vodyanoi Energetichesky Reaktor; Water-Water Power Reactor) have vertical core and horizontal steam generators. So HHVC configuration is the representative of an Indian PHWR. The VHVC configuration is representative of a PWR and VHHC is the representative of VVERs. The steady state as well as transient characteristics of these different configurations of NCLs is different and hence each configuration has to be individually studied. Working fluid in a NCL can be water, CO_2, liquid metal or molten salt. The working fluid also influences behaviour of a NCL. In the present work, molten salt has been considered as a working fluid in a NCL.

1.3 Molten salt as a coolant

High Temperature Reactor (HTR) and solar thermal power plants use molten salts as a coolant. Molten salts have comparatively low melting point and high boiling point at atmospheric pressure. This is highly desirable because a high temperature system can be designed without increasing system pressure. Hence design and operation of molten salt based system gets simplified. Molten nitrate salt is useful as a coolant in the 300^{o}C to 600^{o}C temperature range whereas fluoride salt (FLiNaK) is useful in the 454^{o}C to 1570^{o}C temperature range. There are numerous salt compositions that can be considered for use. However, the nitrates of sodium and potassium can be shown to be of great interest as a coolant/heat transfer fluid particularly in solar power plants and at moderate high temperature systems. The sulphates and phosphates are too corrosive. The melting points of the carbonates and fluorides are too high. Hence these are not useful. The nitrates show the low melting points (around 238^{o}C for mixture of $NaNO_3$+KNO_3 in 60:40 by weight) and the high boiling point (upper limit of liquid phase of mixture of $NaNO_3$+KNO_3 in 60:40 by weight is around 600^{o}C). Because of these reasons and also due to low cost and easy availability of nitrates made them suitable as heat transfer fluid/coolant in solar power plants. The fluorides show high melting point and high boiling point compared to nitrates. Hence they are suitable for high temperature systems such as high temperature reactor. Molten fluoride salt has been proposed as candidate coolants for HTR (Dulera and Sinha, 2008). The commercial molten salt, consisting of sodium nitrate ($NaNO_3$) and potassium nitrate (KNO_3) in 60:40 ratio by weight, is normally used in solar power plants. This molten nitrate salt has been proposed as a coolant/heat transfer fluid in solar power plant (Jaiswal et al., 2011). The mentioned molten nitrate salt has the volumetric heat capacity similar to water and has similar viscosity as water and flows much like water does. The major advantage of molten salt over water is higher temperatures attainable in the molten salt state and if the salt solidifies (freezes) it contracts versus expanding like water. Thus, molten salt freezing in a pipe would not burst the pipe as water would. However there are certain challenges in the operation of a molten nitrate salt based system which are described later.

1.4 Objective of present work

Nuclear reactors continue to generate heat even after shutdown due to radioactive decay of fission products. In the absence of cooling, this decay heat is large enough to cause fuel overheating and subsequent melting in case of complete loss of power as exemplified by Fukushima plant, which experienced long term station block out following a massive earthquake and the resultant Tsunami. Further, next generation nuclear reactors are being designed to remove even full power by natural circulation of coolant. Similarly, the solar power plant can be designed to transfer the solar heat by natural circulation system. Natural circulation heat removal is inherently safe. The process of heat removal by natural circulation has been studied using the natural circulation loops. Most of the studies in the literature show that major work has been carried out by taking water as a fluid in natural circulation loop. But water cannot be used to remove the heat at a high temperature system at low pressures. Molten salts have the desirable properties to remove the heat of a high temperature system even at low pressure condition (Forseberg et al., 2005). Hence, an experimental and computational study on molten salts as a working fluid in natural circulation system is required to understand the thermal hydraulic behaviour of molten salt natural circulation loop.

In the present research work, natural circulation with molten salt has been undertaken. The study on thermal-hydraulic behavior of Molten Salt Natural Circulation Loop (MSNCL) is performed experimentally as well as through three-dimensional (3D) Computational Fluid Dynamics (CFD) simulation. The main objectives of the present study are given below.

- To perform experiments in high temperature molten salt natural circulation loop.
- To collect experimental data during steady state and transient operation of molten salt natural circulation loop.
- To perform CFD simulations of molten salt natural circulation loop.
- To study the effect of orientation of heater and cooler in a natural circulation loop using CFD simulation.

- To estimate the minimum and maximum heater power limits which ensures that molten salt remains in a stable liquid state in the experiment. Below certain heater power, molten salt will freeze in the loop while above a certain heater power, molten salt stability is lost. Finding these limits in an experimental loop is not possible. Computational studies have been carried out to find these limits.
- Experiments on NCL working with water indicated oscillatory flow for HHHC configuration. A main goal of this work is to understand the reason behind oscillatory flow obtained in HHHC configuration of natural circulation loop working with water. In the experiments, limited data only can be extracted and hence it's not possible to understand in detail the physics behind formation of typical flow patterns. But in 3D transient CFD simulations there is no such limit.
- To study detailed heat transfer characteristics of molten salt natural circulation loop, especially in heater section of the loop.

Steady state and transient characteristics of molten salt loop are required to understand the loop behaviour. In solar power tower system due to the variation of sunlight intensity, the power raising and power step back will occur. This situation can be simulated in a NCL by changing heater power.

To understand the steady state and transient behaviour of molten salt natural circulation loop at different heater and cooler configuration, theoretical studies are also required to be carried out. In theoretical studies many researchers (Welander, 1967, Creveling et al., 1975, Vijayan and Austergesilo, 1994) performed studies by solving one-dimensional mass, momentum and energy equations. Various phenomena have been studied by them. In their studies, various steady state correlations for determination of mass flow rate have been developed. In 1967, Welander (Welander, 1967) explained the instabilities occurring in the natural circulation loop on the basis of hot and cold packets. Later, Vijayan et al. (2001), also explained the instabilities in the natural circulation loop by plotting centre line temperature distribution in the loop at different instants of time obtained from their 1D simulations. Their observation also confirms the Welander's observation. Many simplified assumptions are used while performing one-dimensional modelling. Some of the assumptions used by researchers are as follows:

- Neglect of 3D flows in horizontal heater/cooler, elbows, expansion tank etc.
- The use of constitutive laws for friction and heat transfer derived from steady state forced convection experiments.
- The neglect of developing boundary layer conditions in heated and cooled sections
- The neglect of axial heat conduction along the heated walls and in the bulk fluid.
- The use of first order numerical schemes.
- The use of 1-D balance equations based on cross-section averaged variables.
- Expansion tank used in experimental set up are not modeled.

Because of these short-comings in the one-dimensional models developed by researchers, the present study has been carried out by using three-dimensional (3D) Computational Fluid Dynamics (CFD). In 3D CFD model, there is no need to make these simplified assumptions. 3D CFD simulations are now possible due to the following reasons.

❖ In 3D CFD simulations, exact geometry of NCL can be modeled including elbows, coolers, expansion tank etc. (there is no need to incorporate estimated loss coefficients, approximate accounting of effect of expansion tank, other local heat transfer and flow phenomena, roughness factor of pipe and fittings etc.).

- ❖ The loop geometry demands large number of grids and structured/unstructured grid based solvers with parallel computation. These are available in commercial CFD softwares.
- ❖ Multi-core computers are easily available to perform computationally expensive parallel simulations.
- ❖ 3D CFD simulations offers certain advantages over experimental studies as experiments cannot be performed for all systems with different geometries, flow conditions, different fluids etc., as they are expensive and time consuming. Also in experimental investigation, only a limited number of probes can be put and hence limited data can be extracted. In 3D CFD simulations, very large amount of data is generated in the form of spatial and temporal variation of all primitive variables (**u**, T, k, ε).

The 3D temperature field computed from simulation can be analysed and it is possible to explain various phenomenon associated with natural circulation systems.

In CFD simulation there is no need to use heat transfer correlations. Heat transfer phenomenon occurring in the heater and cooler can be studied for various orientations and geometries of heater and coolers. In natural circulation loop the fluid flow and heat transfer are associated with hydro-dynamically and thermally undeveloped flow, local recirculation effect, mixed convection phenomenon etc. All these studies can be performed with 3D CFD simulation.

1.5 Accomplishment of present project

In accordance with the objectives mentioned earlier, various steady state and transient studies were successfully carried out in molten salt natural circulation loop. 3D CFD simulations of the same are performed and excellent agreement between experiment and computational results is obtained in all the cases. The 3D CFD simulations of natural circulation loop working with water were also carried out. These studies are carried out using various models such as laminar, low-Re k-ε turbulence model and high Re standard k-ε turbulence model until good agreement with experimental data was obtained. This thesis gives detailed information about the above in following chapters.

1.6 Organization of the thesis

The outline of the thesis includes seven chapters and brief description of these is given below.

Chapter 1: This chapter describes the introduction to natural circulation loop, molten salts and their applications and the objective of present research work.

Chapter 2: In this chapter, literature review is presented. In literature review chapter, molten salts and their thermo-physical properties have been described. Experimental studies carried out in natural circulation loops by various researchers have been reviewed. The review of theoretical studies for steady state and instabilities has been carried out. The review work for heat transfer is also given in this chapter.

Chapter 3: This chapter describes the experimental set-up and procedure followed to conduct various steady state and transient studies. The various experiments conducted are explained with the experimental results. Steady state experiments are performed in the molten salt natural circulation loop for VHHC configuration. Transient studies are also carried out for power raising, power step back, power trip and loss of heat sink conditions. Results obtained in test set up are explained in this chapter.

Chapter 4: This chapter describes the 3D CFD analysis of NCL working with water for various steady state and transient cases. Experimental data for the same is available in literature. The comparison of computed results with available experimental data and correlations in the literature is also done. The formation of different types of instabilities and the reason for their occurrence in NCL has been explained with the help of temperature contours obtained at different instants of time.

Chapter 5: This chapter describes the 3D CFD simulations performed for molten salt natural circulation loop (VHHC configuration). The steady state simulations have been performed to estimate the primary fluid (molten salt) mass flow rate induced in the loop at various heater powers. The steady state Reynolds number calculated from CFD simulations at different heater powers is plotted as a function of Grashof number and geometrical parameter. Comparison of computational and experimental temperatures at different locations and at different heater powers is performed. Various transient simulations for power raising from steady state and power step back, power trip and loss of heat sink are performed for VHHC configuration and compared with experimental data collected in experiment. Simulations for power trip and loss of heat sink are also carried out by considering the expansion tank in the CFD model.

Chapter 6: This chapter describes the heat transfer characteristics of molten salt natural circulation loop using 3D CFD simulation. The laminar heat transfer characteristics of MSNCL over a range of Reynolds number have been estimated. Effect of mixed convection has been studied at low Reynolds numbers. The Nusselt number obtained in CFD has been compared with the correlation for mixed convection. The heat transfer characteristics of hydro-dynamically developed and thermally developing molten salt flow in laminar region have been obtained from CFD and are compared with the available correlations. The unsteady heat transfer characteristics in the oscillatory flows are studied. The computed turbulent heat transfer characteristics of MSNCL are compared with Dittus-Boelter, Sieder and Tate correlations and also with the correlation by Liu.

Chapter 7: This chapter describes the summary of the work and conclusions made from the study. Recommendations for future work also described in this chapter.

1.7 Closure

This chapter introduces the need of renewable and nuclear energy in India, natural circulation system, molten salts and their properties. Natural circulation loop and its working principle have been explained. Classification of natural circulation loops based on the location of heater and cooler and their relevance with existing nuclear reactors has been explained. Molten salts and their favourable thermo-physical properties those made them suitable as a coolant in high temperature systems has been explained. Necessity of studying steady state and transient characteristics of molten salt natural circulation loop has been explained. Objectives of the present research work are explained.

CHAPTER 2

REVIEW OF LITERATURE

In this chapter, literature review on molten salts and their properties and applications have been explained. An overview of the properties which make molten salts suitable as a coolant/heat storage fluid in high temperature systems has been given. Literature survey on natural circulation loops and their heat transfer characteristics has been presented.

2.1 Molten salts

Molten Salt is a rather dreadful name for a useful category of materials and processes. The term "Molten Salt" is self-descriptive; it is melted salt(s). Another common name is Fused Salt(s). Molten salt refers to a salt that is in the liquid phase that is normally a solid at standard temperature and pressure (STP). The simplest example of a molten salt is common salt. Take sodium chloride ("table salt") and heat it to a red hot (greater than 801° C) where it would melt into a liquid. This liquid is stable, has a heat capacity similar to water (by volume) and flows much like water. The major differences are the obvious *higher temperatures attainable in the molten salt state* and when the salt solidifies (freezes) it contracts versus expanding like water. Thus, molten salt freezing in a pipe would not burst the pipe as water would. Besides these properties, molten salts show low melting point and high boiling point at low pressure. These favourable characteristics of molten salts make them useful as a coolant/fuel salt in nuclear applications and also coolant/heat transfer fluid in solar thermal power plants.

2.1.1 Thermo-physical properties of molten salts

2.1.1.1 Melting point

The molten salt coolants are binary/ternary systems. Multi-component mixtures have lower melting points than single salts (David Samuel, 2009). For example, melting point of $NaNO_3$ is 308°C and KNO_3 is 334°C but the solar salt which is the mixture of $NaNO_3+KNO_3$ (60:40 by weight) has melting point of 220°C.

2.1.1.2 Boiling point and Vapour pressure

Apart from melting point, the boiling point and vapour pressure of the liquid coolant are the major properties of concern. In general, higher the boiling point of a liquid, the lower the vapour pressure of the liquid (i.e. less volatile). High boiling point is desirable because it allows us to operate a system over a wider temperature range.

2.1.1.3 Density

Molten salt density (ρ) decreases linearly as temperature increases (David Samuel, 2009). It is an important property since it affects heat transfer characteristics (such as volumetric heat capacity). This is very important for natural circulation systems. Ferrie et al. (2008), mentioned that, the molten salt mixture of $NaNO_3+KNO_3$ (60:40 by weight) can be used between 533 K and 873 K. With decreasing temperature, the mixture begins to crystallize at 511 K and is completely solid at 494 K. They also mentioned the correlation to find out the liquid specific volume in terms of temperature (unit of temperature as K) of the above mentioned salt, that is

$$v = \frac{1}{2090 - 0.636\text{x}(\text{T} - 273.15)} \qquad \left(\text{m}^3/\text{kg} \right) \tag{2.1}$$

According to them, the density can be written as,

$$\rho = 2090 - 0.636\text{x}(\text{T} - 273.15) \qquad \left(\text{kg}/\text{m}^3 \right) \tag{2.2}$$

Figure 2.1 shows the linear variation of density of molten salt (mixture of NaNO3+KNO3 in 60:40 by weight) with temperature. The unit of temperature is in Kelvin.

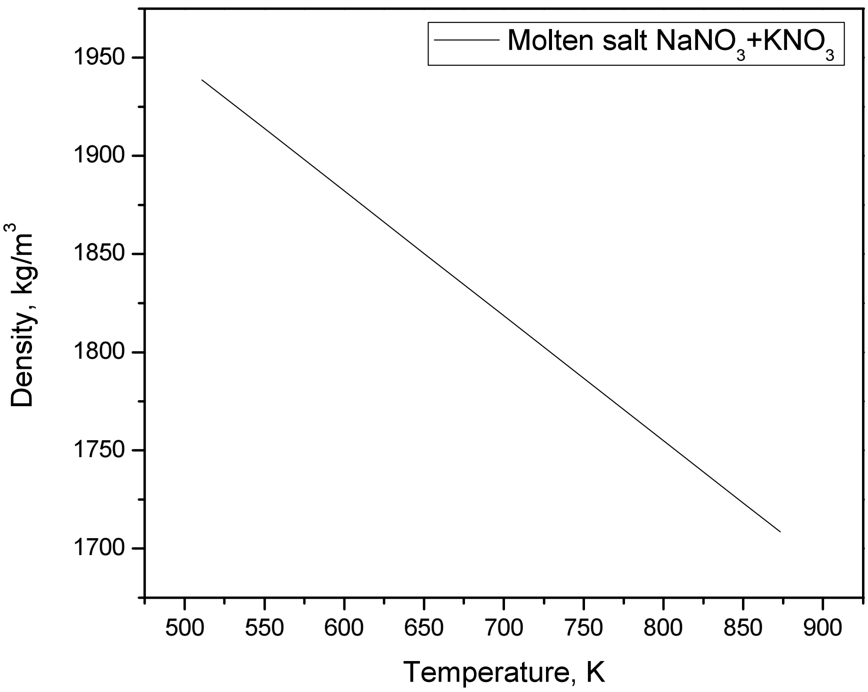

Figure 2.1: Density variation of molten salt (mixture of $NaNO_3$+KNO_3 in 60:40 by weight) with temperature

2.1.1.4 Heat capacity and volumetric heat capacity

Compared to water, the heat capacities of molten salts are low. However, the volumetric heat capacity of molten salt is comparable with that of water, which is a desirable characteristic for a coolant (Forsberg, 2004).

Ferrie et al.(2008), provided a correlation to obtain the liquid specific heat of the molten salt $NaNO_3$+KNO_3 (60:40 by weight) and it is given as:

$$Cp = 1443 + 0.172x(T - 273.15) \qquad \left({}^{J}\!/_{kgK} \right) \qquad (2.3)$$

Figure 2.2 shows the linear variation of specific heat of molten salt (mixture of NaNO3+KNO3 in 60:40 by weight) with temperature.

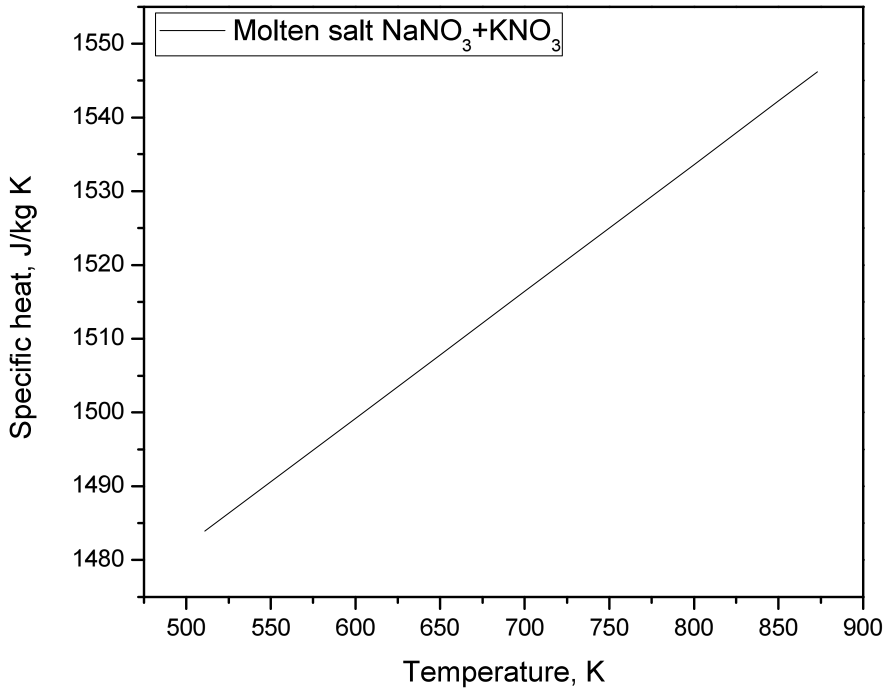

Figure 2.2: Variation of Specific heat of molten salt (mixture of $NaNO_3$+KNO_3 in 60:40 by weight) with temperature

2.1.1.5 Dynamic viscosity

Viscosity (μ) of molten salts is dependent on temperature, such that as the temperature increases, typical fluid viscosity will decrease exponentially. This is particularly important factor for high temperature applications. Salt composition also affects viscosity, and should be considered when selecting a salt coolant for application. In general, all the candidate salts show reasonably low viscosity (<10cP) allowing their use as industrial coolants. Ferrie et al.(2008), mentioned the correlation to find out the liquid dynamic viscosity of the molten salt $NaNO_3$+KNO_3 (60:40 by weight) and it is expressed as

$$\mu = \frac{22.714 - 0.12(T - 273.15) + 2.281\text{x}10^{-4}(T - 273.15)^2 - 1.474\text{x}10^{-7}(T - 273.15)^3}{1000} \; (\text{Pa s}) \qquad (2.4)$$

Figure 2.3 shows the variation of dynamic viscosity of molten salt (mixture of NaNO3+KNO3 in 60:40 by weight) with temperature. The unit of temperature is in Kelvin.

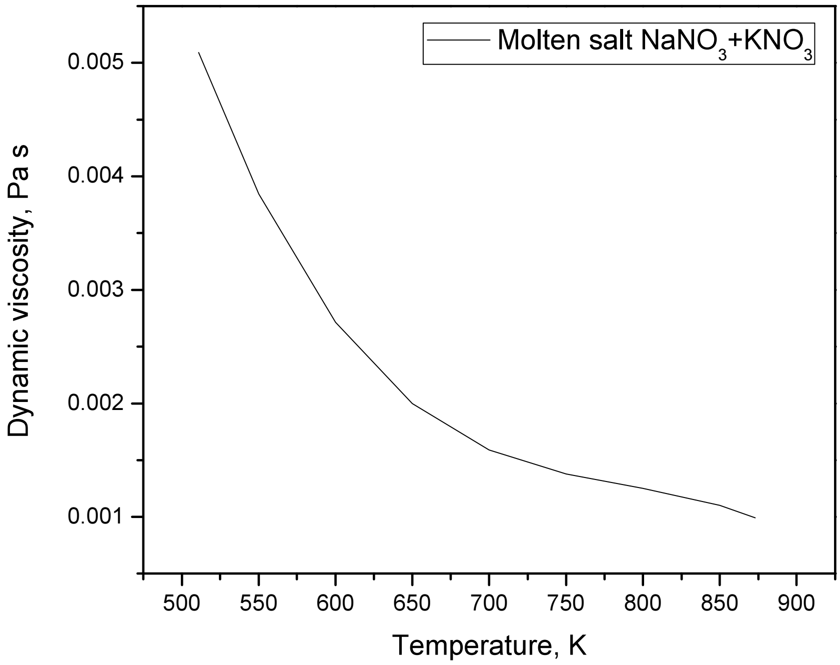

Figure 2.3: Variation of dynamic viscosity of molten salt (mixture of $NaNO_3$+KNO_3 in 60:40 by weight) with temperature

2.1.1.6 Thermal conductivity

In general, thermal conductivity of liquid salts (k_l) decreases with increase in temperature. Ferrie et al. (2008), mentioned the correlation to find out the liquid thermal conductivity of molten salt $NaNO_3$+KNO_3 (60:40 by weight) and it is expressed as

$$k_l = 0.443 + 1.9x10^{-4}(T - 273.15) \qquad \left(W/_{m\,K}\right) \tag{2.5}$$

Figure 2.4 shows the variation of thermal conductivity of molten salt (mixture of NaNO3+KNO3 in 60:40 by weight) with temperature. The unit of temperature is in Kelvin.

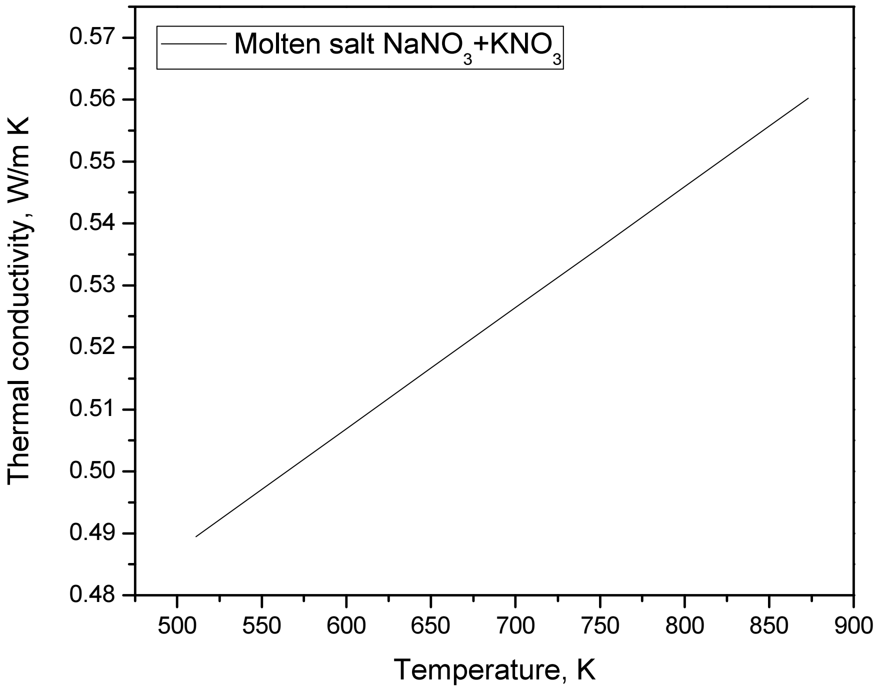

Figure 2.4: Variation of thermal conductivity of molten salt (mixture of $NaNO_3$+KNO_3 in 60:40 by weight) with temperature

2.1.2 Molten salts applications

2.1.2.1 Applications of molten salts in nuclear industry

Various sources in open literature provide an overview of the different applications of molten salt in the proposed nuclear reactors. Table 2.1 summarizes the different applications of molten salts and gives the reference molten salt composition for each application.

Table 2.1: Different applications and types of molten salts in nuclear reactors [David Samuel, (2009)]

Reactor type	**Neutron spectrum**	**Application**	**Reference Salt**
MSR Breeder	Thermal	Fuel	$^{7}LiF\text{-}BeF_2\text{-}AnF_4$
	Fast	Fuel	$^{7}LiF\text{-} AnF_4$
		Secondary coolant	$NaF\text{-}NaBF_4$
MSR Burner	Fast	Fuel	$LiF\text{-}NaF\text{-}BeF_2\text{-}AnF_3$
AHTR	Thermal	Primary coolant	$^{7}LiF\text{-}BeF_2$
VHTR	Thermal	Heat Transfer Coolant	LiF-NaF-KF
MS-FR	Fast	Primary coolant	$LiCl\text{-}NaCl\text{-}MgCl_2$
SFR	Fast	Intermediate coolant	$NaNO_3\text{-}KNO_3$

From Table 2.1, it is clear that there are two distinct uses of molten salts in nuclear reactor systems. For the Molten Salt Reactor (MSR) systems, molten salts are used as a fuel-carrier (or “fuel” as given in table), in which the liquid salt acts as both fuel and coolant (called as Fuel-Salt). For the Advanced High Temperature Reactor (AHTR) and also for the Very High Temperature gas cooled Reactor (VHTR), the molten fluoride salt are coolants; “Primary coolant” (for AHTR) and “Heat transfer coolant” for intermediate circuit (for AHTR and VHTR). So in nuclear applications molten salts can be classified as Primary coolant salts, Heat transfer coolant salts and Fuel-salts.

The NGNP/NHI heat transfer loop (USA Program) aims to transfer heat from the Next Generation Nuclear Plant (NGNP) to the Nuclear Hydrogen Initiative (NHI) hydrogen production plant (Williams, 2006). Heat transfer loop application include secondary or intermediate loop of the next generation high temperature reactor, which functions to carry heat from the primary loop to either the Brayton electricity generator or the hydrogen plant. The main screening factors for the primary coolant salts also apply to these heat transfer salts: favourable melting points and vapour pressures, chemical stability above 800^0C, compatibility with high temperature alloys.

The AHTR is one of the principle concepts of a high temperature molten salt cooled reactor. The AHTR core uses the graphite-matrix nuclear fuel designs of the High Temperature Gas cooled Reactor (HTGR) (Ingersoll et al., 2004). Instead of a gas coolant, the primary loop uses a molten fluoride salt coolant to transport the high temperature heat from the core to an intermediate loop; the intermediate loop coolant uses a secondary liquid salt to transport heat either to a Brayton power cycle, for electricity production, or to a hydrogen production plant (Forsberg et al., 2005). High Temperature Reactor (HTR) is being designed in India (Dulera and Sinha, 2008) and it uses molten salt in the primary loop.

The molten fluoride salt were selected because of their low melting points, chemical stability at higher temperatures (>800^oC), compatibility with graphite, better neutronic properties, and their successful use and operation during the ARE (Aircraft Reactor Experiment) and MSRE (Molten Salt Reactor Experiment) experiments (Forsberg, 2005). But fluorides are highly corrosive, which is a main drawback.

Chlorides are not considered in the literature because of their higher thermal neutron absorption cross sections (Forsberg, 2004) and undesirable neutron activation properties, generation of a long lived radionuclide ^{36}Cl, (Ingersoll et al., 2004). Nitrates, sulfates and carbonates are oxygen containing salts and are also not relevant for the primary AHTR coolant. At the higher temperature they are not stable as fluorides and they decompose to release oxygen, which corrodes carbon composites (Williams, 2006).

The neutronic properties (such as low absorption cross section) do not apply to the secondary salts because the secondary/heat transfer loop will operate outside the neutron field of the reactor core (Williams, 2006). Hence chlorides and fluoroborates are also considered for the heat transfer loop.

In the Molten Salt Reactor (MSR), the liquid salt containing the fuel circulates in the primary loop. The fuel-salt flows through the moderator in the core, fission occurs within the salt. The liquid then flows to the primary heat exchangers, through which heat is transferred to the secondary (heat transfer) molten salt coolant (Forsberg, 2004). This is the way the primary salt liquid in an MSR acts as both fuel and coolant.

Table 2.2 gives the details of past MSR programs undertaken at ORNL during the 1950s/60s/70s. The experience gained during this period resulting over 1000 technical reports (David Samuel, 2009), provides significant knowledge base for the new Generation IV MSR systems.

Table 2.2: *ORNL MSR systems and key features (David Samuel, 2009)*

	Aircraft Reactor Experiment 1954	***Molten salt Reactor Experiment 1965-1970***	***Molten Salt Breeder Reactor (design) 1970-1976***
Peak power output (MWth)	~2.5	~8	Not available
Peak temperature (^oC)	860	650	705
Solid Moderator	BeO	Graphite	Graphite
Fuel-Salt composition (% mol)	NaF-ZrF_4-UF_4 (53-41-6)	^7LiF-BeF_2-ThF_4- UF_4 (65-30-5-0.1)	^7LiF-BeF_2-ThF_4- UF_4 (72-16-12-0.4)
Secondary coolant	Na metal	^7LiF-BeF_2	NaF-$NaBF_4$

The molten salt FLiBe has also been recommended as a blanket coolant in the design of fusion reactors. The paper *"Molten Salts in fusion nuclear technology"* (Moir et al., 1998) gives an overview of the applications and favourable properties of FLiBe in fusion systems, as well some of the key links between molten salts in fission (MSRE) and fusion technologies.

2.1.2.2 Application of molten salts in solar power plants

Concentrating Solar Power (CSP) plants concentrate solar radiation to heat a fluid (normally called the heat transfer fluid) and produce steam (or vapor of another working fluid). The working fluid runs an engine (steam turbine, Sterling engine, etc.) connected to a generator, producing electricity. There are four major types of CSP technologies: parabolic troughs, central receiver towers (also known as power towers), parabolic dish-Sterling engine systems, and linear Fresnel reflectors, all of which can be integrated with thermal storage system, although a dish system would require a special design (Kurvi et al., 2013). Table 2.3 provides a description of the few existing solar thermal power plants that have integrated storage.

Table 2.3: Operational solar thermal facilities with molten salt as thermal energy storage system (Kurvi et al. 2013)

Project	**Type**	**Nominal Temperature (^oC)**		**Plant capacity**	**Storage capacity**
		Cold	**Hot**		
La Florida Badajoz, Spain	Parabolic trough	292	386	50 MWe	7.5 h
Andasol-1 Granada, Spain	Parabolic trough	292	386	50 MWe	7.5 h
Andasol-2 Granada, Spain	Parabolic trough	292	386	50 MWe	7.5 h
Extresol-1 Badajoz, Spain	Parabolic trough	292	386	50 MWe	7.5 h
Manchasol-1 Ciudad Real, Spain	Parabolic trough	292	386	50 MWe	7.5 h
Manchasol-2 Cluda Real, Spain	Parabolic trough	292	386	50 MWe	7.5 h
La Dehesa Badajoz, Spain	Parabolic trough	292	386	50 MWe	7.5 h
Archimede Sicily, Italy	Parabolic trough	292	550	5 MWe	8 h
Torresol Gemasolar Seville, Spain	Central receiver	292	565	17 MWe	15 h

Thermal energy storage systems reduce the mismatch between energy supply by the sun and energy demand (Hermann and Kearney, 2002). Depending on variation in solar insolation throughout the day and year, as well as the electricity demand, thermal energy storage systems can be integrated.

Tyner and Wasyluk (2013), described the molten salt based eSolar plant design, which will have the molten salt solar power tower of storage capacity of 50 MWth. This eSolar plant comprised of a tower mounted molten salt receiver, which is surrounded by a heliostat field to utilize eSolar's small heliostat technology.

Kearney et al. (2004), mentioned that by using Molten salt as a heat transfer fluid in a parabolic solar through plant, it may be possible to raise the solar field output temperature to 450-500^{o}C, thereby increasing the Rankine cycle efficiency of the power block steam turbine to the 40% range, compared to 393^{0}C with the current high-temperature oil and a cycle efficiency of 37.6%. The major challenge of the usage of molten salt is its high freezing point compared to synthetic oil, leading to complications related to freeze protection in the solar field. The synthetic oil currently used in solar plant freezes at about 15^{o}C, whereas the binary molten salt (solar salt, mixture of 60% $NaNO_3$ and 40% KNO_3) freeze at about 220^{o}C.

2.2 Natural circulation systems

Molten salts are used as a coolant/heat transfer fluid in various high temperature engineering systems owing to their high boiling point at low pressure. Natural circulation of molten salt is being preferred in some systems like solar power plant and molten salt reactors. Such systems can be studied with the help of a natural circulation loop.

Natural circulation systems find several engineering applications in conventional as well as in nuclear industries. In nuclear industry, some of the innovative reactors, for example, MASLWR (Modro et al., 2002), CAREM (Mazzi, 2005), LFR (Smith et al., 2008), ABV (Kostin et al., 2004), SSTAR and STAR-LM (Farmer et al., 2004) are designed to remove core heat by single-phase natural circulation. Many researchers studied the steady state and transient behavior of natural circulation loop using experimental and theoretical approaches. Few of these studies are explained in the following sections.

2.2.1 Experimental studies on natural circulation loop

Alstad et al. (1956) experimentally measured the transient response of natural circulation loop working with normal water (they called it as free convection loop). They used the rectangular natural circulation loop having both heater and cooler placed in left and right vertical legs. They did not observe any instability. Damerell and Schoenhals (1979) used the same toroidal loop used by Creveling et al. (1975) to investigate the effect of an angular displacement (tilt) of the heated and cooled sections on the flow and stability in the toroidal loop. They found that, the instabilities occurring in the toroidal loop can be minimized by tilting the loop. They further reported the presence of three-dimensional effects, such as flow reversals. Later, Gorman et al. (1984, 1986) carried out experiments in a toroidal thermo-siphon to study the non-linear dynamics of the system.

Stern and Grief (1987) carried out detailed fluid temperature measurements in a toroidal loop using a small movable thermocouple probe and also performed 1D simulations. The loop was oriented in the vertical plane and was heated over the lower half and cooled over the upper half. They made the comparison of results obtained from one-dimensional calculations with their experimental data. They found that results from one-dimensional calculations yielded temperatures that were substantially greater than the measured values. Flow visualization in their experiments indicated the presence of recirculating flow/secondary flow in the loop.

Acosta et al. (1987) made an experimental study of a tilted square loop. Heating was carried out with an electrical resistance heater and cooling utilized a coaxial cylindrical heat exchanger. The heating and cooling were on opposite sides of the square loop. The loop was mounted on a vertical frame that permitted rotation about horizontal axis. Different types of flow patterns were observed. These included time-independent flows as well as oscillatory flows, which persisted for at least 40 min with no apparent change in amplitude or frequency. In addition, flow instabilities due to a small change in the tilt angle were also observed.

Vijayan et al. (2001) carried out an experimental investigation on the effect of orientation of heater and cooler in single-phase rectangular natural circulation loop working with water. They observed from steady state analysis that the maximum flow rate was observed when both heater and cooler were horizontal. However, this orientation was found to be least stable and the orientation with vertical heater and vertical cooler was found to be more stable and shows less mass flow rate compared to other heater and cooler configurations of the loop. They studied Hysteresis phenomenon in Natural Circulation Loop (NCL) for VHVC configuration. In this study, the power was increased in steps of 100 W and loop is allowed to attain steady state for each power and various parameters were noted. The procedure was repeated till the power reached 1000 W. The power was then brought down to 950 W. After achieving steady state, the power was brought down in steps of 100 W and the procedure was repeated till the power reached 50 W. Thus the steady state data could be generated in the range of 50 to 1000 W. They also observed, Horizontal Heater and Horizontal Cooler (HHHC) configuration showed the instability. At low power they observed sustaining unidirectional oscillations and at high power bi-directional oscillations were observed.

Misale and Forgoheri (2001) carried out the experimental study to understand the influence of pressure drop induced by orificing on behaviour of single-phase natural circulation loop. They observed that additional pressure drop leads to stabilization of the loop. Stability was induced for smaller orifice diameters of 10 mm and 22mm, but the orifice of diameter 26 mm, 30 mm and 36 mm were not able to stabilize the loop.

Vijayan (2002) carried out an experimental study on the general trends of the steady state and stability behaviour of single-phase natural circulation loops. He developed a correlation to predict steady state parameters of the loop and validated his correlation with experimental data. The correlation was derived from 1D conservation equations. In natural circulation loops, the driving force is usually low as it depends on the riser height which is generally of the order of a few meters. The heat transport capability of natural circulation loops (NCLs) is directly proportional to the flow rate it can generate. With low driving force, the straightforward way to enhance the flow is to reduce the frictional losses. A simple way to do this is to increase the loop diameter. Further, the loop diameter also plays an important role on the stability behaviour. An extensive experimental and theoretical investigation of the effect of loop diameter on the steady state and stability behaviour of single- and two-phase natural circulation loops have been carried out by Vijayan et al. (2007). They used four single-phase loops of differing diameter. Instability was observed only in the two large diameter loops. The instability threshold was found to decrease with increase in loop diameter. Also, they found that the threshold of instability is not a unique value as it depends on the operating procedure.

Misale et al. (2007) carried out an experimental investigation in a single phase natural circulation mini-loop characterized by an internal uniform diameter of 4 mm. They observed a good agreement between the correlation proposed by Vijayan (Vijayan, 2002) and their experimental data. Devia et al. (2012) carried out an experimental study on transient behaviour of rectangular natural circulation loop having inner diameter of 30 mm and height of 980 mm. The working fluid in the loop was distilled water. The heater and cooler were situated on horizontal pipes (HHHC configuration). They also observed the instabilities in the experimental study.

In the above mentioned literature most of the researchers used water as a working fluid. The operating limit of the water in subcritical region is limited. Researchers observed the boiling of water in the heater section, during low flow period for power greater than 480 W in HHHC configuration of rectangular natural circulation loop. The way to operate the natural circulation loop working with water at high temperature is to use the water at high pressure or supercritical condition. But this is very expensive. Studies on NCL working with supercritical CO_2 have been carried out by Swapnalee et al. (2011), Sharma et al. (2013). The use of working fluid in the NCL at subcritical condition with single-phase of fluid has been economical and safe also. Hence many researchers used different fluids in single-phase condition in the natural circulation loop. The paper "Reactors with Molten Salts: Options and Missions" (Forsberg et al. 2004) outlines that, gases at high-pressure such as helium and fluids with high boiling points at low-pressures, traditionally molten salts, are the options for high temperature coolants. Liquid metals, and in particular liquid lead or lead-bismuth eutectic, are alternative low pressure high temperature liquids proposed for Advanced Fast Reactor and Accelerator Driven System coolants. Borgohain et al. (2011) carried out an experimental study on rectangular natural circulation loop working with Lead Bismuth Eutectic (LBE). They performed steady state and various transient studies. The experiments have been carried out on the loop having vertical heater and horizontal cooler position. They observed that, the LBE coolant shows quite stable behaviour during all transients. Presence of lead makes the coolant toxic, which is undesirable. Also oxygen free environment is required, which is an additional issue.

2.2.2 Theoretical studies on natural circulation loop

Keller (1966) observed periodic oscillations from a one-dimensional model of thermal convection. The model consists of a fluid–filled tube bent into rectangular shape and standing in a vertical plane. The fluid is heated at the centre of the lower horizontal segment (point heat source) and cooled at the centre of the upper horizontal segment (point heat sink). They concluded that inertia is unimportant for this oscillation. Oscillation depends upon the interplay between frictional and buoyancy forces. Welander et al. (1967) explained the instability in a natural circulation loop by means of a warm packet and cold packet generated in the loop. The loop considered by them is formed by the tube and it is bent at top and bottom to form closed loop. The finite heat source at bottom and finite heat sink at top of the loop were considered. As the consequence of heat supply at heater, hot packet gets formed in heater at some instant and cold packet gets formed in cooler at the same instant. After some time, hot packet gets released in left or right leg and it has tendency to rise upwards. Fluid being incompressible, the cold packet will gets pushed to opposite leg and it will have tendency to fall down due to high density. This situation is favourable to circulation and high mass flow rate is achieved. But after some time, the hot plug which has gained high momentum crosses cooler and doesn't get converted into cold packet as it goes very fast through the cooler. Similarly, cold packet crosses heater without getting heated. These hot and cold plugs enter vertical legs at top and bottom positions respectively. The hot plug due to high velocity moves down in the vertical leg but due to high density fluid below it, it faces retardation. Similarly, cold plug moves up somewhat in other vertical leg but due to its high density, it also faces retardation. Hence induced mass flow rate in the loop reduces very fast when warm packet is going downwards. In this way, the flow fluctuates and in other words the occurrence of instability in the NCL. Later, Creveling et al (1975) studied the stability characteristics of a single-phase natural circulation (they called it as single-phase free convection) in a toroidal loop. They observed the instabilities in one-dimensional model as well as in experiment. They also mentioned that if the flow rate increases above the steady state value, there would be a corresponding increase in the friction and decrease in the total buoyancy. This results in a decreased flow rate, which then acts to return the system to the original steady state condition. Welander (1967) and Creveling et al. (1975) provided a plausible argument to clarify the possibility of instabilities. According to them, if the loop is presumed to be operating in the steady state condition, then a small disturbance causes a "packet" of fluid to leave the heating section (at the bottom) at a temperature that is higher than normal for the steady state condition. The hotter than the normal packet then moves upward more rapidly than as usual (due to the increased buoyancy) and therefore, when it emerges from the cooling section (at the top), it is at a temperature that is higher than normal. As the packet now moves downward, it is lighter and decelerates. Thus, the packet enters the heated section once more, but at a higher inlet temperature and at a lower velocity. When it emerges from the heater, it is even hotter than before, and moves still more rapidly (upward) than before; the process is repeated and ultimately results in an unstable flow. A similar description holds for a cold packet that originates at the exit from the cooling section. This argument provides a simple physical description for the possible build-up of oscillations. Mousavian et al. (2004), carried out the transient and nonlinear stability analysis in single-phase natural circulation loop by using one-dimensional finite difference method, linear analysis using perturbation method and RELAP5 system code. They obtained a stability map of rectangular loop for different values of modified Stanton number and Grashof number. Bernier and Baliga (1982) proposed a new coupled 1D and 2D model for closed loop thermo-siphons of VHVC configuration. This model improves the results of traditional 1-D models for cases where: (i) mixed-convection effects are important in the heated and cooled sections of the loop; and (ii) heat losses (or gains) from the insulated portions of the loop are significant. This has been achieved by iteratively coupling local results of 2-D numerical simulations of mixed-convection flows, performed in the heated and cooled sections, and a 1-D analysis in remaining sections (i.e piping connecting heater and cooler). Chen (1985) also carried out theoretical investigation of the loop and showed that the aspect ratio (height/width) plays an important role in the stability of NCL.

Lavine et al. (1987) performed three-dimensional (3-D) studies on natural convection in a toroidal loop. They observed from their results that, both one-dimensional (1-D) and two-dimensional (2-D) analysis over predicts the total buoyancy. One-dimensional model under predicts the friction also. Both 1-D and 2-D models over predict the average axial velocity. They found that, flow reversal and secondary motion are possible with 3-D simulations. The flow reversal and secondary motion depends on Grashof number and on the thermal boundary condition. The strength of secondary motion and flow reversal is greater for the higher Grashof number case.

Vijayan et al. (1994) worked on the scaling laws for single-phase natural circulation loops. They used the power-to-volume scaling laws for the design of a scaled test facility simulating the primary heat transport system of nuclear power plants, which results in loops of the same elevation with reduced diameters. They checked adequacy of the scaling laws for simulating single phase natural circulation by testing in three rectangular loops, each having same elevation and but different diameters of 6 mm, 11 mm and 23.2 mm respectively. The experiments showed that the power-to-volume scaling principle adequately describe the steady state behavior. The 1-D codes are based on the conventional forced flow correlations for friction and heat transfer coefficient. Later, Vijayan and Austregesilo (1994) observed that friction factor in natural circulation loop was higher than that given by constant property forced flow friction factor correlations. Huang and Zelaya (1988) studied natural circulation in a rectangular natural circulation loop and observed that the conventional forced convection friction factor correlation predict the loop behaviour well if the form losses for the bends are accounted. Later, Ambrosini et al. (1998) studied the effect of truncation error on the numerical prediction of linear stability boundaries in a single-phase natural circulation loop.

Misale et al. (2000), developed a 2D code and studied the influence of the wall thermal capacity and axial conduction on flow transient in a single-phase natural circulation loop. They investigated the steady state and transient behaviour of the loop.

Vijayan (2002) extended their work on scaling laws for both uniform and non-uniform diameter single-phase natural circulation loop. They derived the correlation for steady state Reynolds number. According to them, the steady state flow in uniform and non-uniform diameter single-phase natural circulation loops can be expressed as $\mathrm{Re_{ss}} = \mathrm{C}[\mathrm{Gr_m}/\mathrm{N_G}]^{\mathrm{r}}$ $Re_{ss} = C[Gr_m/N_G]^r$ where the constants C and r depend on the nature of the flow (i.e laminar or turbulent), $\mathrm{Gr_m}$ is the modified Grashoff number and $\mathrm{N_G}$ is the geometrical parameter. The details of these parameters are given in Chapter 4. Simulation of the steady state flow in single-phase natural circulation loops (NCLs) can be achieved by simulating the non-dimensional parameter $(\mathrm{Gr_m}/\mathrm{N_G})$. They also mentioned that, for 1000 < Re < 4000, the loop is neither fully laminar nor fully turbulent.

Mousavian et al. (2004), carried out the transient and nonlinear stability analysis in single-phase natural circulation loop by using one-dimensional finite difference method, linear analysis using perturbation method and RELAP5 system code. They obtained a stability map of rectangular loop for different values of modified Stanton number and Grashof number. Ambrosini et al. (2004) studied the effect of wall friction in single phase natural circulation stability at the transition between laminar and turbulent flow. They mentioned choice of appropriate friction law; recommendations are given to use friction laws providing larger friction factors than in forced flow.

Pilkhwal et al. (2007) studied the unstable behaviour of single phase natural circulation loop with one-dimensional and 3D CFD models. They observed the inability of the one-dimensional code in predicting the start up from zero flow condition for HHHC configuration. They observed that 3D CFD model provide improved modeling capabilities which are quite promising for solving the classical problems raised by the use of 1D code. CFD models do not use any correlations for heat transfer coefficient as they required in 1D/2D models.

It has been clearly brought out that natural convection and mixed convection plays a very important role in the thermal hydraulic behaviour of single-phase natural circulation loops. Mere inclusion of axial fluid conduction based on thermodynamic fluid conductivity does not help in improving the 1-D model predictions (Naveen Kumar et al. (2010)). The loop behavior can be predicted only by accounting for natural convection currents (natural convection currents due to secondary flows in the heater section). Naveen Kumar et al. (2011), carried out an investigation on the effect of secondary convection currents in horizontal heater of a single phase natural circulation loop dynamics. Their main aim was to develop the 1-D model for simulating the "startup from rest" of HHVC and HHHC of NCL. They mentioned the existing 1-D models are based on several simplified assumptions. The new model developed by them was based on the non dimensional analysis. The functional form for taking account of natural convection has been established from scale analysis and the coefficients of proportionality have been obtained from CFD simulations. The model has been successfully incorporated in a 1-D model. In summary, they added the extra terms in the energy equation of conventional 1-D models to account for the effect of natural convection and mixed convection. Their 1-D model is capable to predict the start-up from rest behaviour of single-phase natural circulation loop having horizontal heater.

Swapnalee et al. (2011), developed a generalized flow equation for single phase natural circulation loops obeying multiple friction laws. They mentioned the constants for transition flow regime in Vijayan correlation as C = 1.216 and r = 0.387 along with the constants for laminar flow as C = 0.1768, r = 0.5 and the constants for turbulent flow as C = 1.96, r = 0.364. They mentioned that the laminar flow exists if $Re<898$, transition flow exists if $898<Re<3196$ and turbulent flow exists, if $Re>3196$ in a rectangular natural circulation loop.

Devia et al. (2012) carried out experimental and computational studies on transient behaviour of rectangular natural circulation loop having inner diameter of 30 mm and height of 980 mm. They carried out CFD analysis using FLUENT 6.3 commercial CFD code. The computational model used by them includes fluid and the solid (pipes and insulation) and both heater and cooler are situated at horizontal pipes of the loop (HHHC configuration). They did not model the cooler duct, instead the cooler has been modelled as a bare pipe subjected to convective heat transfer to the coolant. The mesh used by them involved 122960 cells and the time step of 1 s is used to carry out transient simulations. Their CFD results show good agreement with experimental data. They observed the instabilities from both experimental and CFD study.

Lousis et al. (2013) carried out the computational study to investigate the nonlinear dynamics of unstable convection in a 2D thermal convection loop with heat flux boundary condition. They used the toroidal type loop with water as working fluid. Wang et al. (2013) studied flow and heat transfer characteristics in a rectangular natural circulation loop using 3D CFD code, namely FLUENT. They also proposed a correlation to find out the steady state Reynolds number.

Naveen Kumar et al. (2014) proposed a new friction factor correlation for horizontal heater natural circulation loop. Recently, Naphade et al. (2014) studied the steady state characteristics of LBE in a rectangular natural circulation loop using experimental and 3D CFD simulations using PHOENICS CFD software.

2.3 Heat transfer characteristics of molten salt natural circulation loop

In a natural circulation loop, fluid flow and heat transfer is mainly due to the formation of hot and cold plug as explained by Welander (1967). A hot packet once formed in heater passes through cooler at a high speed and similarly, a cold packet of fluid formed in cooler passes through heater at a high speed. In heater/cooler, such a packet gains/losses heat. This heat transfer results into buoyancy force. Hence, in NCL, even in the absence of a pump, the conditions are similar to mixed convection conditions. The earlier work on this topic of mixed convection is being reviewed here.

The effect of free convection on heat transfer for laminar flow was systematically studied by Boelter (1948). He proposed the following correlation to find out the average Nusselt number in heated part.

$$Nu_{avg} = 1.75\left[Gz + 0.0722\left(\frac{Gr.Pr.D}{L}\right)^{3/4}\right]^{1/3} \tag{2.1}$$

Where Greatz number, $Gz = RePr\left(\frac{D}{L}\right)$, Pr is the Prandtl number, Re is the Reynolds number, D is the diameter and L is the characteristic length.

For vertical surfaces, the height of the surface is to be used as the characteristic dimension for calculating Nusselt and Grashof numbers.

Later, Hoffman and Lones (1955) conducted experiments on FLiNaK flowing in forced convection through circular tubes. The test section included 61-cm long tubes of nickel, Inconel, and Type 316, stainless steel. Each tube was long enough to allow fully developed flow. Twenty four equally spaced thermocouples were used to monitor the outside surface temperature profile of the test section. The data obtained under predicted the Dittus-

Boelter correlation. Vriesema (1979) performed forced convection heat transfer experiment in a vertical test section of Inconel-600 alloy. The data obtained was compared with Dittus-Boelter correlation and it shows deviation of 15%. Ignat'ev et al. (1984) have performed heat transfer studies using FLiNaK in a circular tube of iron based steel. The data was compared with the Sieder-Tate and modified Petukhov correlations. Jackson et al. (1989) explained various cases of mixed convection in vertical tube. If flow is in upward direction past a heated surface (or downward past a cooled surface) heat transfer is enhanced. On the other hand, if the flow is in downward direction past a heated surface (or upward direction past a cooled surface), heat transfer is impaired. They also mentioned that the transition to turbulent flow may occur earlier in free convection in a vertical pipe flow compared to that in the forced convection.

Ferng et al. (2012) studied the turbulent thermal-hydraulic characteristics of FLiNaK salt in a pipe flow using 3D CFD code FLUENT. Recently, Srivastava et al. (2013) studied the heat transfer and pressure drop characteristics of molten fluoride salt in a circular pipe using a 2D axi-symmetric CFD code NAFA. Sona et al. (2014) performed the investigation of flow and heat transfer characteristics and structure identification of FLiNaK in pipe using 3D CFD simulations using Large Eddy Simulation (LES).

2.4 Summary and Discussion on literature review

Based on literature review on molten salt thermo-physical properties, applications and natural circulation loops, following observations were made.

Molten salts exhibit low melting point and high boiling point at low pressure. Besides, their volumetric heat capacity is nearly equal to that of water and their viscosity is comparable with water (especially beyond 400°C for molten nitrate salt). The molten nitrate salt can be used in the range of 300°C to 600°C at atmospheric pressure. Fluoride salt (FLiNaK) can be used in 454°C to 1570°C range. These favourable properties make them suitable as coolant/heat transfer fluid for high temperature systems. The only drawback is their high freezing point which needs to be taken care of during design and operation of systems employing them. Molten salts find their applications in nuclear power plants as primary/secondary coolants and also as fuel salt. In solar power plants, molten nitrate salts are used as coolant and heat transfer fluid. Thus, molten salt can be used in variety of ways.

Studies on properties of molten nitrate salt reveal following observations:

a) Density changes by only 10% over temperature range of 300^oC to 600^oC and density versus temperature is linear. Hence for simulation Boussinesq approximation can be easily used.

b) Specific heat (Cp) changes just by 5% over a temperature range from 300^oC to 600^oC. Hence for modelling purpose Cp can be taken constant.

c) Viscosity changes by around six times over the working temperature range and hence cannot be considered constant for simulation.

d) Thermal conductivity changes by 5% and hence can be taken as constant for simulation purpose.

It was observed that, natural circulation of molten salt in solar thermal power plant or reactors is increasingly being preferred. A lot of research work on steady state, transient and stability characteristics of natural circulation loops is published. Various observations from this survey is given below.

- Most of the studies are carried out with water as working fluid. The NCL working with water operates in temperature range of 30^oC to 80^oC. However, a molten salt natural circulation loop is supposed to work in temperature range of 300^oC to 600^oC. Hence there is much difference between these loops as far as their thermal characteristics are considered. There is hardly any study done for natural circulation loop with molten salt as a working fluid. Hence the experimental studies on molten salt natural circulation loop are required to be carried out.

- Earlier efforts involved mostly 1D simulations. Various simplifying assumptions, as described earlier, need to be used in 1D models. Literatures shows the inability of the 1D codes in predicting for HHHC configuration (i) the start up from zero flow condition, (ii) thermal stratification and secondary flows in horizontal heater. Similarly, 2D simulations are also not adequate. Hence 3D transient CFD simulations are required for accurate predictions.
- In NCL working with water, uni-directional and bi-directional pulsing are observed at different powers. However, the reason for their formation was not satisfactorily given. It is expected that detailed 3D data from CFD simulations can give explanation of formation of these uni-directional and bi-directional pulsing.
- Steady state and transient studies performed with NCL working with water should be separately carried out for MSNCL. These studies should include (i) effect of power on Steady State characteristics of the loop, (ii) flow initiation transients, (iii) power step up or power step down transients, (iv) loss of source/sink transients.
- In the heater and the cooler, most of the part is occupied by developing hydrodynamic and thermal boundary layers. Hence the pressure drop and heat transfer is affected. In literature, focus was on heat transfer in fully developed flow conditions. Heat transfer characteristics in MSNCL are hence required to be studied.

In view of the above requirement, in the present research work, a molten salt natural circulation loop (MSNCL) is set up. Experimental and computational study on natural circulation loop working with $NaNO_3$+KNO_3 (60:40 by weight) is performed in detail. CFD simulations are performed with FLUENT CFD software. The details of experimental loop and CFD model are given in later chapters.

The experiments are performed on VHHC configuration of the loop. From literature survey it is observed that, HHHC configuration is unstable. VHVC configuration is very stable but gives minimum induced mass flow rate. Hence for experimental work VHHC configuration was chosen.

Detailed information about the experimental and computational investigation on MSNCL as well as NCL working with water is given in forthcoming chapters.

CHAPTER 3

EXPERIMENTAL STUDIES ON MOLTEN SALT NATURAL CIRCULATION LOOP

3.1 Introduction

As discussed in the previous chapters, molten salts are one of the most suitable coolants for high temperature applications like reactors and solar thermal power plants. Molten salts exhibit low melting point and high boiling point, enabling us to operate the system at low pressure (Forseberg, 2005). Molten salts have the volumetric heat capacity similar to water and flows much like water does. The major advantage of molten salt over water is higher temperatures attainable in the molten salt state. Also if the salt solidifies (freezes) it contracts, unlike water (Samuel, 2009). Thus, molten salt freezing in a pipe would not burst the pipe as water would. The above mentioned properties of the molten salt are highly desirable for their use as a coolant in high temperature system without increasing system pressure. Because of this, molten salts find their application as heat transfer/heat storage medium in solar power plant (Kurvi et al., 2013, Jaiswal et al. 2011) and fuel salt as well as coolant in high temperature nuclear reactors (Dulera and Sinha, 2008, Borghoain et. al., 2015). Most of the usage of molten salt in high temperature system involves the natural circulation mode. Natural circulation loop is the representative of primary heat transport system of nuclear reactor. It is required to understand the natural circulation of molten salt in the natural circulation loop. In view of this molten salt natural circulation loop test facility has been fabricated and installed. Schematic diagram of the same is shown in Fig. 3.1.

The steady state and various transient studies have been carried out in this experimental facility to study the thermal-hydraulic behaviour of molten nitrate salt (generally called as solar salt having the composition of $NaNO_3$+KNO_3 in 60:40 by weight). These thermal-hydraulic characteristics are helpful to nuclear reactor designer to estimate heat removal capacity of molten salt based system in natural circulation mode. Molten Salt Natural Circulation Loop (MSNCL) comprises five parts: heater, cooler, melt tank, expansion tank and main loop piping. The material used to construct the experimental facility, type of instrumentation, various components used in the experimental facility and experimental procedure has been discussed after the loop description in the following sections.

3.2 Description of the loop

The rectangular natural circulation test facility has been fabricated with ½" (15 NB) uniform diameter pipe. A schematic diagram along with the geometrical details of the test loop is shown in Fig. 3.1. There is a provision of selecting any one of the two heat sources at any of the two locations at the bottom horizontal pipe or left vertical leg. Similarly heat sink can be chosen in the top horizontal pipe or in the right vertical leg. Therefore, any combination of heater and cooler could be operated at a time. Four configurations thus possible are (1) Vertical Heater Vertical Cooler (VHVC), (2) Vertical Heater Horizontal Cooler (VHHC), (3) Horizontal Heater Vertical Cooler (HHVC) and (4) Horizontal Heater and Horizontal Cooler (HHHC). The heaters are made of 1 mm diameter Nichrome wire which is evenly wound on the outside surface of the pipe while coolers are of the tube-in tube type with the secondary coolant (air) flowing through the annulus. The loop also has an expansion tank located at the highest elevation of the loop, to allow for the thermal expansion of fluid. An adequate thermal insulation has been provided in the loop to reduce heat losses. Band heaters have been provided for melting and keeping the salt at desired temperature in both the melt tank and expansion tank. The arrangement has been made to measure the temperature of the molten salt as well as the pipe surface temperature of the loop using K-type thermocouples, which are installed on various locations as shown in Fig. 3.1. The photograph of the experimental facility installed is given in Fig. 3.2. Differential pressure was measured in bottom leg of the loop using a differential pressure transmitter.

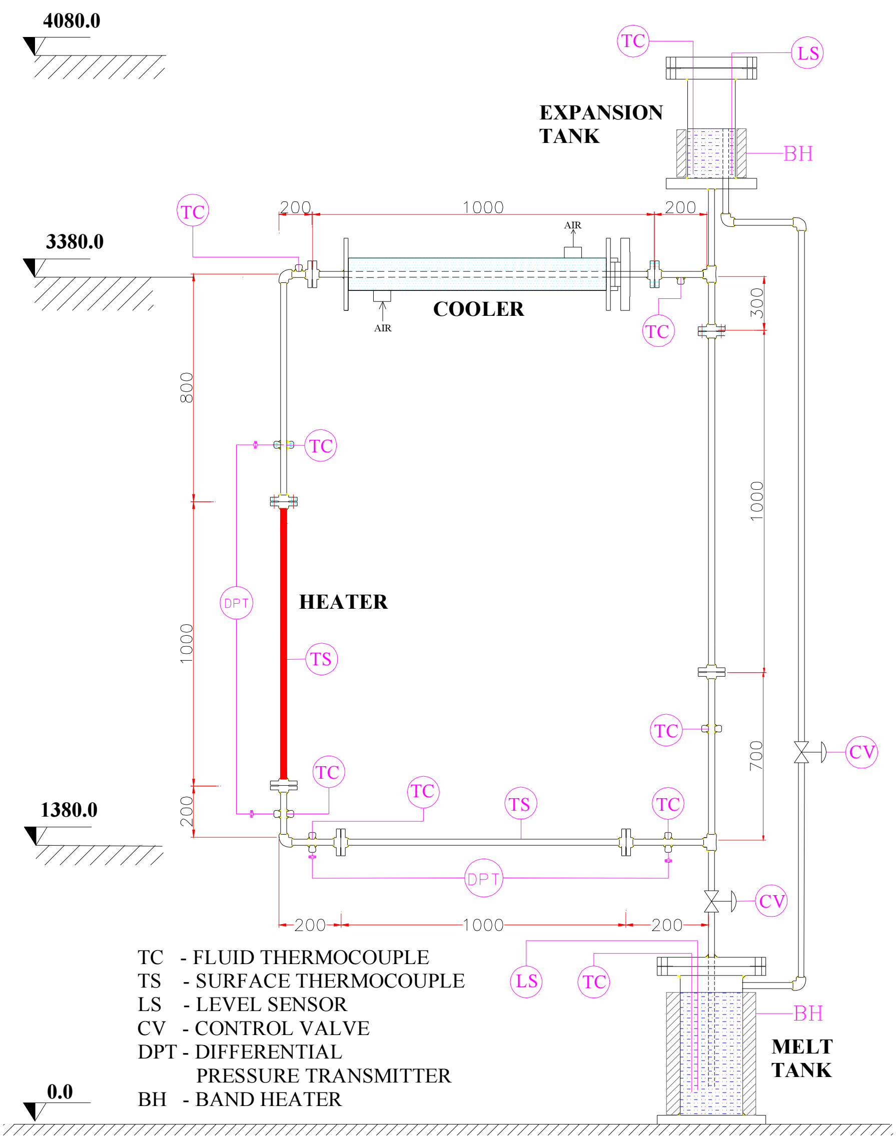

Figure 3.1: Schematic diagram of molten salt natural circulation loop (MSNCL)

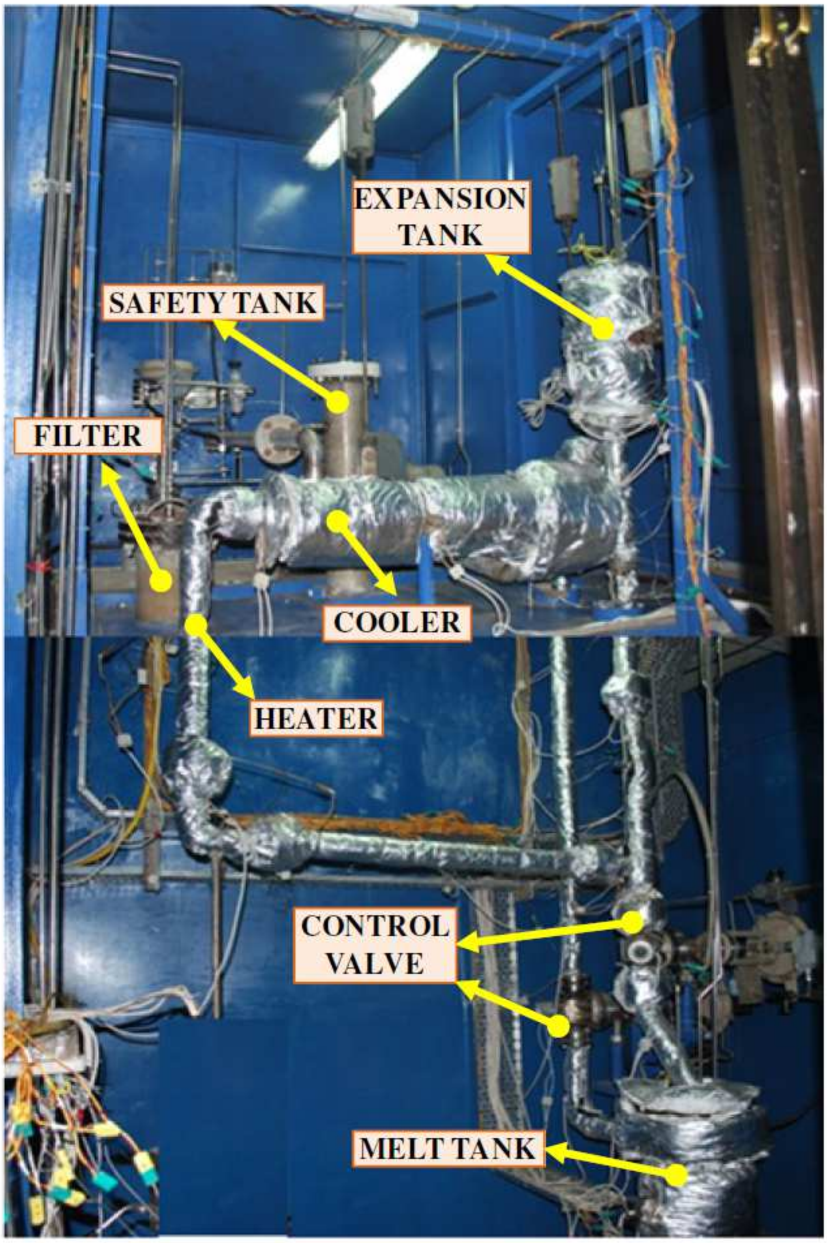

Figure 3.2: Photograph of MSNCL experimental facility

The instrumentation and control of the MSNCL was realized by means of Piping and Instrumentation Diagram/Drawing (P&ID) based controllers and Data Acquisition and Control System (DACS). The flow sheet (P&ID) of MSNCL is shown in Fig. 3.3. DACS used in MSNCL consists of an industrial PC with a 12 bit ADC card, 16 channel amplifiers with multiplexer, Windows XP 32 bit operating system and 32 bit ELIPSE SCADA Software. The overall accuracy of DACS was ±0.165% of range. Monitoring of various parameters like pressure, temperature, levels in different components of the loop, valve positions etc. have been done through DACS.

High temperature pressure transmitters with an accuracy of ±0.1% of range were used to measure the gas pressure in the main loop. The accuracy of K-type thermocouples and temperature transmitters was ±0.4% of the readings and ±0.1% of range respectively.

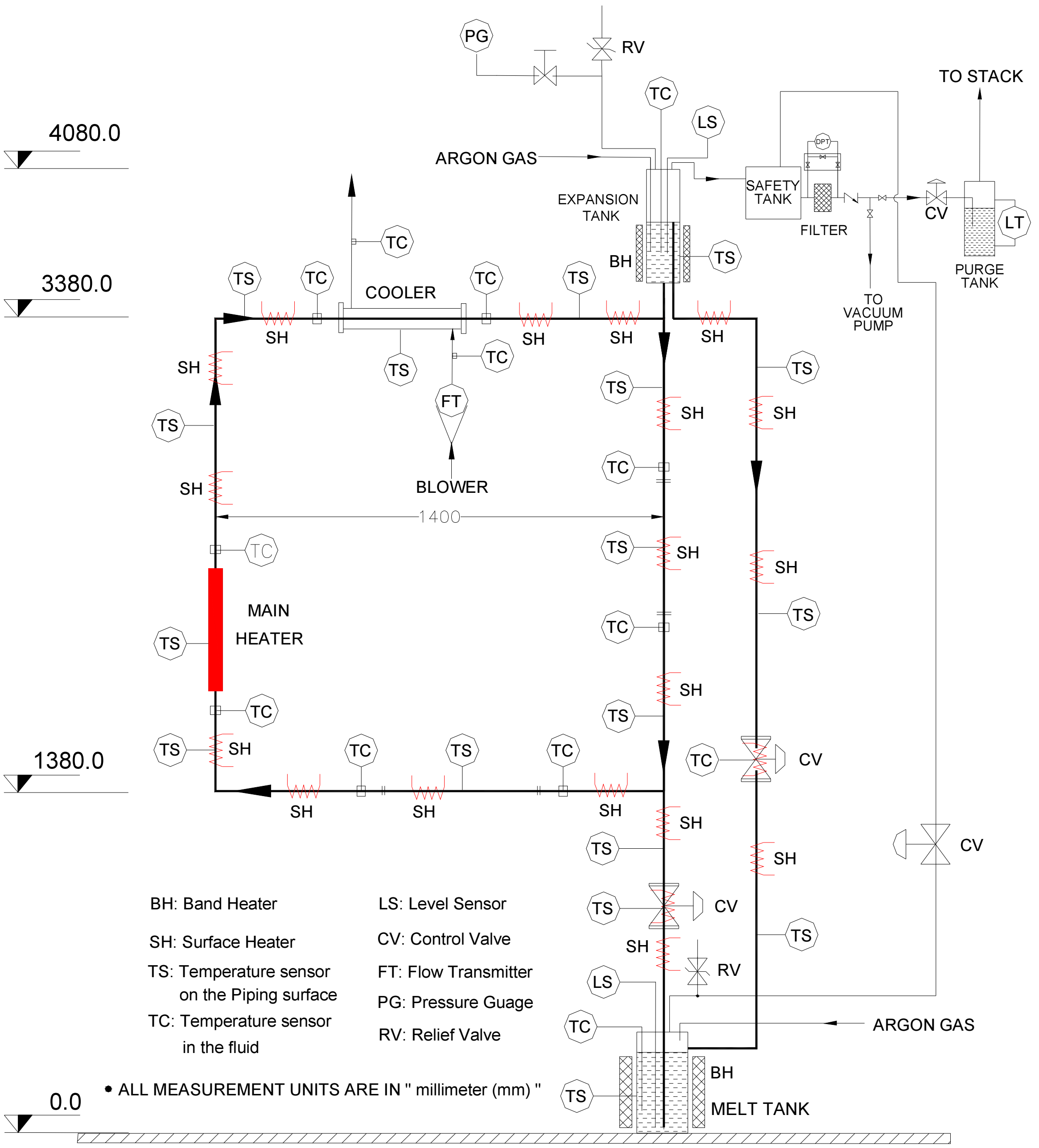

Figure 3.3 Flow sheet (P&ID) of MSNCL

The experimental study of the molten salt natural circulation loop is carried out for the VHHC configuration. 3D CFD simulations were parallely performed to predict the steady state and transient characteristics of molten salt natural circulation loop.

3.3 Materials used in nitrate salt environment

Generally, for the application to nitrate salt environment, SS 304 and Carbon steel can be used up to 350^oC. For application to higher temperature up to 600^oC, SS 347, SS 321, SS 316L, Incolloy 800, Hynes 242, Inconel 718, Inconel 625 can be used. Design parameters of the test facility are listed in Table 3.1.

Table 3.1: *Material used to construct the MSNCL*

Description	Material	Design Pressure (bar)	Design Temperature (^oC)
Main loop	Inconel-625	5	800
Expansion Tank	SS-316	5	600
Melt Tank	SS-316	5	600

Maximum operating temperature of the molten nitrate salt in the molten salt natural circulation loop is 565^0C and the operating gauge pressure is 0.5 bar.

In the present work, molten nitrate salt (mixture of molten sodium nitrate and potassium nitrate salt in the ratio of 60:40 by weight) is used. This salt remains in liquid state between 238^oC and 600^oC at atmospheric pressure. Hence the maximum loop operating limit is limited to 565^oC and loop operating pressure was 0.5 bar. This avoids the decomposition of the salt at high temperature. The expansion tank and melt tank used in the facility have been fabricated from SS 316L, since the SS 316L can be used up to 600^oC.

3.4 Design of various components

As explained earlier MSNCL comprises five parts: heater, cooler, melt tank, expansion tank and main loop piping. The detailed design and specifications of the parts/ components are as follows:

3.4.1 Main loop

The main loop is a 1/2” (ID=13.88 mm), uniform diameter, 2.0 m x 1.4 m rectangular loop. Inconel 625 is used as a material of loop piping. Coolers and heaters have been installed on the loop piping as shown in Fig. 3.1.

3.4.2 Melt tank

The melt tank has been installed at the bottom of the loop. As the name indicates, salt is melted in this tank. Then, with the help of the gas pressure, the molten salt is raised to fill the loop. Melt tank is fabricated with SS 316L, 8” (200 NB) SCH 40 (ID = 202.74 mm), uniform diameter pipe having 500 mm height. A blind flange is used to cover the top of the tank. It has total 9 holes drilled for instrumentation purpose.

3.4.3 Expansion tank

An expansion tank is used to accommodate the volumetric expansion of the salt. Expansion in the molten salt due to heating and contraction due to cooling is accommodated with the help of the expansion tank which gets partially filled with molten salt. The tank has been installed at the top of the loop as shown in Fig. 3.1. It is fabricated with SS 316L, 6” (150NB) SCH 40 (ID = 153.96 mm) pipe having top blind flange drilled for instrumentation purpose. A cover gas is provided over the surface of the molten salt in the expansion tank. During experiment, half of the tank was filled with molten salt and half of it with cover gas Argon. The cover gas pressure is maintained with the help of a regulating valve provided in the cover gas system.

3.5 Blower

Air is used as a cooling media in the secondary side of the loop. The air is blown in outer annulus of cooler using a blower. The cooling load of the cooler is 2.5 kW. The specifications of the blower are as follows:

Power supply	: 3 Phase
Motor power	: 3HP
Maximum Flow	: 0.472 m^3/s

3.6 Various heaters used in the loop

The mixture of sodium nitrate and potassium nitrate of 60:40 compositions by weight freezes at 238°C. Piping and vessel used in the loop are provided with electrical heaters on the outer pipe surface and band heaters on the vessels for keeping the nitrate mixture in molten condition. Surface temperatures on piping and vessels have been monitored. Once the fluid in the loop attains 300°C, all the surface heaters and band heaters are switched off and immediately the main vertical heater is switched ON.

In the main heater section of the loop, heat is generated by electrical heaters and transferred to the molten salt coolant as sensible heat. Heating of molten salt in this section is carried through coil type heaters having ceramic insulation.

3.7 Instrumentation for the loop

The instrumentation provided for this facility has three major objectives. These are (a) data acquisition during experiments, (b) monitoring, and (c) control of various parameters for operational requirements and process safety requirements. All the process parameters have been transmitted electronically to the control room.

Central control system has been located in the control room for processing all the electronic signals transmitted from the field transmitters. The control system digitizes the analog signals, computes the control signals and sends out to the control devices. The supervisory computer serves as operator interface as well as database server.

Monitoring of various parameters like pressure, temperature, levels in different components of the loop, valve positions etc., have been carried out through DACS. Different sensors of the loop provide inputs to the DACS. All operational and safety conditions were fed into the controllers. Warnings, alarms and automatic trips were incorporated into the program for safe operation of the loop. The instrumentation of the loop was designed to control the loop parameters in case of failures. High temperature pneumatically operated Control Valves (CV) and Pressure Regulating Valves (PRV) are used for the control and operation of the loop. Besides these, pressure relief valves were used to relieve Argon gas in case of high system pressure. Non-return valves were used to prevent ingress of molten salt into the impulse lines from the main loop, during any event. All the valves were PID controlled. The instrumentation and control systems were designed in such a way that the loop can be operated remotely as much as possible. High temperature pressure transmitters were used to measure the gas pressure in the main loop.

3.7.1 Pressure measurement

Pressure of the cover gas (Argon) in the melt tank and expansion tank has been measured by SMAR make remote seal diaphragm based electronic smart transmitters. Due to unavailability of high temperature (~560^{o}C) pressure or differential pressure measurement instruments for molten salt, pressure drop measurement for molten salt was not possible in the experiment, though in the design provision for DPT was made.

3.7.2 Level measurement

Levels in the tanks have been measured by measuring differential pressure between cover gas and the liquid at the bottom of the tanks. The pressure of the liquid at the bottom of the tank was sensed by slow purging of argon gas at a constant rate achieved by purge rotameter. This differential pressure has been measured by differential pressure transmitters. Since the molten salt level measurement was important requirement of the loop, two types of level sensors have been used; discrete type and continuous type. The discrete type level sensor is based on electrical conduction principle, where the electrical circuit is closed when molten salt surface touches a metallic rod hanging from the top flange of melt tank and expansion tank. The continuous type level sensor is based on gas bubbling technique. Here, inert gas is bubbled by injecting it via a stainless steel tube into the liquid. While measuring the differential gas pressure between the bubble tube and the cover gas in the tank, the level of molten salt was recorded continuously.

3.7.3 Temperature measurement

All the temperatures in the loop are measured by mineral insulated, 1 mm, SS316 and Inconel 625 sheathed; K-Type thermocouples along with ASTRON make isolated electronic temperature transmitters giving 4 to 20 mA normalized floating signals. The transmitters have been calibrated in groups depending on temperature zone in the process.

Locations of thermocouple are on the inner surface of the pipes and vessels in most of the cases. However, some thermocouples have been inserted in the pipe to sense bulk temperature of the fluid using 1 mm Inconel 625 thermocouple fittings.

3.7.4 Control valves, PRVs and RVs

Control valves used in this loop are made up of SS316 with bellow seal. The size of the valves installed on molten salt line is ½” and they have been rated for 500^{o}C and ANSI 900 class where as ¼” size, 400^{0}C and ANSI 600 class valves are used on gas (argon) pressure line. The valves on molten salt lines are jacketed with 230 V AC electrical heaters controlled by built-in bi-metallic sensors/solid state power controllers. Thermocouple sensors are also brazed on the surface of the valves and these signals are transmitted to control system for continuous monitoring and controlling the surface temperature of the valves.

Redundant relief valves (RVs) have been provided on the top of each tank for relieving excess cover gas pressure. Their discharges have been collected in a common header, which is connected to the exhaust of loop ventilation system.

3.8 Experimental procedure

Initially, salt mixture is in powder form which is melted in the melt tank provided at the bottom. Molten salt in the melt tank is then pressurized by Argon gas system. Due to pressurization molten salt starts to flow into the loop and subsequently fills the entire loop. After filling, the loop is isolated from the melt tank by a control valve. Adequate care has been taken to prevent contact of air with the molten salt to avoid formation of carbonate precipitate from CO_2 present in the air which may choke the piping of the loop. Before filling up with molten salt, the loop was preheated and purged with Argon gas to drive out air from the loop. The process of natural circulation of molten salt in the loop can be explained in detail as follows.

Before the steady state and transient experiment, preparatory test was carried out to commission the loop. For filling the salt, the whole loop was heated above 300^{o}C. Molten salt temperature in the melt tank was then increased to 350^{o}C. With the help of Argon gas pressure, the molten salt from the melt tank was pushed to fill the entire loop and finally to expansion tank. An overflow line was provided from expansion tank to melt tank which prevented the excess filling of molten salt into the loop. After a fixed level of the salt in the expansion tank, excess molten salt came back to the melt tank through overflow line.

Natural circulation of the molten salt takes place in the loop due to heating of the salt in the heater section and cooling in the cooler section. K-type, Inconel sheathed thermocouples were installed in the loop for temperature measurement. Most of the thermocouples were installed on the surface and some were inserted into the piping and vessels through special fittings to measure the molten salt temperature. Thermocouple readings were read through analogue input modules of the PID.

3.9 Experimental Results and Discussions

Various steady state and transient experiments were performed in molten salt natural circulation loop of VHHC configuration. The transient studies carried out in the experimental facility involve; (1) power raising from one power to another power, (2) power step back from one power to another power, (3) loss of heat sink and (4) loss of heat source i.e. heater trip transients. These transients have been considered important for the safety assessment of molten salt based systems. In addition to these, the operational transients concerned with start-up of the loop have also been performed. Prior to each transient, steady state conditions were established in the loop which were the initial conditions of the transients. The steady state runs also help to check the performance of the instrumentation before the transient begins. For the integrity and safety of the loop, most transients were mitigated by re-starting the cooler or changing the main heater power for retaining safe operating range of 300^{o}C to 580^{o}C. The test matrix for the experiments is shown in Table 3.2. The results of the experiments are discussed in subsequent sections.

Table 3.2: Test matrix for experiments in MSNCL

Experiment	Initial condition	Procedure
1) Step change in power transient (Power rising from steady state and power step back transient).	Molten salt temperature in the loop is constant with time at a fixed heater power and secondary coolant mass flow rate of 0.02 kg/s	Increase or decrease the power of the main heater and allow the system to achieve new steady state.
1st transient	Steady state at 1200 W	Main heater power changed to 1500 W
2nd transient	Steady state at 1500 W	Main heater power changed to 1600 W
2) Loss of heat sink	Steady state at 1500 W, secondary coolant mass flow rate of 0.02 kg/s and molten salt temperature at heater outlet = 372°C	Secondary side air flow is stopped by switching of the blower (i.e secondary coolant mass flow rate is 0 kg/s)
3) Heater trip	Steady state at 2000 W, secondary coolant mass flow rate of 0.02 kg/s and molten salt temperature at cooler outlet = 410°C	Main heater power setting is changed to zero

3.9.1 Steady state tests

In the steady state natural circulation experiment, the loop was allowed to reach steady state conditions at different powers. When the heater power is applied to the molten salt natural circulation loop, flow gets initiated. With increase in flow velocity, frictional resistance also increases. After some time, balance of frictional resistance and buoyancy force leads to a steady state. The temperature rise across heater settles to the value: $\frac{\text{Power}}{\dot{m} \times C_p}$. The actual temperatures at different locations of the loop, like heater inlet (T_{hi}), heater outlet (T_{ho}), cooler inlet (T_{ci}), cooler outlet (T_{co}), settle to appropriate values depending on heater power and secondary side parameters (coolant inlet temperature and coolant mass flow rate). The steady state mass flow rate depends on heater power and loop configuration. By observing the trend of molten salt temperature at different locations, the steady state conditions were judged. Figure 3.4 shows the steady state temperature obtained at different locations of the MSNCL for different heater powers. It can be seen that, with increase in power, T_{hi}, T_{ho}, T_{ci}, T_{co} temperatures are found to increase.

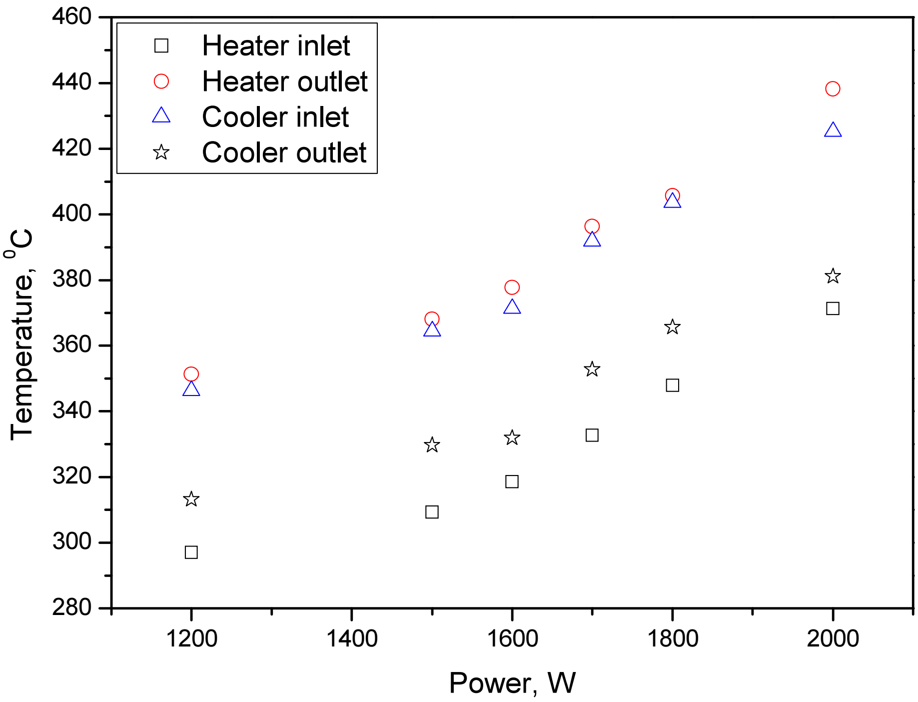

Figure 3.4: Experimental data obtained at steady state condition achieved by MSNCL at different heater powers

Vijayan (2002) derived the relationship for steady state flow obtained at a fixed heater power. The relationship was derived in the form of non-dimensional numbers. The steady state flow in single-phase natural circulation loops can be expressed as $Re_{ss} = C[Gr_m / N_G]^r$ where the constants C and r depend on the nature of the flow (i.e laminar or turbulent). Based on the heater power and obtained heater inlet and outlet temperatures, mass flow rate is calculated using the expression, $Q = \dot{m} C_p (T_{HO} - T_{HI})$ and steady state Reynolds number will be calculated by the expression $Re_{ss} = \frac{\dot{m}D}{A\mu}$. In this equation, Q is heater power, $\dot{m}$ is mass flow rate, C_p= specific heat and it is calculated at mean temperature of heater inlet and outlet, T_{HO}= Temperature at heater outlet, T_{HI}= Temperature at heater inlet, D= loop diameter, A= cross sectional area of the pipe. Figure 3.5 shows the variation of steady state Reynolds number obtained from the experimental data with the non-dimensional parameters $\left(Gr_m / N_G \right)$ where Gr_m is the modified Grashof number and N_G is the non-dimensional geometrical parameter. The modified Grashof number is $\left(Gr_m\right)_{\Delta z} = \frac{D^3 \rho^2 \beta g Q_h \Delta z}{A \mu^3 C_P}$ where ρ is the density, g is the acceleration due to gravity, Q_h is the heater power, β is thermal expansion coefficient and C_p is the specific heat. The geometrical parameter N_G for uniform diameter loop is, $N_G = \frac{L_t}{D}$, where the total length of the loop, $L_t = \sum_{i=1}^{N} L_i$, L_i is the length of each segment and N is the number of segments. Thermo-physical properties to find out Gr_m have been calculated at loop mean temperature.

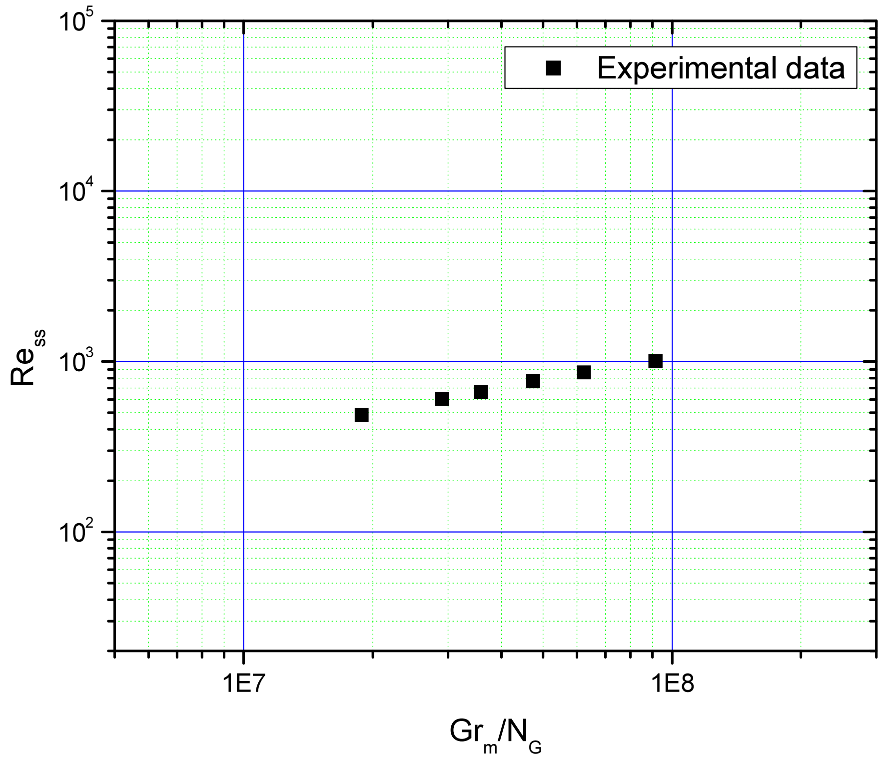

Figure 3.5: Variation of experimental steady state Reynolds number with non-dimensional parameter $\left(Gr_m / N_G \right)$.

In the VHHC configuration, distance from heater outlet to cooler inlet is small. Hence there is no significant heat loss in piping between vertical heater and horizontal cooler. Hence T_{ci} is almost same as T_{ho}. But distance between cooler outlet and heater inlet is large. Hence there is a significant heat loss although the connecting piping is provided with ceramic wool insulation. Hence T_{hi} is less than T_{co} by approximately 20°C. The high mean temperature of the loop leads to some inevitable loss.

3.9.2 Transient tests

Transient studies were carried out to study the loop behaviour. The transient experimental studies include the following transients.

(1) Power raising from steady state (power step up) transients

(2) Power step back from steady state transients

(3) Power trip transients

(4) Loss of heat sink transients

The above mentioned studies are important to validate the theoretical models used.

3.9.2.1 Power Raising from Steady State (PRSS) transients

The experimental study of power raise from steady state at low power to higher power for VHHC configuration was carried out in the experimental facility. The objective of this study is to understand the loop behaviour with the step change in heater power. In the solar power tower due to solar insolation changes, the heat flux on the receiver will vary with time. This kind of variation in heat flux may change the loop dynamics and the same has been studied using step change in heater power of the loop.

In PRSS transient study, the steady state at a lower power is first obtained. Then the power is raised to higher level and the same is maintained till new steady state is achieved. Figure 3.6 shows the experimental observation of temperature variation at different locations of the loop in PRSS transient of 1200 W to 1500 W. This means, power has been raised from 1200 W to 1500 W in this transient study. In the Fig. 3.6, time at which the power change from steady state has been taken as initial point (0 second) on time axis. It has been observed that, the heater inlet temperature has been raised from 297.1^{o}C at 1200 W to 309^{o}C (the heater inlet temperature at steady state condition of 1500 W). Similarly, the heater outlet temperature, cooler inlet and cooler outlet temperatures has been raised from 351.3^{o}C to 372.4^{o}C, 346.4^{o}C to 369.4^{o}C and 313.2^{o}C to 341.8^{o}C respectively.

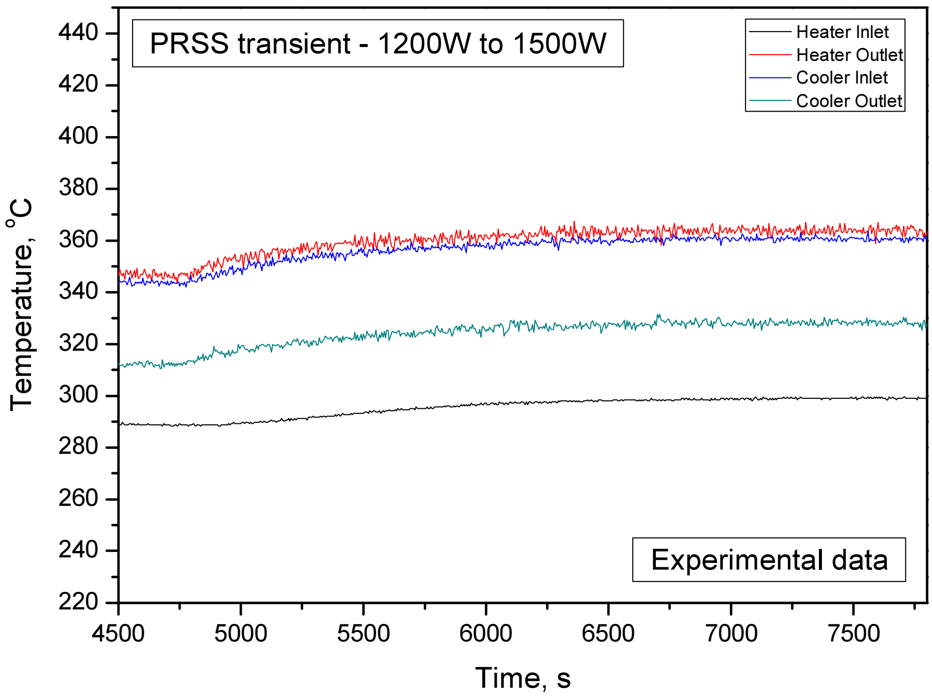

Figure 3.6: Experimental observation of transient variation of temperature at different location in PRSS transient of 1200 W to 1500 W

Figure 3.7 shows the experimental observation of temperature variation at different locations of the loop in PRSS transient of 1500 W to 1600 W. This means power has been raised from 1200 W to 1500 W in this transient study. In the Fig. 3.7, time at which the power change from steady state has been taken as initial point (0 second) of the PRSS transient study. It has been observed that, the heater inlet temperature has been raised from 316.1°C at 1500 W to 324.9°C (the heater inlet temperature at steady state condition of 1600 W). Similarly, the heater outlet temperature, cooler inlet and cooler outlet temperatures has been raised from 377.7°C to 386.1°C, 371.3°C to 382.6°C and 344°C to 331.9°C respectively.

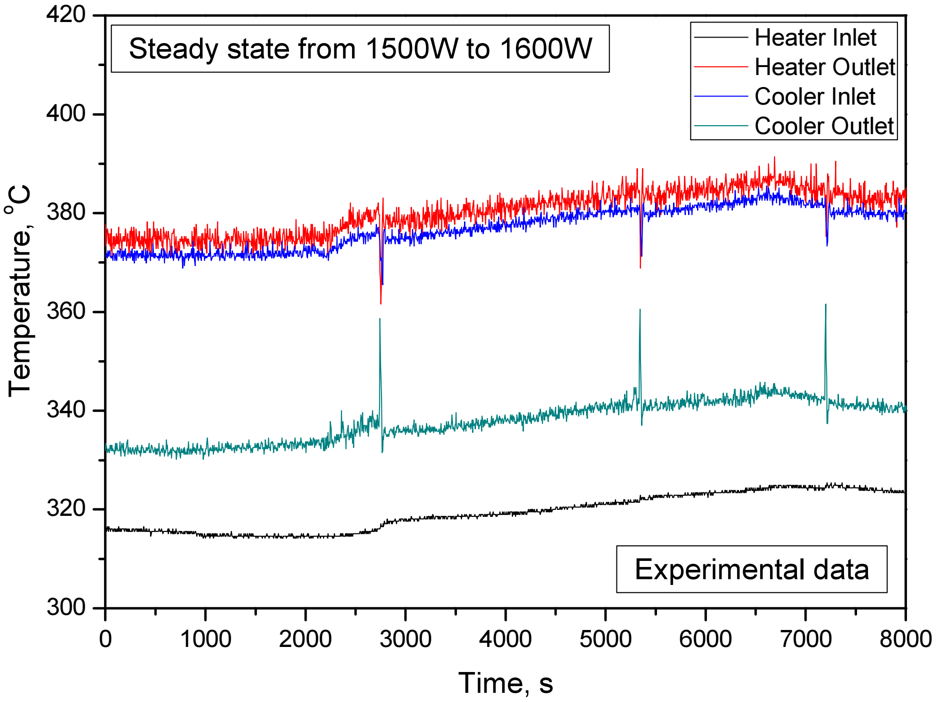

Figure 3.7: Experimental observation of transient variation of temperature at different location in PRSS transient of 1500 W to 1600 W

The experimental observation of temperature variation at different locations of the loop in PRSS transient of 1600 W to 1700 W is shown in Fig. 3.8. This means power has been raised from 1600 W to 1700 W in this transient study. In the Fig. 3.8, time at which the power change from steady state has been taken as initial point (0 second) of the PRSS transient study. It has been observed that, the heater inlet temperature has been raised from 319°C at 1600 W to 332.7°C (the heater inlet temperature at steady state condition of 1600 W). Similarly the heater outlet temperature, cooler inlet and cooler outlet temperatures has been raised from 378.2°C to 396.3°C, 373.8°C to 391.9°C and 334.8°C to 352.8°C respectively.

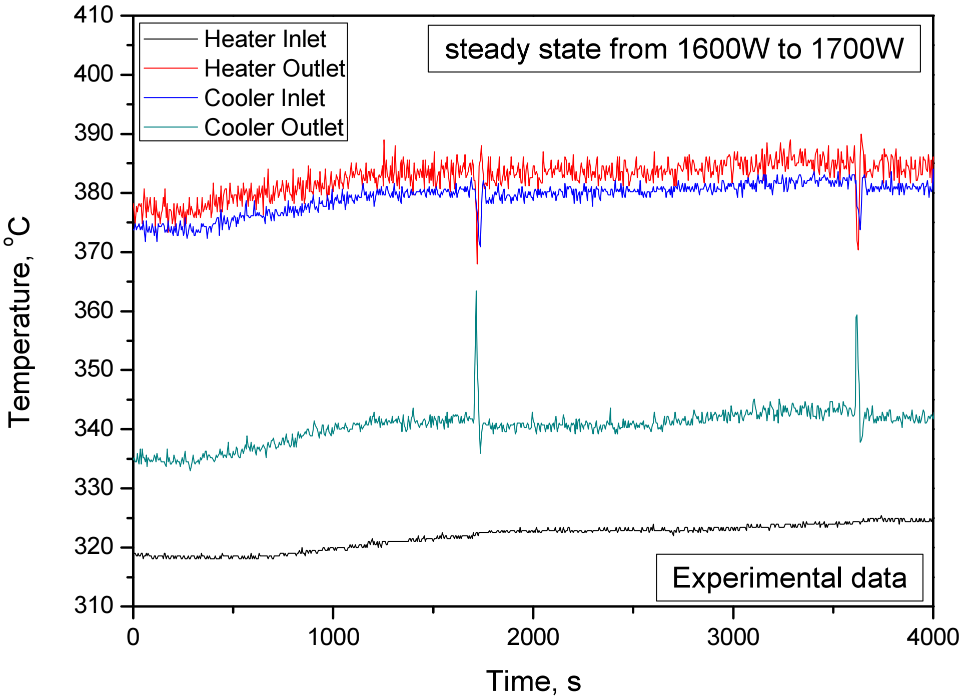

Figure 3.8: Experimental observation of transient variation of temperature at different location in PRSS transient of 1600 W to 1700 W

The experimental observation of temperature variation at different locations of the loop in PRSS transient of 1800 W to 2000 W is shown in Fig. 3.9. This means power has been raised from 1800 W to 2000 W in this transient study. In the Fig. 3.9, time at which the power change from steady state condition of 1800 W has been taken as initial point (0 second) of the PRSS transient study. It has been observed that, the heater inlet temperature has been raised from 347.9°C at 1800 W to 371.3°C (the heater inlet temperature at steady state condition of 2000 W). Similarly the heater outlet temperature, cooler inlet and cooler outlet temperatures has been raised from 405.6°C to 427.2°C, 403.7°C to 428.7°C and 365.6°C to 387.7°C respectively.

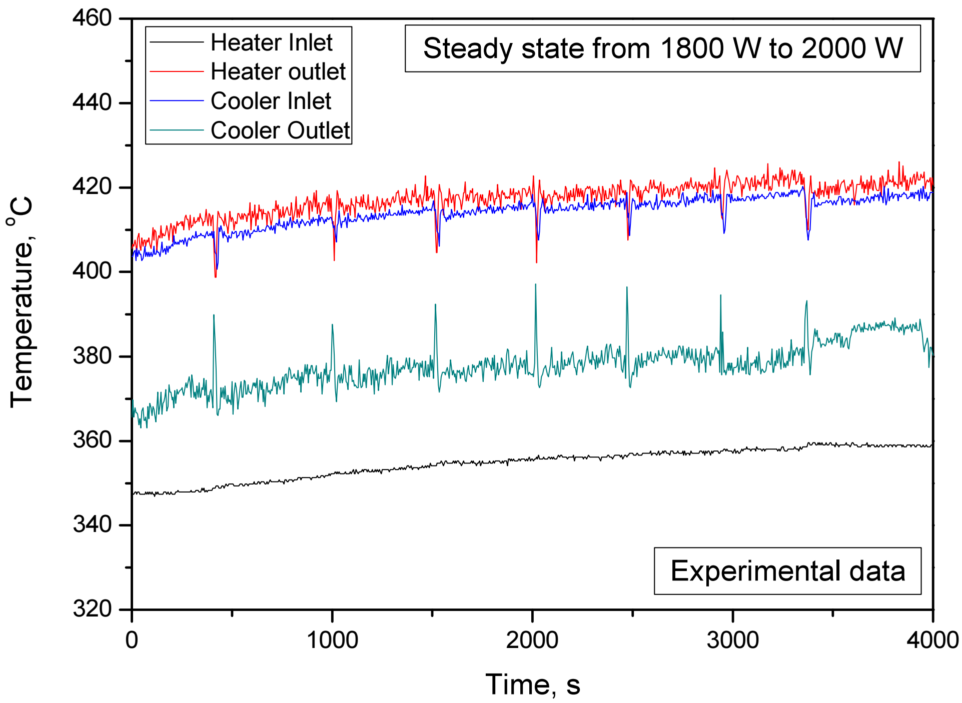

Figure 3.9: Experimental observation of transient variation of temperature at different location in PRSS transient of 1800 W to 2000 W

The following observations were made from the experimental study on PRSS transients (from Fig. 3.6 to Fig. 3.9):

1. Temperature at all the locations (such as at heater inlet, heater outlet, cooler inlet and at cooler outlet) increases with increase in power.
2. Minimum power rise leads to smooth variation of temperature at all the locations of the loop.
3. For a larger power rise, the rise in temperatures is larger.
4. Sudden change in power did not result into oscillatory flow. Thus system stability is not affected during this experiment.

3.9.2.2 *Power step back transients*

In this study, the loop is allowed to achieve steady state at a specific power level and then the power was suddenly reduced to a lower level and the loop behaviour was observed. This procedure is known as power step back transience. These kind of transient studies are helpful to know the molten salt loop behavior during power variation. In case of solar power tower during solar isolation changes, the heat flux falling on the receiver will change. This is similar to power step back from higher power to lower power. Figure 3.10 to Fig. 3.13 shows the power step back transients obtained during the experimental study. It can be seen from the figures, the loop attains new steady state in all the cases. There are no large scale oscillations affecting stability of the system.

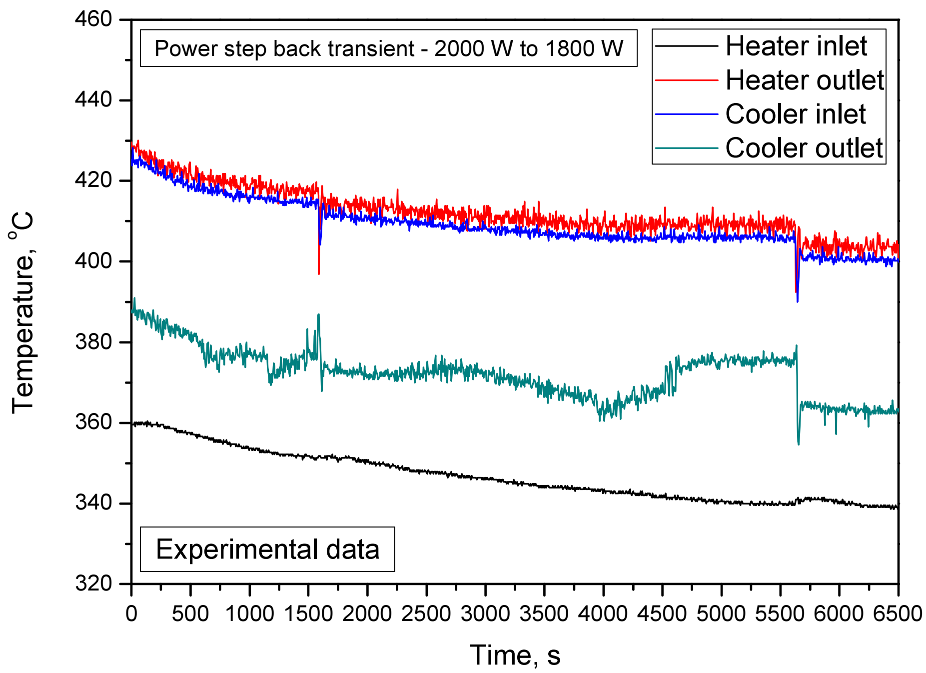

Figure 3.10: Transient variation of temperature at different location in power step back transient of 2000 W to 1800 W by experimental observation

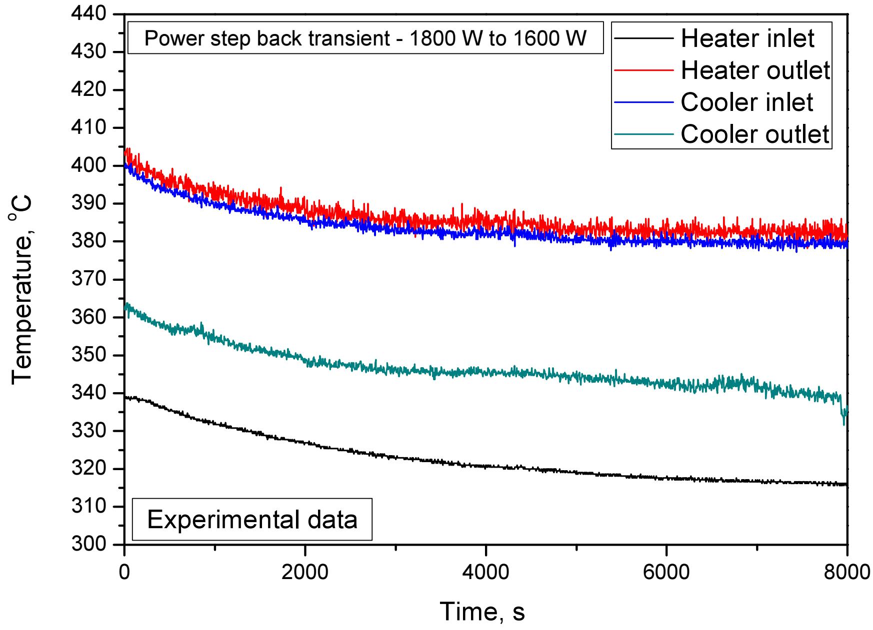

Figure 3.11: Transient variation of temperature at different location in power step back transient of 1800 W to 1600 W by experimental observation

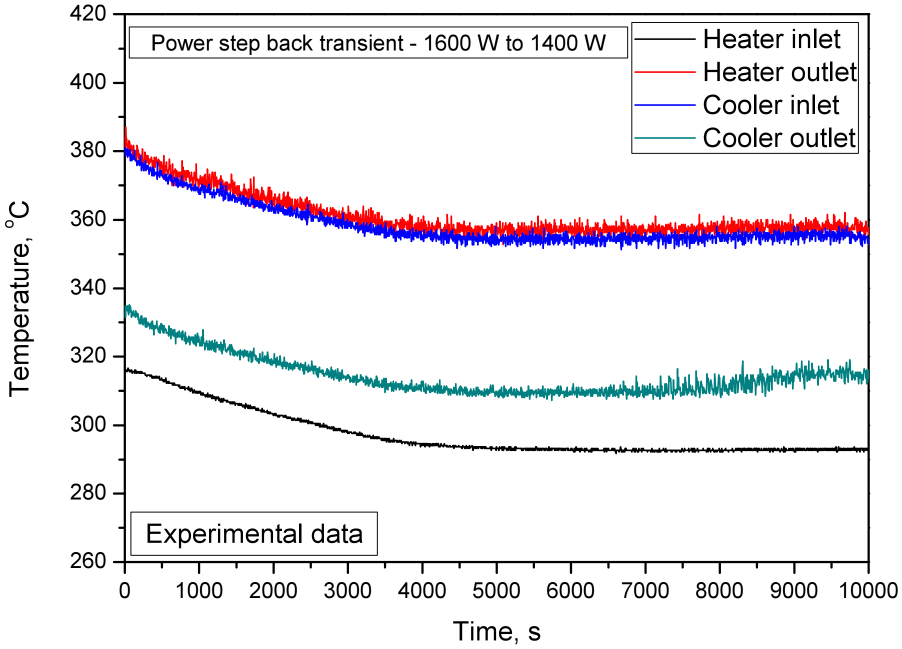

Figure 3.12: Transient variation of temperature at different location in power step back transient of 1600 W to 1400 W by experimental observation

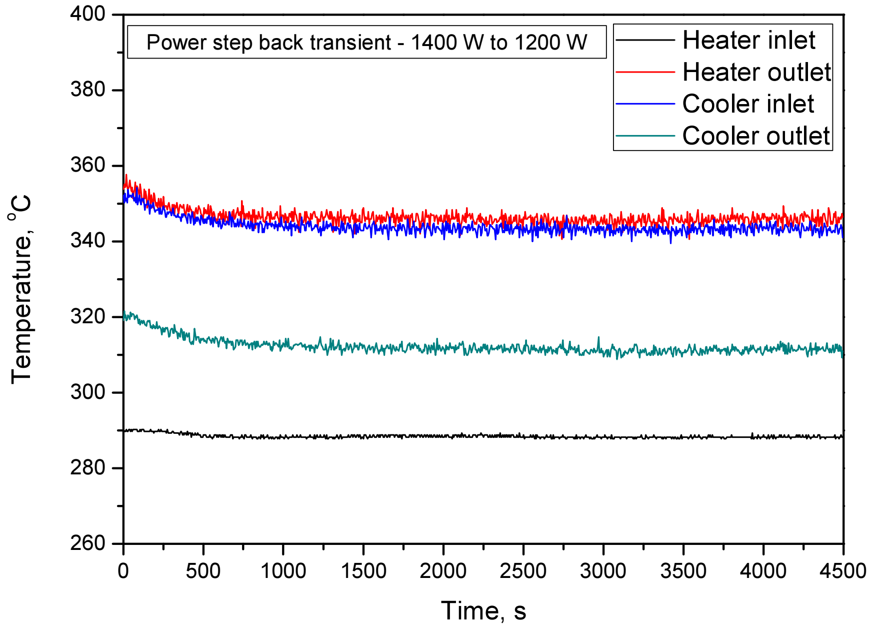

Figure 3.13: Transient variation of temperature at different location in power step back transient of 1400 W to 1200 W by experimental observation

New steady state temperature achieved at heater inlet, heater outlet, cooler inlet and cooler outlet locations in these transients are summarized in Table 3.3 given below.

Table 3.3: Experimental data obtained from Power step back transient study

Initial Power (W)	Final Power (W)	Heater inlet Temperature (°C)		Heater outlet Temperature (°C)		Cooler inlet Temperature (°C)		Cooler outlet Temperature (°C)	
		Initial	Final	Initial	Final	Initial	Final	Initial	Final
2000	1800	359.6	338.6	429.6	400.7	425.2	400.2	387.3	363.1
1800	1600	338.6	316.6	403.2	381.7	399.8	378.2	362	336.3
1600	1400	315.6	289.7	384.1	355.7	379.2	352.2	333.7	321.6
1400	1200	290.2	288.3	353.8	346.4	352.2	341	319.1	311

Table 3.1 shows that, temperatures at all the locations decrease with the power step back. It can be seen that, the temperature difference between cooler out let to heater inlet is very less comparable to the same in PRSS transient cases. This reduction in the temperature difference

is mainly due to the heat addition from the hot fluid in the expansion tank during the transient. This will leads to increase the heater inlet temperature. This does not change if power is reduced from 1200 W to 1000 W. The temperature variation at all the locations of the loop is smooth, there is no random variation.

3.9.2.3 Loss of heat sink transients

The loss of heat sink is considered in the safety analysis of reactors. This experiment was carried out at 1200 W and 1500 W heater powers. The loop was started and steady state was established. After achieving steady state, secondary flow in the cooler duct (i.e. air flow) was stopped completely by switching off the power supply to the blower

Figure 3.14 and Fig. 3.15 show the transient variation of temperature at different locations of the loop during loss of heat sink transients for heater powers of 1200 W and 1500 W respectively. It can be seen that, after the loss of heat sink, there is significant increase in the temperature at different locations of the loop. This causes an overall increase in the loop average temperature, which is justified as heat is getting deposited in a constant mass of fluid without getting rejected anywhere else.

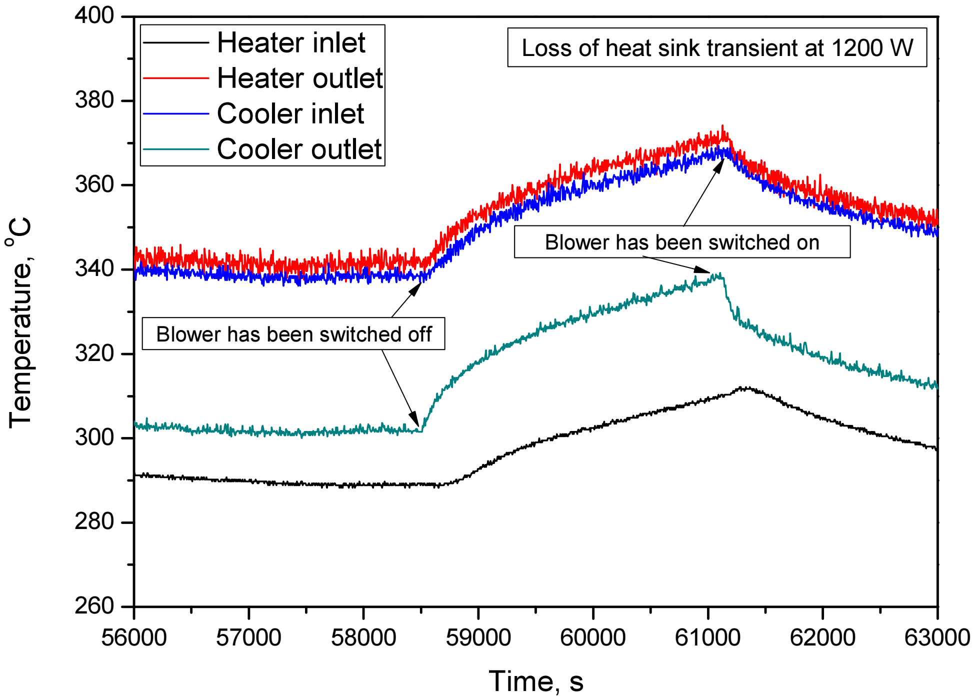

Figure 3.14: Transient variation of temperature at different location in loss of heat sink transient of 1200 W by experimental observation

For loop operating at 1200 W, the time taken for the heater outlet temperature to rise from 342°C to 368°C is around 3000 s. Hence it will take another 27000 s to reach 600°C, which is the maximum limit of stable liquid state of the nitrate salt. Thus around 9 hours time is available to restore cooling at this power.

For loop operating at 1500 W, the time taken for the heater outlet temperature to rise from 359°C to 410°C is around 3500 s. Hence it will take another 14000 s to reach 600°C, which is the maximum limit of stable liquid state of the nitrate salt. Thus around 5 hours time is available to restore cooling at this power.

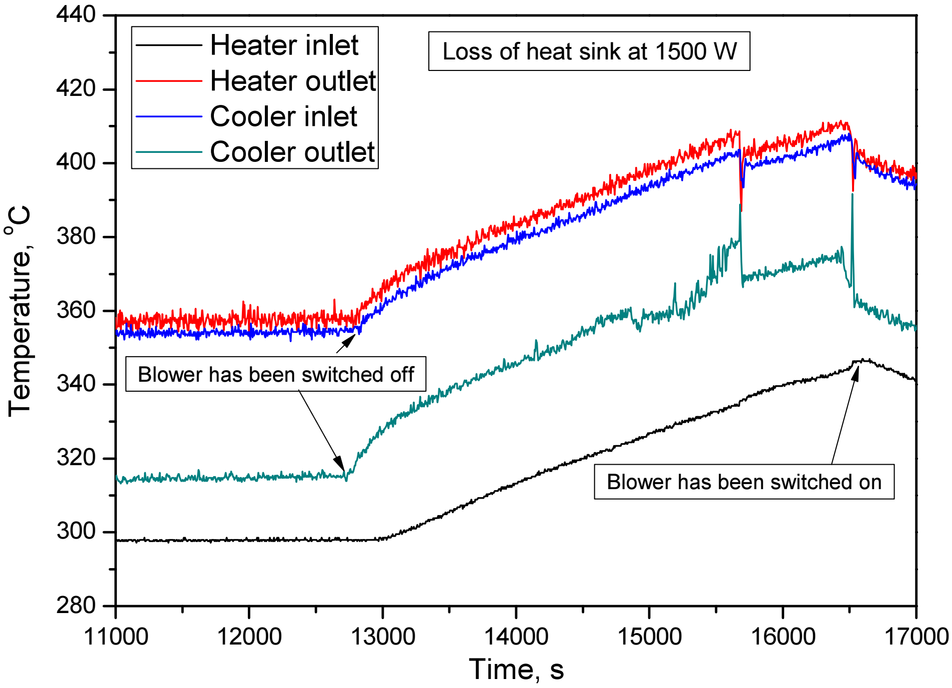

Figure 3.15: Transient variation of temperature at different location in loss of heat sink transient of 1500 W by experimental observation

This study helps to estimate the time available to restore cooling before the molten salt reaches limiting temperature in case of loss of heat sink (after taking care of all the scaling parameters with respect the actual system).

3.9.2.4 Heater trip transients

Power trip transients are helpful to know the thermal-hydraulic behaviour of molten salt during sudden power trip. Such power trip may occur in nuclear reactors when, due to some abnormal occurrence, the reactor is scrammed to shut-down. Further, molten salt are used as heat carrying fluid in solar power plants wherein the molten salt gets heated by concentrating solar rays in solar receiver. During night and cloudy weather, the solar heating is not available. In that scenario, the consequence of sudden non-availability of heat source is simulated using heater trip transient.

The steady state condition of MSNCL corresponding to 2000 W heater power was achieved. The power trip at this steady state condition is carried out by switching of the electrical supply to heater. Figure 3.16 shows the transient variation of temperature at heater outlet, heater inlet, cooler outlet and cooler inlet locations. Due to continuous cooling and circulation of coolant, whole loop fluid gets cooled and temperature gradient in loop keeps reducing. The loop fluid temperature homogenization takes place with time and hence difference between heater outlet and cooler inlet keeps reducing. This leads to reduced mass flow rate also. After heater trip the cooler inlet keeps receiving fluid filled between heater outlet and cooler inlet, whereas heater outlet gets fluid filled between cooler outlet to heater outlet (which is at less temperature than that between heater outlet and cooler inlet before power trip). This may be the reason for cooler inlet temperature being more than heater outlet temperature for the transients of heater trip. The observed heater inlet temperature is more than the cooler outlet temperature. This increase in heater inlet temperature is due to the heat addition from the high temperature fluid in the expansion tank, which is situated between cooler outlet and heater inlet in this configuration. It can be seen that there is gradual decrease in loop temperature without any oscillations, which is desirable. Using this data, it's possible to compute time to reach a freezing temperature and thus time available to restore power or dump salt in storage.

For loop operating at 2000 W, the time taken for the cooler outlet temperature to decrease from 387^{o}C to 297^{o}C is around 1000 s. Hence it will take another 600 s to reach 238^{o}C, which is the minimum temperature limit of stable liquid state of nitrate salt. Thus around 27 minute time is available to switch ON the power supply to avoid solidification of molten salt in the loop.

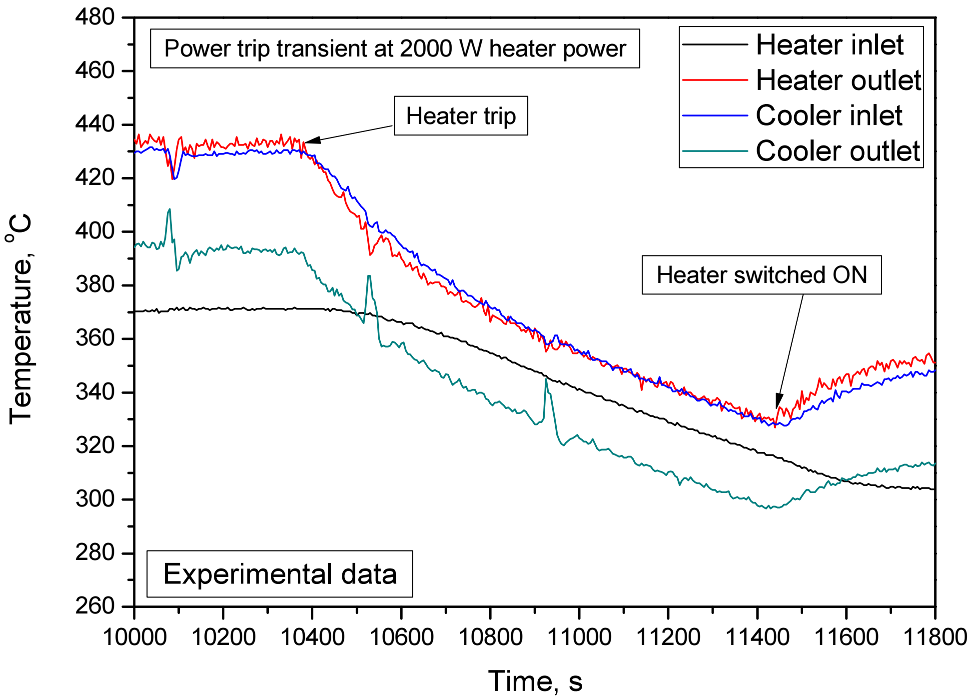

Figure 3.16: Transient variation of temperature at different location in Power trip transient of 2000 W by experimental observation

3.10 Closure

This chapter gives the details of the experimental test facility of molten salt natural circulation loop and associated equipments. The experimental procedure to conduct steady state and transient studies is explained. The experiments are performed for different heater power to achieve steady state condition. At the steady state condition, temperatures in various sections of the loop are collected and are plotted as a function of heater power. The various transient studies are performed at different heater powers of VHHC configuration. Variation of temperatures in different sections of the loop has been plotted for various transients studied. This experimental data have been compared with computational studies in chapter 5 and details of this exercise are given therein.

CHAPTER 4

STEADY STATE AND TRANSIENT CHARACTERISTICS OF NATURAL CIRCULATION LOOP WORKING WITH WATER

4.1 Introduction

The objective of this work is to obtain complete 3D steady state and transient simulation of a Natural Circulation Loop (NCL) working with water. In the previously reported experimental studies, it was found that in HHHC configuration, sustaining uni-directional/bi-directional oscillations were observed (Vijayan et al., 2001). However, reason for formation of uni-directional oscillations at low power or bi-directional oscillations at higher power could not be explained. Subsequently, 1D simulations were successful for modeling VHVC, VHHC configurations, but were unable to compute transient flow in HHHC configuration. Naveen Kumar et al., (2014) developed a new 1D model for simulating the start-up from rest of water cooled single-phase natural circulation loop having horizontal heaters by adding extra source term in the energy conservation equation. In present research work, 3D CFD simulation of natural circulation loop working with water is carried out to access the capability of CFD methodology for predicting various transients in natural circulation loop especially in HHHC configuration. Also it is expected that from the detailed 3D simulations, reason behind formation of uni/bi-directional oscillations in HHHC configuration of natural circulation loop will be explored.

The computational domain for CFD simulation of NCL working with water includes primary fluid (fluid in the loop), secondary fluid (fluid in cooler duct) and pipe thickness. The flow initiation transient simulations are carried out for all the four configurations. Such a transient simulation is highly time consuming and expensive, but it generates the flow field data which can be used to understand complete evolution of flow and temperature fields in the loop leading to various types of instabilities. The main contribution of present work is to confirm the hot plug and cold plug transport theory used to explain the various types of instabilities (like unidirectional or bi-directional pulsing) formed in NCL of HHHC type. Steady state characteristics of various configurations are also obtained and compared with various correlations and experimental data. The comparison of transient simulations data with experimental data is also carried out.

Figure 4.1 shows schematic diagram of the loop. Many experiments have been carried out by Vijayan et al. (2001, 2002, 2007) on this loop. The CFD results are compared with the experimental data obtained from this facility. The instability in the natural circulation loop is successfully computed in present 3D CFD simulations. For the first time the reason behind the formation of uni-directional/bi-directional oscillations is explained with the help of temperature contours.

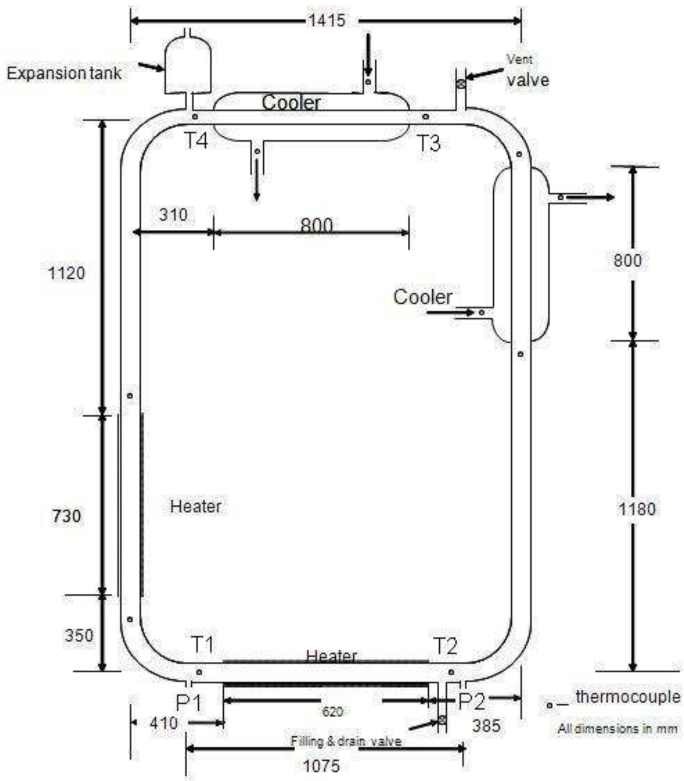

Figure 4.1: Schematic diagram of water loop (Vijayan et al., 2001)

4.2 Loop description

The natural circulation loop which is used for analysis has been taken from literature (Vijayan et al., 2001). The loop was made up of borosilicate glass tube which has inside diameter of 26.9 mm and outside diameter of 28.9 mm. It had two heaters and two coolers. One of the heaters was in bottom leg and the other one is in left vertical leg. The lengths of the vertical and horizontal heaters were 620 mm and 735 mm respectively. One of the coolers is placed in top horizontal leg and the other cooler is placed in right vertical leg. Only one of the heater and cooler combination was used in the experiment. Based on the heater and cooler orientations, as shown in Fig. 4.1, four different configurations were obtained viz. (i) Vertical Heater Vertical Cooler (VHVC), (ii) Vertical Heater Horizontal Cooler (VHHC), (iii) Horizontal Heater Vertical Cooler (HHVC) and (iv) Horizontal Heater Horizontal Cooler (HHHC) configuration. The dimensions of the various sections are shown in Fig. 4.1. Each cooler was 800 mm long, having outside diameter of 49.2 mm with 1.5 mm wall thickness. Constant coolant flow in the secondary side of the cooler was maintained. The inlet temperature of secondary side coolant was maintained constant. The loop also has an expansion tank connected to top horizontal leg to take care of the thermal expansion of water. To minimize the heat loss to atmosphere, the loop was insulated with ceramic wool. In the experiments, the pressure difference across a 1065 mm long section of bottom horizontal leg was measured with the help of a calibrated differential pressure transmitter $\left(\Delta P_{bottomleg} = P_2 - P_1\right)$, which had a measuring accuracy of 0.05% of the span (-100 to +100 Pa). The time varying $\Delta P_{bottom\ leg}$ data obtained from this facility is used for validation of present simulation model. Temperatures are measured at heater and cooler inlets and outlets. In natural circulation loop working with water, the operating temperature range is only 30^{o}C to 80^{o}C. Further there is a thick layer of insulation wrapped all over piping including heater. Hence, heat loss in heater can be safely assumed to be negligible and mass flow rate can be estimated from heat balance over the heater section. The steady state natural circulation mass flow rate, W_{ss}, is obtained as follows:

$$W_{ss} = \frac{Q_h}{Cp_h \left(\Delta T_h\right)_{ss}} \tag{4.1}$$

Where the specific heat, Cp_h, was calculated based on the average temperature (T_h) of the fluid in heater section (taken as the mean of the inlet and outlet temperatures). ΔT_h is the difference of the measured outlet and inlet temperatures of the heater section at steady state. Using this mass flow rate, the steady state Reynolds number was calculated. This specified formula is used only for those cases in which steady state conditions are reached and not for those cases in which sustaining oscillatory flow patterns gets generated.

4.3 CFD simulation

The simulations are performed using 3D CFD code.The modeling methodology and the details about the CFD model incorporated in the present CFD simulation are explained in the following sections.

4.3.1 Computational domain and mesh

In modelling a natural circulation loop there are two options.

1. Model only primary side by specifying convective heat transfer coefficient and ambient temperature.
2. Model both primary and secondary side.

The cooler is tube in tube type heat exchanger as shown in Fig. 4.2. Hence there is heat transfer from primary coolant to pipe thickness by convection, heat conduction within pipe thickness and eventually convective heat transfer to secondary coolant which flows in annulus.

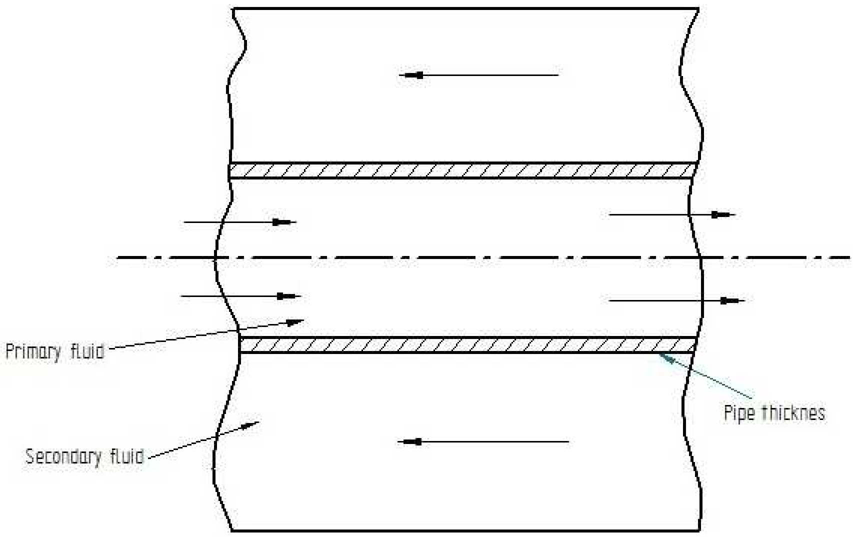

Figure 4.2 Cross-sectional view of cooler section

If secondary side is not considered, then one has to calculate outer convective heat transfer coefficient using appropriate correlation (like Dittus-Boelter correlation) and the heat transfer coefficient has to be assumed constant over entire cooler section.

A more accurate way is to actually model the secondary side. It was found that for modeling flow initiation transients, first approach gives results which deviate much from experimental data. Hence second approach was opted for all further simulations.

The geometry modeled for CFD simulation involves primary side fluid region, pipe thickness and secondary side cooler section. It is assumed that heat loss to ambient from loop piping is negligible due to insulation and also due to lower loop mean temperatures. Hence, in the model, the piping is taken as adiabatic wall boundary. The computational domain is discretized by a 3D multi-block body fitted mesh. Figure 4.3 shows 3D mesh generated for the computational domain pipe cross section and in a transverse plane. Mesh is selected based on mesh independence study described later.

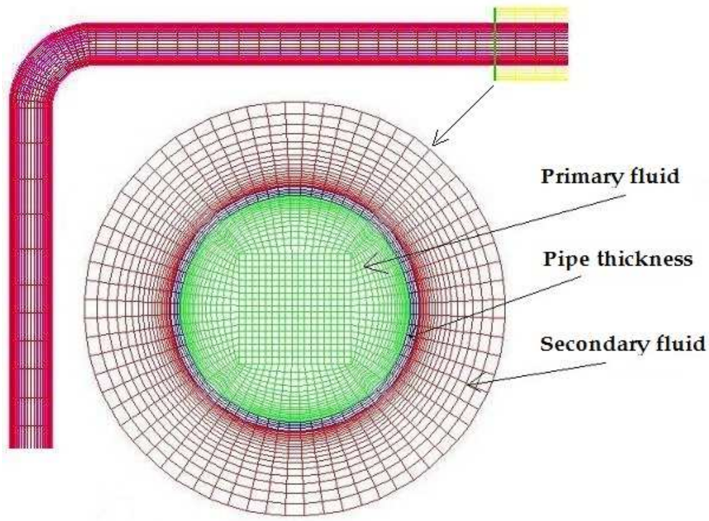

Figure 4.3: Mesh generated for the computational domain

4.3.2 Formulation and numerical settings

4.3.2.1 Governing equations

Depending on heater power, final steady state flow may be laminar/transition/turbulent. From published experimental data, the flow regime is known. In laminar cases, conservation equations are solved to get instantaneous velocity and temperature fields. For turbulent cases, appropriate turbulent conservation equations are solved to get mean velocity/temperature fields.

To compute 3D transient turbulent flow and temperature fields in the computational domain, Reynolds Averaged Navier-Stokes equations are solved along with the transport equations for thermal energy, turbulent kinetic energy $(k)$and its dissipation rate(ε). Natural circulation of a fluid in the rectangular natural circulation loop is due to the density-driven phenomenon in the gravitational field. Density difference is caused by the temperature difference in the loop. Hence variable density model is used in which density is specified as a function of temperature. Temperature dependent thermo-physical properties of the fluid (density, dynamic viscosity, specific heat and thermal conductivity) are incorporated. The fluid is subjected to gravity. The standard k-ε turbulence model with standard wall functions and low-Reynolds k-ε turbulence model (Launder and Sharma, 1974) are used for different cases. The role of turbulent flow is significant due to secondary flow motion in the horizontal heater. As is illustrated later, choice of turbulent model is crucial.

Mass conservation equation is as given below.

$$\frac{\partial \rho}{\partial t} + \overline{\nabla} \cdot (\rho \overline{v}) = 0 \tag{4.2}$$

Where t is time (s) and ρ is the density (kg/m^3). For laminar cases $\overline{v}$ represents instantaneous velocity and for turbulent cases $\overline{v}$ represents instantaneous mean (with respect to turbulence) velocity.

Momentum conservation equation is given below.

$$\rho\left(\frac{\partial \overline{v}}{\partial t} + \overline{v} \cdot \overline{\nabla v}\right) = \overline{\nabla} \cdot (\mu + \mu_t)\overline{\nabla v} - \overline{\nabla p} + \rho \overline{g} \tag{4.3}$$

Where p is the static pressure, $\rho\overline{g}$ is the gravitational body force, μ is the viscosity and μ_t is the turbulent viscosity.

The above form (Equation (4.3)) is for turbulent flow. For laminar cases, momentum equation is obtained by setting μ_t to zero in Equation (4.3).

The Boussinesq approximation

Boussinesq approximation treats density as a constant in all solved equations, except for the body (buoyancy) force term in the momentum equation. The approximation is given below.

$$(\rho - \rho_0) \approx -\rho_0 \beta (T - T_0) \tag{4.4}$$

where ρ_0 is the reference density, T_0 is the reference operating temperature and β is the thermal expansion coefficient. This approximation is accurate as long as changes in density are small; specifically, the Boussinesq approximation is valid when $\beta(T - T_0) << 1$. For water, the value of $\beta(T - T_0)$ is 0.021 and hence Boussinesq approximation is valid.

Energy conservation equation

$$\frac{\partial}{\partial t}(\rho E) + \overline{\nabla} \cdot [\overline{v}(\rho E + p)] = \overline{\nabla} \cdot \left(K_{eff} \overline{\nabla T}\right) \tag{4.5}$$

where E is the total energy (W), K_{eff} is the effective heat conductivity (W/m K) and is given by $K_{eff} = K + K_t$ (where K_t is the turbulent thermal conductivity, defined according to the turbulence model being used) and T is the temperature (K). The right-hand side of Equation (4.5) represents energy transfer due to conduction.

Energy equation in solid regions

In solid regions, energy transport equation used has the following form,

$$\frac{\partial}{\partial t}(\rho h) = \overline{\nabla} \cdot \left(K \overline{\nabla T}\right) + S_h \tag{4.6}$$

Where h is the sensible enthalpy given by $\int_{T_0}^{T} C_p dT$, K is the thermal conductivity and S_h is the volumetric heat source.

The interface between fluid region and solid region

At the interface between fluid region and solid region in the conjugate heat transfer model, the conductive heat transfer through the solid is coupled with the conductive heat transfer in the fluid by

$$\left(K \frac{dT}{dx}\right)_{fluid} = \left(K \frac{dT}{dx}\right)_{wall} \tag{4.7}$$

Standard k-ε Turbulence model:

The turbulent cases are solved using standard k-ε turbulence model. The transport equations for the two equation standard k-ε turbulence model are given below:

$$\frac{\partial}{\partial t}(\rho k) + \overline{\nabla} \cdot (\rho \overline{v} k) = \overline{\nabla} \cdot \left[\left(\mu + \frac{\mu_t}{\sigma_k} \right) \overline{\nabla k} \right] + G_k + G_b - \rho\varepsilon \tag{4.8}$$

and

$$\frac{\partial}{\partial t}(\rho \varepsilon) + \overline{\nabla} \cdot (\rho \overline{v} \varepsilon) = \overline{\nabla} \cdot \left[\left(\mu + \frac{\mu_t}{\sigma_\varepsilon} \right) \overline{\nabla \varepsilon} \right] + C_{1\varepsilon} \frac{\varepsilon}{k} (G_k + C_{3\varepsilon} G_b) - C_{2\varepsilon} \rho \frac{\varepsilon^2}{k} \tag{4.9}$$

where G_k represents the generation of turbulence kinetic energy due to mean velocity gradients, G_b represents the generation of turbulence kinetic energy due to buoyancy, $C_{1\varepsilon}$, $C_{2\varepsilon}$ and $C_{3\varepsilon}$ are constants. σ_k and σ_ε are the turbulent Prandtl numbers for k and ε respectively (Fluent manual).

The turbulent (or eddy) viscosity, μ_t is computed by combining k and ε as follows:

$$\mu_t = \rho C_\mu \frac{k^2}{\varepsilon} \tag{4.10}$$

The model constants $C_{1\varepsilon}$, $C_{2\varepsilon}$, C_μ , σ_k and σ_ε have the following default values:

$$C_{1\varepsilon} = 1.44,\ C_{2\varepsilon} = 1.92,\ C_\mu = 0.09,\ \sigma_k = 1.0,\ \sigma_\varepsilon = 1.3$$

At the inner diameter of loop piping, wall shear stress is computed by standard wall functions, if standard k-ε turbulence model is used. In laminar cases or low-Re turbulence model, no slip boundary condition is used for momentum equations.

Some cases are solved by using low Reynolds number turbulence model. In the low Reynolds number k-ε turbulence model (Launder and Sharma, 1974), the turbulent kinetic energy (k), and energy dissipation rate (ε) are obtained by solving the following equations:

$$\frac{\partial(\rho k)}{\partial t}+\overline{\nabla}\cdot\left[\rho k\overline{v}-\left(\mu+\frac{\mu_t}{\sigma_k}\right)\overline{\nabla k}\right]=P-\rho\varepsilon-\rho D_k \tag{4.11}$$

$$\frac{\partial(\rho\varepsilon)}{\partial t}+\overline{\nabla}\cdot\left[\rho\varepsilon\overline{v}-\left(\mu+\frac{\mu_t}{\sigma_\varepsilon}\right)\overline{\nabla\varepsilon}\right]=\left(C_{\varepsilon1}f_1P-C_{\varepsilon2}f_2\rho\varepsilon\right)\frac{\varepsilon}{k}+\rho E_\varepsilon \tag{4.12}$$

Where $\mu_t=C_\mu f_\mu \rho\frac{k^2}{\varepsilon};\quad P=\tau_{t,ij}\frac{\partial u_i}{\partial x_j};\quad \tau_{t,ij}=\mu_t\left(\frac{\partial u_i}{\partial x_j}+\frac{\partial u_j}{\partial x_i}\right)-\frac{2}{3}k\delta_{ij}$

$$f_1=1;\quad f_2=1-0.3\exp\left(-Re_t^2\right);\quad f_u=\exp\left[\frac{-3.4}{\left(1+{Re_t}/{50}\right)^2}\right];\quad \delta_{ij}=1,\ \text{for } i=j;\ \delta_{ij}=0\ \text{ for } i\neq j$$

$$Re_t=\frac{k^2}{\nu\varepsilon};\quad D_k=2\nu\left(\frac{\partial\sqrt{k}}{\partial y}\right)^2;\quad E_\varepsilon=2\nu\nu_t\left(\frac{\partial^2 u}{\partial y^2}\right)^2$$

$C_{\varepsilon1}, C_{\varepsilon2}, C_\mu, \sigma_k$ and σ_k are the model constants. The damping functions f_μ, f_1, f_2 and extra source terms D and E are only active close to solid walls, which make it possible to solve k and ε in the viscous sub-layer. The values of these constants are listed below,

$C_{\varepsilon1}=1.44,\ C_{\varepsilon2}=1.92,\ C_\mu=0.09,\ \sigma_k=1.3,\ \sigma_\varepsilon=1.0$

4.3.2.2 Discretization schemes

Modeling of combined convection and diffusion terms of the governing equations is as per power law scheme (Patankar, 1980) for all equations. The coupled momentum, turbulence and energy equations are solved by SIMPLE algorithm which is an iterative segregated solution procedure (Patankar, 1980).

4.3.2.3 Boundary and initial conditions

The surface heat flux is provided in heater section. In cooler section, heat is transferred from primary fluid to secondary fluid. Mass flow rate of the secondary side coolant is 5 lpm and coolant inlet temperature is 34^0C. So the corresponding velocity was calculated and incorporated at the cooler inlet as a boundary condition. The piping connecting heater and cooler are considered as adiabatic pipes. Initial flow field is stagnant at atmospheric conditions for steady state cases and for flow initiation transients cases. For transients like power rising from steady state transients, power step back transients, power trip transients and loss of heat sink transients, initial computed flow fields are those from steady state simulations at corresponding power.

4.3.2.4 Computational time

Various time steps were taken for transient simulations and time step independency was checked. The detail of time step independence study is given in next section. In each time step, enough iterations are performed to ensure proper convergence. Due to fine mesh and small time step, computational time for the transient analysis is of the order of 200 hours for each simulation case on a 3.0 GHz single CPU machine.

4.4 Mesh and time step independence

To decide the requirement of mesh size and computational time step size, mesh and time step independence studies were first carried out. Mesh independence test is carried out by computing flow initiation transients in HHHC configuration at 220 W power. The mesh independence is achieved properly by fixing the cross-sectional mesh (Cross-sectional mesh involves 825 cells which includes 11x11x5 in primary fluid side cross-section and 11x5x4 in the pipe thickness) and varying the axial mesh size. The variation of $\Delta P_{bottom\text{-}leg}$ with time is shown in Fig. 4.4. $\Delta P_{bottom\text{-}leg}$ is defined as the pressure difference (ΔP) across a 1075 mm long section of bottom horizontal tube (difference of P1 and P2 in Fig. 4.1) which was measured in experimental facility. From Fig. 4.4, it is clear that, to capture the bi-directional instabilities as observed by experiments, fine mesh in the computational domain is required. It can be seen that there is negligible difference between 776985 cells mesh and 1001640 cells mesh. Hence the optimum mesh size for further CFD simulations is the mesh size having 776985 cells. Coarser meshes could not compute bi-directional flow pattern. Hence, in this work, the mesh with 776985 cells is used to carry out all simulations. With the mesh consisting of 776985 cells, time step independence was then performed. The flow initiation transient in HHHC configuration was computed with time steps of 0.5 s, 1 s and 2 s. The result is shown in Fig. 4.5. It can be seen that, there is hardly any difference between 0.5 s and 1 s result. For computational purposes, the time step of 1 s was finally chosen.

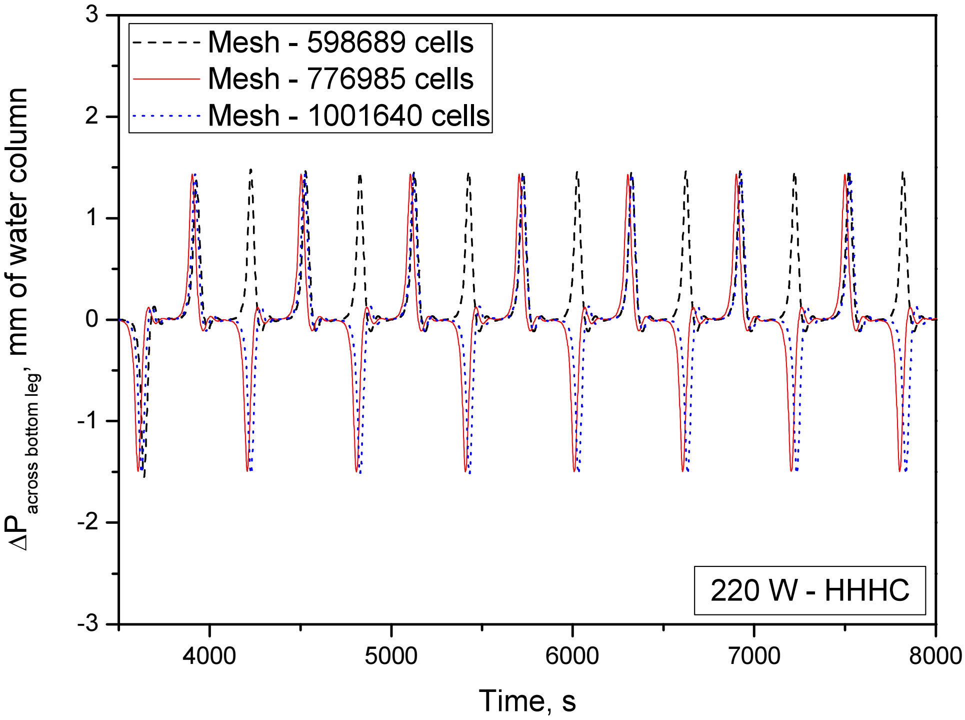

Figure 4.4: Mesh independence study

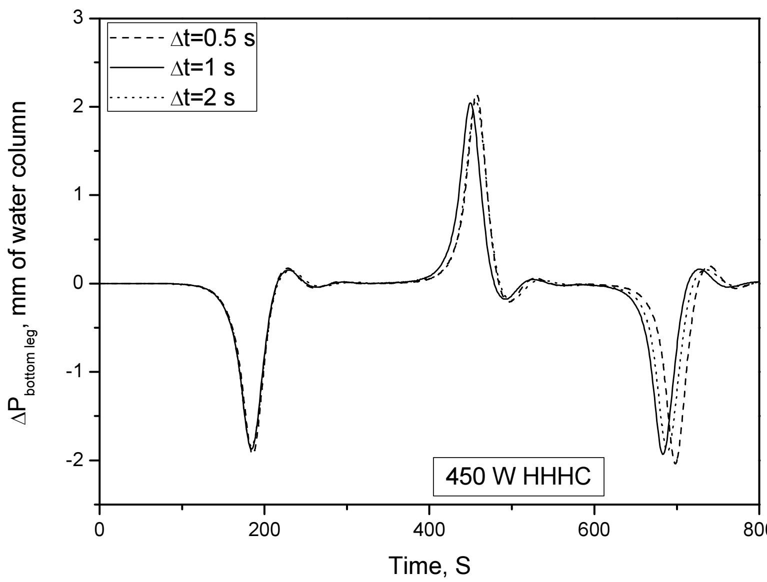

Figure 4.5: Time step independence study

4.5 Steady state characteristics

When power is applied to a natural circulation loop, flow gets initiated. With increase in flow velocity, frictional resistance also increases. After some time, balance of frictional resistance and buoyancy force leads to a steady state. The temperature rise across heater settles to the value: $\frac{\text{Power}}{\dot{m} \times C_p}$. The actual temperatures like $T_{hi}, T_{ho}, T_{ci}, T_{co}$ settle to appropriate values depending on secondary side parameters (coolant inlet temperature and coolant mass flow rate). The steady state achieved depends on heater power and loop configuration. For simulation, as initial guess, water at 30°C is assumed stagnant inside a rectangular loop. The coolant inlet temperature is 34°C. The steady states corresponding to different heater powers are computed. This exercise is done for VHVC and VHHC configurations. In each case, the loop mean temperature, primary side mass flow rate and temperatures at heater and cooler inlets and outlets are obtained from simulations. From these parameters, modified Grashof number (Gr_m) and steady state Reynolds number (Re_{ss}) are computed. The computed steady state Reynolds number, $Re_{ss} = \frac{\dot{m}D}{A\mu}$, where $\dot{m}$ is the mass flow rate, D is the diameter, A is the cross sectional area and μ is the dynamic viscosity. The computed variation of Re_{ss} with Gr_m/N_G is compared with experimental one (Vijayan et al., (2001)) and also with Vijayan correlation.

Vijayan (2002) proposed the following correlation for single-phase NCL.

$$Re_{ss} = C\left(\frac{Gr_m}{N_G}\right)^r \qquad (4.13)$$

The modified Grashof number is $(Gr_m)_{\Delta z} = \frac{D^3 \rho^2 \beta g Q_h \Delta z}{A \mu^3 C_P}$ where ρ is the density, g is the acceleration due to gravity, Q_h is the heater power, β is thermal expansion coefficient and C_p

is the specific heat. The geometrical parameter N_G for uniform diameter loop is, $N_G = \frac{L_t}{D}$,

where the total length of the loop, $L_t = \sum_{i=1}^{N} L_i$, L_i is the length of each segment and N is the number of segments.

The constants, C and r, in Vijayan correlation for laminar and turbulent flows are given in Table 4.1. Many authors (Pilkhwal et al., (2007), Swapnalee and Vijayan (2011), Naveen Kumar et al., (2011), Wang et al., (2013)) have used Vijayan correlation to validate their CFD codes. Swapnalee and Vijayan (2011) modified the above correlation to take into account for transition regime apart from laminar and turbulent regimes (in single-phase natural circulation loop). Their correlation is same as Equation (4.13) but with different constants. Naveen Kumar et al., (2011) proposed that the constants depend on configuration and not on the flow regime. Wang et al., (2013) performed CFD simulation of NCL using low Re k-ε model and validated their results with the experimental data. Based on their research, they obtained same form as Equation (4.13) but different values of constants r and C. These are tabulated in Table 4.1.

Table 4.1: Constants used in Eq. 4.13

Author	Condition	C	r
Vijayan (2002)	Laminar (Re<1100)	0.1768	0.5
	Turbulent (Re>1100)	1.956	0.3636
Swapnalee and Vijayan (2011)	Laminar (Re<898)	0.1768	0.5
	Transition (898<Re<3196)	1.216	0.387
	Turbulent (Re>3196)	1.956	0.364
Wang et al. (2013)	Laminar	0.1653	0.493
	Transition	0.9833	0.403
	Turbulent	0.8422	0.3962
Naveen Kumar et al. (2011)	VHVC (736<Re<4757)	1.4092	0.3757
	VHHC (816<Re<5758)	0.40879	0.43471

Steady state characteristics for VHVC and VHHC configurations were computed. They are compared with previously published experimental data and also with various correlations. Figures 4.6 and Fig. 4.7 show the same for VHVC and VHHC configurations respectively. It is seen that the computed steady state characteristics match well with Vijayan correlation and there is marginal deviation from other data/correlations.

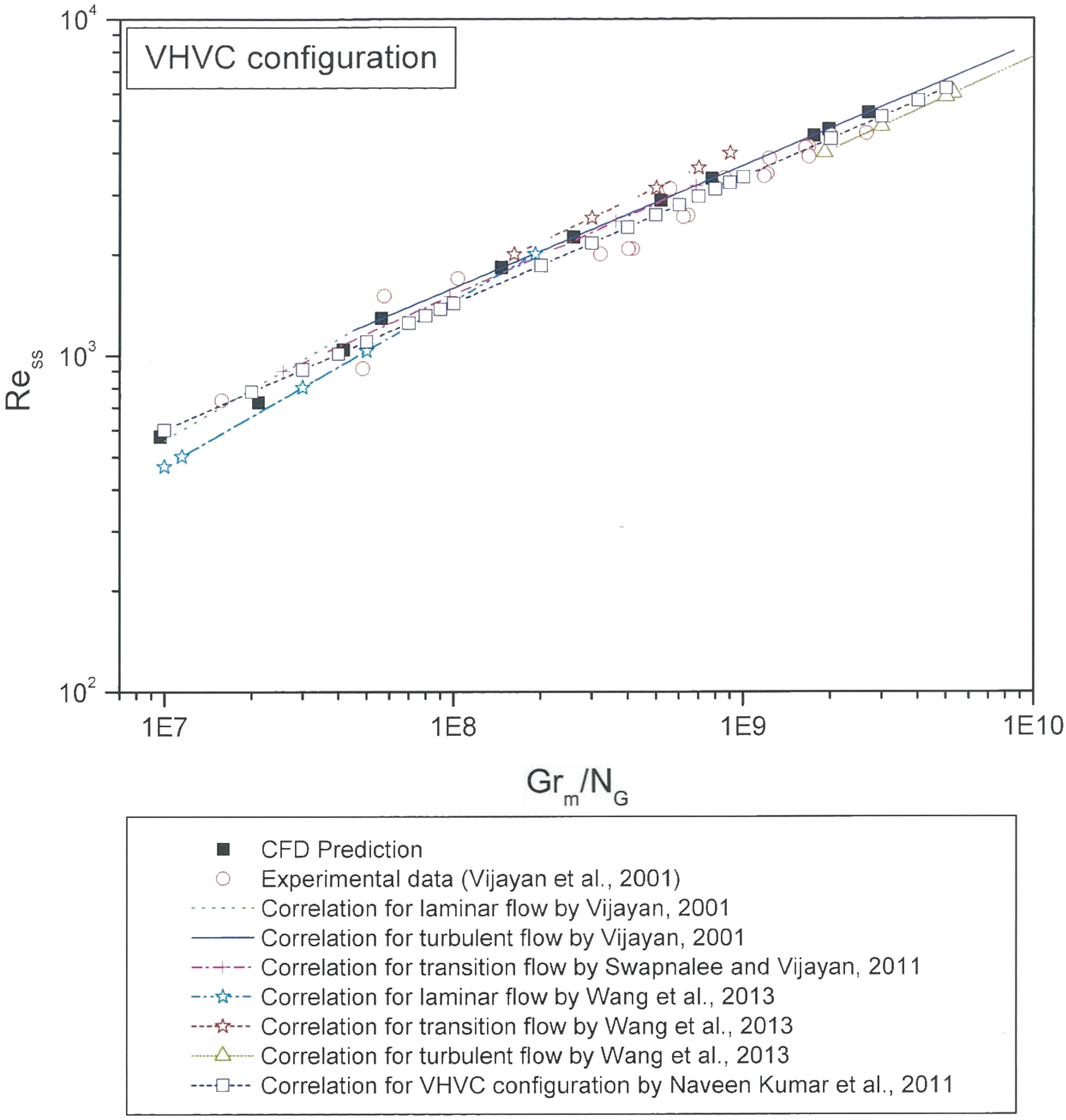

Figure 4.6: Steady state characteristics of VHVC configuration; Comparison of computed result with experimental data and correlations

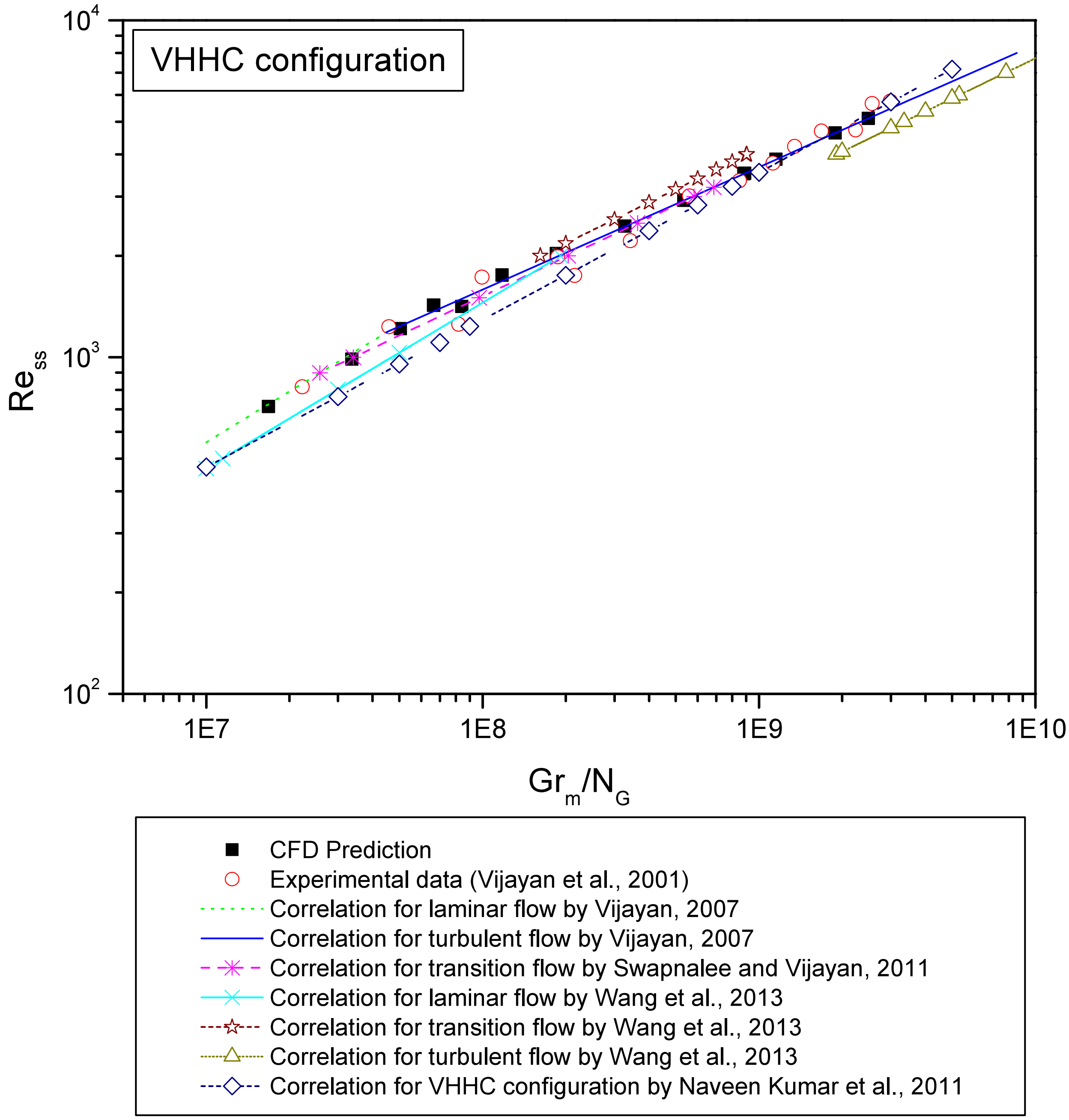

Figure 4.7: Steady state characteristics of VHVC configuration; Comparison of computed result with experimental data and correlations.

4.6 Transient characteristics

Apart from steady state characteristics, it is interesting to study transient characteristics e.g. flow development from an initial stagnant state to final steady state via a transience (called flow initiation transient) and reaches in some configurations. For this, transient 3D simulations were performed for all the four configurations i.e. VHVC, HHHC, etc.

Further, the flow pattern in a NCL may depend on heat addition path. It may be possible to eliminate/reduce oscillations, set in the NCL under certain conditions, by changing heater power. These various transients are categorised as,

(a) Flow initiation transients

(b) Power rise from steady state/oscillatory state

(c) Power step back from steady/oscillatory state

In the present work, these transients are computed using transient 3D CFD simulations. The nature of the flow and its relation with the developing temperature field is explained.

4.6.1 Flow initiation transient in VHHC configuration

In VHHC and VHVC cases, due to vertical heater, the time lag between the start of the heating process and flow initiation is far less than that in HHHC and HHVC cases. For VHHC configuration, experimental data is available at different powers. In natural circulation loop, researchers have mentioned at low Re flow can be turbulent. Vijayan et al., (1995) mentioned that, for $Re > 1100$, flow can be treated as turbulent, Swapnalee and Vijayan (2011) mentioned that flow is in transition region for $898 < Re < 3196$ and above that it is turbulent. Due to this and also based on the Rayleigh number (which is 3.94×10^{13} for 232 W and 6.25×10^{13} for 368 W VHHC), it was thought that flow should be better modeled as turbulent. Figure 4.8 shows the computed flow initiation transient and its comparison with experimental data. There is a large deviation is visible. Hence simulations are done with laminar model. The obtained result from laminar model is also included in the Fig. 4.8. With laminar model, computed results show very good match with experimental data. Explanation for this is given below.

In VHHC or VHVC configurations of NCL, the heater being vertical, as soon as power is given, flow is initiated. After some time, it reaches steady state. The steady state Reynolds number is less than 2000 within the considered power range. Reynolds number for 232 W is 1383 and for 368 W VHHC is 1742. The heater acts similar to a pump and once the flow gets initiated, the flow behaves like a forced flow in a circular pipe. Hence, the flow should be treated as laminar taking Reynolds number as the criteria for transition. Fig. 4.9 shows the variation in ΔP with time for VHHC case for heater power 368 W. The result computed with turbulence model deviates much from experimental data, whereas laminar model predicts a much better result.

In VHHC configuration, the flow initiation profile is similar to that of VHVC case. The only difference between VHHC and VHVC is that, in the former, the cooler is placed closer to heater. The formation of hot plug, its transport to left top elbow leading to accelerating flow, its transport to top horizontal cooler leading to flow deceleration and eventually achieving a steady state flow and temperature fields are all similar to the previous case.

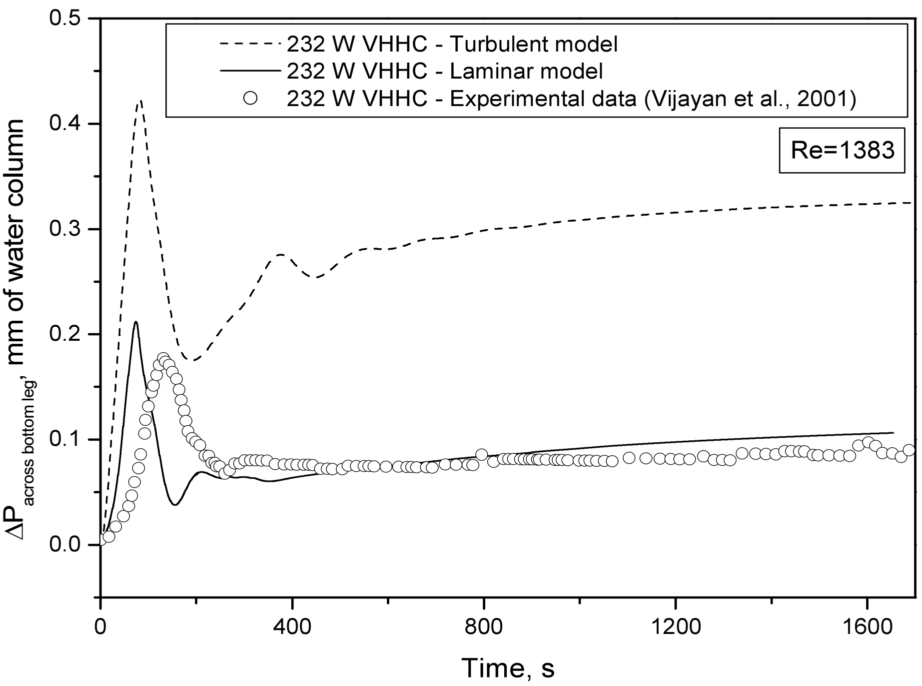

Figure 4.8: Comparison of computed transient variation of pressure drop with time in VHHC configuration at 232 W

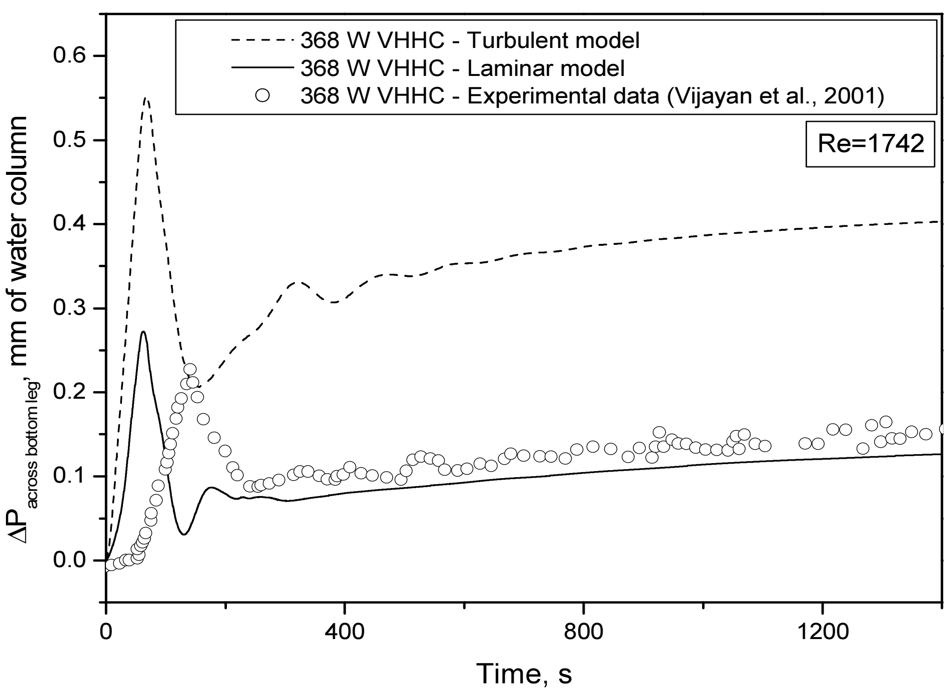

Figure 4.9: Comparison of computed transient variation of pressure drop with time in VHHC configuration at 368 W

4.6.2 Flow initiation transient in VHVC configuration

Flow initiation transient is computed by setting the initial field to stagnant conditions and applying desired power to heater section and then performing time marching calculations. These simulations were performed using laminar model because from previously reported VHHC configuration studies, it was found that laminar model gives better result than standard k-epsilon turbulence model. Since it is difficult to present a 3D transient flow field, hence the nature of the flow can be understood in terms of transient variation of pressure difference in bottom leg (P_2-P_1). If $\Delta P_{\text{bottom leg}} = \text{Constant}$, flow is steady. If $\Delta P_{\text{bottom leg}} > 0$ flow is clockwise and if, $\Delta P_{\text{bottom leg}} < 0$ flow is in anti-clockwise direction.

Figure 4.10 shows the computed transient variation of $\Delta P_{\text{bottom leg}}$ at 105 W heater power in VHVC configuration. Figure 4.11 shows the temperature fields at different time instants.

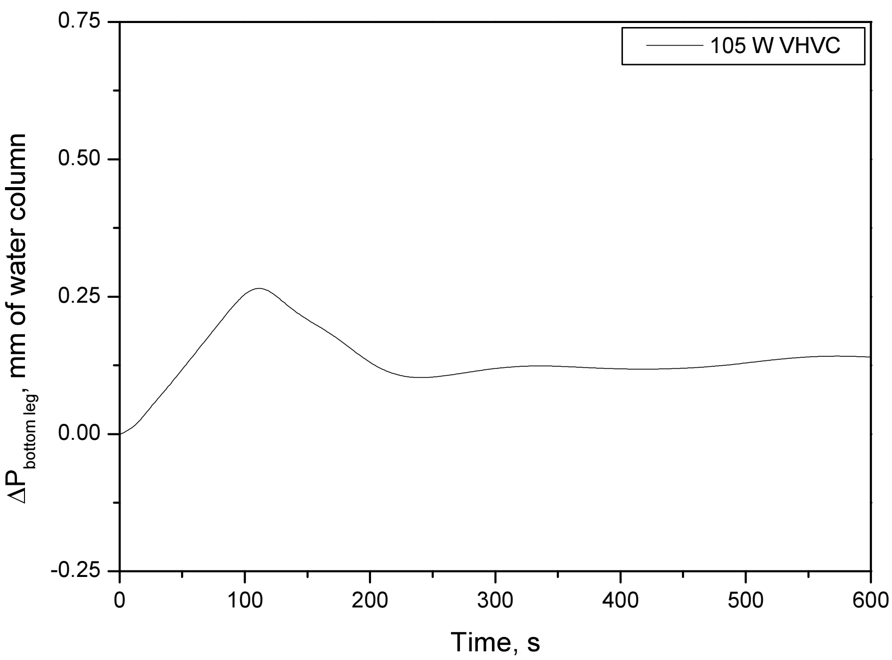

Figure 4.10: Computed transient variation of $\Delta P_{\text{bottom leg}}$ ***in VHVC configuration at 105 W***

The formation of hot plug and its moment along the loop is explained with the help of temperature fields captured by 3D CFD simulation at different time intervals, which are shown in Fig. 4.11. The flow is generated due to heating. The temperature field drives the flow field. Hence the reason for flow transient profile can be understood by studying temperature field in the NCL at different instances of time. Initially, temperature in the whole loop is uniform at initial value. Once the heating starts, temperature in the heater starts rising, simultaneously inducing flow in the loop. The temperature field after 25 seconds is shown in Fig. 4.11(A). It can be seen that, a hot plug of the size of the heater is formed in heater. Due to small initial velocity, there is hardly any convection of energy outside of heater section. Hence, rest of the domain is still at initial temperature. After 100 seconds as shown in Fig. 4.11(B), this hot plug is in between vertical heater and left top elbow. This shows that hot plug gets convected upwards due to local convection and upward buoyancy force. The heater gets filled with cold water. At this time instant, maximum mass flow rate is obtained and indicated by the peak in ΔP at t=100 s in Fig. 4.10. After this, hot plug enters horizontal top leg. The elbow offers large resistance. Also after the hot plug enters horizontal top leg, its contribution to buoyancy force reduces. Hence, after 100 s, there is a flow retardation. At 150 seconds, as shown in Fig. 4.11(C), hot plug occupies larger part of the top leg. At 200 s, the hot plug is about to enter the cooler section as shown in Fig. 4.11(D). After this, hot plug further advances in the cooler as shown by the temperature field corresponding to 225 s in Fig. 4.11(E). Here it losses its heat to the secondary coolant. After this, nearly steady state conditions are reached with buoyancy force balancing the total resistance to the flow in the loop and steady state temperature field as shown in Fig. 4.11(F) is established. In this case flow becomes stable after undergoing one peak. Sustained oscillations are not observed.

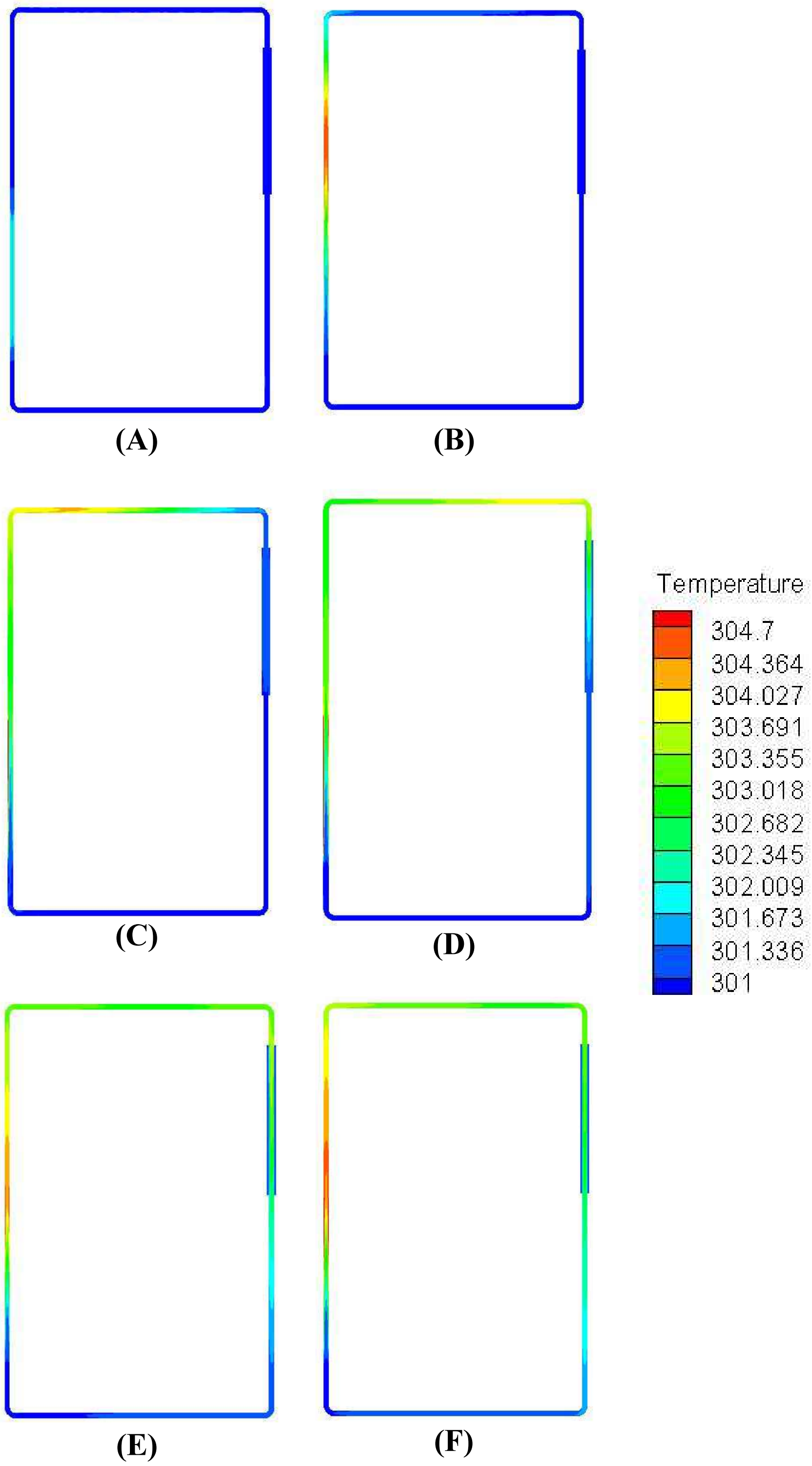

Figure 4.11: Temperature fields in central vertical plane at different instants of an oscillatory cycle for VHVC configuration at 105 W; (A) 25 s, (B) 100 s, (C) 150 s, (D) 200 s, (E) 225 s, (F) 300 s

4.6.3 Flow initiation transient of HHHC configuration

Due to horizontal orientation of heater and cooler, the flow dynamics in this configuration is most complex. In this case also initially simulations are carried out using standard k-ε turbulence model. The flow initiation transients of HHHC configuration are computed for heater powers of 120 W and 220 W shown in Fig. 4.12 and Fig. 4.13 respectively**.** The comparison of predicted $\Delta P_{bottom\ leg}$ with experimental data is shown[1]. CFD predictions match the experimental data qualitatively; however, there is a difference in the frequency and amplitude of oscillations. The frequency of oscillations observed by CFD is 0.0026 Hz whereas in the experiment it is 0.00316 Hz for 120 W. The frequency of oscillations observed by CFD for 220 W is 0.003 Hz whereas as that observed in the experiment is 0.004 Hz.

Figure 4.12 and Fig. 4.13 shows that, at 120 W, uni-directional pulsing is obtained while at 220 W, initial unidirectional oscillations eventually become bi-directional. Figure 4.14 shows that, at 450 W, bi-directional oscillations are observed right from the start. In the experimental study by Vijayan et al. (2001, 2002), it was found that (i) steady flow is obtained at powers less than 90 W, (ii) unidirectional pulsing is obtained between 105 W to 135 W and (iii) bi-directional pulsing is obtained above 196 W.

Hence it can be concluded that the simulation results show the same trend as experimental results. At all the powers, zero flow conditions are reached in every cycle. But the duration of zero flow gets reduced with increase in power. At high power of 450 W, there is negligible zero flow condition.

---

[1] In this case, ΔP_{expt} is compared with $-\Delta P_{CFD}$. This is because, in this configuration, computed flow direction is opposite to that of experimentally observed flow direction. Hence the sign of ΔP_{CFD} is opposite to that of ΔP_{expt}. Hence for comparison, instead of comparing ΔP_{CFD} with ΔP_{expt}, $-\Delta P_{CFD}$ is compared with ΔP_{expt}. In this configuration, due to symmetry, both flow directions are possible and hence comparison of $-\Delta P_{CFD}$ with ΔP_{expt} is justifiable (Vijayan et al., (2001)).

In this configuration flow is changing from zero to certain maximum flow. Hence it was decided to study the flow pattern in HHHC configuration with laminar model also. Figure 4.15 and Fig. 4.16 shows the comparison of computed transient ($\Delta P_{across\ bottom\ leg}$ with time) obtained from laminar model with experimental data for 120 W HHHC and 220 W HHHC configurations respectively. It is clear that, the laminar model is unable to predict the transient behaviour of HHHC configuration. Hence, the CFD simulation with the turbulence model, which can take care of both laminar and turbulent flow regimes may be suitable to predict the transient behaviour of HHHC configuration.

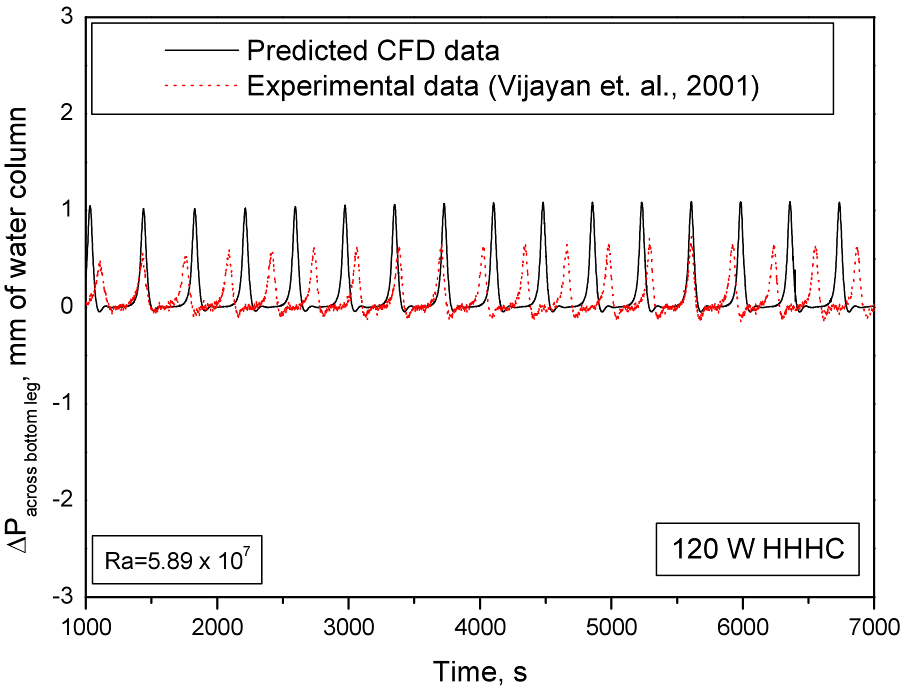

Figure 4.12: Transient variation of ΔP in HHHC configuration at 120 W; Comparison of computed results with experimental data.

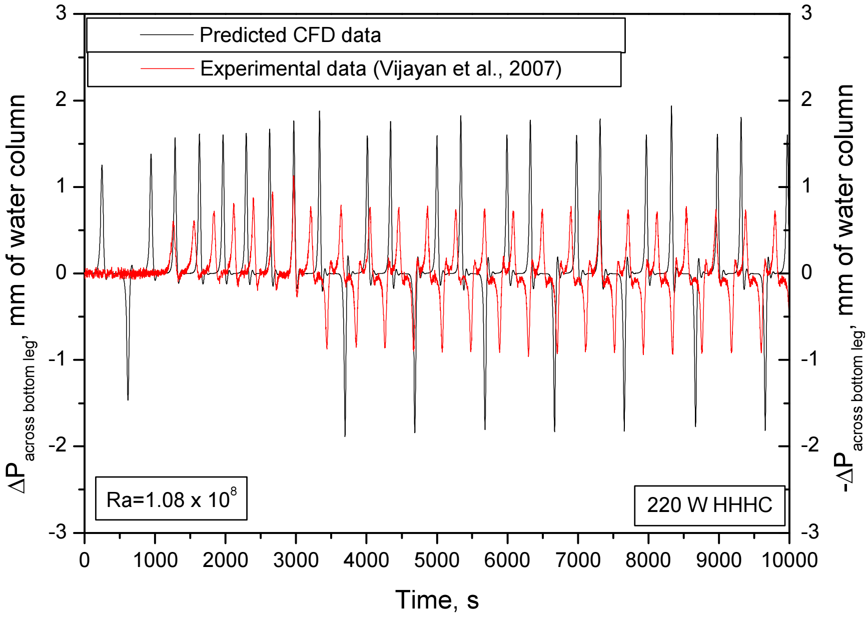

Figure 4.13: Transient variation of ΔP in HHHC configuration at 220 W; Comparison of computed results with experimental data

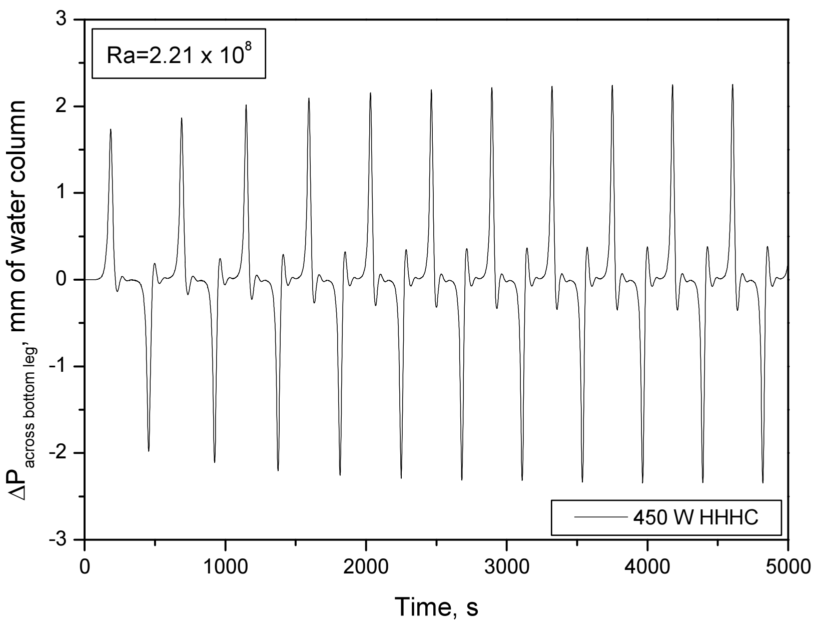

Figure 4.14: Predicted transient variation of $\Delta P_{across\ bottom\ leg}$ at 450 W HHHC configuration

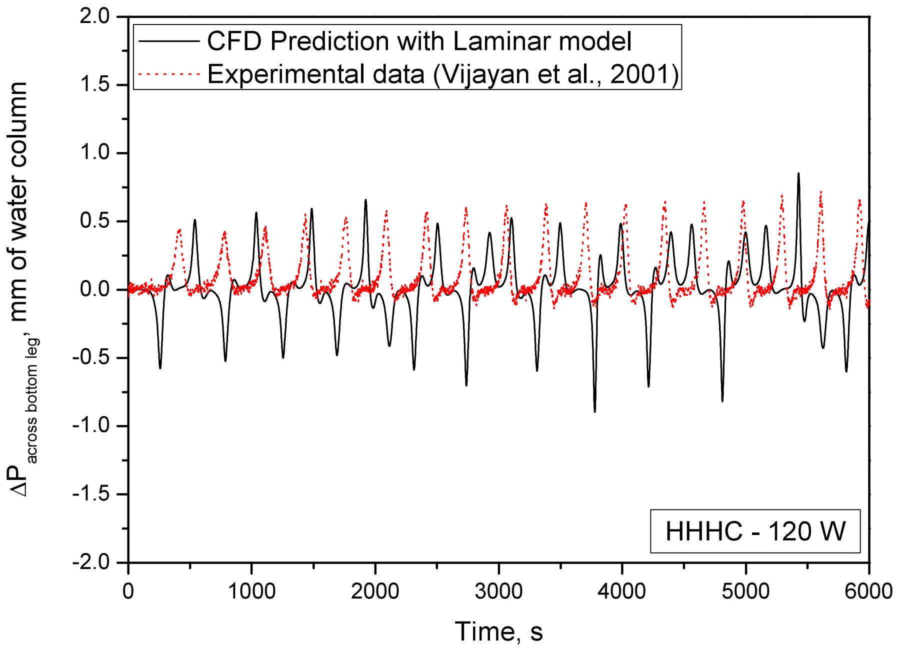

Figure 4.15: Comparison of computed transient ($\Delta P_{across\ bottom\ leg}$ with time) obtained from laminar model with experimental data for 120 W HHHC configuration

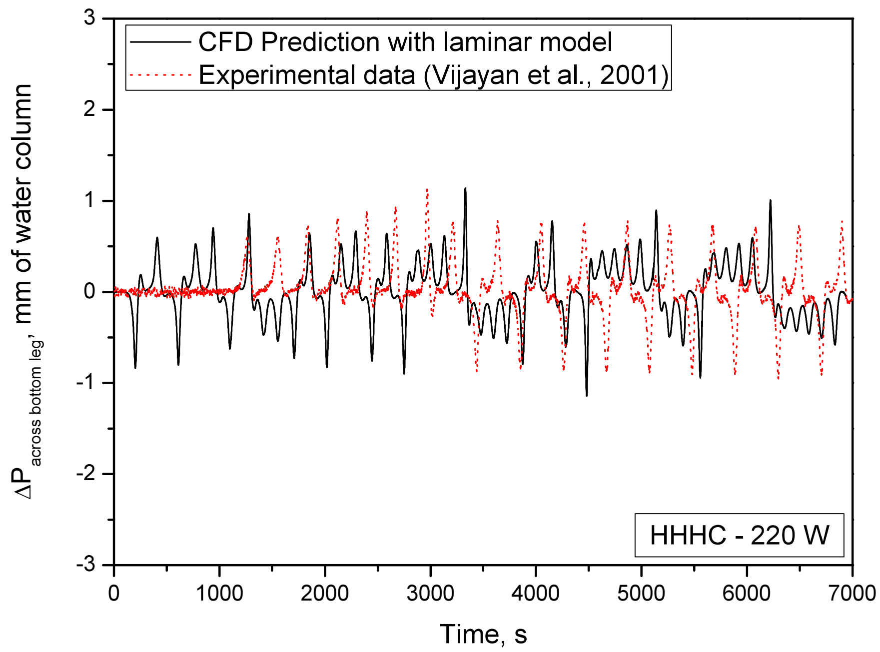

Figure 4.16: Comparison of computed transient ($\Delta P_{across\ bottom\ leg}$ with time) obtained from laminar model with experimental data for 220 W HHHC configuration

In HHHC configuration, during flow initiation transient, the flow is initially stagnant. After application of power, the flow in heater gets established. This flow is not axial but it is from bottom to top in heater as shown in Fig. 4.17. This flow is similar to natural convection flow in a cavity for which laminar / turbulent regime is decided by Rayleigh number. Hence, initial flow in HHHC is to be modeled as turbulent natural convection. However, after some time, the hot plug gets formed and gets released in left or right vertical leg and main (axial) flow is established. Hence, again, due to low Re, the flow behaves like a laminar pipe flow. In HHHC, this flow pattern change, i.e. changing from "turbulent natural convection in heater and cooler with zero net loop flow" to "laminar forced convection flow in loop", keep happening indefinitely. In summary, in HHHC, the flow regime keeps changing from laminar to turbulent then again to laminar flow. The repetitive change in the flow regime will takes place. This is very difficult to capture in numerical simulation as the modeling can be done with either laminar or turbulent formulations. The better prediction is possible only with the model which can take care of both laminar and turbulent flow patterns. Hence the CFD simulations are carried out using low-Reynolds number k-ε turbulence (Launder and Sharma, 1974) model.

Figure 4.18 shows the comparison of CFD prediction of 220 W HHHC configuration by standard k-ε turbulence and low-Reynolds number k-ε (Launder and Sharma, 1974) turbulence model with experimental data. It can be seen that low-Reynolds number k-ε turbulence model gives better results compared to standard k-ε model, in terms of improved prediction of amplitude and frequency of oscillations. However, for 120 W heater power (shown in Fig. 4.19), result obtained using low Re k-ε model shows bi-directional oscillations instead of unidirectional oscillations as observed in experiment. But the amplitude of oscillations matches with experimental data.

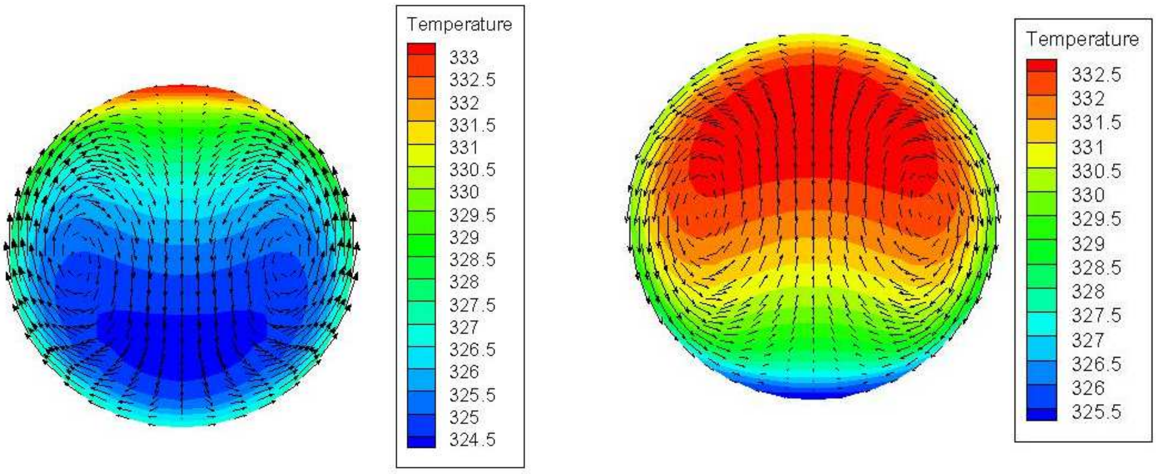

(a) **(b)**

Figure 4.17: Temperature contour and vector representation in a cross-sectional plane (a) at heater (b) at cooler in HHHC configuration

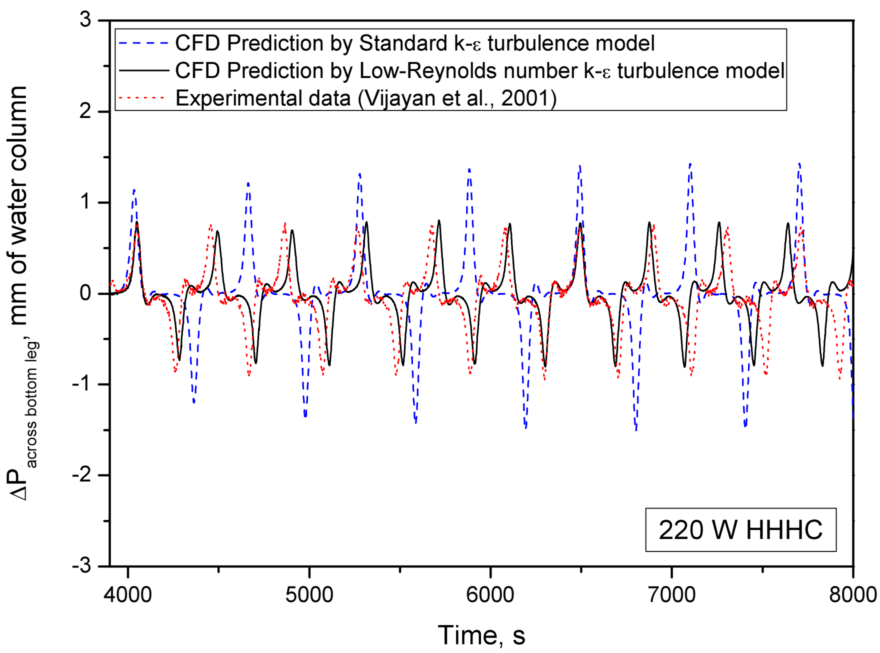

Figure 4.18: Comparison of computed transients ($\Delta P_{across\ bottom\ leg}$ with time) obtained from Standard k-ε turbulence and low-Re k-ε turbulence models with experimental data for 220 W HHHC configuration

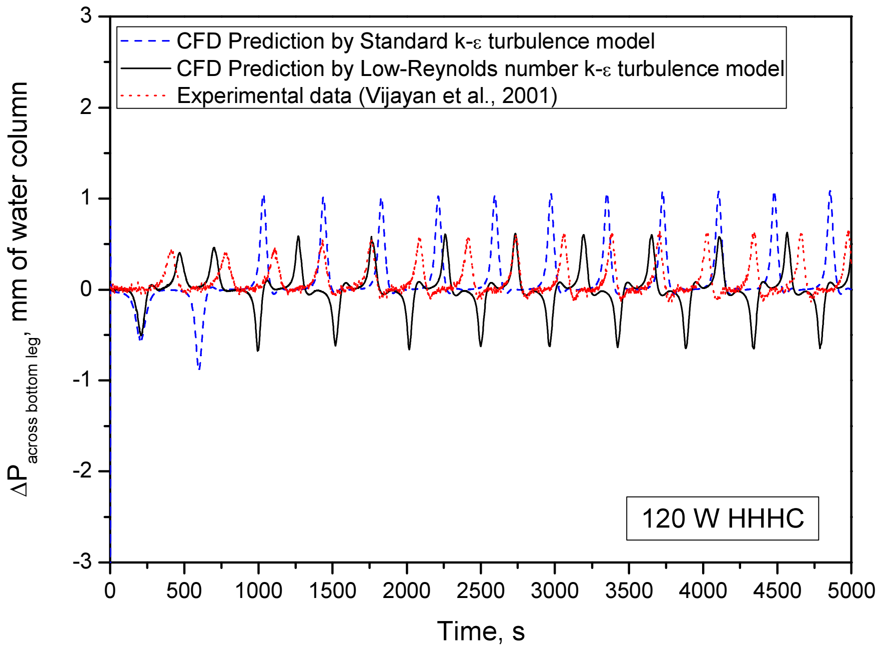

Figure 4.19: Comparison of computed transients ($\Delta P_{bottom\ leg}$ with time) obtained from Standard k-ε turbulence and low-Re k-ε turbulence models with experimental data for 120 W HHHC configuration

4.6.4 Flow initiation transients in HHVC configuration

Flow initiation transient for HHVC configuration of NCL working with water is computed at 257 W heater power. As mentioned in the previous sections, in this case also, initially the simulations are carried out using standard k-ε turbulence model. The obtained computational Reynolds number at this power is 1490, whereas Rayleigh number is 1.26 x 10^8. At this power, experimental data is available and validation of computed profile is possible. Figure 4.20 shows the comparison of computed transient variation of $\Delta P_{bottom\ leg}$ with that of experimental data. It can be seen that simulation results are following the trend of the experimental data. It shows that, initially anti-clockwise flow (indicated by -ve ΔP) is formed and then it reverses direction and forms steady clockwise flow(indicated by +ve ΔP).

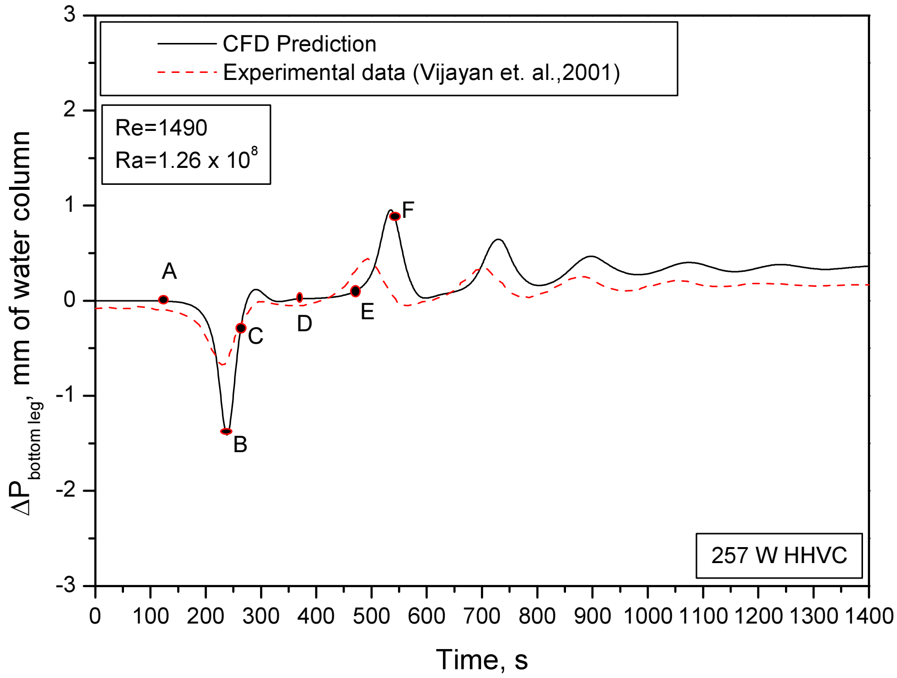

Figure 4.20: Transient variation of $\Delta P_{bottom\ leg}$ ***for HHVC configuration at 257 W***

In the previous section of 4.6.3, it is proved that low-Reynolds number k-ε turbulence model gives better result compared to laminar and high Re turbulence model. Hence for better accuracy the flow initiation transient is computed with low-Reynolds number k-ε turbulence model. Figure 4.21 shows the comparison of computed transient variation of ΔP with that of experimental data for 257 W HHVC configuration. It can be seen that low-Reynolds number k-ε turbulence model gives good match with experimental data in terms of amplitude and frequency of oscillations. The mesh selected for the low-Reynolds number turbulence model involves the very fine mesh near the wall and the obtained peak value of y^+ is 1.36. Though the predicted result obtained by standard k-ε model shows high amplitude than the experimental data but it is able to predict the trend of experimental observation. In HHHC as well as HHVC, at 220 W and 257 W, low Re results match well with experiment data. Hence the applicability of low Re model at low power needs to be further assessed.

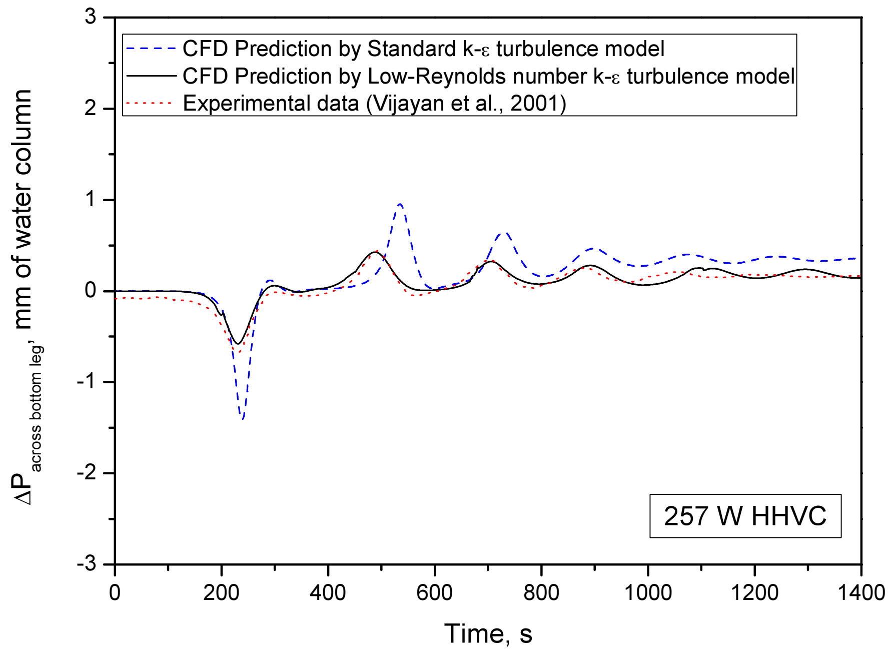

Figure 4.21: Comparison of computed transients ($\Delta P_{bottom\ leg}$ with time) obtained from Standard k-ε turbulence and low-Re k-ε turbulence models with experimental data for 257 W HHVC configuration

In this configuration, since vertical cooler is located in right leg, clockwise flow is expected. In simulation as well as in experiment, it is observed that, initially flow is anti-clockwise. This is because, initially, hot plug is formed in the horizontal heater, while rest of loop is still filled with stagnant cold water. This is shown in Fig. 4.22(A). The hot plug becomes bigger and occupies whole bottom horizontal leg. At this time, the cooler has no influence on the flow field as it is filled with stagnant cold water. Hence, there is equal probability for the hot plug to escape in right or left vertical legs. The hot plug escapes in right vertical leg (as shown in Fig. 4.22(B)) leading to anti-clockwise flow. The hot plug then rises in the right vertical leg, crosses cooler. Hot plug, while passing through the cooler, doesn't get cooled sufficiently due to high velocity. It reaches top horizontal leg as shown in Fig. 4.22(D). At this time, the hot plug loses its momentum completely. Due to the presence of cold fluid in left vertical leg, hot plug cannot move downward. Then it will take a small reverse flow. So hot plug enters the top horizontal leg and this leads to hot plug deceleration and loop reaches zero velocity. Due to stagnant loop conditions, after some time, 2^{nd} hot plug is formed in the horizontal bottom leg (Fig. 4.22(E)) and in the same time cold plug is formed in the cooler. Due to the cooler effect at right leg, cold plug moves down in right vertical leg and pushes second hot plug to left vertical leg, as shown in Fig. 4.22(F). Second peak in ΔP variation is observed when 2^{nd} hot plug is rising in the left vertical leg. The subsequent hot plugs get lesser residence time in heater. Hence the amplitude of oscillations keeps reducing and a steady flow condition is reached as shown in Fig. 4.20.

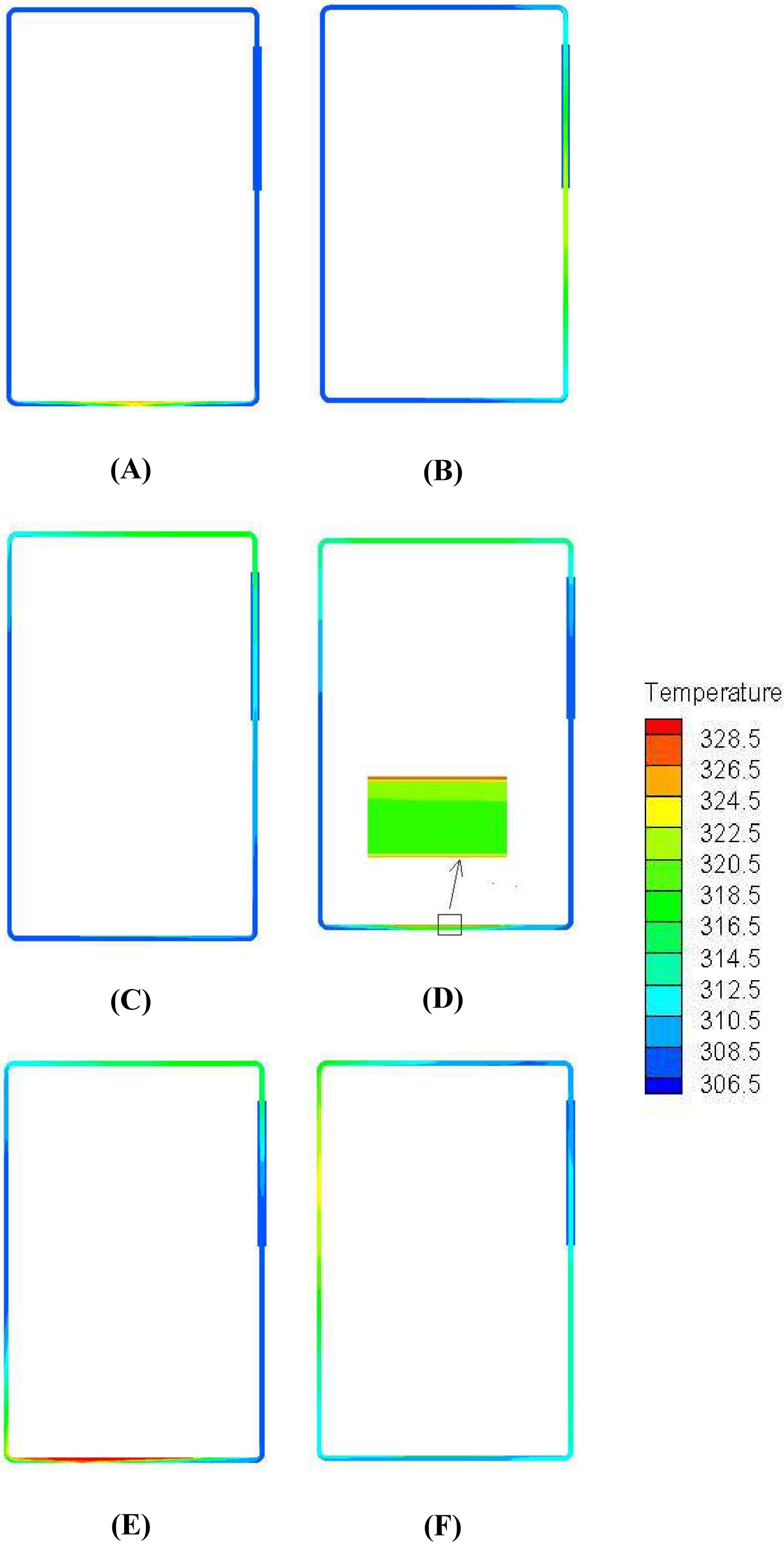

Figure 4.22: Temperature contours at different time instants in 257 W HHVC (mentioned temperature is in Kelvin)

4.7 Explanation of uni/bi-directional oscillations in HHHC configuration at low and high powers

4.7.1 Uni-directional oscillations at low power

In the transient simulation of 120 W of HHHC, repetitive unidirectional oscillations are observed. To explain the instabilities, temperature contours between 4800 seconds to 5250 seconds were taken, which cover one cycle of unidirectional oscillation (shown in Fig. 4.23). During the flow initiation transients, once the heater is switched on, heat is transferred from the heater to the fluid in the loop. Initially flow is almost stagnant. But due to heating, at first, flow in cross-sectional plane gets established as shown in Fig. 4.17(A). Due to surface heating, the fluid near surface rises and it comes down to the centre. So the heat transfer from heater to fluid will be through conduction as well as natural convection. Due to continuous heating all along heater surface, hot plug is formed. This hot plug diffuses axially on both sides of heater. Finally it covers the entire bottom horizontal leg as shown in Fig. 4.24(A). After that, the hot plug will try to move into the one of the vertical legs. At the same time, due to continuous cooling, cold plug is formed at the cooler. After this, entry of the hot plug into right vertical leg takes place as shown in Fig. 4.24(B). Simultaneously, cold plug is entering left vertical leg from top. After this, hot plug rises through the right vertical leg and cold plug decelerates through left vertical leg. The flow accelerates during this phase. The maximum flow rate is observed, when the entire hot plug is in the right vertical leg (which is much longer than the hot plug length) and the entire cold plug is in the left vertical leg. This is shown Fig. 4.24(C). As the head of the hot plug enters the top horizontal section, the buoyancy force no more increases and due to wall friction/elbow resistance, the flow tends to decelerate (Fig. 4.24(D)). Entry of cold plug into bottom horizontal leg also affects flow retardation. However, due to flow inertia, hot and cold plugs travel fast through cooler and heater sections respectively. Although, the hot plug passes through the cooler, it does not get sufficiently cooled due to the high velocity while passing through the cooler. The hot and cold plugs enter into left and right vertical legs respectively, as shown in Fig. 4.24(E). Hot plug descends along the left vertical leg in rapidly decelerating flow conditions. The deceleration is due to presence of cold fluid in left vertical leg below hot plug and also due to continuous frictional resistance offered by wall and left top elbow. This continues till the buoyancy force contribution of the right vertical leg is slightly more than that of the left vertical leg leading to small reverse flow. During the reverse flow (very short duration), the hot plug in the left vertical leg returns back to the cooler. Cold plug returns to heater section. Again the flow becomes forward flow i.e. anti-clockwise direction but flow rate is very small. During this time, hot fluid in the top horizontal pipe gets cooled and becomes a cold plug (cold pocket). At the same time cold fluid in the bottom horizontal pipe gets heated and becomes a hot plug (hot pocket). This is shown in Fig. 4.24(F). Subsequently, next hot plug is formed and it enters right vertical leg again due to small forward flow existing in the loop and whole cycle gets repeated leading to uni-directional oscillatory flow.

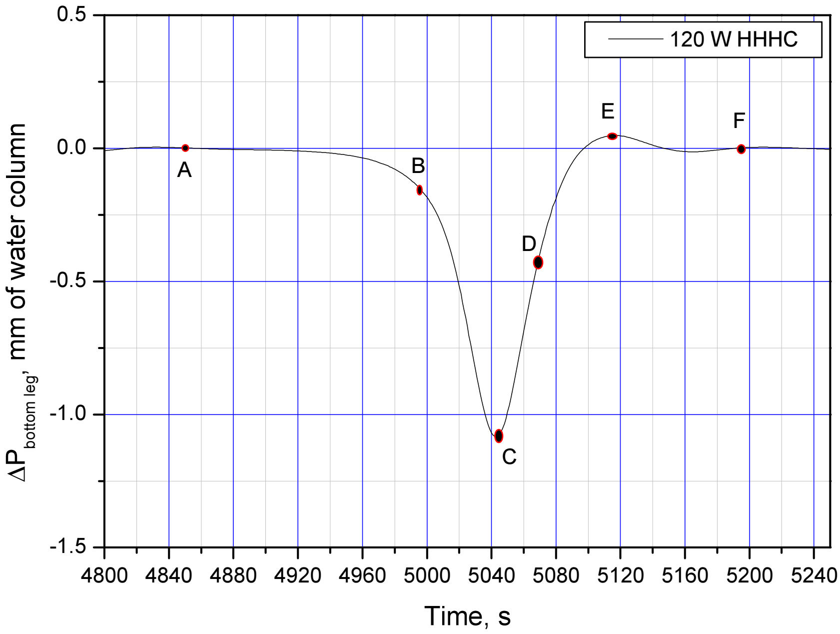

Figure 4.23: Enlarged portion of flow initiation transient for HHHC at 120 W showing one cycle of unidirectional oscillation

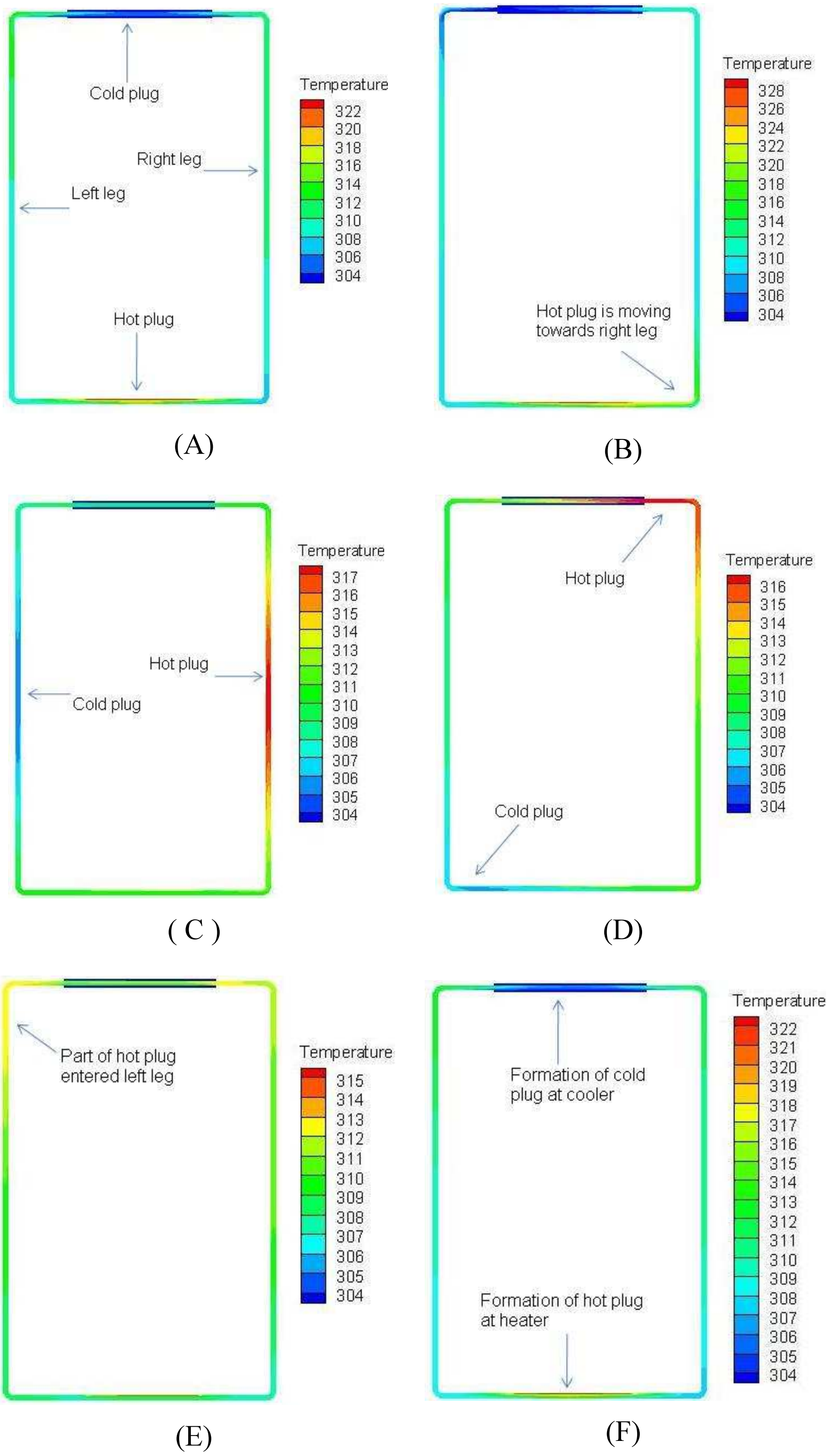

Figure 4.24: Temperature contours at various time instants of an oscillatory cycle for HHHC configuration at 120W

4.7.2 Bi-directional oscillations at high power

The thermal-hydraulic behaviour of the loop which causes the bi-direction flow has been studied with the help of temperature contours obtained during the flow initiation transient simulation. Figure 4.25 shows the transient variation of ΔP between 3650 seconds to 4200 seconds, which cover one cycle of bidirectional flow. The mechanism of bidirectional flow is explained with the help of temperature contours captured by 3D CFD simulation at different time instants marked in Fig. 4.26.

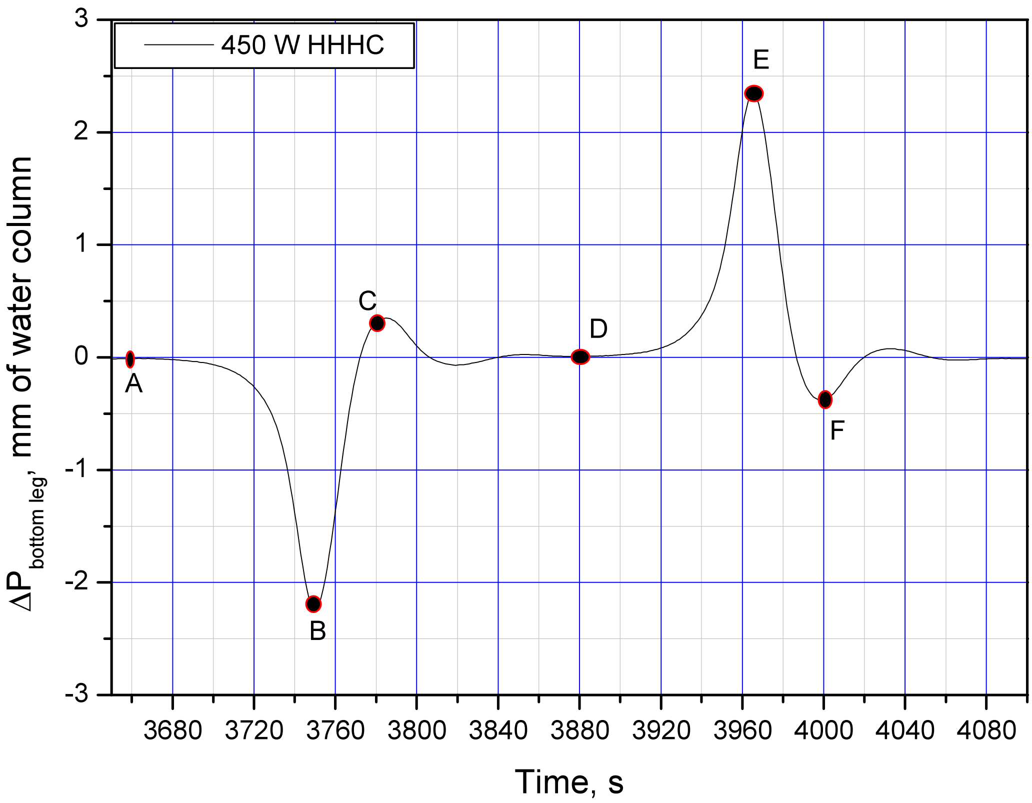

Figure 4.25: Enlarged portion of flow initiation transient for HHHC at 450 W showing one cycle of bi-directional oscillation

In this case, the cycle consists of one anticlockwise pulse and one clockwise pulse. In bi-directional pulsing, part of the cycle from 1 to 4 is same as previous case of unidirectional pulsing. Hence hot and cold plug formed in the heater and cooler respectively (refer Fig.

4.26(A)). The hot plug enters the right vertical leg, gets accelerated and reaches top of the right vertical leg by covering the entire vertical leg (refer Fig. 4.26(B)). Then due to momentum, it enters top horizontal leg and its head enters left vertical leg (refer Fig. 4.26(C)). At this time, head of cold plug passes through heater and reaches bottom of the right vertical leg. Then a small reverse and forward flow occurs, after that flow comes to stagnant condition for few seconds. After this, due to rapid heating of fluid, hot plug gets quickly formed in heater (refer Fig. 4.26(D)). The strong reverse flow at high power is capable of keeping the cold plug at the bottom of the right vertical leg. Due to the presence of cold plug at the bottom of the right vertical leg, the newly formed hot plug will enters the left vertical leg and reaches a maximum flow in clockwise direction (refer Fig. 4.26(E)). Then the whole cycle is repeated. Continuation of this whole process leads to bi-directional oscillations at high powers. Compared to the low power unidirectional flow, the flow acceleration is fast and stagnation period is negligible. At low power there is a significant stagnation period.

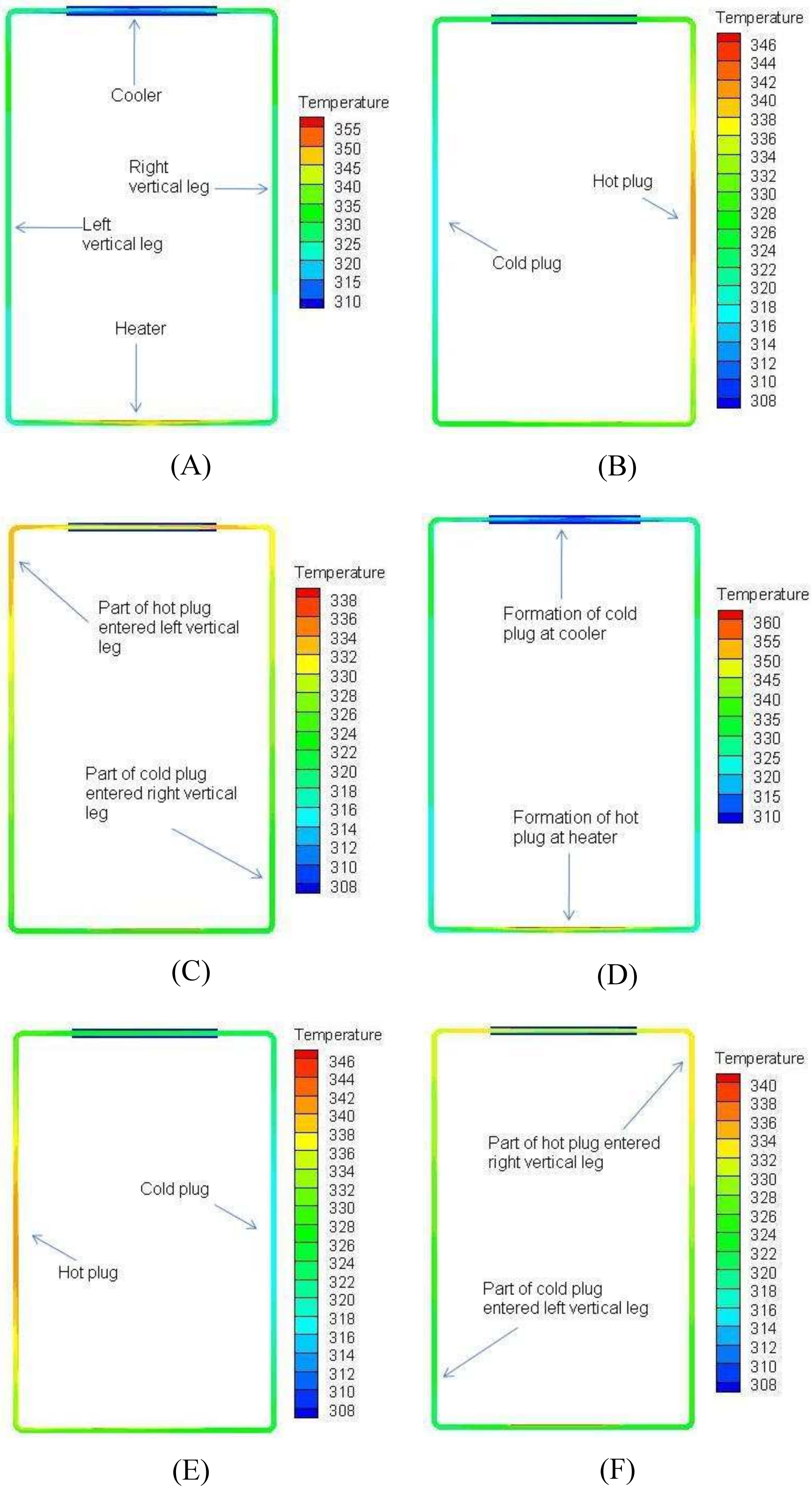

Figure 4.26: Temperature field in central vertical plane at different time instances for HHHC at 450W

4.7.3 Oscillatory behaviour of temperature at different locations

Figure 4.27 and Fig. 4.28 show the oscillatory behavior of temperatures at points T1 and T3 in the loop as shown in Fig. 4.1, during unidirectional and bi-directional pulsing respectively. These computational results are taken from the CFD simulation of 120 W and 450 W HHHC configuration with standard k-ε turbulence model. It is noticed that the fluid temperature oscillations are out of phase by 180^0. The temperature locations (i.e. point T1 and point T3) will divide the loop into exactly two halves. The occurrence of 180^0 phase difference is an indication of the equality of the period of oscillation to the loop circulation time. Similar results were obtained by Vijayan et al. (1995, 2001) from both theoretical calculations (using computer code ATHLET) and experimental observations.

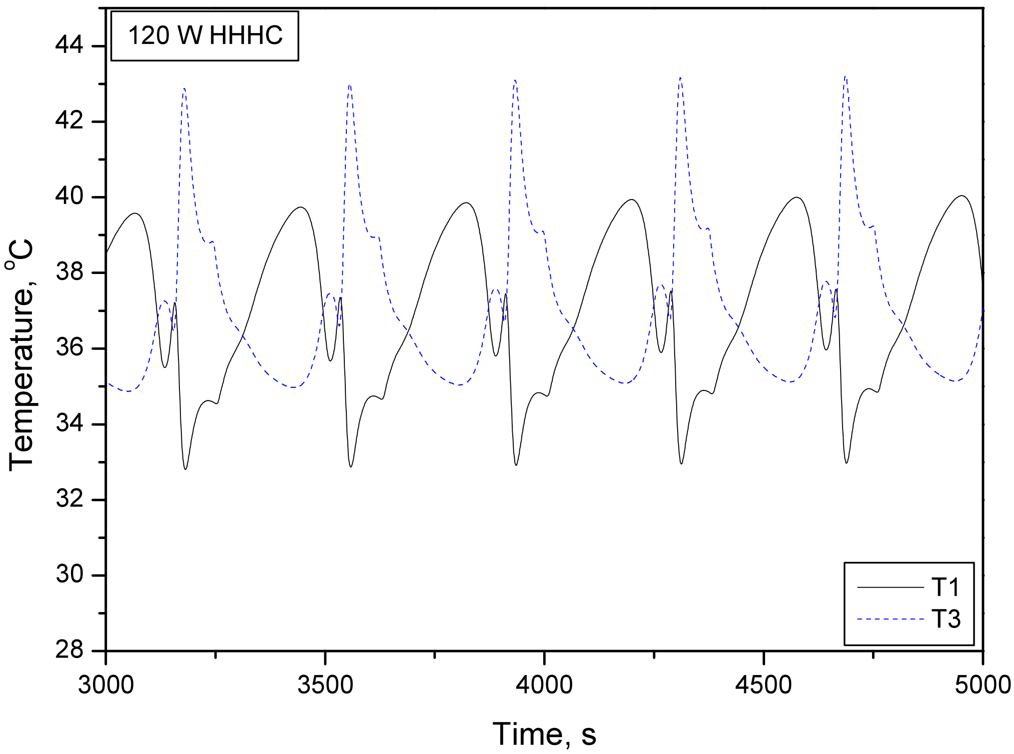

Figure 4.27: Predicted transient variation of Temperature at different locations in 120 W HHHC configuration

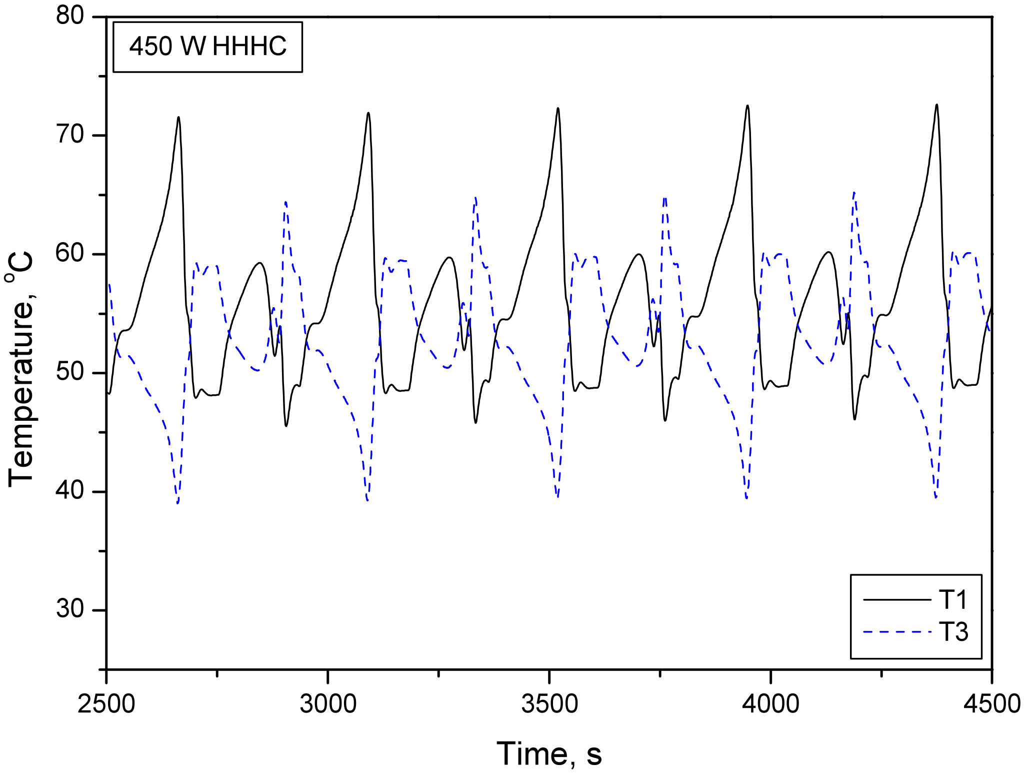

Figure 4.28: Predicted transient variation of Temperature at different locations in 450 W HHHC configuration

4.7.4 Oscillatory behaviour of temperature difference across heater

Figure 4.29 and Fig. 4.30 show the oscillatory behaviour of temperature difference across heater for unidirectional and bi-directional pulsing respectively. These computational results also taken from the CFD simulation of 120 W and 450 W HHHC configuration with standard k-ε turbulence model It is observed that with increase in power, the frequency of oscillations increases (though not linearly). The occurrence of the negative ΔT across heater (ΔT_h) is a clear indication of flow reversal. In lower power, such as in 120 W, small portion of cycle shows negative ΔT_h. This indicates that reverse flow occurs for small duration. At higher power, like 450 W, equal distribution of ΔT_h in positive and negative zone is observed. It shows that, in bidirectional flow, equal amount of forward and backward flow takes place.

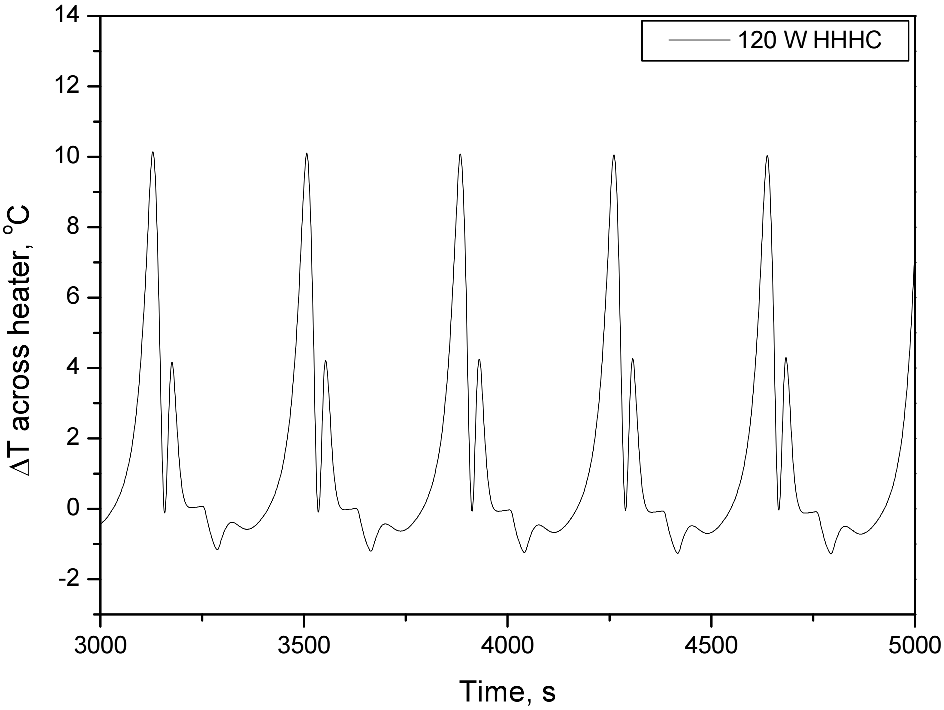

Figure 4.29: Predicted transient variation of ΔT across heater at 120 W HHHC configuration

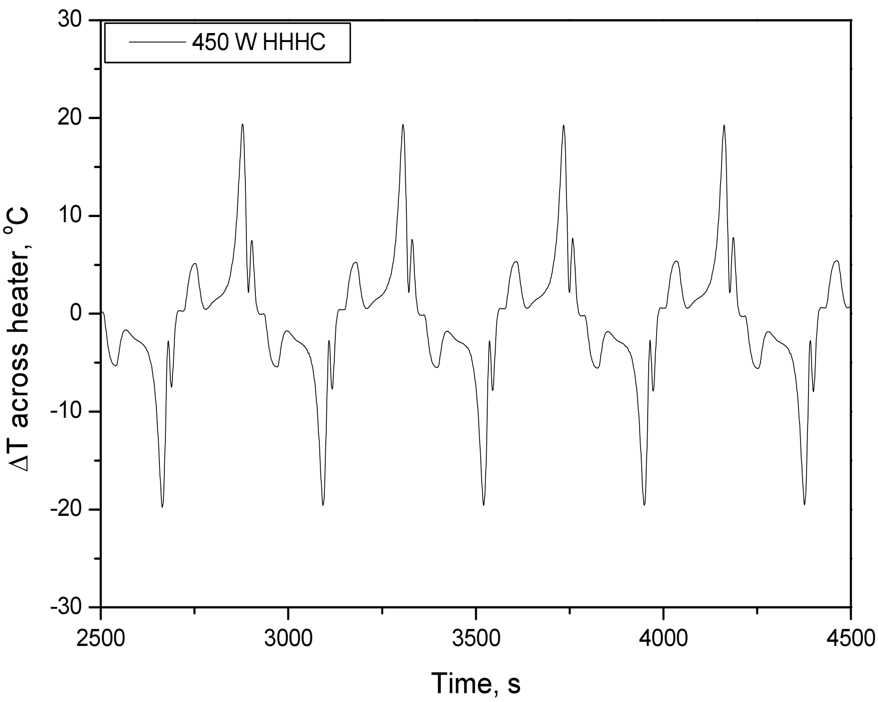

Figure 4.30: Predicted transient variation of ΔT across heater at 450 W HHHC configuration

4.8 Power raising transients

In the previous section, various flow patterns occurring during flow initiation transient are explained. In this section, flow transients during step rise in power are computed. For HHHC configuration at 220 W, as explained earlier, bi-directional pulsing is obtained. Under this condition, the power is suddenly raised to 450 W. The resulting transient variation of ΔP is shown in Fig. 4.31. It can be seen that, at 450 W power, unidirectional oscillatory flow is established. Comparing this result with flow initiation transient at 220 W, in which bi-directional flow was obtained, it can be concluded that the flow pattern in the system depends not only on the operating conditions but also on the path followed to reach those operating condition.

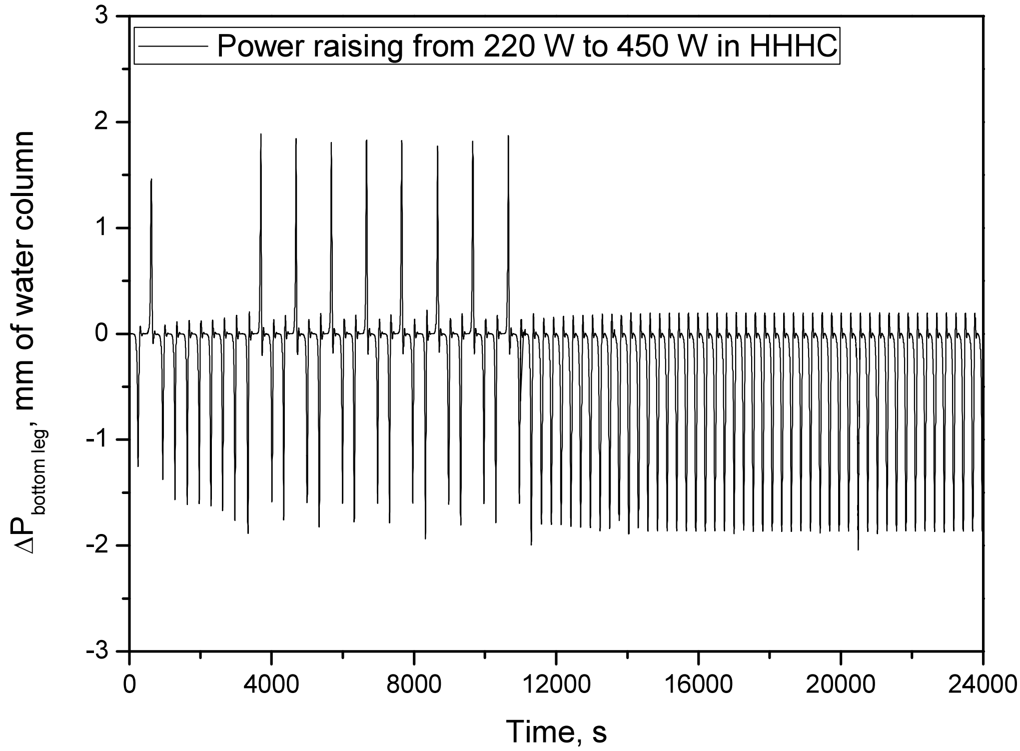

Figure 4.31: Computed transient variation of $\Delta P_{bottom\ leg}$ during power raising from 220 W to 450 W in HHHC configuration

4.9 Power step back transient

The objective of this test was to study the effect of power step back on oscillating flow in HHHC configuration. In this case, power is reduced from 220 W to 120 W and 220 W to 45 W. The resulting transient variation in ΔP is shown in Fig. 4.32 and Fig. 4.33 respectively. It can be seen that bi-directional oscillations transform into unidirectional oscillations for both the cases.

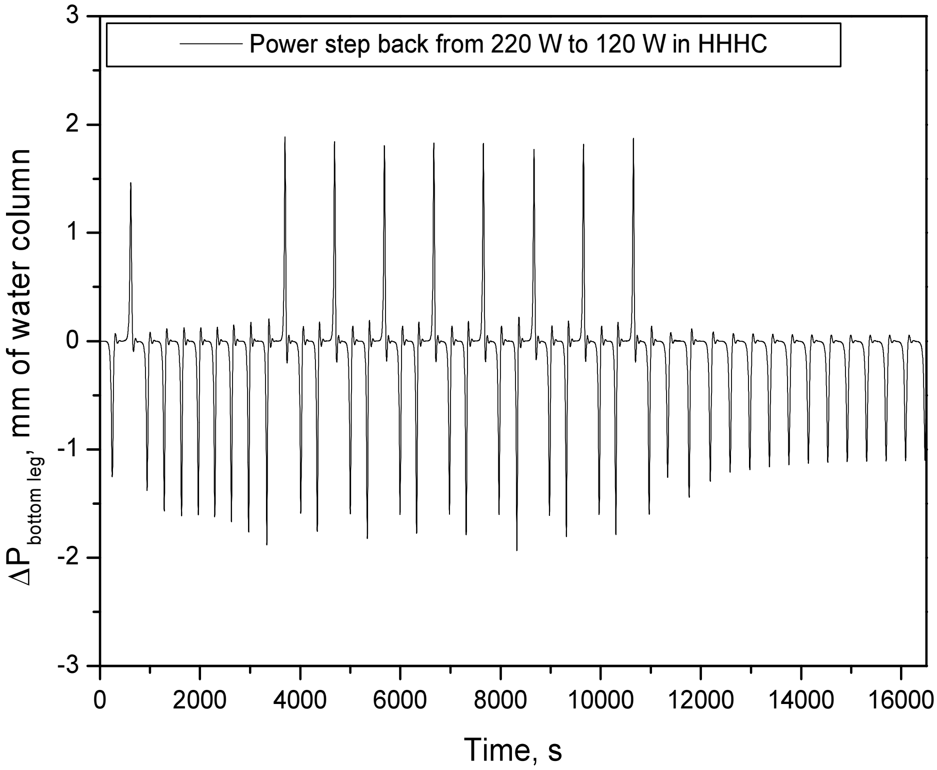

Figure 4.32: Prediction of transient variation in power step back from 220 W heater power to 120 W heater power in HHHC configuration

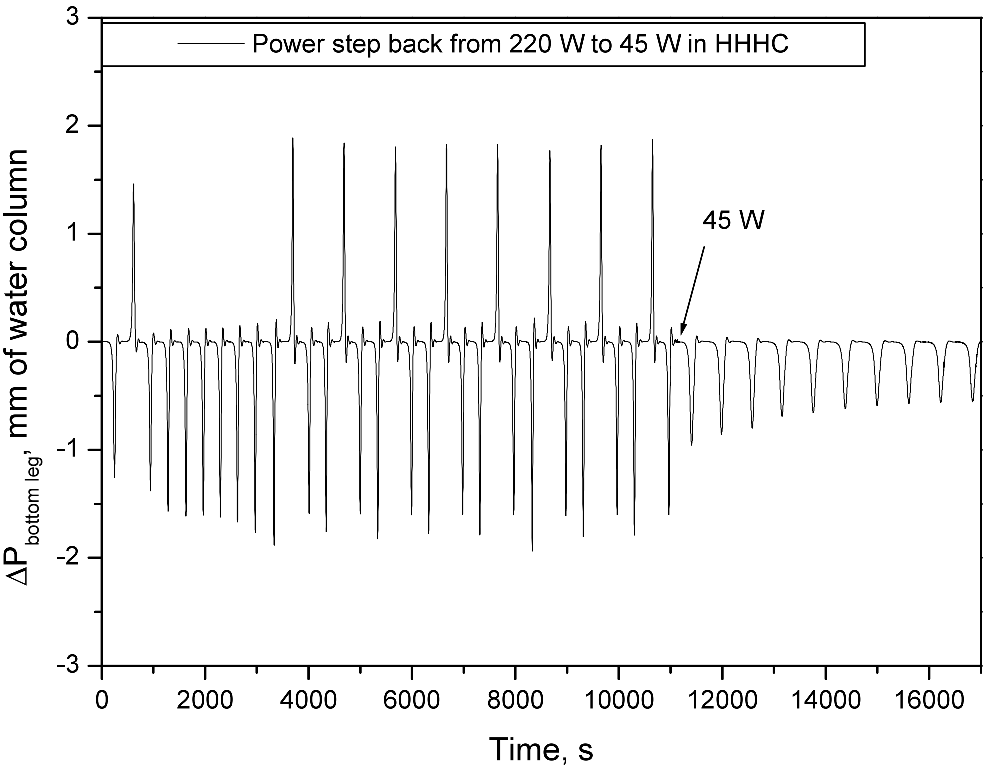

Figure 4.33: Prediction of transient variation in power step back from 220 W heater power to 45 W heater power in HHHC configuration

Figure 4.33 shows the transient variation of power step back from 220 W to 45 W heater power in HHHC configuration. Initially, CFD simulation has been started from rest condition of the loop (flow initiation transient) with a heater power of 220 W and secondary coolant flow rate of 0.472 m^3/s. After 11000 seconds of simulation also the loop has not come to steady state but loop shows initial unidirectional oscillation up to 3800 s and there after it shows bi-directional oscillations. Power step back from 220 W to 45 W has been initiated at 11000 s. Then the simulations were carried out up to 17000 s. It has been observed that the power step back from 220 W to 45 W reduces the oscillations from bi-directional oscillations to unidirectional oscillations and also the amplitude of oscillation has been reduced.

4.10 Closure

In this chapter, 3D transient CFD simulations are performed to compute steady state and transient characteristics of rectangular natural circulation loop working with water. The primary as well as secondary sides of the natural circulation loop are included in the 3D CFD simulation. Multi-block body fitted grid has been used for discretizing the computational domain. In turbulent cases, standard k-ε turbulence model and low–Reynolds number k-ε turbulence models have been used.

Steady state results at different heater powers were computed for VHVC and VHHC configurations. The steady state results were compared with correlations and experimental data and good match was obtained, especially with Vijayan and Swapnalee correlations. In HHHC configuration, steady state may not be achieved. Hence transient characteristics were computed. Flow initiation transient for VHVC, VHHC and HHVC showed initial oscillations in flow parameters but eventually flow reaches a steady state. In vertical heater configurations, laminar model gives better results than that with turbulent model. The flow gets initiated immediately after application of power. In the vertical heater configurations, heater acts similar to a pump. The flow is similar to pipe flow. Hence due to low Re encountered, laminar model gives good match with experimental data. In HHHC configuration, either unidirectional/bi-directional pulsing is observed depending on heater power.

In HHHC configuration steady state was not achieved and due to continuous laminar to turbulent transition, flow initiation transient results computed with fully laminar/turbulent models always showed some deviation from experimental ones. However, the results obtained by low-Reynolds number k-ε turbulence are better than standard k-ε model when compared with experimental data.

The flow in the loop is driven by buoyancy force which in turn depends on temperature gradients. Hence flow pattern in natural circulation loop depends on how temperature field evolves. An important contribution is the explanation of formation of uni-directional/bi-directional pulsing in HHHC with the help of temperature fields at different time instances. The verification of hot plug transport theory is also carried out.

CHAPTER 5

3D CFD SIMULATION OF MOLTEN SALT NATURAL CIRCULATION LOOP

5.1 Introduction

Major contribution of this work is to study behaviour of molten salt natural circulation loop (MSNCL) working with mixture of sodium and potassium nitrates in 60:40 ratio by weight, using experimental method as well as 3D CFD simulations. In this chapter, the studies carried out by using 3D CFD simulations are explained.

Steady state characteristics are computed for VHHC, VHVC and HHVC configurations of the Molten Salt Natural Circulation Loop (MSNCL). For VHHC configuration, computed data is compared with experimental data measured in the experimental facility previously described. For all these three configurations, the steady state characteristics are compared with various correlations. In HHHC configuration, owing to symmetric geometry and boundary conditions, steady state flow is not obtained. Hence steady state characteristics cannot be obtained for this configuration.

Solidification of molten salt at 238^0C and decomposition of molten salt at 600^0C are the important parameters to be considered in the experiment. Once molten salt solidifies it will damage the test facility hence it is not possible to conduct the experiment at the extreme upper and lower limit of heater power. Hence, the maximum and minimum heater powers that can be imposed on the MSNCL are computed from CFD simulations.

Transient simulations are performed for flow initiation transients for all the four configurations. For each configuration, the flow initiation transients are computed at different powers. Other transients studied in present work include power step rise, power step back, heater trip and loss of heat sink.

For computing these steady state and transient characteristics, at first, mesh and time step independence studies were carried out to choose the appropriate mesh and time step sizes. Validation of the CFD model is then performed.

In this chapter, the CFD model of MSNCL, mesh and time step independence studies, validation, steady state and transient characteristics are explained in details.

5.2 CFD model of molten salt natural circulation loop

5.2.1 Computational domain

The geometry and dimensions of the rectangular natural circulation loop working with molten salt are shown in Fig. 3.1 (ref. chapter 3). A CFD model is developed accordingly. The model involves primary side i.e. heater section, cooler section, and connecting piping filled with molten salt. It also involves secondary side i.e. cooler duct with its inlet and outlet. The thickness of the pipe is accounted for. The effect of thermal conductivity and heat capacity of loop piping significantly affect simulation results especially transient ones. The insulation over the piping was not modelled but its effect is accounted for by incorporating conductive resistance in the overall heat transfer co-efficient supplied at outer radius of connecting pipes in the model. For the studies of sudden power trip and loss of heat sink transients, expansion tank is included along with the above mentioned CFD model. Inclusion of expansion tank significantly increases mesh size and is very expensive for transient calculations.

5.2.2 Mesh

Figure 5.1 shows the mesh adopted in the computational domain. The multi-block hexahedral structured body fitted mesh is generated. The mesh selected to carry out the CFD simulation has been selected after detailed mesh independence study, which is given in detail in a later section

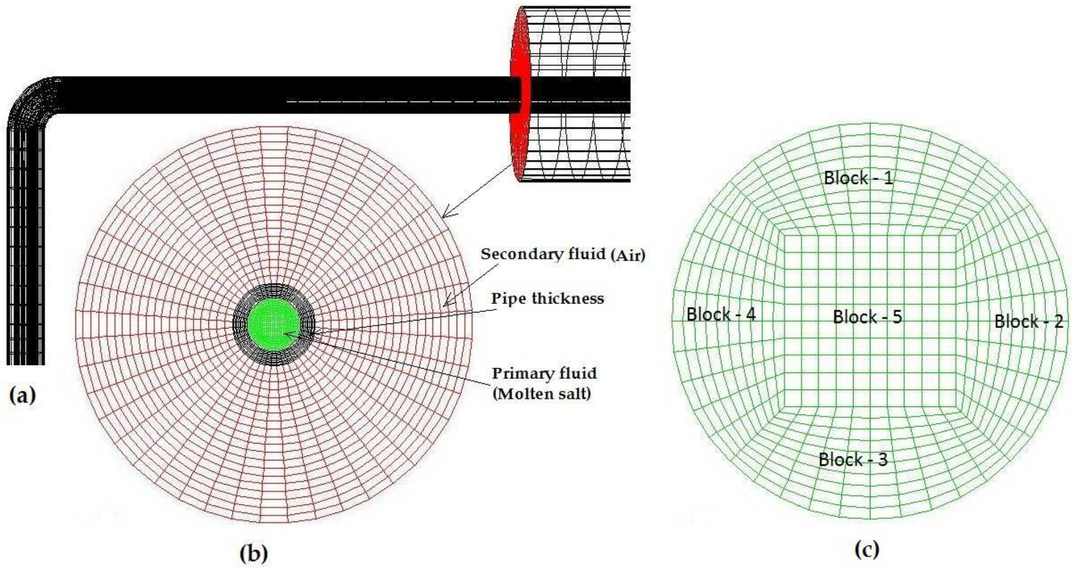

Figure 5.1: Mesh adopted in the CFD model (a) mesh in a vertical plane, (b) mesh at cooler outlet cross-section, and (c) mesh in the primary fluid cross-section

5.2.3 Governing equations and numerical parameters

From experimental data, it was ascertained that, flow induced in MSNCL is low Reynolds number and hence is laminar. To compute 3D transient laminar flow and temperature fields in the computational domain, Navier-Stokes equations are solved along with the transport equations for thermal energy. In present work, the power law scheme is convection scheme is chosen. The scheme exhibits good accuracy over a range of Peclet number (Patankar et al., 1980). The coupled momentum and energy equations are solved by SIMPLE algorithm which is an iterative segregated solution procedure.

5.2.4 Thermo-physical properties of primary and secondary fluids

Thermo-physical properties of primary and secondary fluids, i.e. molten salt and air respectively, are specified. Fluid is subjected to gravity. For primary fluid, Boussinesq approximation is used by specifying reference density, reference temperature and thermal expansion coefficient.

Nissen (1982), based on experimental data, mentioned the thermo-physical properties of molten salt ($NaNO_3$+KNO_3), except thermal conductivity, in the form of polynomial expressions. Ferrie et al., (2008) mentioned the polynomial expression for thermal conductivity, density, specific heat and viscosity. The polynomial expression mentioned by both of them is given in Eq. 5.1. As per Ferrie et al., when it is fitted for different physical properties, the estimate of error is ±1.10%.

$$\varphi = a + b(T - 273.15) + c(T - 273.15)^2 + d(T - 273.15)^3 \qquad (5.1)$$

The constants in the above equation for each property as mentioned by them are listed in Table 5.1. In the above equations, the temperature is in Kelvin.

MSNCL operating temperature limit is from 300°C to 600°C. Hence reference temperature is chosen to be 300°C. Using *Equation 5.1* and constants from Table 5.1, the values of thermal conductivity, density, dynamic viscosity and specific heat for molten nitrate salt at 300°C are computed and used for CFD simulation of MSNCL. Thermal expansion coefficient $\left(\beta = -\frac{1}{\rho_{ref}} \left.\frac{\partial \rho}{\partial T}\right|_{Tref}\right)$ is obtained by differentiating equation for density. Following are the thermo-physical property values used in present simulations (Table 5.2).

Table 5.1: Constants used to evaluate the thermo-physical properties of solar salt [Nissen (1982), Ferrie et al., (2008)]

	a	**b**	**c**	**d**
Density (kg/m^3)	2090	-0.636	0	0
Thermal conductivity (W/m-K)	0.443	1.954E-4	0	0
Specific heat (J/kg-K)	1443	0.172	0	0
Viscosity (mPa-s)	22.714	-0.12	2.281E-4	-1.474E-7

Table 5.2: Thermo-physical properties of solar salt (at 300^{o}C) obtained from Eq. 5.1

Thermo-physical property	Value of the Thermo-physical property at 300^{o}C
Density (kg/m^3)	1899.2
Thermal conductivity (W/m-K)	0.501
Specific heat (J/kg-K)	1494.6
Viscosity (Pa-s)	3.26E-3

Over a temperature range of 300^{o}C to 600^{o}C, property values change by 10%. Hence use of constant properties is justifiable.

5.2.5 Boundary conditions

Heat flux at outer diameter was specified in heater section. In MSNCL, the loop temperature is much higher than ambient temperature and there is significant heat loss from loop to ambient. Hence the effect of heat loss at heater and connecting pipes is modelled in the CFD model. The heat loss to the ambient is incorporated in the CFD model by using convective boundary condition at outer diameter of piping connecting heater and cooler. The outside heat transfer co-efficient on the pipe connecting cooler to heater is calculated using empirical correlation based on the measured surface temperature on the pipe. In secondary side, at inlet boundary, coolant mass flow rate of 0.02 kg/s is specified and kept unchanged in all cases. The temperature of coolant (air) at inlet is also specified.

At the inner diameter of loop piping, wall shear stress is computed by standard wall functions, if standard k-ε turbulence model is used. In laminar cases or low-Re turbulence model, no slip boundary condition is used for momentum equations.

5.2.6 Initial conditions

In steady state cases as well as flow initial transient cases, initial flow field is stagnant. Hence, all three velocity components are set to zero. The initial temperature is set to 300^{o}C. In other transients, like power step-up, power step-down, power trip, loss of sink, the initial conditions of flow and temperature are exactly same as steady state conditions achieved at a previous power level.

5.3 Mesh independence study

Computing 3D transient flow is very expensive. Hence optimum mesh has to be first decided. Mesh independence study was carried out to choose the appropriate mesh size. Cross-sectional mesh was first decided by keeping fixed number of axial nodes. Then using optimum cross-sectional mesh, optimum axial nodes were determined by varying the axial nodes.

As shown in Fig. 5.1, a butterfly mesh is used in present work. In a cross-section, there are 5 blocks. The number of cells in each block has to be same for structured meshing. A mesh specification of 11x11x5x354 means, in each block, there are 11x11 control volumes and there are 5 such blocks in each cross-section and there are 354 nodes along axial direction (i.e. along the direction which is normal to the cross-section).

The steady state is computed for VHHC configuration at heater power of 1400W.The variations of axial velocity at heater inlet and at some distance downstream heater are shown in Fig. 5.2 and Fig. 5.3. It can be seen that the mesh size of 7x7x5 shows slightly different profiles while all other meshes show same profiles. To reduce the computational cost, 11x11x5 mesh size is selected for further simulations. To study effect of the axial spacing, the case is computed using various axial nodes viz. 354, 499, 714 and 1368 axial nodes in the computational domain. Thus, simulations are carried out with meshes involving 11x11x5x354 cells, 11x11x5x499 cells, 11x11x5x714 cells and 11x11x5x1369 cells.

The axial variation of temperature and velocity in the centre line location of the left leg are shown in Fig. 5.4 and Fig. 5.5 respectively. It is found that, all the meshes considered predict same profiles. The mesh with 354 axial nodes show slight deviation at some points but all other meshes show exactly same result. Hence the mesh size of 11x11x5x499 is selected to carry out the CFD simulations.

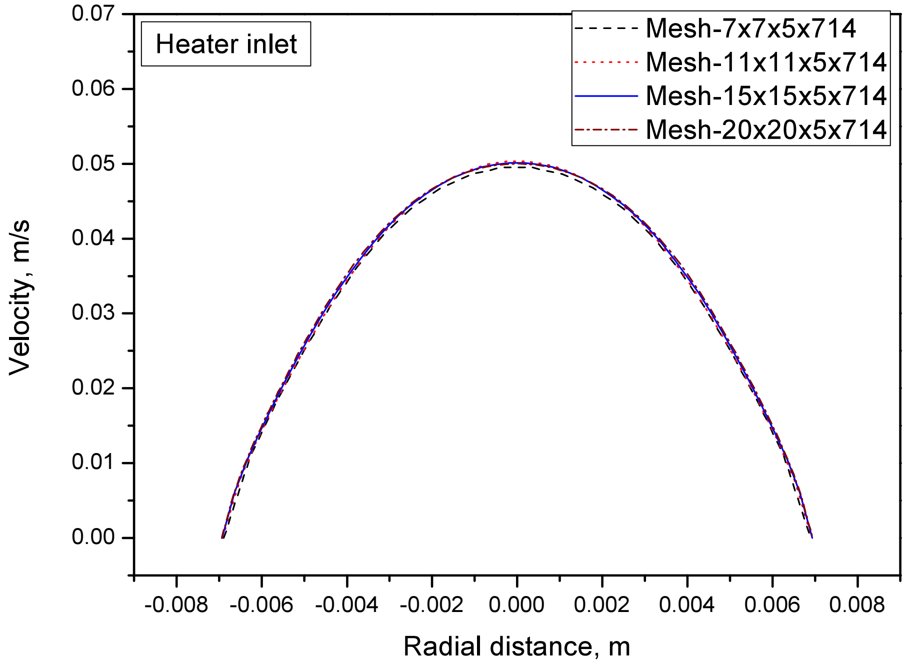

Figure 5.2: Velocity variation at heater inlet using different mesh size in radial direction

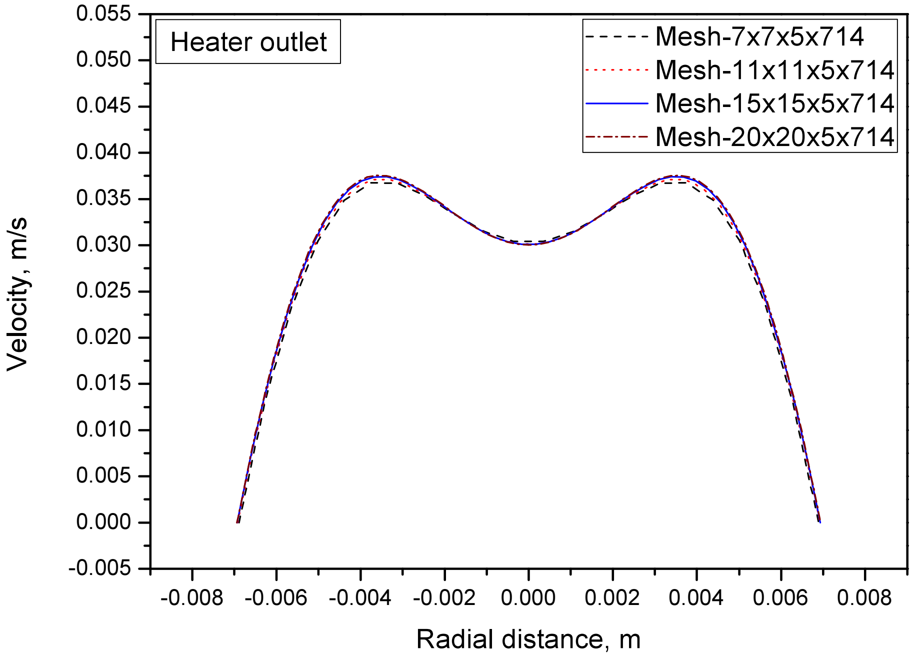

Figure 5.3: Velocity variation at heater outlet using different mesh size in radial direction

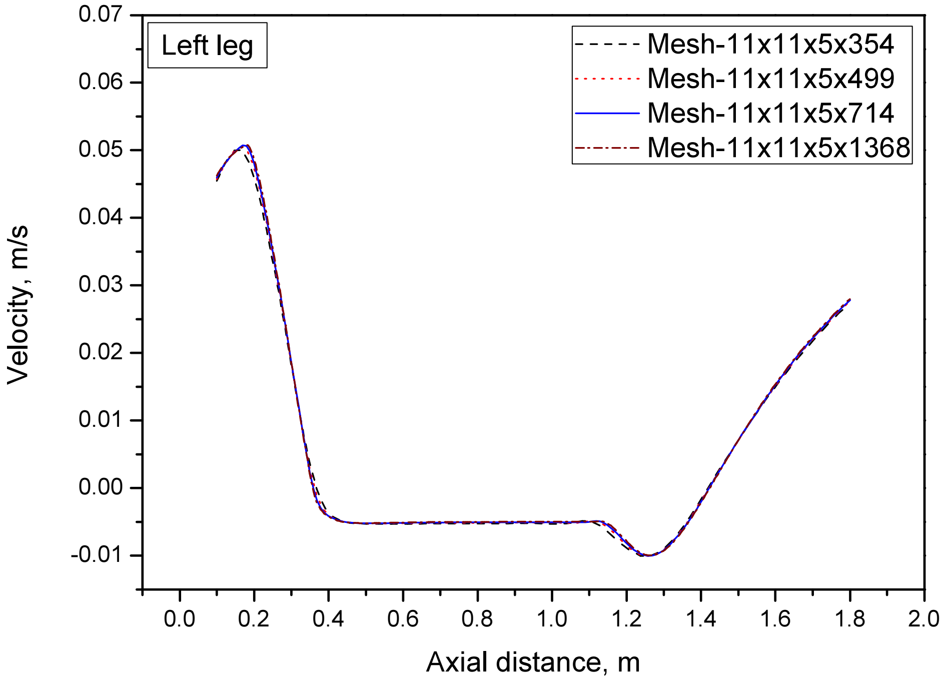

Figure 5.4: Velocity variation at left leg using different mesh size in axial direction

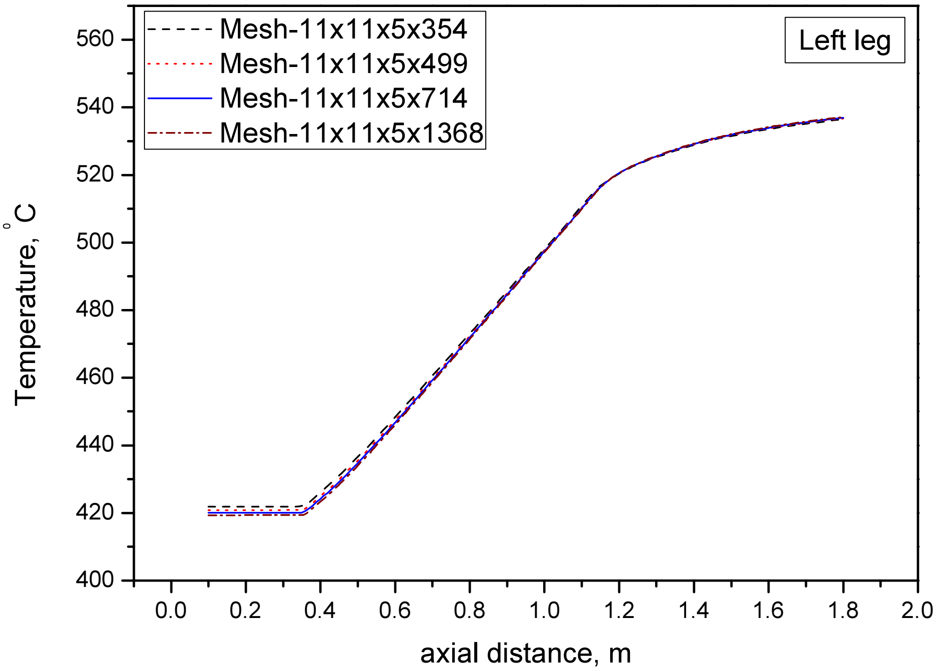

Figure 5.5: Temperature variation at left leg using different mesh size in axial direction

Further to check the selected mesh, the CFD simulation was carried for a well known problem of laminar flow through a pipe (Cengel et al., 2011). The simulation of fluid flow in a pipe using 11x11x5 mesh size in a pipe of 13.88 mm diameter with molten salt ($NaNO_3$+KNO_3) as working fluid is carried out. The schematic diagram of the pipe flow has been shown in Fig. 5.6. Mass flow rate corresponding to Re=500 is specified as inlet boundary condition and atmospheric pressure as outlet boundary condition. The computed velocity profile is plotted at pipe outlet and it is compared with analytical expression. The analytical expression for the velocity profile in fully developed laminar flow region is $u(r) = u_{max}\left(1 - \frac{r^2}{R^2}\right)$ where $u_{max} = 2V_{avg}$. In this expression, r is the radial distance from the axis (m), R is the radius of the pipe, u_{max} is the maximum velocity and u(r) is axial velocity at radial distance r from axis. $u/u_{max} = 1 - (r/R)^2$ Fig. 5.7 shows the comparison of computed velocity profile in the fully developed region and the analytical velocity profile. It shows that the selected mesh is able to compute accurate velocity profile.

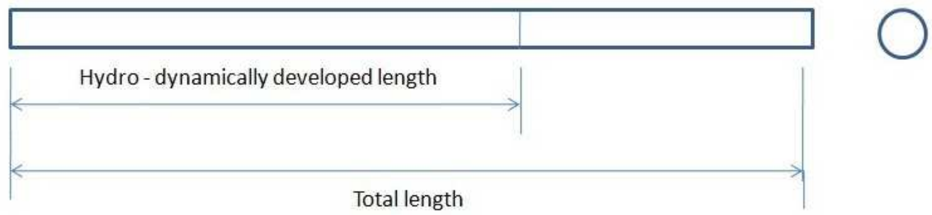

Figure 5.6: Schematic diagram of pipe flow problem

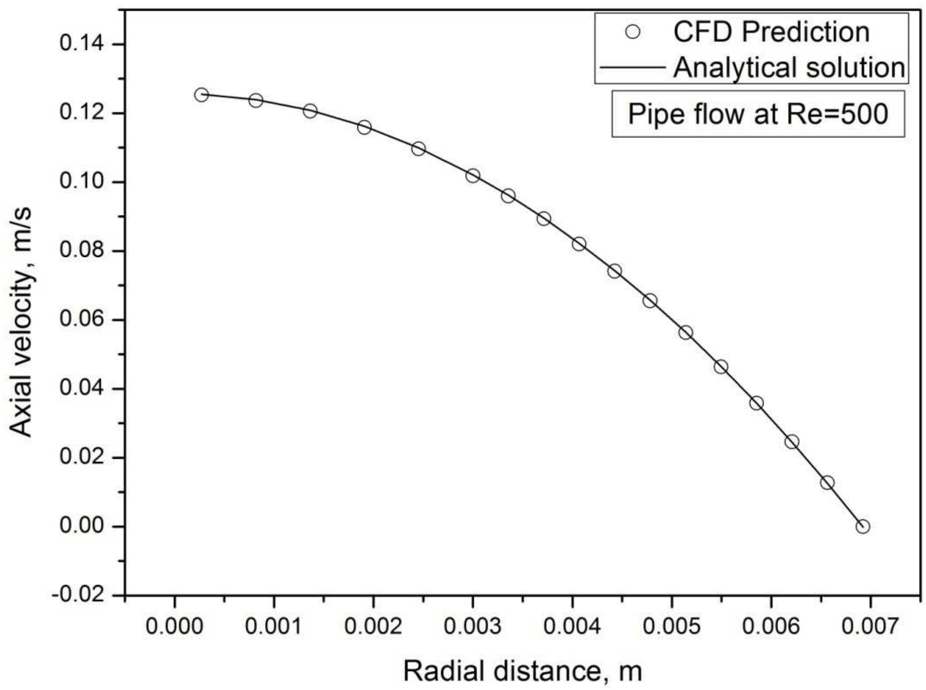

Figure 5.7: Comparison of computed axial velocity profile with the velocity profile obtained from analytical expression in a laminar pipe flow problem

5.4 Time step independence study

In the present work, 3D transient simulations are carried out, which are computationally very time consuming. So an optimum time step is first determined using time step independence study. For this, flow initiation transient simulations were carried out by using different time steps of 0.05 s, 0.1 s, 0.5 s, 1 s, 2.5 s and 5 seconds. Figure 5.8 and Fig. 5.9 show the transient variation of temperature at centre point locations of heater inlet and heater outlet respectively for VHVC configuration at 1400 W heater power. Similarly, Fig. 5.10 and Fig. 5.11 show the transient variation of velocity at centre point position of heater inlet and heater outlet respectively. From Fig. 5.8 to Fig. 5.11, it is clear that the time step size of 0.1 s is required to carry out the transient simulations. Hence the time step size of 0.1 s is used in transient simulations.

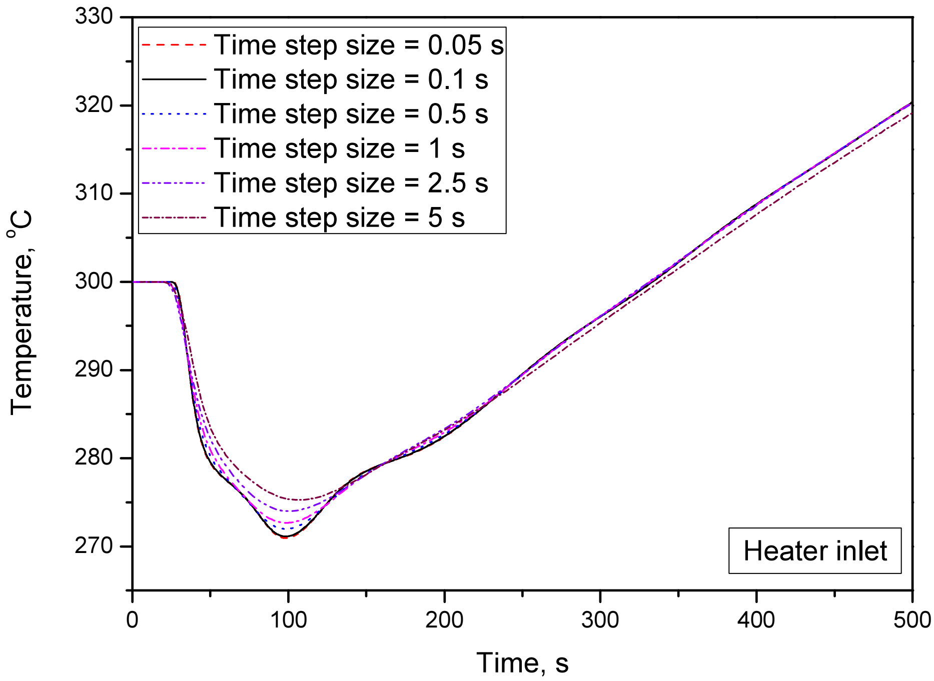

Figure 5.8: Transient variation of temperature at heater inlet

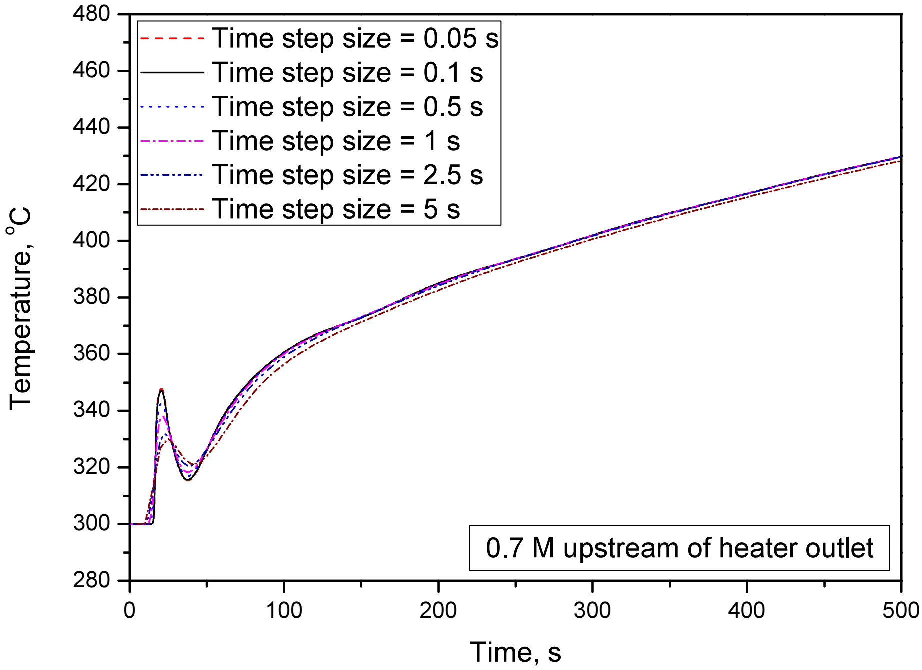

Figure 5.9: Transient variation of temperature at heater outlet

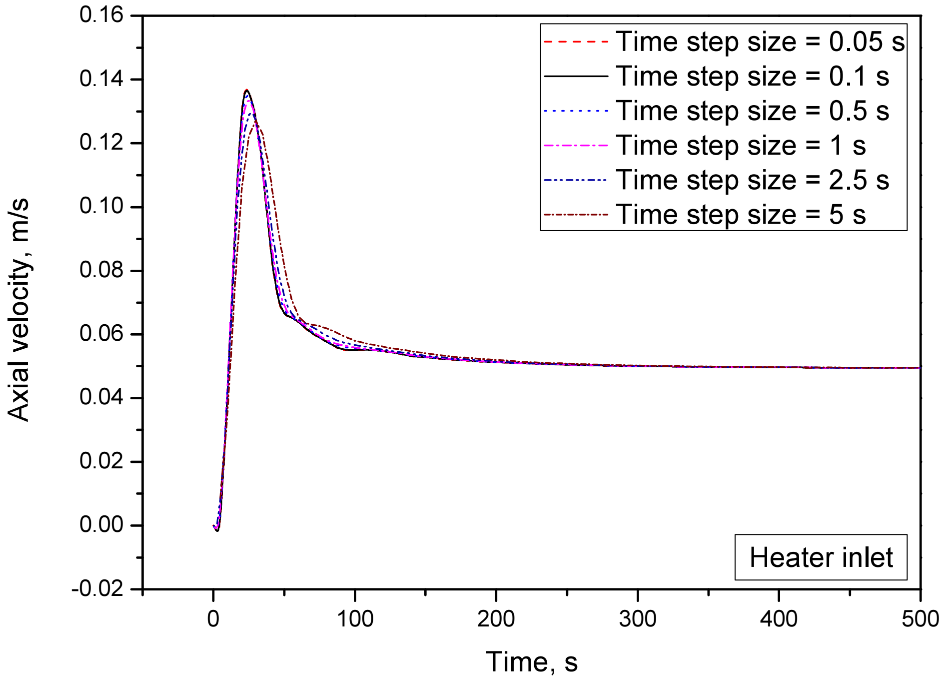

Figure 5.10: Transient variation of velocity at heater inlet

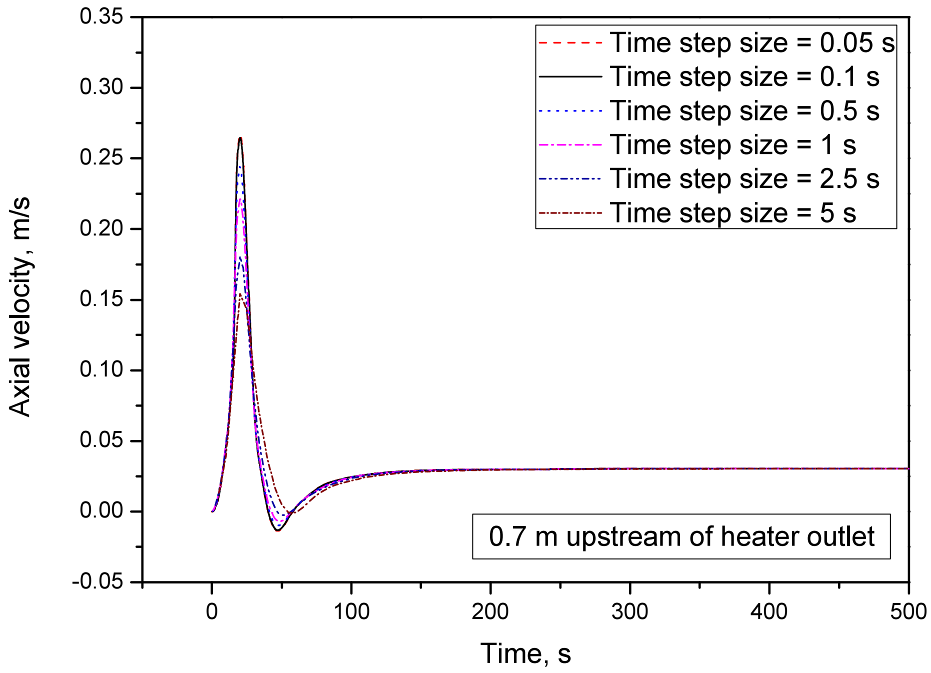

Figure 5.11: Transient variation of velocity at heater outlet

Further to ensure the time step chosen, time step independence study have been carried out on a heater trip transient of 2000 W VHHC configuration. In this case the power changes suddenly from 2000 W to 0 W. Hence it is a fast transient. Figure 5.12 shows the transient variation of heater outlet temperature with different time steps in the sudden power trip. It can be seen that, the chosen time step of 0.1 s is sufficient to carry out the CFD simulations. Further reducing time step won't increase the accuracy whereas using a large time step of 1 s leads to large numerical oscillations.

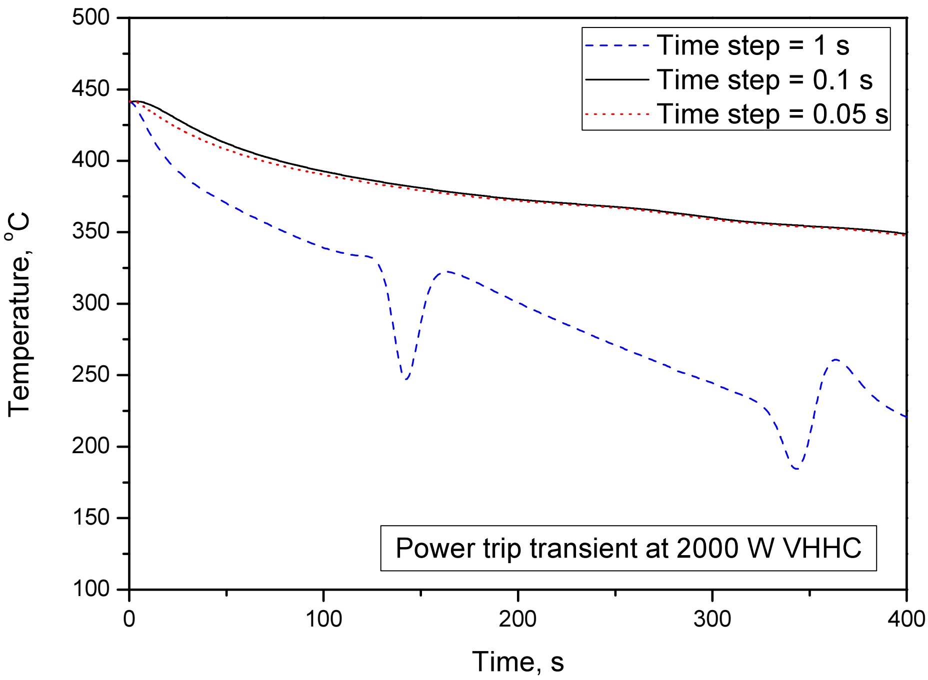

Figure 5.12: Transient variation of heater outlet temperature with different time steps in the sudden power trip of 2000 W steady state condition of VHHC configuration

5.5 Results and Discussions

5.5.1 Steady state characteristics

After application of power in heater and secondary coolant flow in cooler, flow gets induced in NCL and comes to a steady state in which buoyancy forces balance with the frictional forces.

The steady state simulations were carried out to study the thermal hydraulic behaviour and to estimate the primary fluid (molten salt) mass flow rate induced in the loop due to heat flux applied in heater. For VHHC, VHVC and HHVC configurations, simulations were performed at different heat fluxes and in each case steady state is computed. The steady state Reynolds number predicted by CFD simulations at different heater powers has been compared with that calculated by different correlations proposed by the various researchers.

Vijayan et al., (1994) developed a correlation based on scaling laws to estimate the steady state Reynolds number for uniform diameter single-phase natural circulation loop. Later Vijayan (2002) modified this correlation for uniform and non-uniform diameter single-phase natural circulation loops. Vijayan correlation to estimate the steady state Reynolds number is, $Re_{ss} = C\left({Gr_m}/{N_G} \right)^r$, Where Gr_m is the modified Grashof number, N_G is a non-dimensional geometrical parameter. C and r are constants. Their values depend on whether the flow is laminar or turbulent. The details of this correlation have been mentioned in chapter 4. This correlation was validated with the experimental data of rectangular natural circulation loops (having different pipe diameters) working with water by Vijayan et al., (2008). Further many researchers compared their experimental data with Vijayan correlations. Namely, Misale et al., (2011) experimentally investigated the natural circulation of distilled water and FC43 in a rectangular loop characterised by internal diameter of 30 mm and total length of 4.1 m and compared the experimental data with Vijayan correlation and obtained good agreement. Wang et al., (2013) successfully validated their CFD results with the experimental data obtained from Misale et al., (2007) and with Vijayan correlation. Nayak et al. (2008), Borgohain et al. (2011), Kiran Kumar and Ram Gopal (2011), Naveen Kumar et al. (2014) used Vijayan correlation to compare their experimental data.

5.5.1.1 Vertical Heater and Horizontal Heater (VHHC) configuration

The comparison of experimental and computational data on temperature obtained at different locations of the loop is given in Fig. 5.13. The predicted CFD results, such as heater inlet/outlet and cooler inlet/outlet temperatures, are matching well with experimental data at various powers. With increase in power, there is increase in heater inlet as well as heater outlet temperatures. Thus, loop mean temperature also rises with power.

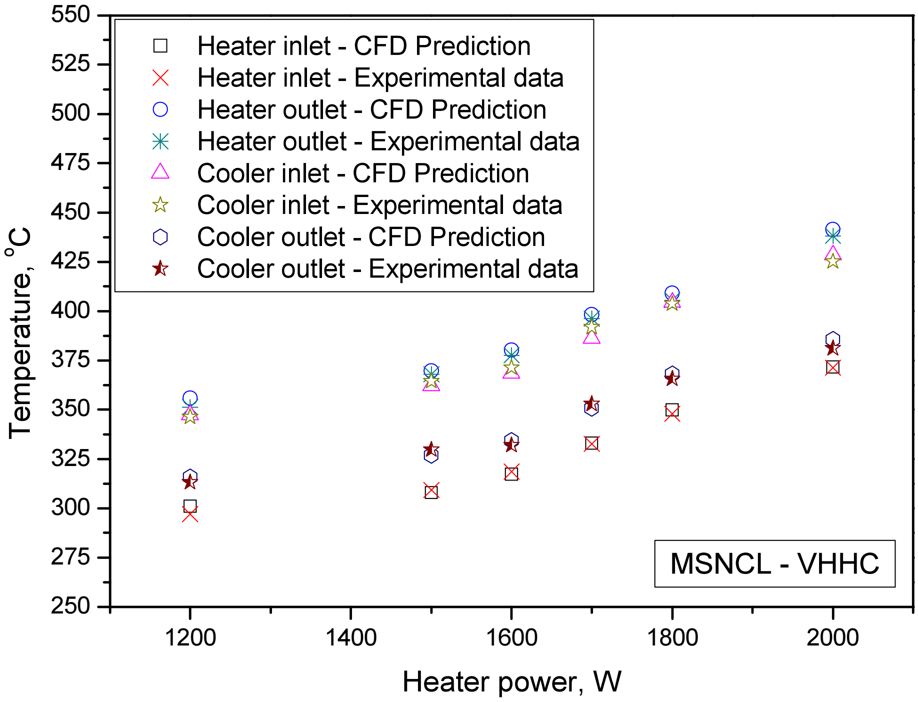

Figure 5.13: Comparison of computed steady state temperature at different locations in the loop with corresponding temperature observed in experiment

The steady state Reynolds number, Re_{ss}, predicted by CFD simulations at different heater powers has been compared with that calculated by different correlations and also the Re_{ss} calculated by using experimental data. The aim of the comparison of computed results with experimental data and various correlations is to validate the CFD model. Figure 5.14 shows the computed steady state Reynolds number (Re_{ss}) and also the same from experiment have been compared with the correlations developed by Vijayan (2002), Naveen Kumar et al., (2011), and Wang et al., (2013). It can be seen that the computed Re_{ss} matches well with the steady state Reynolds number calculated by experimental data. Maximum ±1.36% of error has been observed between predicted computational data and experimental data. The computed Re_{ss} shows good agreement with the correlations. Reynolds number increases due to increase in mass flow rate with power.

The mentioned correlation by Vijayan (2002) is based on the one-dimensional approach, whereas in the NCL at elbows the fluid flow exhibits three-dimensional flow. The fully developed forced convection friction factor correlations are used in the derivation of these correlations but in the actual loop, due to the elbows and heating/cooling of fluid, the fluid flow is not fully developed. Heat loss is also not accounted in the correlation. Hence it is obvious that the exact match of computational/experimental data with these correlations is not possible.

The mentioned correlations are mostly suitable for NCL working with water. NCL working with MSNCL works at much higher temperature. Even after adequate insulation, there are lot of heat losses. This results into reduced buoyancy forces and hence lesser mass flow rate for a given power. The correlations, being developed from NCL (water) do not account for heat losses and hence show higher induced mass flow rate or Re_{ss} for a given power (or Gr_m/N_G). The same CFD model has been used to carry out the steady state and flow initiation transients of different configurations of the MSNCL.

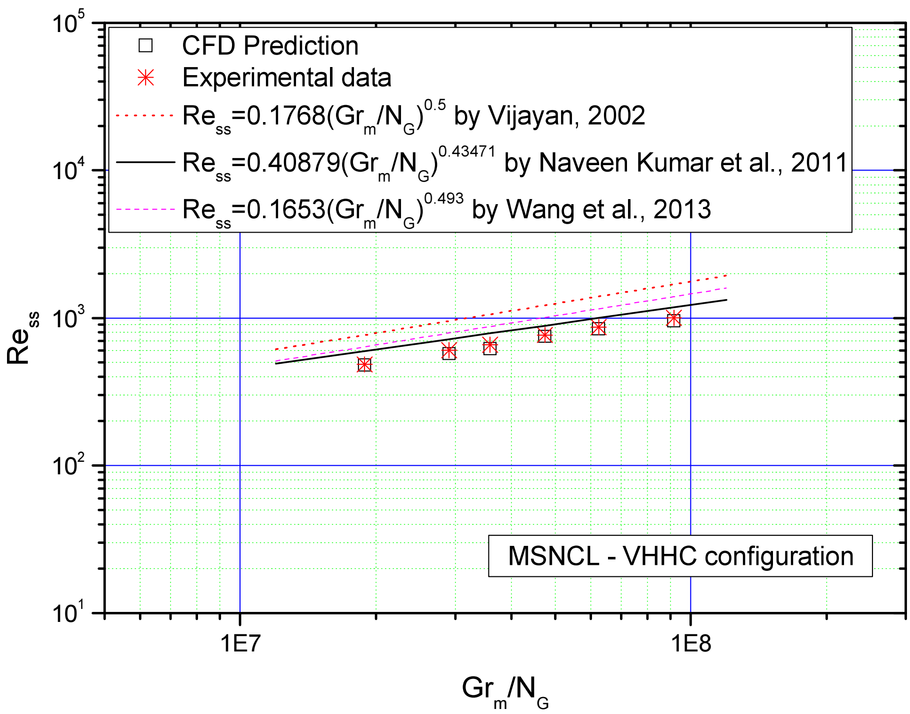

Figure 5.14: Comparison of computed steady state Reynolds number with different correlations and experimental data of VHHC configuration

The steady state temperature field at the central vertical plane of the loop captured in 3D CFD simulation for 1200 W VHHC case is shown in Fig. 5.15. There is increase in temperature from heater inlet to heater outlet. From heater outlet to some distance downstream, uniformity in temperature is obtained. From heater outlet to cooler inlet, temperature decreases due to heat loss to ambient. From cooler inlet to cooler outlet, there is significant decrease in fluid temperature. From cooler outlet to heater inlet, small decrease in temperature occurs, again due to heat loss to ambient.

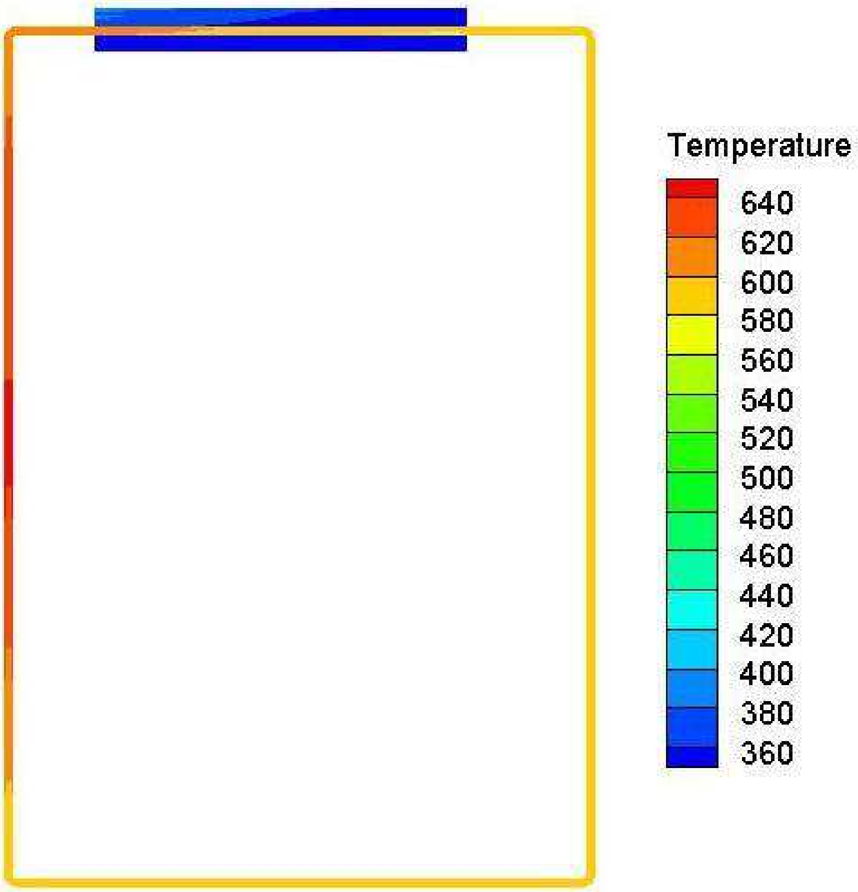

Figure 5.15: Temperature contour at central vertical plane of VHHC configuration at 1200 W (Temperature is in Kelvin)

5.5.1.2 Vertical Heater and Vertical Cooler (VHVC) configuration

The steady state Reynolds number predicted by CFD simulations at different heater powers has been compared with that calculated by different correlations proposed by the various researchers is shown in Fig. 5.16. Reynolds number increases due to increase in velocity with power. The computed steady state Reynolds number has been compared with the correlations developed by Vijayan (2002), Naveen Kumar et al., (2011), and Wang et al., (2013). The computed steady state Reynolds number shows good agreement with the correlation by Wang et al., (2013).

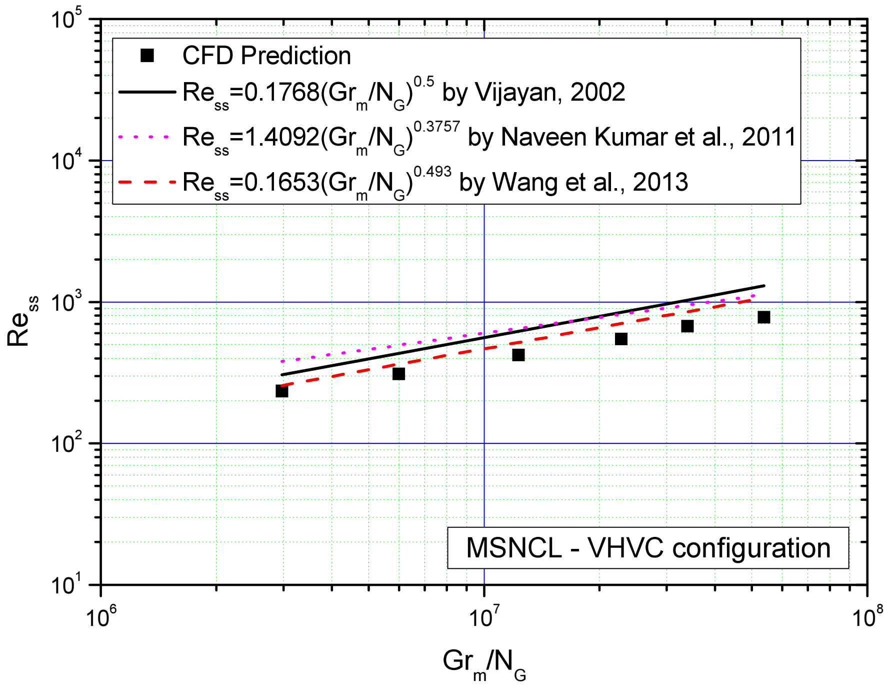

Figure 5.16: Comparison of computed steady state Reynolds number with different correlations and experimental data of VHHC configuration

5.5.1.3 Horizontal Heater and Vertical Cooler (HHVC) configuration

The steady state Reynolds number predicted by CFD simulations at different heater powers has been compared with that calculated by different correlations proposed by the various researchers for HHVC configuration is shown in Fig. 5.17. Reynolds number increases due to increase in mass flow rate with power. The computed steady state Reynolds number has been compared with the correlations developed by Vijayan (2002), Pilkhwal et al., (2007), Wang et al., (2013) and Swapnalee et al., (2011). Out of these correlations Vijayan and Swapnalee and Vijayan correlations are developed based on the 1D solution of the natural circulation loop. Pilkhwal et al., (2007) and Wang et al., (2013) used 3D CFD software to study the behaviour of natural circulation loop and compared there CFD data with experimental data. They have not mentioned how they obtained their correlation. But the mentioned correlations by them are matching well with their CFD results. It can be seen from the Fig. 5.17 that, computed Re_{ss} shows good agreement with the correlations developed by Wang et al., (2013) and Pilkhwal et al., (2007).

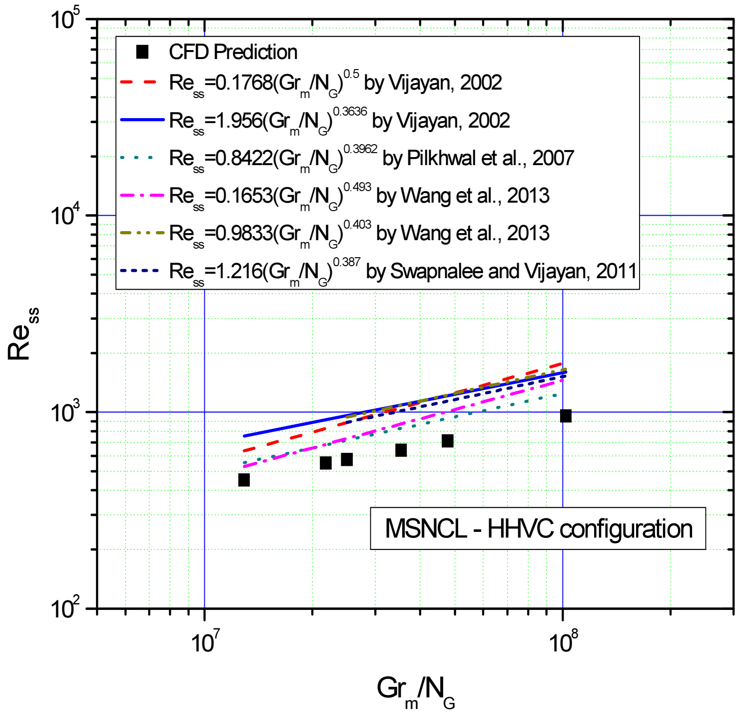

Figure 5.17: Comparison of computed steady state Reynolds number with different correlations and experimental data of HHVC configuration

5.5.2 Loop operating limits

The simulations were performed for heater power of 950 W and 2500 W. The minimum and maximum loop temperatures for these powers are summarized in Table 5.3. The mentioned molten salt is stable between the temperature limit of 238^{0}C to 600^{0}C (Ferrie et al., 2008). With 950 W power, simulations indicate minimum temperature of 237^{o}C. Practically, the solar salt will freeze in the loop at this power. On the other hand, with power as high as 2500 W, the loop maximum temperature is 567^{o}C. Exceeding the power beyond 2500 W will result into solar salt reaching 600^oC which is undesirable because such a high temperature affects the stability of solar salt composition. Hence, simulations predict that, loop can be operated between heater powers of 1000 W to 2500 W (for given secondary side mass flow rate and inlet temperature).

Table 5.3: Computed maximum and minimum temperature of MSNCL

Heater power, W	Minimum Temperature, ^0C	Maximum Temperature, ^0C
950	237.5	289.2
2500	463.1	567.3

5.5.3 Transient simulations

Transient simulations are helpful to understand the dynamic behaviour of natural circulation loop. Flow initiation transient simulations are carried out for all the four configuration of the loop such as VHVC, VHHC, HHVC and HHHC configurations. Experiments were conducted for VHHC configuration. Hence the other transients were carried out for VHHC configuration and obtained computational results are compared with experimental data.

Following transients are simulated.

(1) Flow initiation transients

(2) Power raising from steady state (PRSS) transients

(3) Power step back transients

(4) Power trip transients

(5) Loss of heat sink transients

5.5.3.1 Flow initiation transients

Simulations for flow initiation transients are performed to understand the development of flow and temperature fields in the loop. Flow initiation transient is computed by setting the initial field to stagnant conditions and applying desired power to heater section and then performing time marching calculations. Flow initiation transients are helpful to know the loop behaviour during start up condition.

The flow initiation transient at VHHC configuration of NCL working with water has been explained in the previous chapter 4. In that, the computed transient variation of flow rate was compared with experimental data. There was excellent match between computational results and experimental data. It was proved that 3D CFD modeling using FLUENT gives accurate results for flow initiation transients.

5.5.3.1.1 VHVC configuration

Simulations for flow initiation transients are performed to understand the development of flow and temperature fields in the loop. The transient variation of mass flow rate and temperature difference across heater (ΔT) is shown in Fig. 5.18 for VHVC. This is at 1000 W heater power. As soon as the heating starts, the ΔT across heater rises. Buoyancy force starts increasing, initiating the flow. The flow rate keeps increasing and after some time, the flow rate reduces even if ΔT keeps rising. This is due to increase in the friction. Hence the mass flow rate in the loop reduces. It can be seen that increase in the mass flow rate occurs during the starting period. This is due to the high inertia force induced by heating and cooling during the start-up. This increased mass flow rate is always retarded by the loop friction induced by flow circulation. Finally loop steady state is achieved. Figure 5.19 shows the transient variation of mass flow rate and temperature difference across heater in the flow initiation transient of VHVC configuration at 2000 W heater power. The enlarged plot of computed transient variation of mass flow rate in 2000 W VHVC configuration is shown in Fig. 5.20.

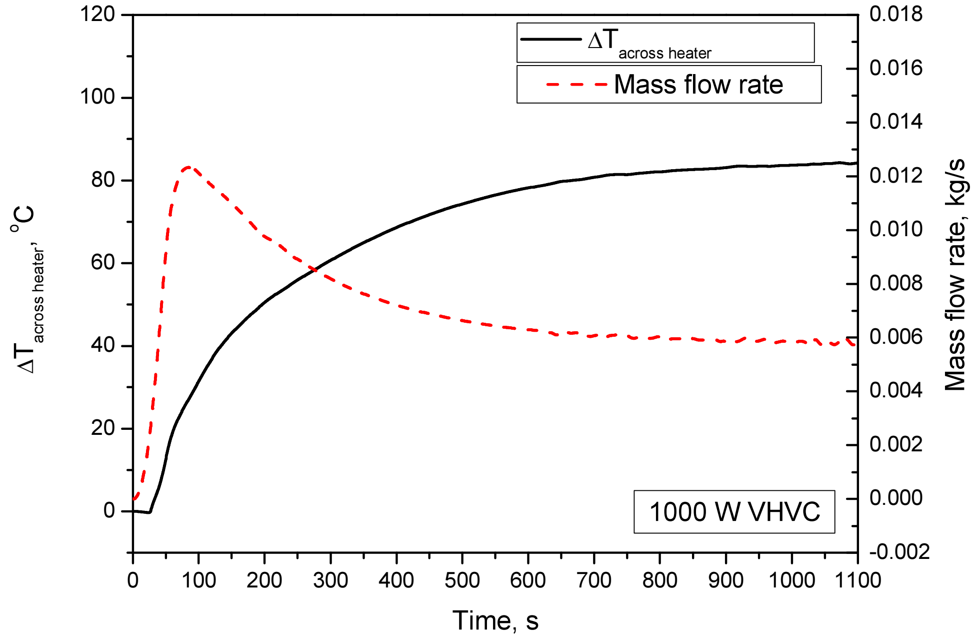

Figure 5.18: Transient variation of computed $\Delta T_{across\ heater}$ and mass flow rate in 1000 W VHVC configuration

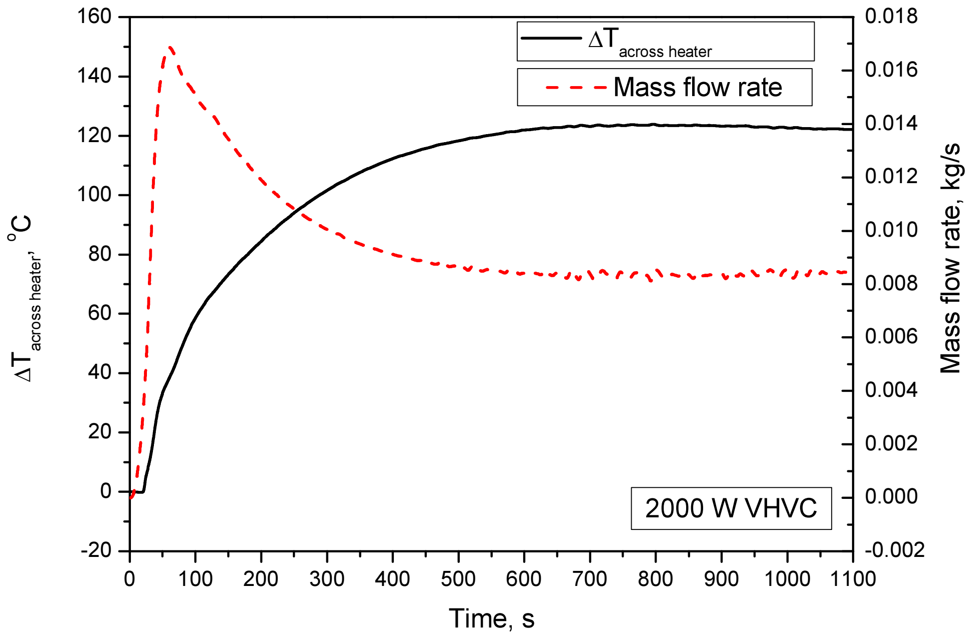

Figure 5.19: Transient variation of computed $\Delta T_{across\ heater}$ and mass flow rate in 2000 W VHVC configuration

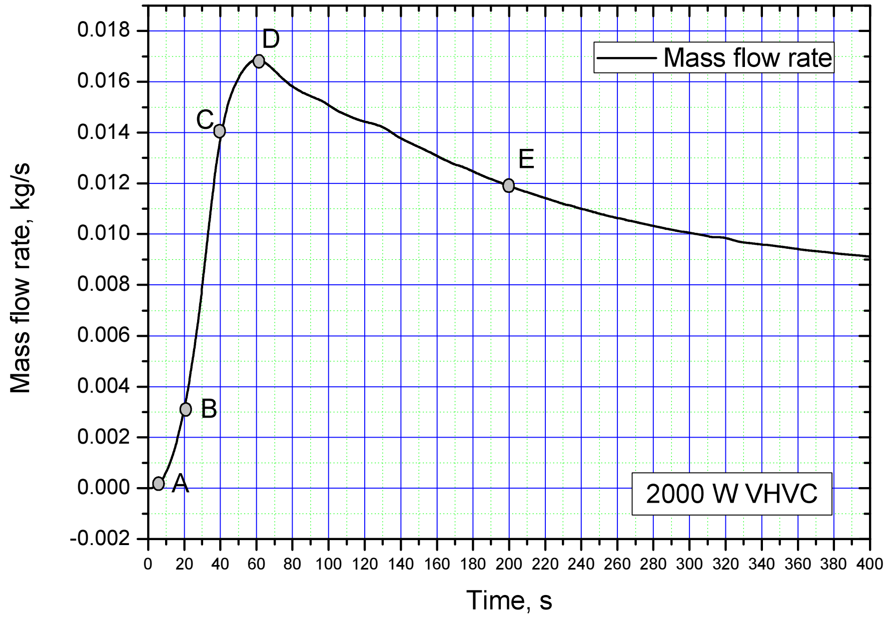

Figure 5.20: Computed transient variation of mass flow rate in 2000 W VHVC configuration

The transient variation of mass flow rate and $\Delta T_{across\ heater}$ can be understood by observing the temperature field at different times. During flow initiation transient, initially temperature in the whole loop is uniform, i.e flow is almost stagnant (shown in Fig. 5.21(A)). After heating starts, temperature in heater starts rising simultaneously inducing flow in the loop. After 20 seconds, a hot plug (hot fluid) of the size of the heater is formed in heater and it is shown by the corresponding temperature contour plot in Fig. 5.21(B). Due to small initial velocity, there is hardly any convection of energy outside of heater section. Hence, rest of the domain is still at initial temperature. The hot plug (hot pocket of fluid generated at heater) is slowly moving and extended its length outside of heater section also (shown in Fig. 5.21(C)). At 60 seconds as shown in Fig. 5.21(D), this hot plug is in between vertical heater and left top elbow. This shows that hot plug gets convected upwards due to local convection and upward buoyancy force. It was observed that maximum mass flow rate is obtained, when the hot plug is near to top left elbow. After this, hot plug enters horizontal top leg.

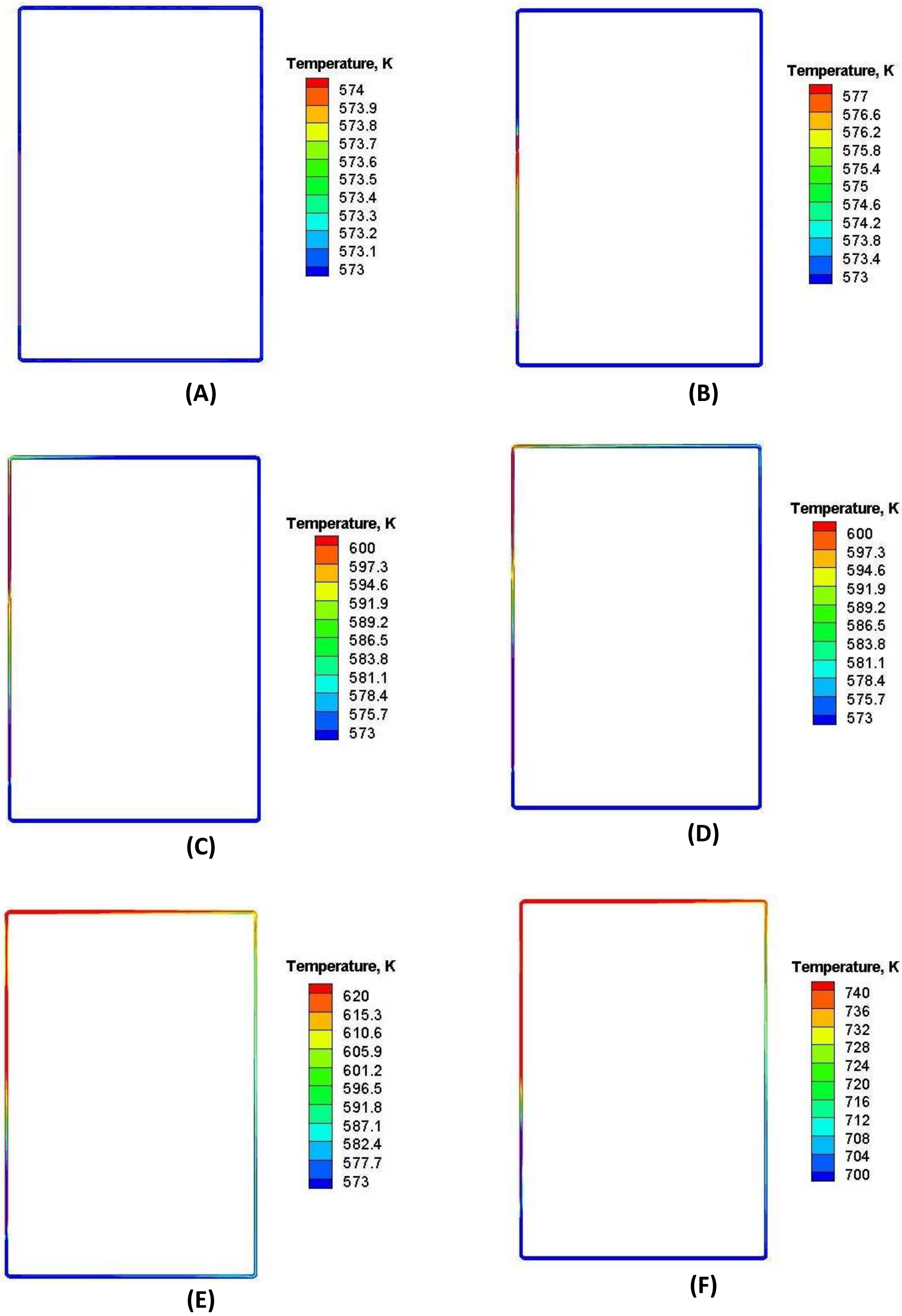

Figure 5.21: Temperature contours at different time instants in 2000 W VHVC configuration

The elbow offers large resistance. Also after the hot plug enters horizontal top leg, its contribution to buoyancy force reduces. Hence, after 60 seconds, there is flow retardation. At 200 seconds, as shown in Fig. 5.21(E), hot plug occupies larger part of the top leg. There is no gain in elevation head. After this, nearly steady state conditions are reached with net buoyancy force balancing the total resistance to the flow in the loop (shown in Fig. 5.21(F)).

Figure 5.22 shows the comparison of computed transient variation of mass flow rate for 1000 W and 2000 W heater power. It can be seen that, the steady state mass flow rate increases with increase in power. Vijayan et al., (2002) observed the same observation in the experimental study of rectangular natural circulation loop working with water.

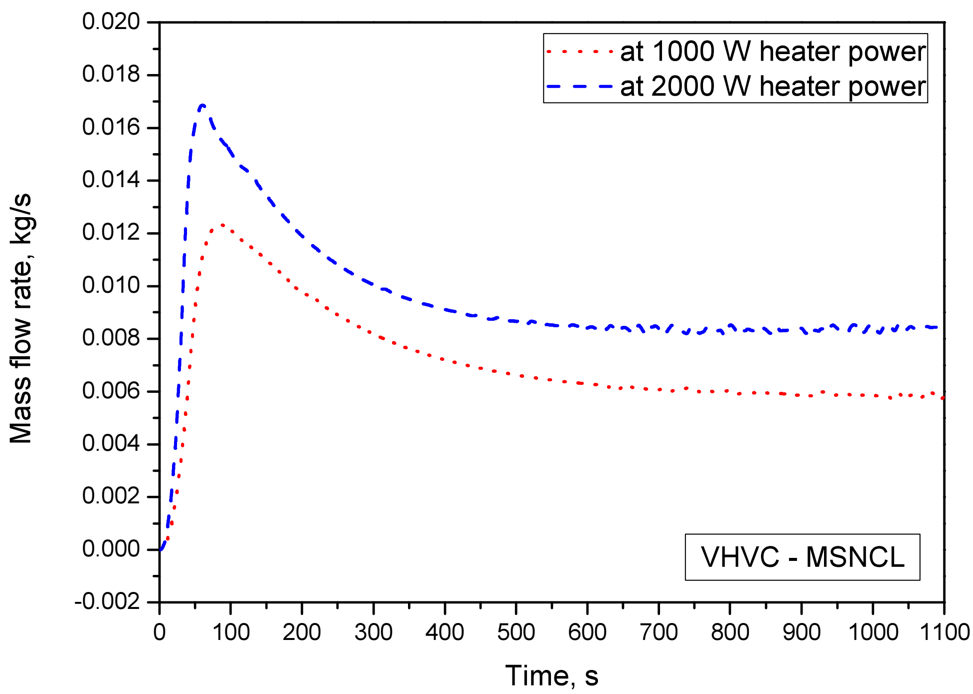

Figure 5.22: Comparison of computed transient variation of mass flow rate in VHVC configuration for different heater powers

5.5.3.1.2 VHHC configuration

The computed flow initiation transients for 1200 W and 2000 W heater powers for VHHC configuration are explained. The transient variation of mass flow rate and temperature difference across heater (ΔT) is shown in Fig. 5.23 and Fig. 5.24 for 1200 W and 2000 W heater powers respectively. From these figures, it was observed that, as soon as the heating starts the $\Delta T_{across\ heater}$ rises. Buoyancy force starts increasing and initiates the flow. However, due to this, the residence time for fluid in heater decreases. Hence, after some time, $\Delta T_{across\ heater}$ starts reducing. It reaches a minimum value. This reduced $\Delta T_{across\ heater}$ reduces buoyancy force. $\Delta T_{across\ heater}$ is minimum at 45 s. After this, mass flow rate reduces due to reduced buoyancy force. Again, due to reduced mass flow rate, residence time, $\Delta T_{across\ heater}$ and buoyancy force start rising and a second peak in $\Delta T_{across\ heater}$ is achieved at 80 s at which time mass flow rate shows minima. It can be seen that oscillations in $\Delta T_{across\ heater}$ and mass flow rate occur during the starting period but eventually die out.

The steady state temperature at 2000 W is 450^{o}C. But during flow initiation, the loop undergoes temperature oscillations. During such oscillations, the instantaneous temperature may breach 600^{o}C limit. Towards this consideration, the time variation of heater outlet temperature is studied. Figure 5.25 shows the time variation of heater outlet temperature. It can be seen that, the initial temperature is 300^{o}C and temperature achieves first peak but the peak temperature is 360^{o}C and afterwards the oscillation in temperature is not observed. The temperature slowly reaches 450^{o}C. Hence initial temperature oscillation does not breach 600^{o}C limit.

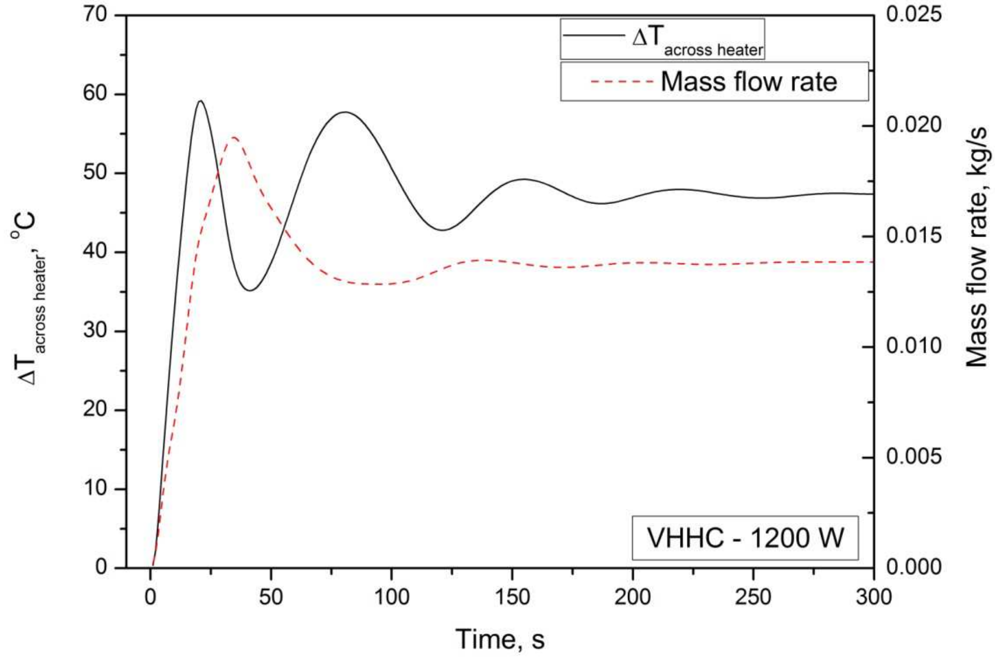

Figure 5.23: Computed flow initiation transient of 1200 W heater power VHHC configuration

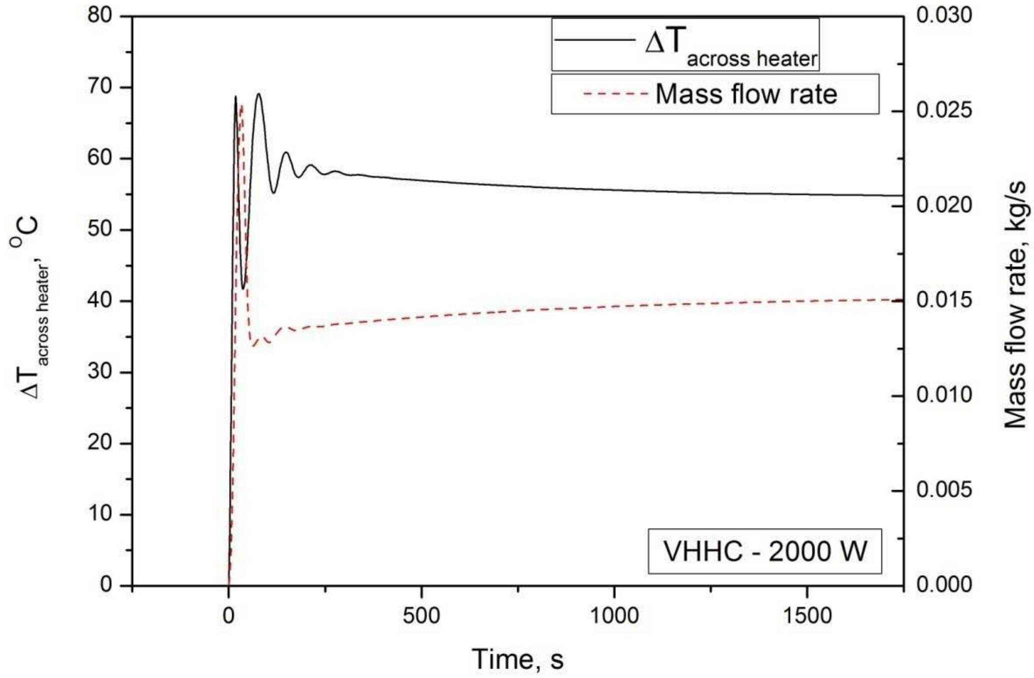

Figure 5.24: Computed transient variation of ΔT across heater and mass flow rate in 2000 W VHHC configuration

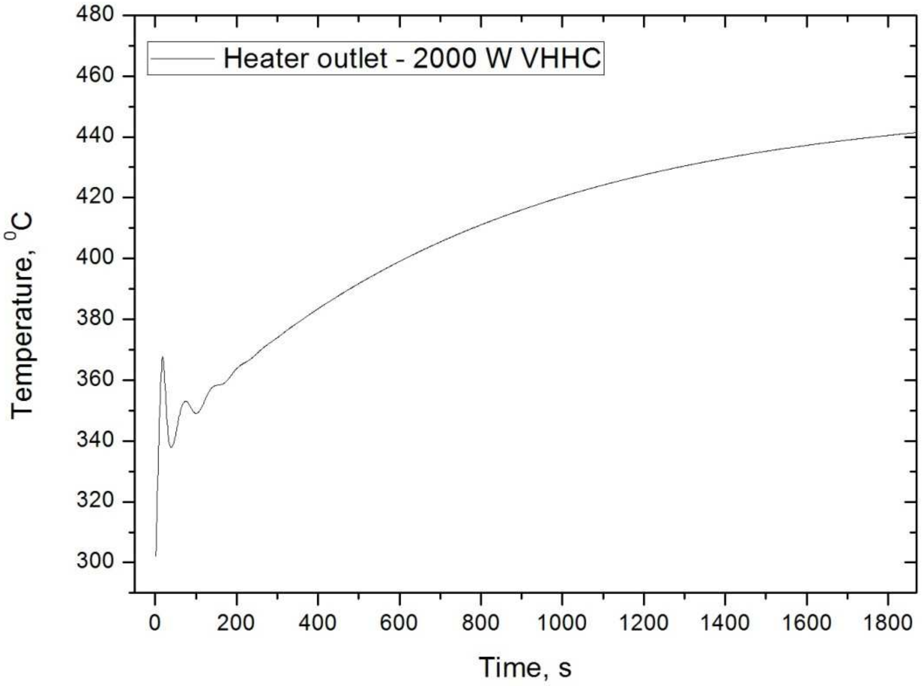

Figure 5.25: Computed transient variation of heater outlet temperature in 2000 W VHHC configuration

In the above flow initiation transients of VHHC configuration, initially formed oscillations get damped eventually. Thus this is a stable configuration. In this configuration, steady state mass flow rate is higher than VHVC, because, the elevation difference between cooler and heater is more for VHHC than that for VHVC.

5.5.3.1.3 HHVC configuration

Transient variation of computed $\Delta T_{across\ heater}$ and mass flow rate for 1000 W HHVC and 2000 W HHVC configurations have been shown in Fig. 5.26 and Fig. 5.27 respectively. In this configuration, flow started and continued in anti-clockwise direction.

Due to heater being horizontal, start of heating doesn't immediately lead to net mass flow rate in the loop. It takes 150 s to 200 s (depending on power) for initiation of flow. However, after that, there is sudden rise in mass flow rate. This leads to reduced residence time in heater. Hence $\Delta T_{across\ heater}$ reduces and buoyancy force reduces. This reduces mass flow rate. Hence at 250 s, a minima in mass flow rate is observed. After this, the flow as well as $\Delta T_{across\ heater}$ reach to constant values.

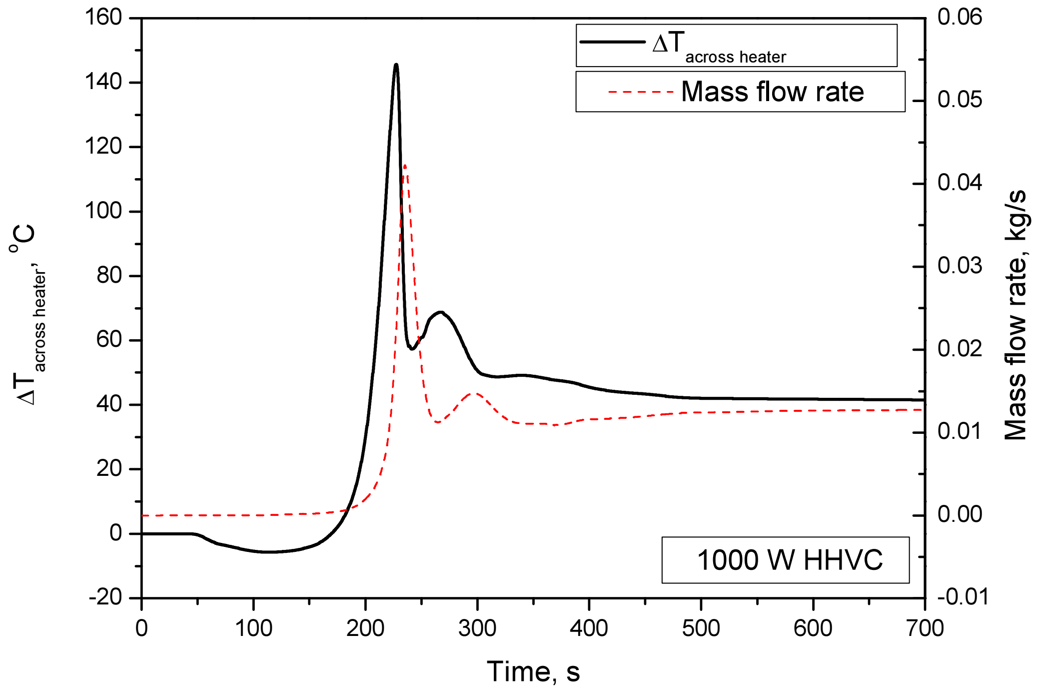

Figure 5.26: Transient variation of computed $\Delta T_{across\ heater}$ and mass flow rate in 1200 W HHVC configuration

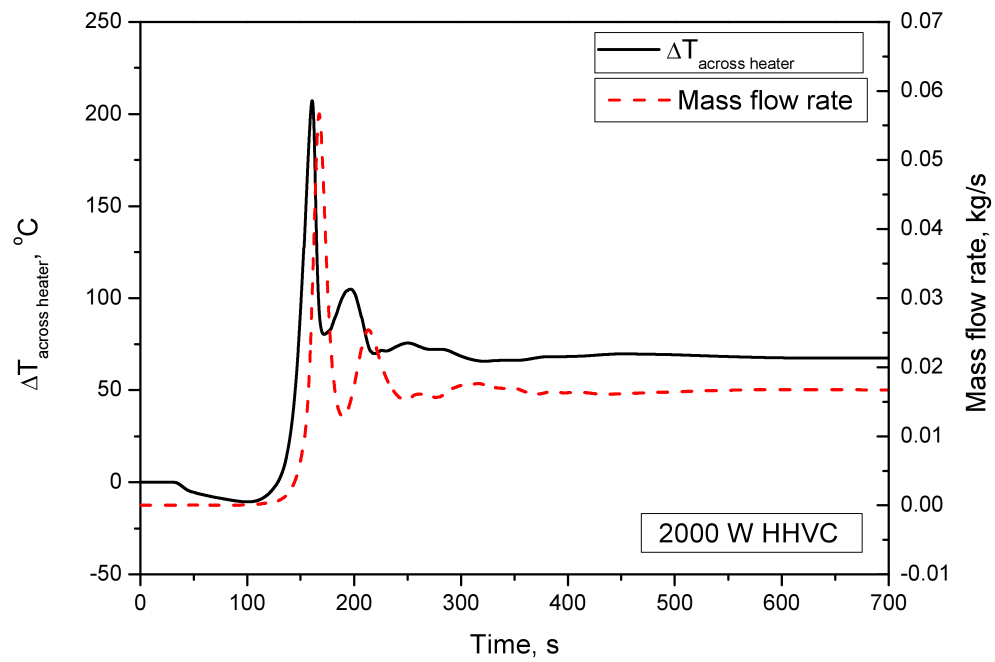

Figure 5.27: Transient variation of computed $\Delta T_{across\ heater}$ and mass flow rate in 2000 W HHVC configuration

The transient variation of mass flow rate and $\Delta T_{across\ heater}$ in HHVC has been studied using the temperature fields at different time instants. This has been explained with the help of transient variation of mass flow rate in 2000 W HHVC configuration during initial 500 seconds (shown in Fig. 5.28) and the corresponding temperature contours of the central vertical plane of MSNCL (shown in Fig. 5.29).

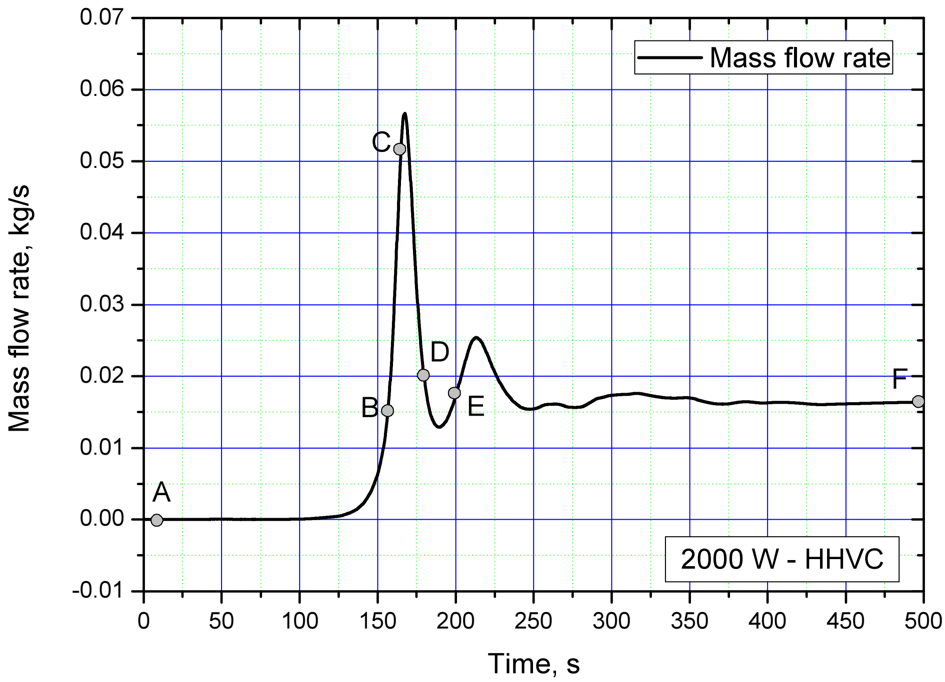

Figure 5.28: Computed transient variation of mass flow rate in 2000 W HHVC configuration

In this configuration, due to the horizontal heater, initial heating creates secondary flow motion in the heater (secondary flow motion is similar to that in NCL working with water which is explained in chapter 4 showing velocity vector and temperature contours in cross-sectional plane). This causes the turbulent natural convection in the horizontal heater along with the formation of hot plug in the heater. This hot plug, due to axial conduction expands in the horizontal bottom leg. Afterwards, this hot plug enters the right vertical leg. Then the flow becomes laminar axial flow. In this case, turbulent cross sectional flow gets converted into laminar axial flow. For NCL working with water, it was shown that for such kind of fluid flow problems low-Reynolds number k-ε turbulence model gives better results than laminar or high Reynolds number turbulence models. Hence the CFD simulation has been carried out using low-Reynolds number k-ε turbulence model. The mesh selected for the low-Reynolds number turbulence model is made very fine near the walls and so that y^+ is limited to 1.25. Fig. 5.29 shows the temperature contours in central vertical plane obtained at different time instants in transient simulation of HHVC configuration at heater power of 2000 W. Before starting the flow initiation transient, loop temperature has been initialized to 573 K. Fig. 5.29(A) shows the temperature contours in central vertical plane at time 5 seconds. It can be seen that the temperature of the primary fluid is almost near to 573 K. As the time marches, the hot plug (hot fluid of the size equals to heater) has been formed in the horizontal heater, while rest of loop is still filled with molten salt at 573 K. The hot plug becomes bigger and occupies bottom horizontal leg. At the same time, cooling of the molten salt (which is at 573 K) forms the cold plug in vertical cooler. Due to the temperature difference between the molten salt in the vertical cooler and the hot molten salt at bottom of the right vertical leg, buoyancy force gets generated. Hence the hot fluid will enter the right vertical leg and cold fluid in the cooler moves upwards, as shown in Fig. 5.29(B). After sometime, hot plug enters the vertical cooler. Now the right vertical leg is occupied with hot fluid as shown in Fig. 5.29 (C). Due to buoyancy, high mass flow rate is observed, corresponding to point C in Fig. 5.28. Then the hot fluid gets cooled in the vertical cooler and after that it enters the top horizontal leg. Due to the continuous cooling of hot fluid in the right vertical leg by vertical cooler, temperature in right vertical leg reduces. Hence the buoyancy force reduces which leads to decrease in mass flow rate. This is shown in Fig. 5.28 at the time instant corresponding to point D. The temperature contour at this time instant is shown in Fig. 5.29(D). During the same time the hot plug is going to form at bottom horizontal leg and at after some time it enters right vertical leg. Due to the entry of the hot plug in to the right vertical again raise in the mass flow rate has been observed due to the increase in buoyancy force. After that, as the time progresses the loop will attains steady state condition which is shown in Fig. 5.29(F).

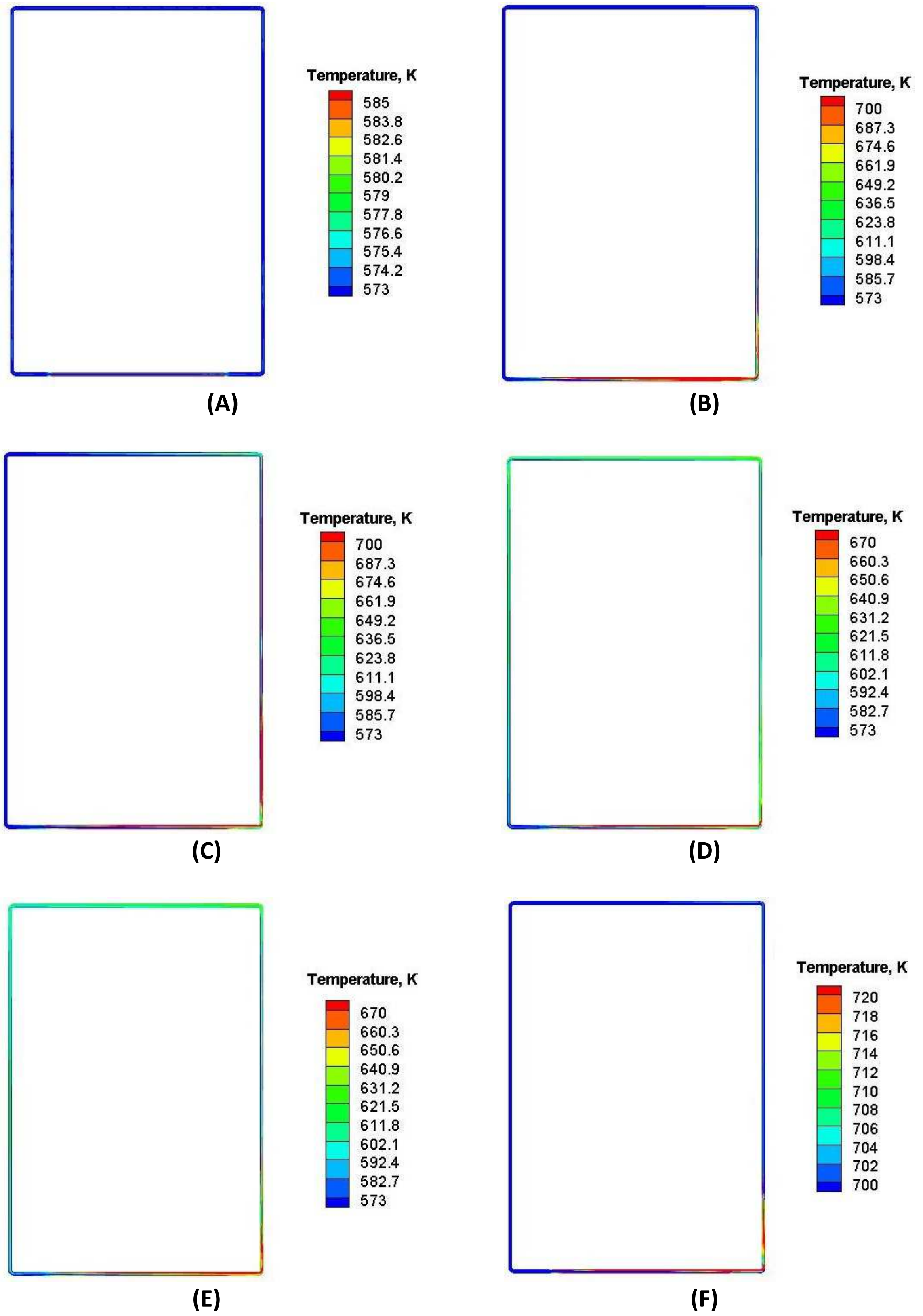

Figure 5.29: Temperature contours at different time instants in 2000 W HHVC configuration

Figure 5.30 shows the comparison of computed transient variation of mass flow rate for 1000 W and 2000 W heater power of HHVC configuration. It can be seen that, in this case also steady state mass flow rate increases with increase in power.

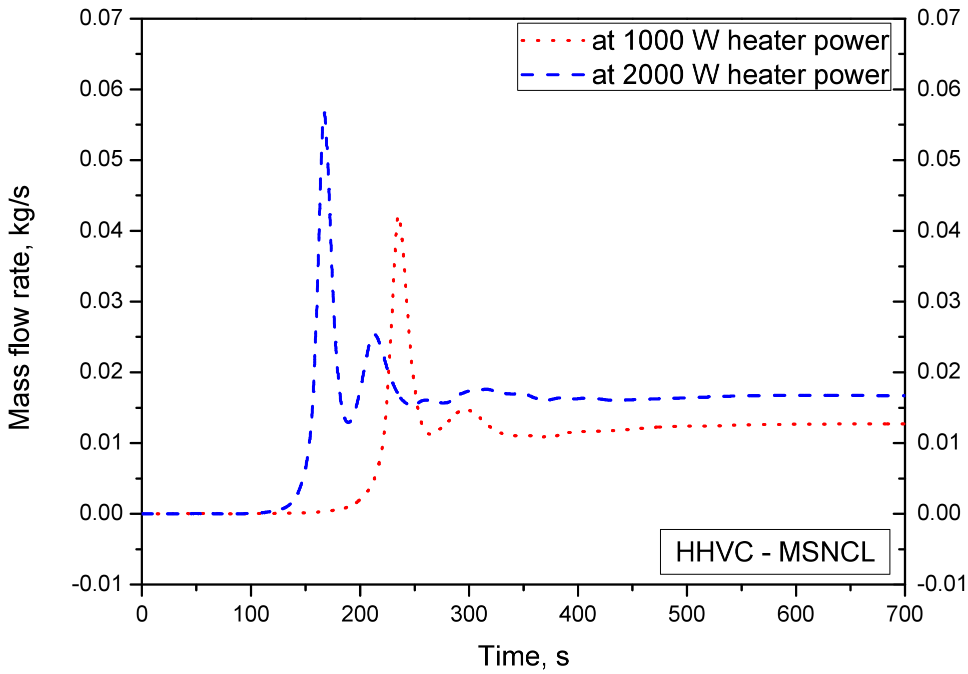

Figure 5.30: Comparison of computed transient variation of mass flow rate in HHVC configuration for different heater power

5.5.3.1.4 HHHC configuration

In this configuration also low-Reynolds number k-ε turbulence model is used to carry out CFD simulations. Figure 5.31 shows the computed transient variation of mass flow rate for 1000 W power. Unidirectional oscillations are observed. Figure 5.32 shows the transient variation of mass flow rate and temperature difference across heater for two cycles of oscillation. It can be seen from Fig. 5.32 that, as the temperature difference across heater ($\Delta T_{across\ heater}$) increases, the mass flow rate gets initiated and it increases as $\Delta T_{across\ heater}$ increases. The time lag between $\Delta T_{across\ heater}$ and mass flow rate has been observed which is due to the effect of working fluid inertia. Figure 5.33 shows the comparison of transient variation of mass flow rate and $\Delta T_{across\ heater}$ HHHC configuration at 1800 W power.

It can be seen that in HHHC configuration, at both powers, repeating oscillations get generated and flow does not reach steady state condition. For 1000 W as well as 1800 W heater powers, uni-directional oscillations were observed. The occurrences of uni-directional oscillations have been explained in the following sections.

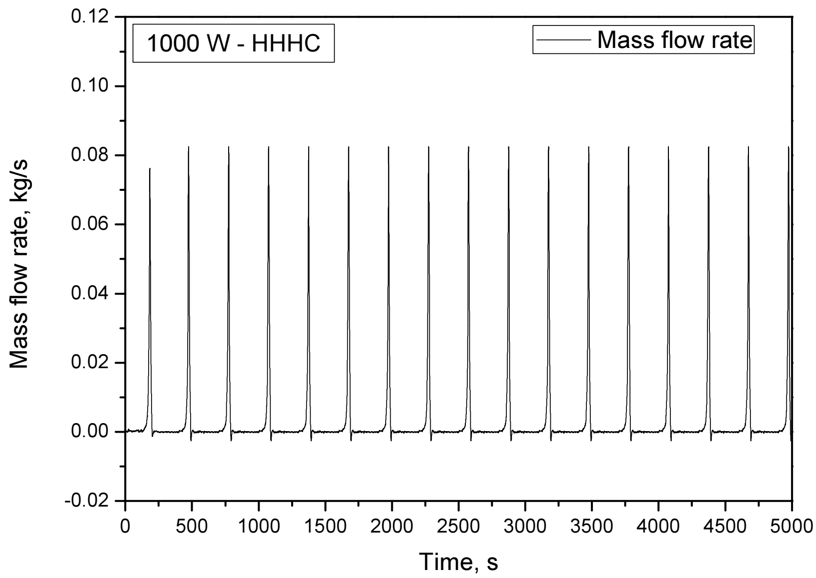

Figure 5.31: Computed transient variation of mass flow rate in 1000 W HHHC configuration

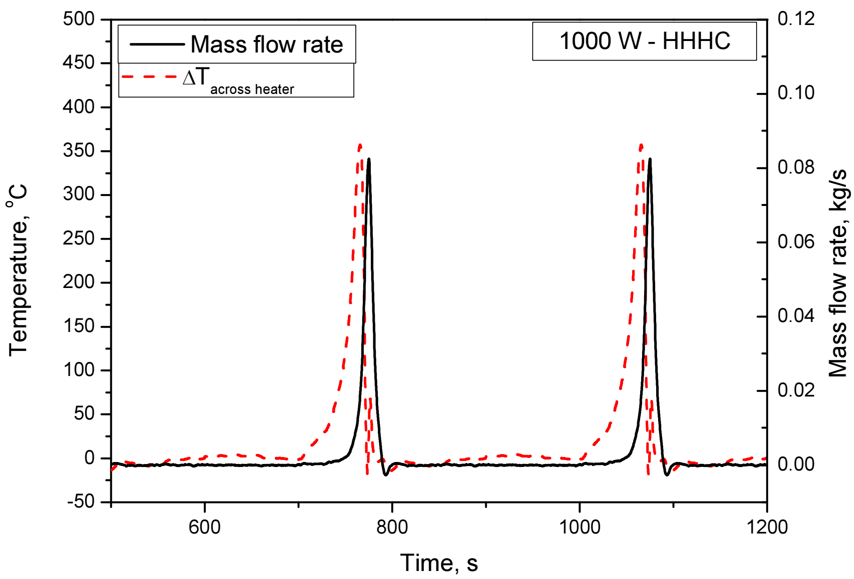

Figure 5.32: Comparison of computed transient variation of $\Delta T_{across\ heater}$ with mass flow rate in 1000 W HHHC configuration

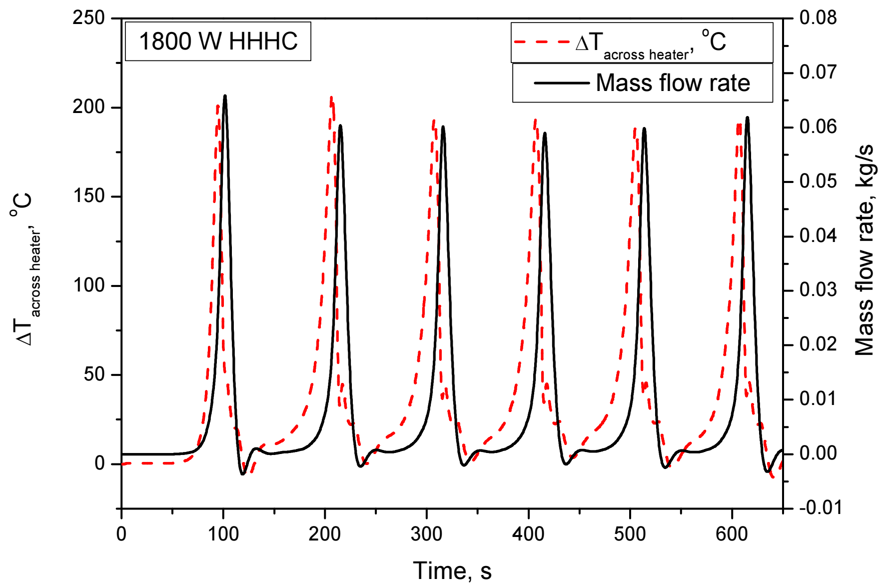

Figure 5.33: Comparison of computed transient variation of $\Delta T_{across\ heater}$ with mass flow rate in 1800 W HHHC configuration

5.5.3.1.4.1 <u>Flow pattern at 1000 W HHHC configuration</u>

In HHHC case, the computed transient variation of mass flow rate and $\Delta T_{across\ heater}$ for 1000 W heater power has been shown in Fig. 3.31. Unlike other configurations of MSNCL, a steady state is not obtained even for such a low power. It is observed that, both mass flow rate and $\Delta T_{across\ heater}$ undergo a cycle and a periodic oscillating flow is obtained. The enlarged portion of transient variation of mass flow rate in 1000 W HHHC configuration from 0 s to 400 s is shown in Fig. 5.34. The instability in HHHC configuration has been explained by various states of temperature fields, which are identified by its points from 1 to 6 in the Fig. 5.34. The reason for such a pattern is now explained with the help of temperature fields captured at different instants of time.

During the flow initiation transients, once the heater is switched on, heat is transferred from the heater to the fluid in the loop. Initially flow is almost stagnant. But due to heating, at first, flow in cross-sectional plane gets established. Due to surface heating, the fluid near surface rises and it comes down to the centre. So the heat transfer from heater to fluid will be through conduction as well as natural convection. Due to continuous heating all along heater surface, hot plug (pocket of hot fluid) is formed in the heater section and rest of the fluid in the loop (except at cooler) will be at the normal liquid state (at 573 K, fluid initial temperature). This hot plug diffuses axially on both sides of heater. Finally it covers the entire bottom horizontal leg as shown in Fig. 5.35(A). After that, the hot plug will try to move into the one of the vertical legs. At the same time, due to continuous cooling, cold plug (pocket of cold fluid) is formed at the cooler. After this, entry of the hot plug into right vertical leg takes place as shown in Fig. 5.35(B). Simultaneously, cold plug is entering left vertical leg from top. After this, hot plug rises through the right vertical leg and cold plug decelerates through left vertical leg. The flow accelerates during this phase. The maximum flow rate is observed, when the entire hot plug is in the right vertical leg (which is much longer than the hot plug length) and the entire cold plug is in the left vertical leg. This is shown Fig. 5.35(C). As the head of the hot plug enters the top horizontal section, the buoyancy force no more increases and due to wall friction/elbow resistance, the flow tends to decelerate (Fig. 5.35(D)). Entry of cold plug into bottom horizontal leg also affects flow retardation. However, due to flow inertia, hot and cold plugs travel fast through cooler and heater sections respectively. Although, the hot plug passes through the cooler, it does not get sufficiently cooled due to the high velocity while passing through the cooler. The hot and cold plugs enter into left and right vertical legs respectively, as shown in Fig. 5.35(E). Hot plug descends along the left vertical leg in rapidly decelerating flow conditions. The deceleration is due to presence of cold fluid in left vertical leg below hot plug and also due to continuous frictional resistance offered by wall and left top elbow. This continues till the buoyancy force contribution of the right vertical leg is slightly more than that of the left vertical leg leading to small reverse flow. During the reverse flow (very short duration), the hot plug in the left vertical leg returns back to the cooler. Cold plug returns to heater section.

Again the flow becomes forward flow i.e. anti-clockwise direction but flow rate is very small. During this time, hot fluid in the top horizontal pipe gets cooled and becomes a cold plug (cold pocket). At the same time cold fluid in the bottom horizontal pipe gets heated and becomes a hot plug (hot pocket). This is shown in Fig. 5.35(F). Subsequently, next hot plug is formed and it enters right vertical leg again due to small forward flow existing in the loop and whole cycle gets repeated leading to uni-directional oscillatory flow.

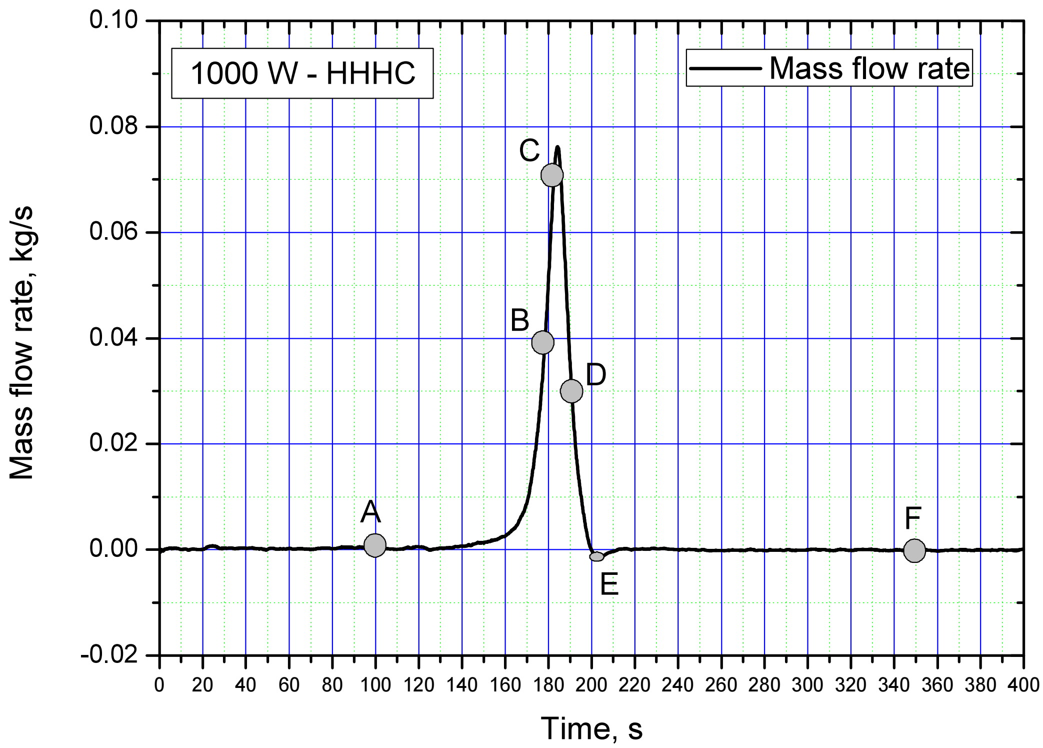

Figure 5.34: Enlarged portion of transient variation of mass flow rate in 1000 W HHHC configuration

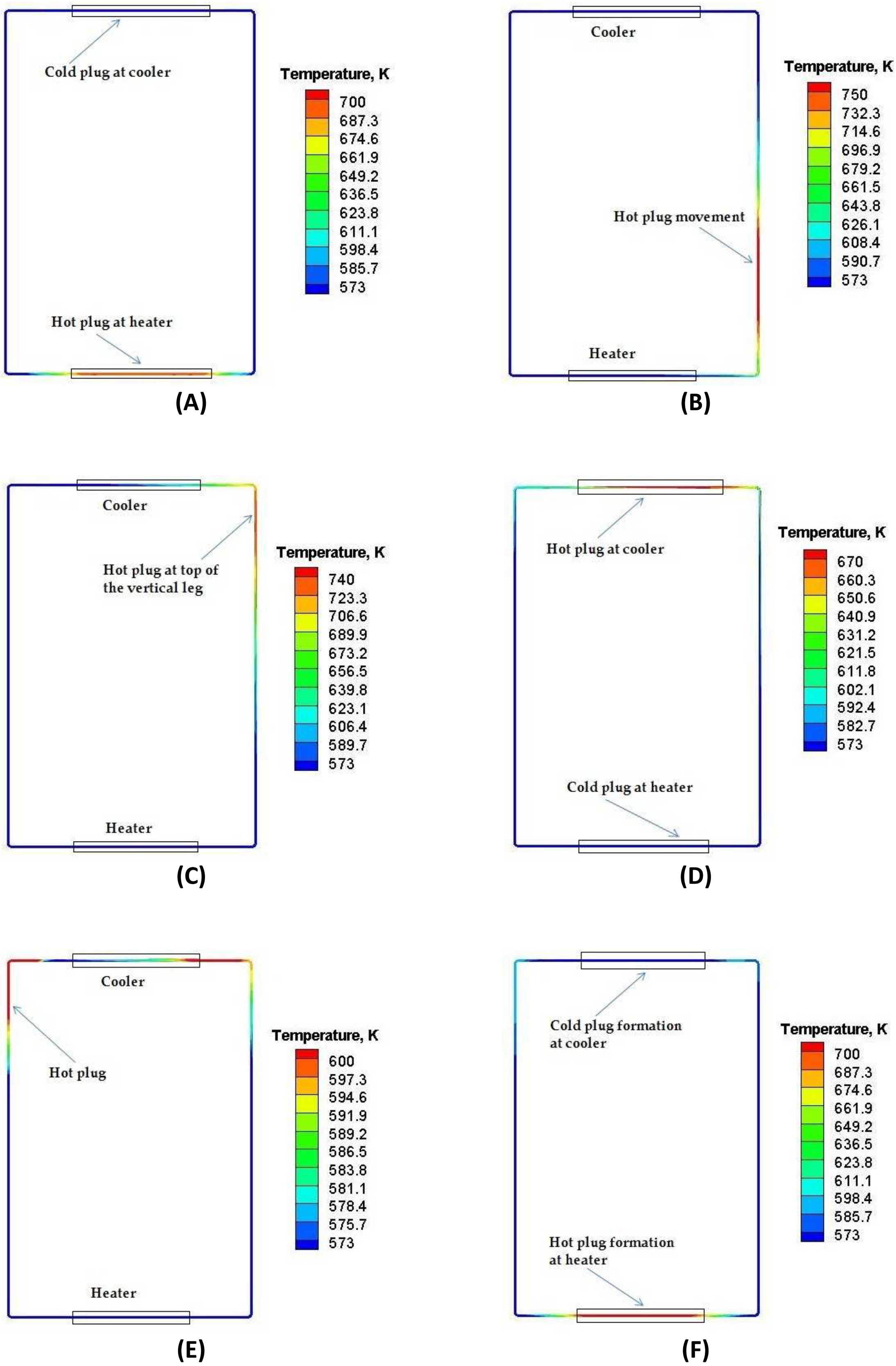

Figure 5.35: Temperature contours of central vertical plane of 1000 W HHHC configuration at different time instants

5.5.3.2 Power Raising from Steady State (PRSS) transients

The experimental study of power rise from steady state at low power to higher power for VHHC configuration was carried out. The same transient is computed using CFD. In experimental facility, the steady state at a lower power is first obtained. Then the power is raised to higher level and the same is maintained till new steady state is achieved. In CFD same procedure is followed. The results of PRSS transient, by CFD and experiment, are shown in Fig. 5.36 to Fig. 5.39. Figure 5.36 shows the variation of temperature at heater inlet (HI), heater outlet (HO), cooler inlet (CI) and cooler outlet (CO) by experimental data as well as CFD predictions for PRSS transient from 1200 W to 1500 W. Similarly, Fig. 5.37 to Fig. 5.39 show the comparison of experimental data with computational data for PRSS transients from 1500 W to 1600 W, 1600 W to 1700 W and 1800 W to 2000 W respectively. In all the cases, CFD simulation predicts the experimental data very well. It can be seen that, in this case, the power rise is given to a fluid which is already circulating in the loop. Hence, unlike previous case in which power was given to a stagnant fluid, in this case, there are no major oscillations in flow or temperature at any location and there is smooth transition from old steady state to new steady state.

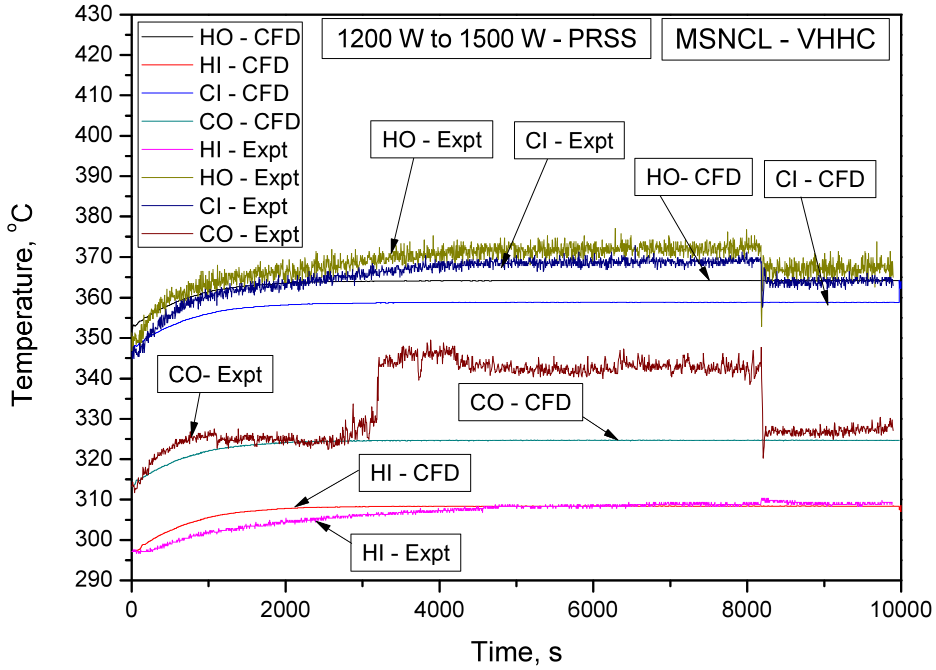

Figure 5.36: Comparison of experimental and computational data of PRSS transient in VHHC configuration at 1200 W to 1500 W

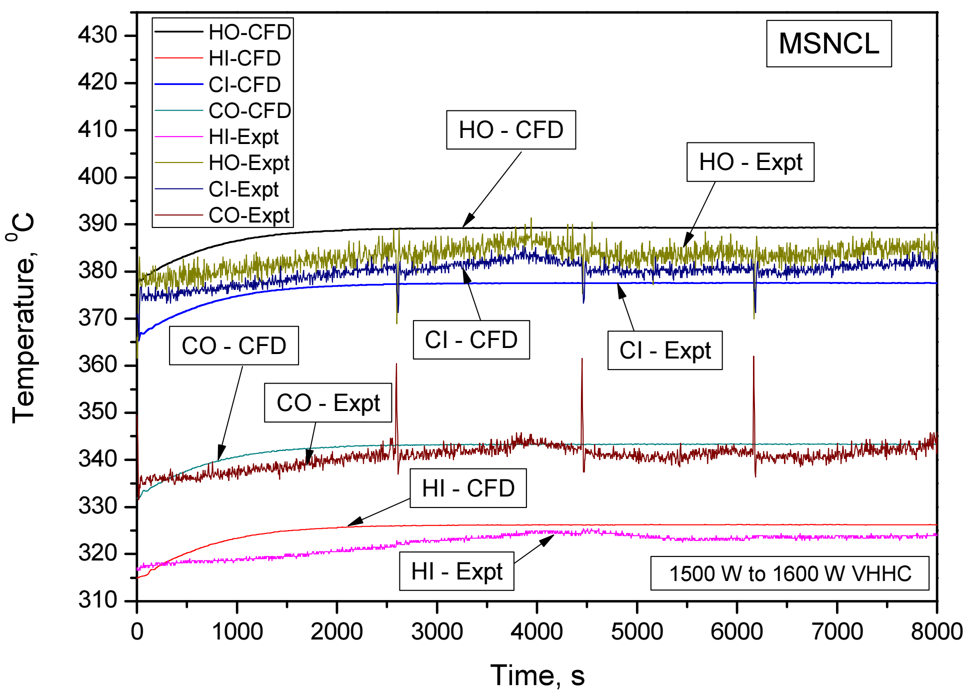

Figure 5.37: Comparison of experimental and computational data of PRSS transient in VHHC configuration at 1500 W to 1600 W

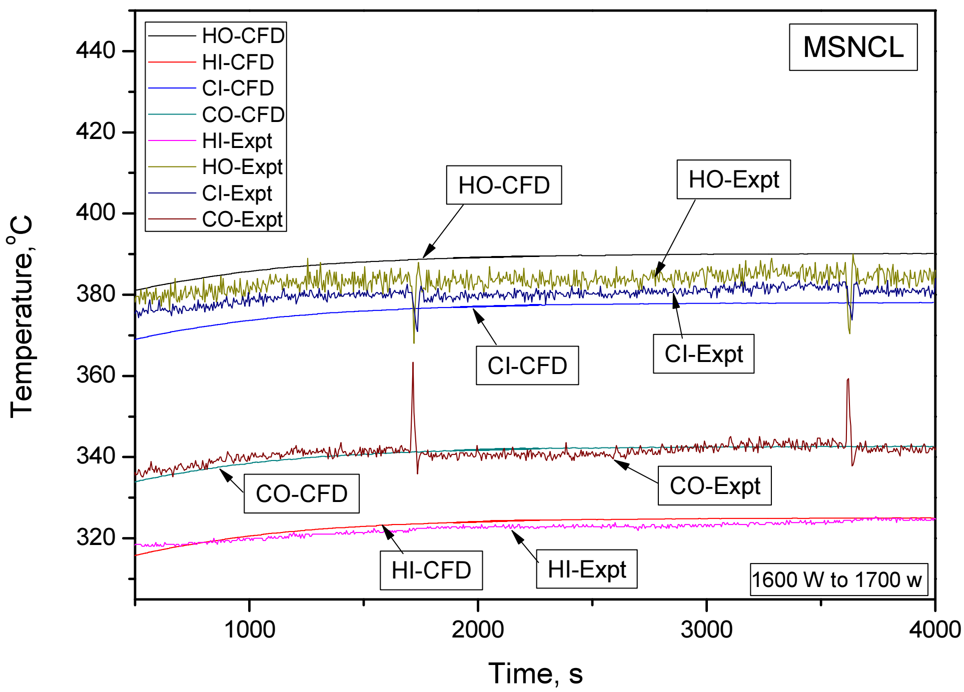

Figure 5.38: Comparison of experimental and computational data of PRSS transient in VHHC configuration at 1600 W to 1700 W

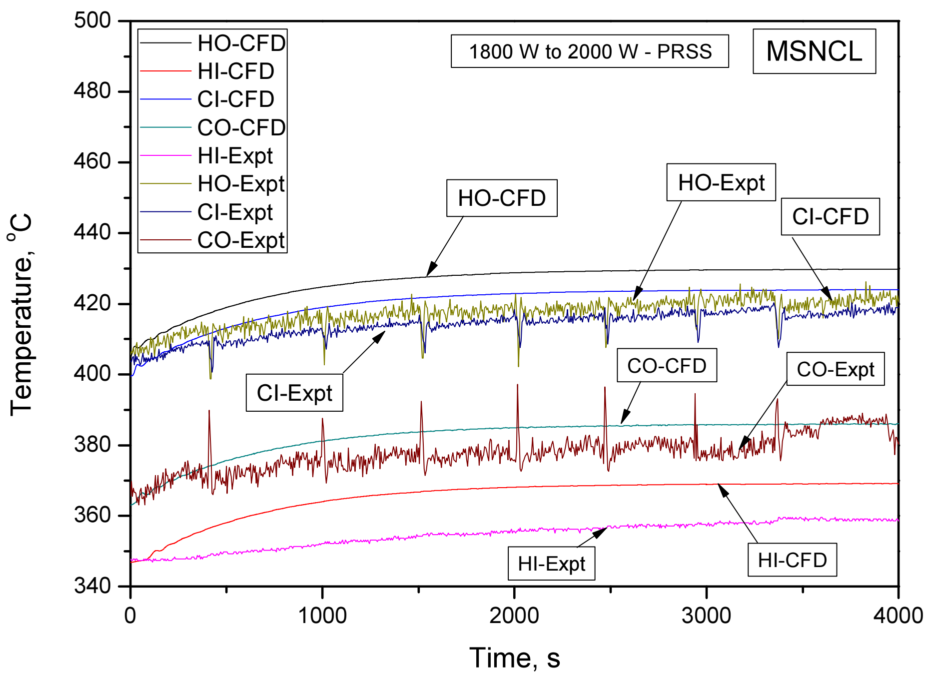

Figure 5.39: Comparison of experimental and computational data of PRSS transients in VHHC configuration at 1800 W to 2000 W

5.5.3.3 Power step back transients

In experimental study, the loop is allowed to achieve steady state at a specific power level and then the power was suddenly reduced to a lower level and loop behaviour was observed. This procedure is known as power step back transience. The transient analysis using CFD for this case is also done. Here, in this section, the comparison of transient variation of temperature by experimental procedure and also by CFD is discussed. Figure 5.40 shows the comparison for power step back from 2000 W heater power to 1800 W heater power. The effect of this power change is shown in terms of change in temperature at different locations of the loop. It is observed that, the experimental temperature is *slightly* higher than computational result at different locations. In experimental facility, expansion tank stores some amount of high temperature fluid which transfers its heat to loop fluid after power step back. The expansion tank is not modelled in simulation. Hence, experimental temperature data is somewhat higher than computed data. The effect of decrease in heater power from 1800 W to 1600 W is shown in Fig. 5.41 in terms of change in temperature at different locations of the loop. Similarly Fig. 5.42 shows the effect of power step back from 1600 W to 1400 W. Figure 5.40 to Fig. 5.42 shows that the sudden power step-back, by 200 W, does not induce any kind of instability.

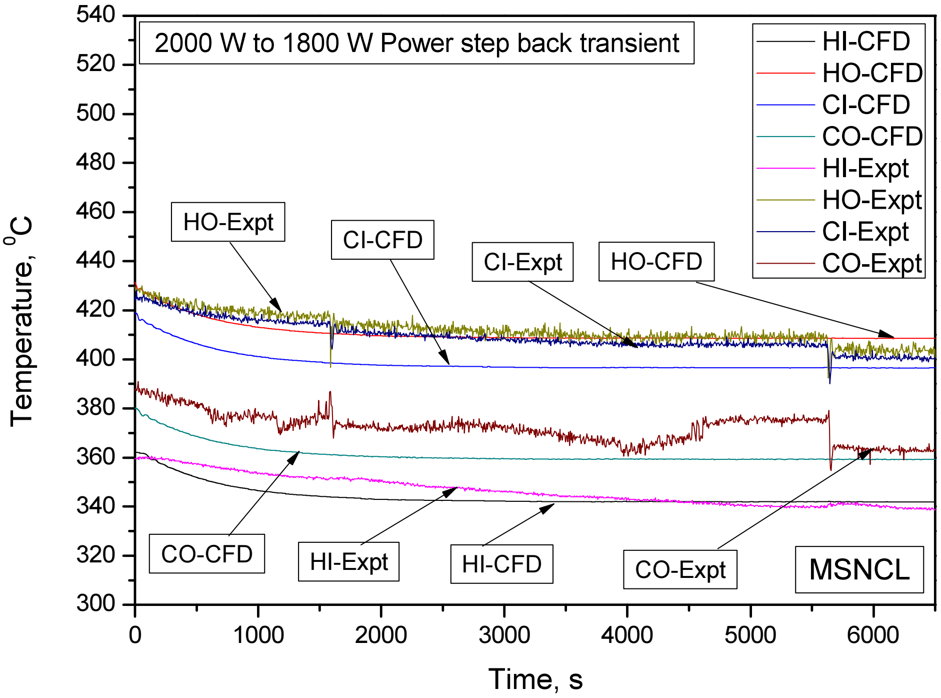

Figure 5.40: Power step back transient: 2000 W to 1800 W in VHHC configuration

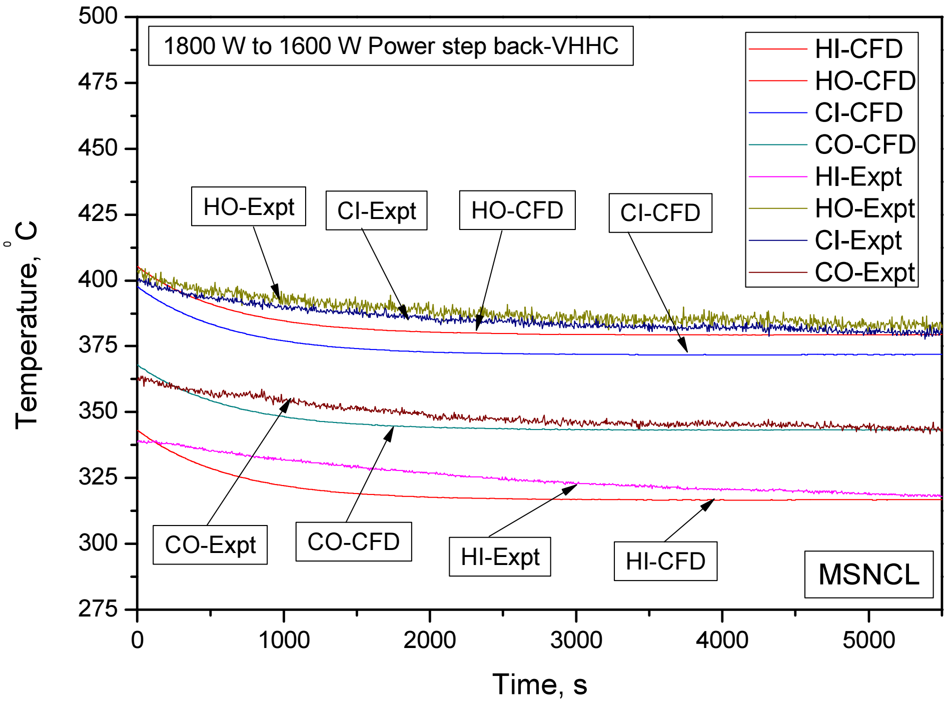

Figure 5.41: Comparison of Power step back transient: 1800 W to 1600 W in VHHC configuration

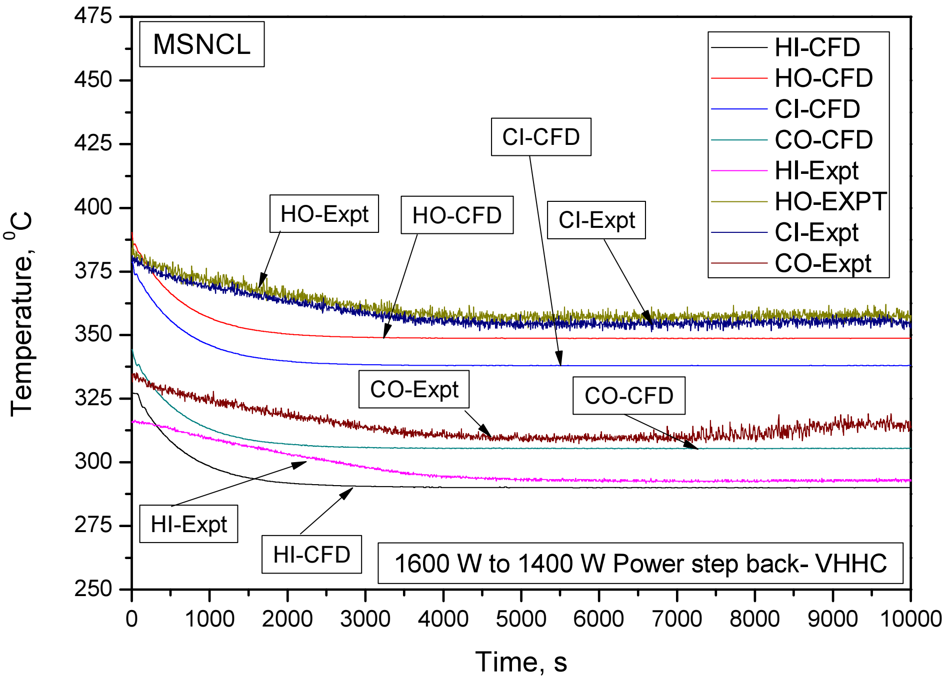

Figure 5.42: Comparison of Power step back transient: 1600 W to 1400 W in VHHC configuration

5.5.3.4 Power trip transients

Power trip transients are helpful to know the thermal-hydraulic behaviour of molten salt during sudden power trip. Such power trip may occur in nuclear reactors when, due to some abnormal occurrence the reactor is scrammed to shut-down. Further, molten salt are used as heat carrying fluid in solar power plants (Kurvi et al., 2013), wherein the molten salt gets heated by concentrating solar rays in solar receiver. During night and cloudy weather, the solar heating is not available. In that scenario, the consequence of sudden non-availability of heat source is simulated using heater trip transient.

Power trip was initiated after steady state condition of MSNCL corresponding to 2000 W heater power by setting the heater power to zero value. Figure 5.43 shows the comparison of computed transient variation of temperature at heater outlet and cooler inlet with corresponding experimental data. It can be seen that, the CFD model originally didn't include expansion tank in the computational domain. The CFD result was significantly deviating from experimental data. Hence CFD model including expansion tank was developed and simulations performed with the same for this case. It is seen from Fig. 5.43 that, there is significant improvement in the computed result and it is matching well with the experimental data.

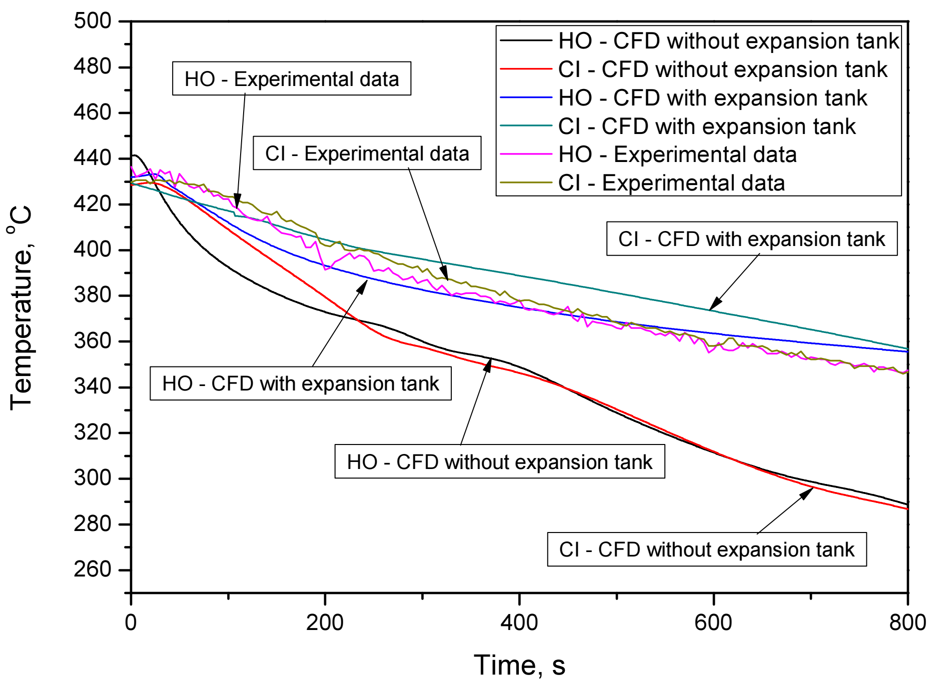

Figure 5.43: Transient variation of temperature at heater outlet and cooler inlet during power trip transient; Comparison of experimental data with CFD models (with and without expansion tank)

Expansion tank is an important component of single-phase natural circulation loops. Expansion tank serves the twin purpose of venting the air out during the loop filling and accommodation of the swells and shrinkage of the loop fluid during the transient. Wacholder et al. (1982) carried out the experimental investigations on the role of expansion tank (referred as pressurizer by them) on flow behaviour in toroidal loop. However, only mass and momentum exchange between the loop and expansion tank were considered. It was assumed that the tank (pressurizer) is connected to the main loop laterally and has negligible effect on the thermal response of the system. Later, Misale et al. (1999) reported for the first time that contrary to the assumption made by Wacholder et al. (1982), significant energy exchange takes place between the main loop and expansion tank. In order to realize the expansion tank, Misale et al. (1999) connected the tank and the primary loop with two pipes. Apparently, this was done to allow some natural convection between tank and the main loop. In their experimental investigations, they noted that the loop dynamics were significantly affected by the expansion tank dynamics. Recently, Naveen Kumar et al. (2015) carried out experimental investigation to understand the role of expansion tank in the loop dynamics of rectangular natural circulation loop. They also modified their 1D-model with the consideration of energy exchange by natural convection between the main loop fluid and expansion tank fluid. Numerical simulations carried out by them show that the expansion tank plays a very complex role in natural circulation loop dynamics.

In the MSNCL, expansion tank is situated between the horizontal cooler and vertical cooler, at the right top most corner. In VHHC configuration, it is after cooler outlet. Earlier the studies on MSNCL, during power raising from steady state and power step back transients, were reported. In those studies, the power variation is only 200 W. The energy transfer between main loop and expansion tank is very small, hence the computational simulations without considering the expansion tank are able to predict the loop behaviour.

In power trip transients, the stored hot fluid in the expansion tank plays a significant role to change the temperature of various locations of the loop. Significant amount of heat energy stored in the expansion tank during at steady state of loop gets transferred to the fluid flowing through the loop. The computed results by the CFD model with expansion tank are matching well with experimental data. Hence it is important to consider the effect of expansion tank in power trip transient and include the same in computational model.

Figure 5.44 shows the temperature contour at central vertical plane (X-Z plane) of the loop at steady state condition corresponding to 2000 W heater power (before starting the heater trip transient). Figure 5.45 shows the transient variation of temperature at heater outlet, heater inlet, cooler outlet and cooler inlet locations. It can be seen that the computational results show good match with experimental data. Before heater trip, the steady state temperature at heater outlet was more than the temperature at cooler inlet. After the heater trip, initially the temperature at heater outlet is more than that at the cooler inlet. This is because the fluid between heater outlet and cooler inlet is already heated to a temperature more than that in cooler inlet at the time of heater trip. But since heater is switched off while cooler is ON, hence the heater outlet temperature (T_{HO}) rapidly reduces and after some time, it becomes lesser than even cooler inlet temperature. This is because, in cooler, fluid loses heat and hence temperature at cooler outlet (T_{CO}) is less than temperature at cooler inlet (T_{CI}). The fluid exiting from cooler, after further losing heat in piping from cooler outlet to heater inlet, enters heater and in this case heater is switched off. Hence $T_{HO} < T_{CI}$ for a lot of time. Due to continuous cooling and circulation of coolant, whole loop fluid gets cooled and temperature gradient in loop keeps reducing. The loop fluid temperature homogenization takes place with time and hence difference between T_{HO} and T_{CI} keeps reducing. This leads to reduced mass flow rate also. In this particular case, it was found that, it is important to include expansion tank in the model without which computational result was deviating from experimental data by a large margin.

Both computational and experimental results show the same heater/cooler inlet/outlet temperatures by the end of power trip transient. In experiment, the heater outlet temperature was reduced from 431^{o}C to 330^{o}C in the span of 1000 s. At the same time the cooler outlet temperature reduced from 395^{o}C to 300^{o}C. To avoid the solidification of the molten salt in the MSNCL, the heater was started at this instant.

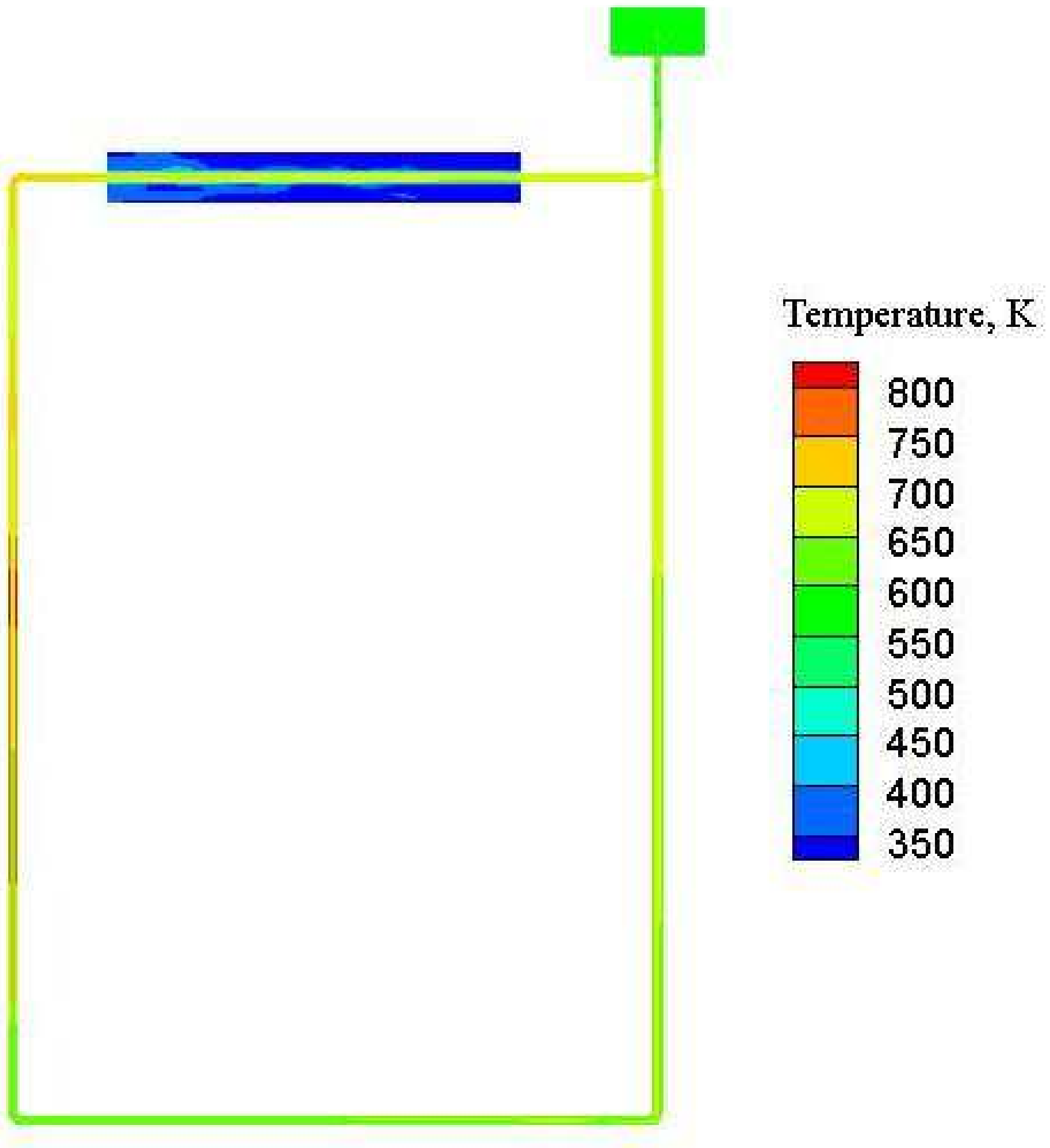

Figure 5.44: Temperature contour at the steady state condition of 2000 W VHHC configuration

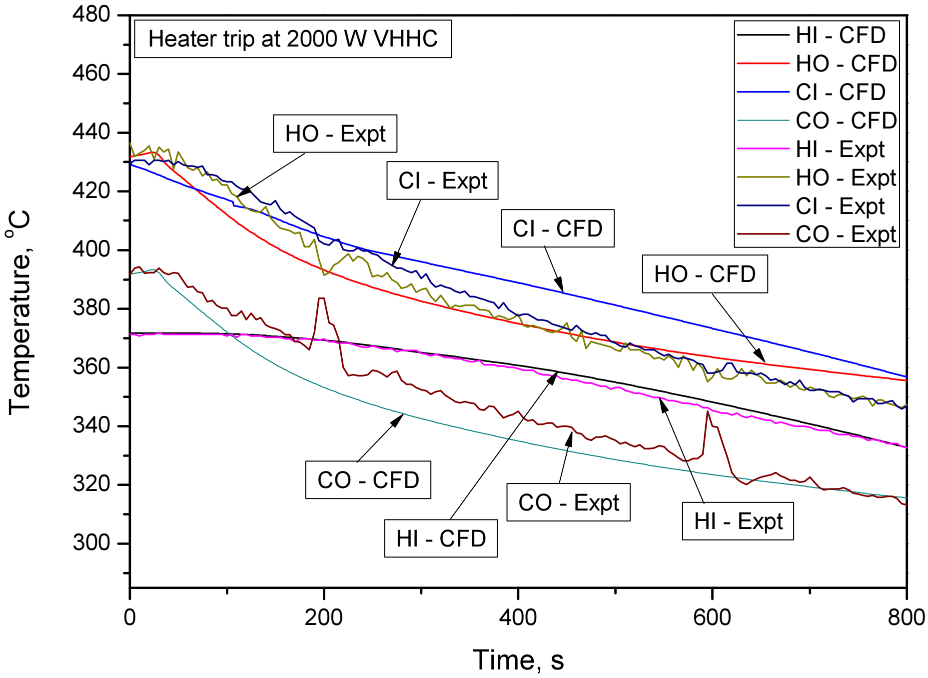

Figure 5.45: Comparison of computed transient variation of temperature at different locations with experimental data during the power trip of 2000 W VHHC configuration

5.5.3.5 Loss of heat sink transients

The loss of heat sink is considered in the safety analysis of reactors. Nuclear reactors continue to generate heat even after shutdown due to radioactive decay of fission products. This decay heat is large enough to cause fuel overheating and subsequent melting in case of Complete Loss Of Power (CLOP) as exemplified by the Fukushima plant which experienced long term loss of coolant activity following a massive earthquake and resultant tsunami. The transient variation of temperature during such conditions can be studied using loss of heat sink transient studies in NCL. In this study, the cooler duct is removed from the NCL. The transient variation of temperature at various locations of the loop has been observed. This experiment was carried out at 1200 W and 1500 W heater powers. In the loss of heat sink transient study at 1500 W heater power, the loop was started and steady state was established. After achieving steady state, secondary flow in the cooler duct (i.e. air flow) was stopped completely at time t=12700 s in experimental study. In CFD simulation, similar procedure was used.

Figure 5.46 and Fig. 5.47 shows the comparison of computational data with experimental data of temperature at different locations of the loop at loss of heat sink transient study at 1200 W and 1500 W heater power respectively. The computational results show good match with experimental data. Figure 5.48 shows the computed transient variation of mass flow rate, T_{max}, T_{min} and T_{avg} in the loop during Loss of heat sink transient. It can be seen that, after the loss of heat sink, there is increase in the loop minimum and maximum temperatures. This causes an overall increase in the loop average temperature, which is justified as heat is getting deposited in a constant mass of fluid without getting rejected anywhere else. Mass flow rate in the system reduces within 400 seconds and then remains constant for a long time.

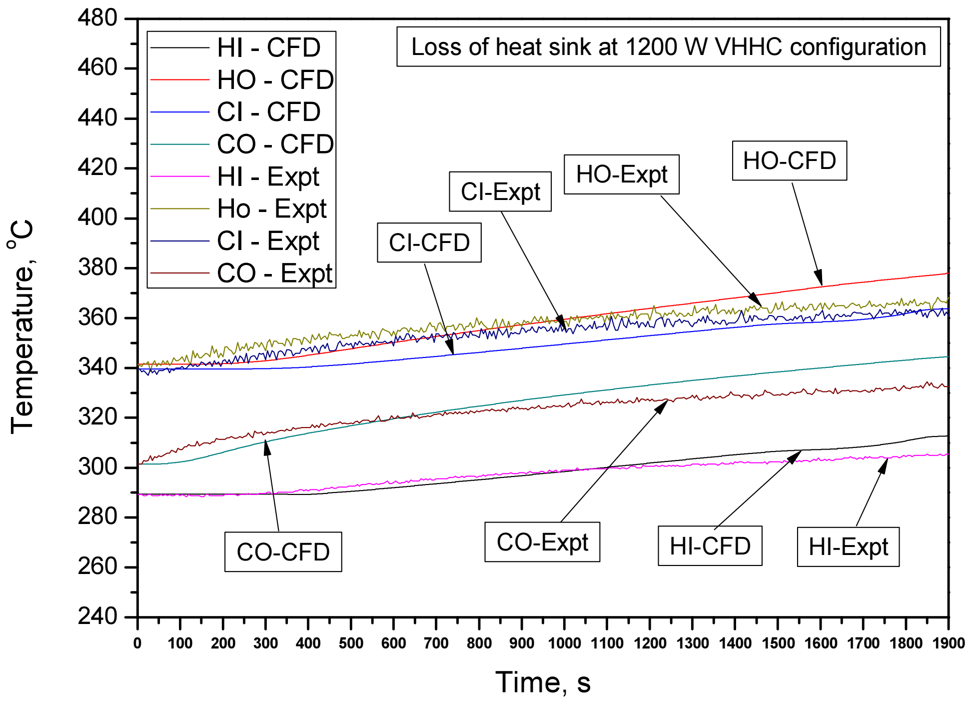

Figure 5.46: Comparison of predicted computational data with experimental data in the transient study of loss of heat sink at 1200 W heater power VHHC configuration

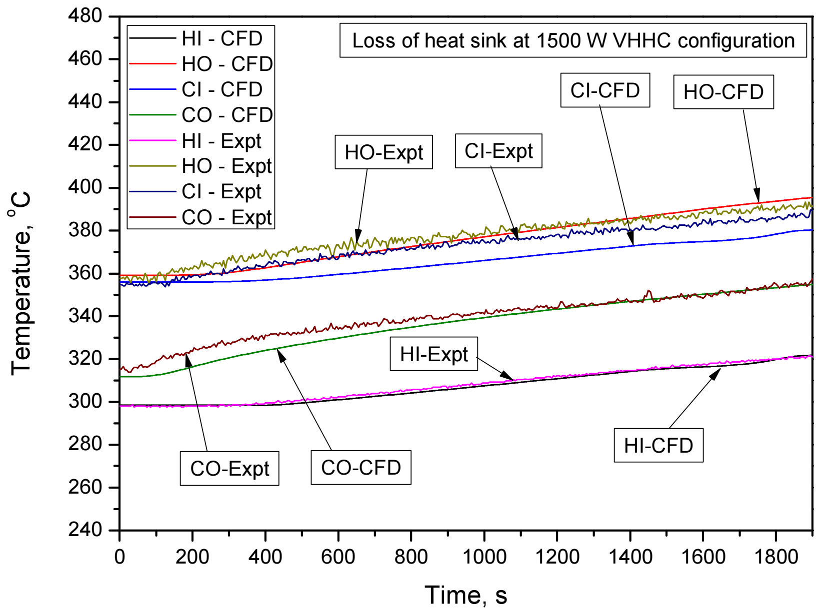

Figure 5.47: Comparison of predicted computational data with experimental data in the transient study of loss of heat sink at 1500 W heater power VHHC configuration

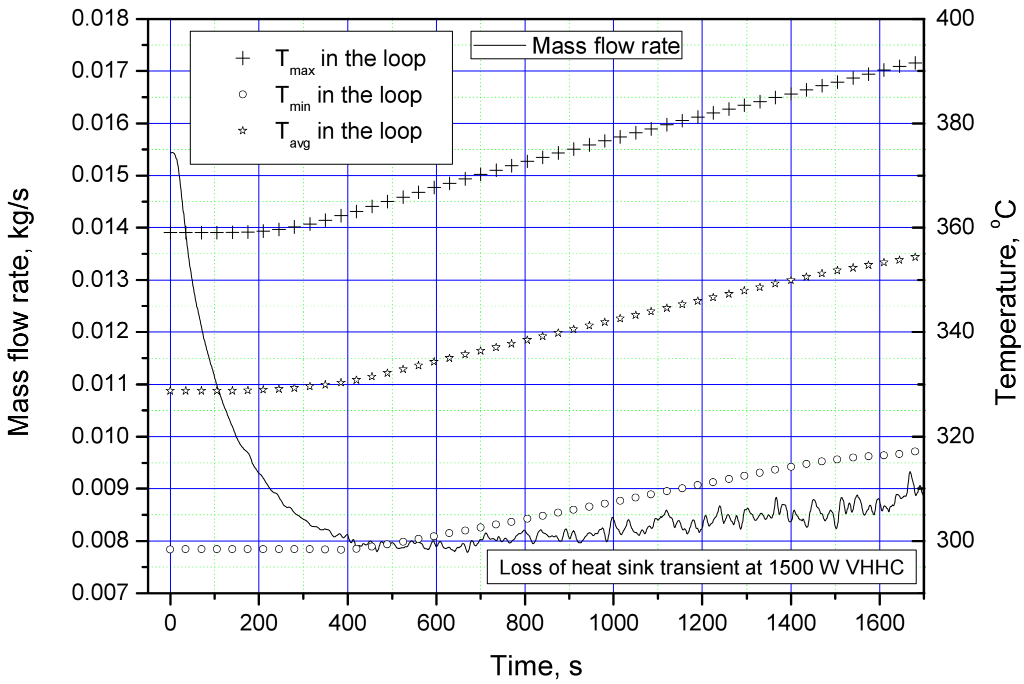

Figure 5.48: Transient variation of mass flow rate, maximum, minimum and average temperature of the loop during loss of heat sink at 1500 W VHHC

5.6 Closure

3D CFD simulations were carried out to study the steady state and transient characteristics of the molten salt natural circulation loop. Simulations included primary as well as secondary side of the loop and also expansion tank. Studies were done for steady state characteristics, power step-up transients, power step-back transients, power-trip transient and loss of heat sink transients. The computational results obtained from the mentioned CFD model shows good agreement with experimental data. Maximum 1.36% of error has been observed between CFD results and experimental data for steady state simulation. Then the CFD model has been used to carry out the CFD simulations at different configurations. The computed steady state characteristics at different configurations have been compared with the available correlations in the literature. The instabilities occur in the HHHC configuration have been explained with the help of temperature contours obtained at different time intervals. The operating limit of the MSNCL at VHHC configuration for the specified mass flow rate and coolant has been mentioned based on the computational data.

CHAPTER 6

HEAT TRANSFER CHARACTERISTICS OF MOLTEN SALT NATURAL CIRCULATION LOOP

6.1 Introduction

In previous chapters, focus was given on explaining flow patterns. However, it is interesting to study heat transfer characteristics of molten salt natural circulation loop (MSNCL) as well. This further enhances our understanding of the working of MSNCL. Heat transfer in a MSNCL is affected by flow pattern but being a natural convection phenomenon, heat transfer also affects flow pattern in the loop. The flow may be steady/periodically oscillating/transient and so is the heat transfer. Heater and cooler are the two main sections in which significant heat transfer takes place. Heat transfer gets affected by many factors like

1) Thermal boundary layer development in heater/cooler sections.
2) Developing flow entering heater/cooler sections.
3) 3D effects due to elbows leading to asymmetric velocity profiles at entrance to heater/cooler sections.
4) Thermal boundary layer development as secondary side of cooler.
5) Heat absorption and release in loop pipe thickness
6) Heat absorption and release from expansion tank.

Hence it is very interesting to study heat transfer aspects of MSNCL under steady state and transient conditions. 3D CFD simulations give 3D temperature fields from which heat transfer analysis is carried out.

When fluids are heated in horizontal ducts, the buoyant force causes a circulation upward the sides due to surface heating and downward at the centre of the duct. A similar effect is noted with cooling; however, the direction of flow is reversed. In natural circulation loop with horizontal heater configuration, the fluid in the horizontal heater rises up and causes local circulation in the cross section of the heated pipes. In vertical heater case, the fluid near the heated surface rises with higher velocity as compared to the fluid towards the centre. Further, in a natural circulation loop, the flow is hydro-dynamically and thermally developing in certain sections of the loop. At low Reynolds numbers, the heat transfer due to mixed convection may be present. In the transient conditions, the heat transfer from heater to fluid is affected due to local recirculation of fluid. To account for all the above phenomena, theoretical studies have been undertaken using 3D CFD code. In the CFD studies effect of thermally developing length, mixed convection effect at different Reynolds numbers, effect of heat transfer due to transient effect have been presented in this chapter. Molten salt natural circulation loop is considered for the analysis.

6.2 Computational study of vertical pipe flow

Before studying actual loop heat transfer, heat transfer studies are done on vertical pipe. The heat transfer characteristics of molten salt $NaNO_3$+KNO_3 in a vertical pipe flow for aiding flow (*upward flow*) using uniform heat flux boundary condition has been carried out using the 3D CFD simulations. These simulations are carried out on a vertical pipe by considering with gravity term in one simulation and without gravity term in another simulation. The simulation of vertical pipe flow with gravity are the simulation of actual vertical pipe flow, whereas the simulation of vertical pipe flow without gravity term was done so that the two results can be compared and it is possible then to understand the effect of buoyancy on heat transfer characteristics. The CFD simulation on vertical pipe flow covers the laminar flow region. Studies in turbulent flow regime have been done on the half loop. This is explained in the later section. The aim of the vertical pipe flow study is to understand the effect of mixed convection in the laminar flow region and also to understand the effect of gravity on heat transfer characteristics. The CFD results are compared with Boelter correlation for mixed convection, Shah-London correlation for hydro-dynamically developed and thermally developing flow and Churchill-Oze correlation for thermally developing flow. These correlations are described later.

The computational study is carried out for different Reynolds number of 500, 1000, 1500 and 2000. There is initial unheated length of 2 m from the inlet. Heating starts after the hydrodynamic development length (*as calculated by using* $L = 0.05ReD$*, where D=diameter of the pipe(m) and Re=Reynolds number*). After the heater, 1 m of unheated length is provided as shown in Fig. 6.1. In these simulations, heat flux boundary condition is used. Heat flux is changed with Reynolds number in such a way that in all cases temperature rise in the heater is 53^0C. This is done because, even in MSNCL, the temperature rise in the heater at various heater powers is around 53^0C.

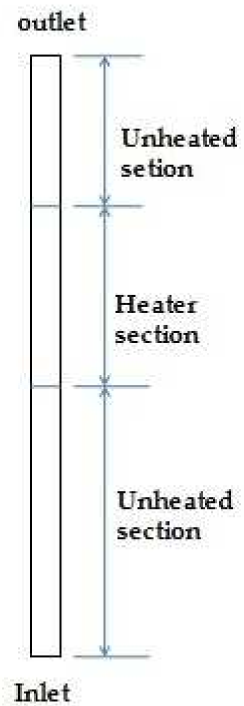

Figure 6.1: Schematic diagram of vertical pipe and half loop

The effect of mixed convection on heat transfer for laminar flow was systematically studied by Boelter (1948). His correlation was based on the flow between a two rectangular vertical plates, the distance between the two plates is mentioned as D in the correlation. His correlation to find out the average Nusselt number in heated part is given below.

$$Nu_{avg} = 1.75\left[Gz + 0.0722\left(\frac{Gr.Pr.D}{L}\right)^{3/4}\right]^{1/3} \tag{6.1}$$

Where Greatz number, $Gz = RePr\left(\frac{D}{L}\right)$

The heat transfer correlation developed by Shah and London ((Shah and Bhatti, 1987), (Bejan, 2013)) for the forced convection hydro-dynamically developed and thermally developing pipe flow with uniform heat flux is given below.

$$Nu_x = \begin{cases} 1.302x_*^{-1/3} - 1, \\ \quad x_* \le 0.00005 \\ 1.302x_*^{-1/3} - 0.5 \\ \quad 0.00005 \le x_* \le 0.0015 \\ 4.364 + 8.68\left(10^3 x_*\right)^{-0.506} \exp(-41x_*) \\ \quad x_* \ge 0.001 \end{cases} \tag{6.2}$$

where $x_* = \frac{x/D}{Re_D Pr}$

Churchill and Oze (1973) developed a closed-form expression that covers both the entrance and fully developed regions of forced convection flow and is given below.

$$\frac{Nu_D}{4.364\left[1+\left(Gz/29.6\right)^2\right]^{1/6}} = \left[1 + \left(\frac{Gz/19.04}{\left[1+\left(Pr/0.0207\right)^{2/3}\right]^{1/2}\left[1+\left(Gz/29.6\right)^2\right]^{1/3}}\right)^{n/2}\right]^{1/n} \tag{6.3}$$

Where Gz= Greatz number and Pr=Prandtle number.

Figure 6.2(a) and Fig. 6.2(b) show the comparison of computed Nusselt number corresponding to Reynolds number of Re=500 and Re=1000 respectively with correlations. It can be seen that the computed results for vertical pipe flow without gravity show good agreement with the forced convection correlations (i.e. Shah and London correlation and Churchill and Oze correlation). Similarly, computed results for vertical pipe flow with gravity show good agreement with Boelter correlation for both the Reynolds numbers. It is observed that the difference between fully developed Nusselt number with and without gravity at Reynolds number of 500 is more than that at Reynolds number of 1000. It shows that the effect of mixed convection is more significant at low Reynolds number flow.

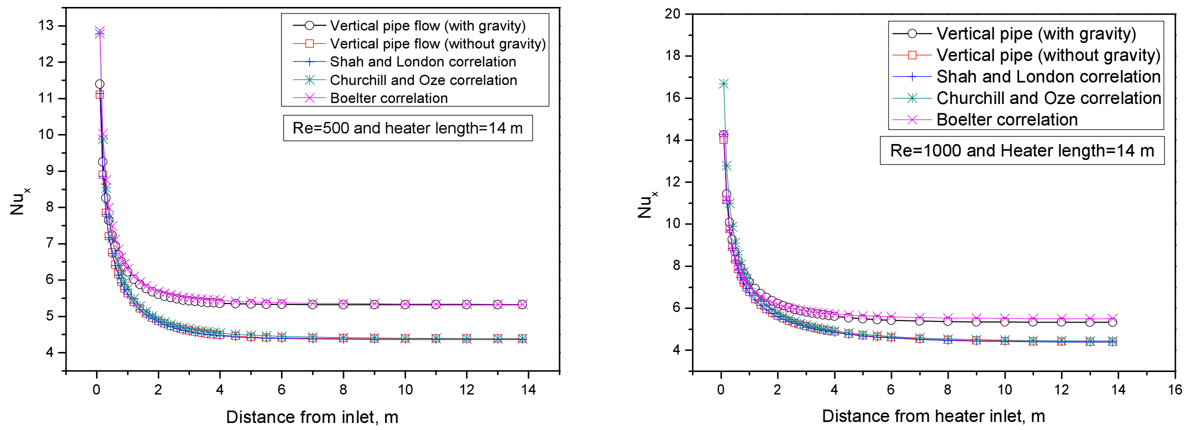

(a) (b)

Figure 6.2: Comparison of computed local Nusselt number with correlations for (a) Re=500 and (b) Re=1000

Figure 6.3(a) and Fig. 6.3(b) show the comparison of computed local Nusselt number corresponding to Reynolds number of 1500 and 2000 respectively. It can be observed that the difference between the local Nusselt number with and without consideration of gravity term in the simulation has been reduced significantly. It shows that the effect of mixed convection in the vertical pipe flow reduces at high Reynolds number. The deviation of computed result with Boelter correlation also proves the same.

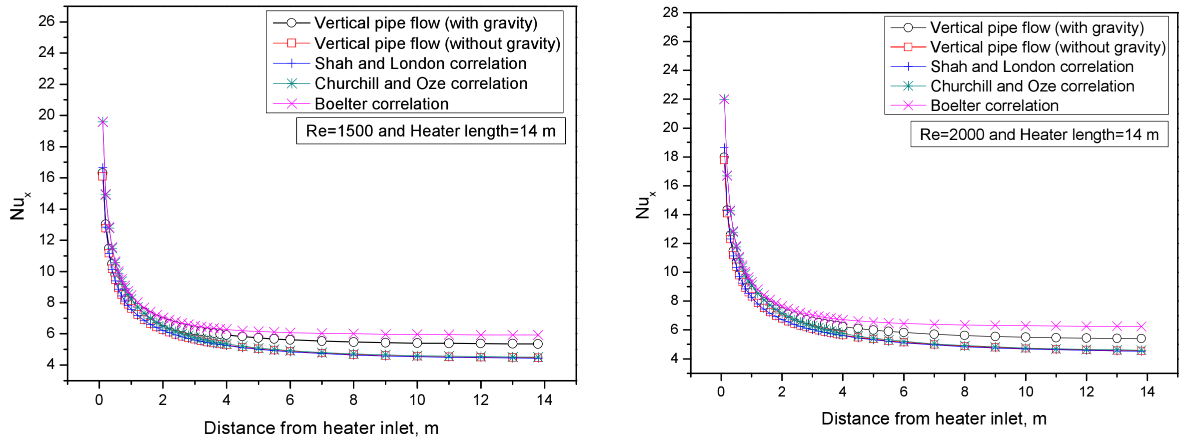

(a) (b)

Figure 6.3: Comparison of computed local Nusselt number with correlations for (a) Re=1500 and (b) Re=2000

Figure 6.2 and Fig. 6.3 show the importance of mixed convection at low Reynolds number. The experimental and computation studies on molten salt natural circulation loop in VHHC configuration from 1200 W to 1800 W shows that the steady state Reynolds number is within 500. Hence the mixed convection plays an important role in the heat transfer characteristic of molten salt natural circulation loop and it is described in the next section.

6.3 Steady state characteristics of MSNCL

Molten salt natural circulation loop has been taken up for heat transfer studies. The details of the loop and operations of the loop were described in Chapter 3. Once it achieves steady state, constant mass flow rate in the loop is observed. The working condition at this stage is more or less similar to forced convection system, in which heater acts like a pump. The flow rate and Reynolds number is small in molten salt natural circulation loop. Flow is in laminar range as shown in Fig. 5.14 of Chapter 5. The heat flux applied in heater causes local buoyancy effect near the heated wall. In view of this, heat transfer characteristics in MSNCL at the steady state condition corresponding to different heater powers are computed using CFD simulations. Temperature field in central vertical plane of heater is shown in following Fig. 6.4. The variation of wall temperature and centreline fluid temperature along the length of the heater is shown in following Fig. 6.5. From these two parameters, local Nusselt number is computed using following expression.

$$Nu_{local} = \frac{h.D}{K}, \quad \text{where} \quad h = \frac{q''}{(T_w - T_b)}$$

Using variation of Nu_{local} along the length of the heater, average Nusselt number over the heater length is computed. The average Nusselt number is the arithmetic mean value of the local Nusselt numbers at different locations along the length of the heater. The corresponding Reynolds number for a particular heater power is calculated from the mean cross-sectional velocity at heater outlet, kinematic viscosity which is considered constant at reference temperature and diameter of pipe.

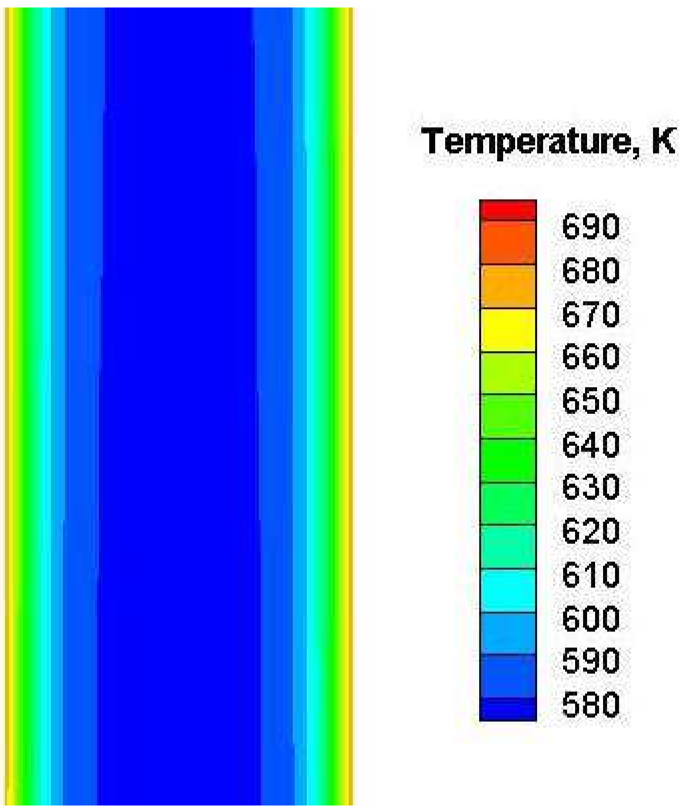

Figure 6.4: Temperature contour at heater section in 1200 W VHHC

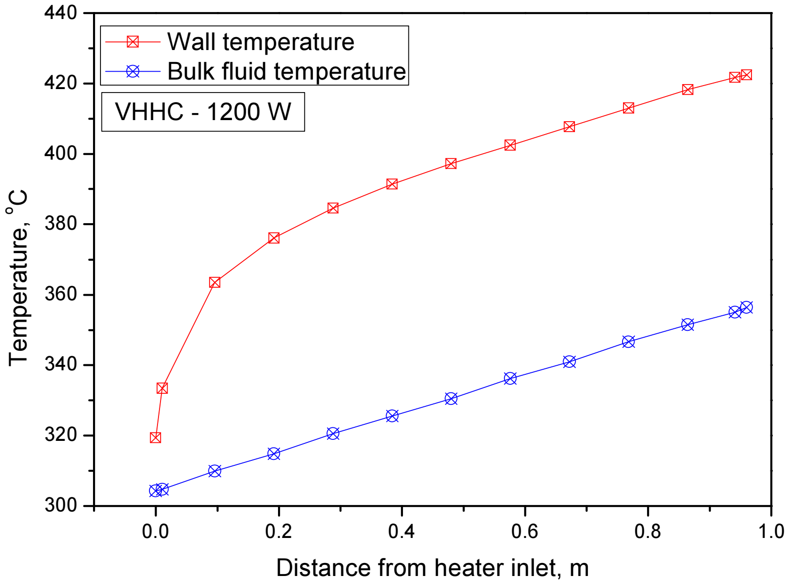

Figure 6.5: Variation of wall temperature and bulk fluid temperature at heater in 1200 W VHHC

Figure 6.6 shows the variation of average Nusselt number with Reynolds number. The comparison of computed result with Boelter correlation is shown in Fig. 6.6 (Boelter, 1948). It has been observed that % of deviation between the computed and correlation values is around 3% only. It can be seen that CFD analysis is able to predict the mixed convective heat transfer characteristics of molten salt natural circulation loop.

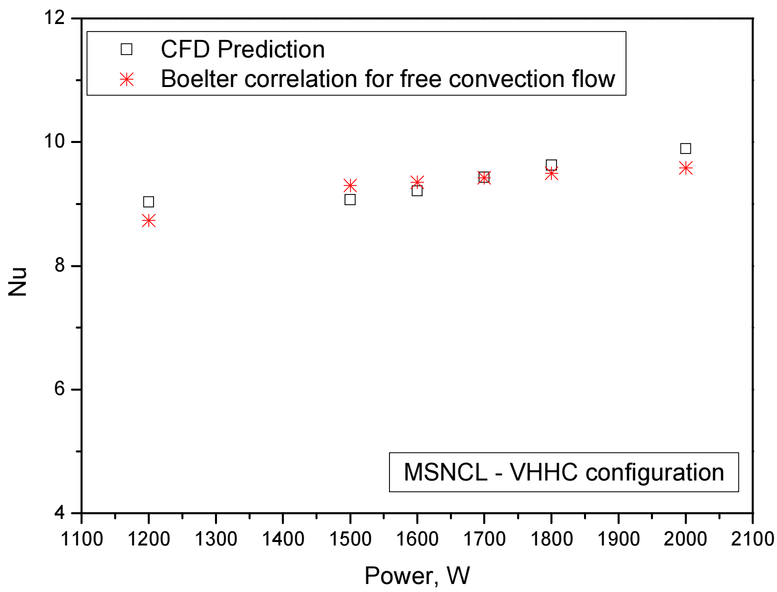

Figure 6.6: Comparison of computed Nusselt number with correlations

6.4 Comparison of computed heat transfer characteristics in the MSNCL with that in the half loop

The operation of molten salt natural circulation loop is limited to certain power level. It is not possible to go above the heater power of 2000 W in VHHC configuration of the mentioned MSNCL. Hence the mass flow rate and Reynolds number attained in the loop is very low. To know the heat transfer characteristics of MSNCL at high Reynolds number, it is required to consider half open loop configuration. The loop is cut half as shown in Fig. 6.7. The two ends are specified to be of type inlet and outlet. With this, it's possible to specify any large Reynolds number. However, it was first verified that half loop behaviour is same as full loop behaviour. This was done by comparing results at low Reynolds number in full loop and half loop. During this study, the steady state mass flow rate obtained for a particular heater power in MSNCL (full loop) is incorporated as the inlet boundary condition in half loop. At the outlet of the half loop, atmospheric pressure is incorporated as boundary condition. Heater power is same in both loops.

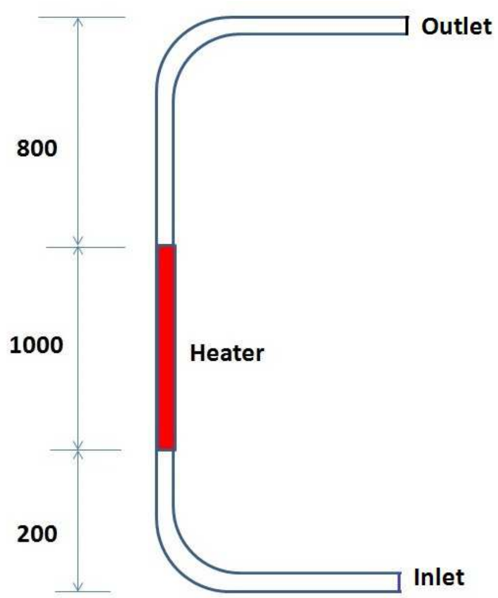

Figure 6.7: Schematic diagram of half loop

Figure 6.8 and Fig. 6.9 show the comparison of local Nusselt number in heater obtained in full loop with that of half loop, at 1200 W and 2000 W heater powers[2]. The predicted local Nusselt number variation in half loop shows good agreement with that in full loop. Thus heat transfer characteristics of half open loop would be same as full closed loop. Hence the heat transfer characteristics of the full loop of MSNCL in the higher mass flow rate range can be studied using the computational study on half loop; which is explained in next section.

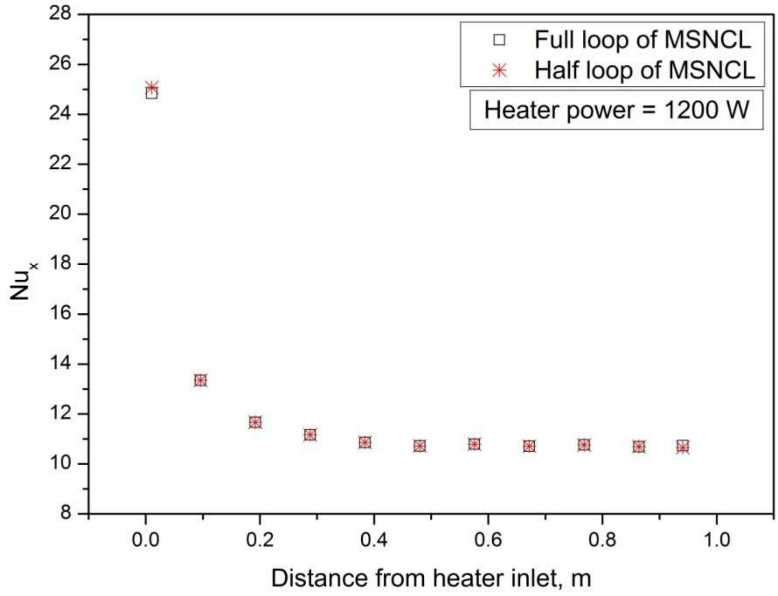

Figure 6.8: Comparison of computed local Nusselt number obtained in full loop of MSNCL with that in half loop at a heater power of 1200 W

In Fig. 6.8 and Fig. 6.9 higher local Nusselt number has been observed near heater inlet. This higher Nu is mainly due to the entrance effect. Nusselt number in fully developed flow is 4.36 (for constant heat flux boundary condition). As shown in Fig. 6.8 throughout the heater length local Nusselt number is much more than 4.36. This is because Reynolds number at 1200 W is 480 and hence flow is laminar. In laminar flow, thermal boundary layer

[2] The first point in these figures has been calculated at 0.01 m from heater inlet so that an infinite value of Nusselt number can be avoided.

development requires length of $0.05ReDPr$ which comes out to be 3.28 m, whereas heater length is 1 m. This shows that in entire heater, thermally developing condition exists and hence high Nusselt number is obtained.

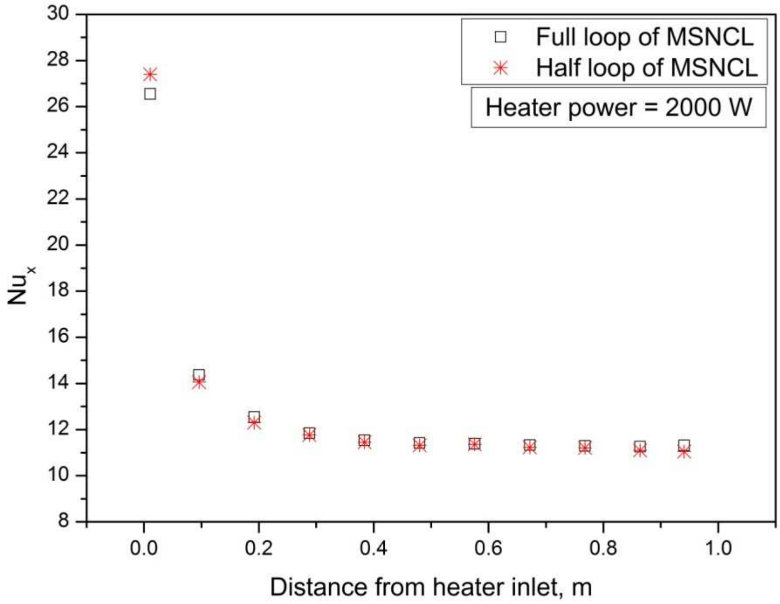

Figure 6.9: Comparison of computed local Nusselt number obtained in full loop of MSNCL with that in half loop at a heater power of 2000 W

It should be noted that the pre heater length (i.e. from elbow end to heater inlet) is small and fully developed flow condition was not established. This can be shown in following Fig. 6.10 in which computed velocity profile at inlet is compared with parabolic fully developed flow profile. There is significant deviation between two profiles which indicate that flow at heater inlet is not fully developed.

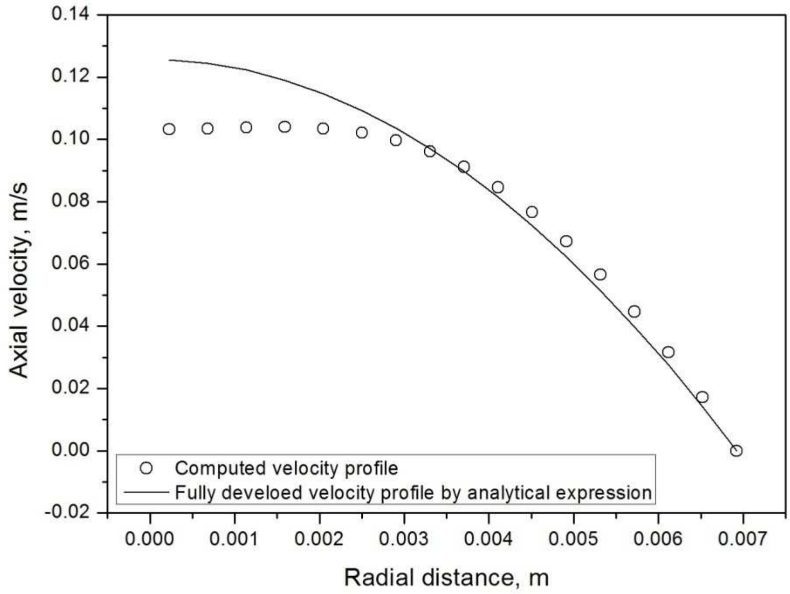

Figure 6.10: Comparison of computed velocity profile at heater inlet of 1200 W VHHC with the fully developed velocity profile by analytical expression

6.5 Heat transfer characteristics in half loop of MSNCL at high Reynolds number flow condition

The heat transfer characteristics over a wide range of Reynolds number has been studied using half loop. For this mass flow rate at inlet is increased and at each mass flow rate heater power is also increased in such a way that $\Delta T_{across\ heater}$ was constant at about 53°C over a range of heater power (induced mass flow rate adjusts accordingly). This makes it sure that open half loop heat transfer characteristics are similar to closed loop MSNCL. The CFD results obtained at various Reynolds number have been compared with the available correlations. Based on the experimental data, many researchers proposed their correlations to find out the heat transfer characteristics in turbulent convection. Dittus and Boelter proposed the correlation for a fully developed turbulent flow in a smooth pipe. The Dittus-Boelter correlation is given below (Dittus and Boelter, 1930).

$$\mathrm{Nu} = 0.023\mathrm{Re}^{0.8}\mathrm{Pr}^{n} \tag{6.4}$$

where n=0.4 for heating and n=0.3 for cooling conditions. Dittus-Boelter correlation is applicable, if $0.7 \le \mathrm{Pr} \le 160$, $\mathrm{Re} \ge 10000$ and $\frac{L}{D} \ge 10$.

For situations involving large property variations, the Sieder and Tate equation is recommended and it is given below (Sieder and Tate, 1936).

$$\mathrm{Nu} = 0.027\mathrm{Re}^{4/5}\mathrm{Pr}^{1/3}\left(\frac{\mu}{\mu_s}\right)^{0.14} \tag{6.5}$$

Sieder-Tate correlation is applicable, for $0.7 \le \mathrm{Pr} \le 16700$, $\mathrm{Re} \ge 10000$ and $\frac{L}{D} \ge 10$ (smooth pipes).

Liu Bin et al. (2009), proposed the following correlation to find the turbulent convective heat transfer in molten salt flow in a circular pipe.

$$\mathrm{Nu} = 0.0242\mathrm{Re}^{0.81}\mathrm{Pr}^{1/3}\left(\frac{\mu_b}{\mu_s}\right)^{0.14} \tag{6.6}$$

Figure 6.11 shows the comparison of computed local Nusselt number in the half loop with and without considering the effect of gravity on flow. The computed results show that there is no effect of gravity on the computed values, in the considered range of Reynolds number. Thus buoyancy effects are not important. Hence high Re results can be compared with forced flow convective heat transfer correlations mentioned above

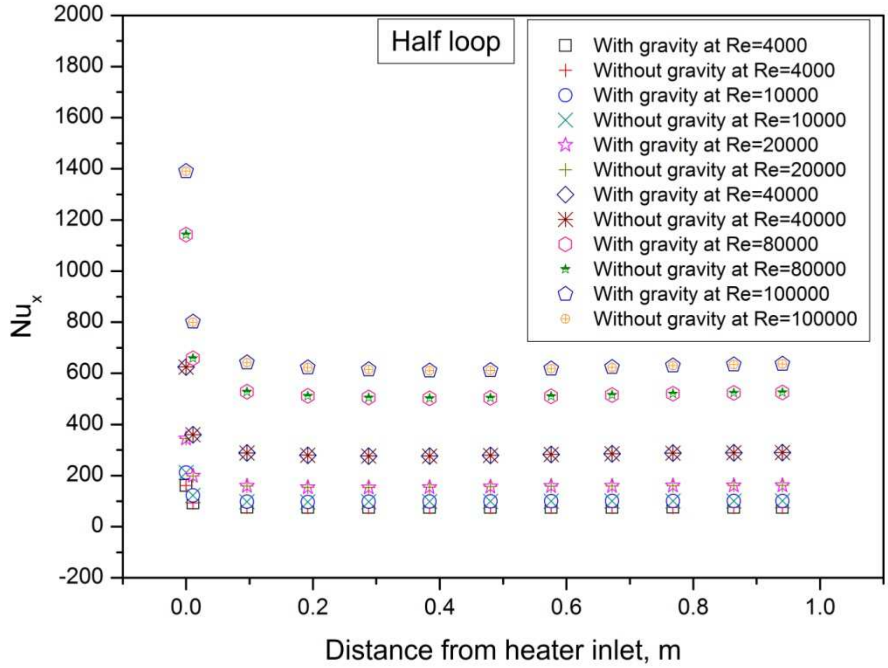

Figure 6.11: Comparison of computed local Nusselt number at different Reynolds number in half loop with and without consideration of gravity term

Figure 6.12 shows the comparison of computed average Nusselt number with the available correlations for fully developed turbulent pipe flow. The computed data shows very good match with Sider-Tate and Bin correlations. The deviation of computed data with these correlations is less than ±3%. The computed results compare well with the forced convection flow correlations at such a high Reynolds number flow regime.

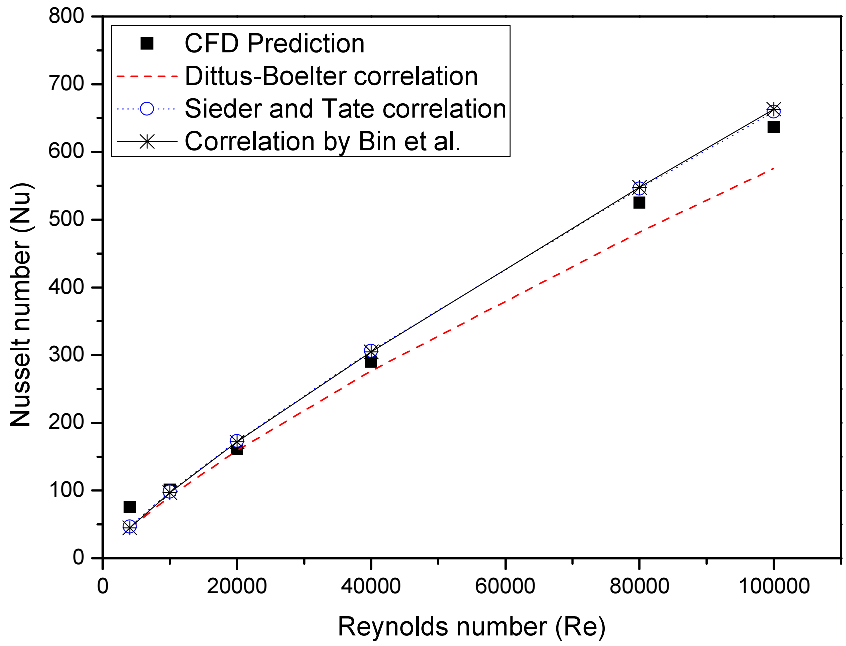

Figure 6.12: Nusselt number of molten salt at turbulent region in half loop

6.6 Heat transfer characteristics in the unsteady oscillatory flow condition

The analysis presented so far was carried out based on steady state data obtained in cases in which heater was vertical, VHHC configuration of MSNCL and its corresponding half loop configuration. But in HHHC configuration of MSNCL, no such a steady state exists. The flow is continuously oscillating as shown in Fig. 6.13. The heat transfer is also affected by flow oscillations. In this section, the heat transfer in such conditions is discussed. The transient flow and heat transfer in HHHC configuration is obtained from 3D CFD simulations using low-Reynolds number k-ε turbulent model. In this configuration (HHHC configuration), standard k-ε turbulence model fails to give good results, which has been proved in Chapter 4 for natural circulation loop working with water.

Figure 6.13 shows the transient variation of mass flow rate in the loop at 1800 W for HHHC configuration. It is observed that, mass flow rate undergo a cycle and a periodic oscillating flow is obtained. The reason behind the oscillatory flow can be understood by using the temperature contours obtained at different time intervals during the transient simulation.

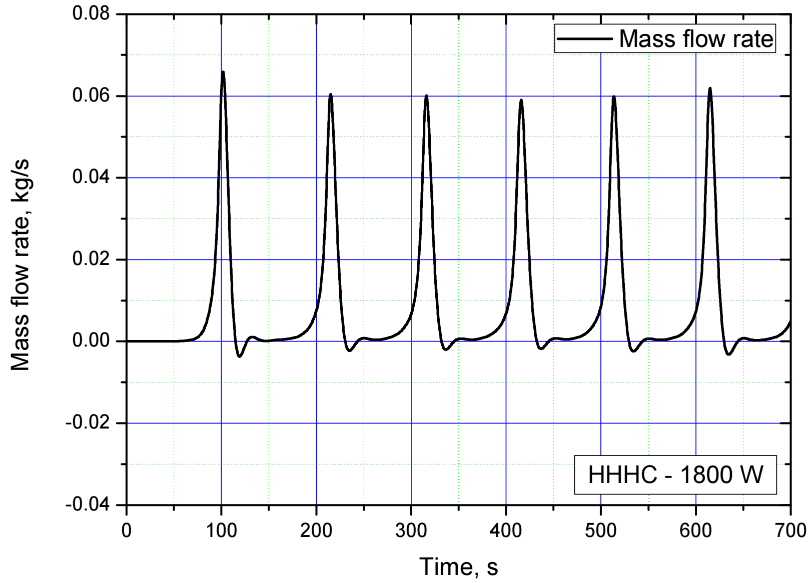

Figure 6.13: Transient variation of mass flow rate for 1800 W HHHC configuration

The enlarged view of a portion of transient variation of mass flow rate shown in Fig. 6.13 is shown in Fig. 6.14 (for period between 150 s to 270 s). The instability in HHHC configuration has been explained by temperature fields, which are plotted at different instants of time as shown by points from A to F in Fig. 6.14.

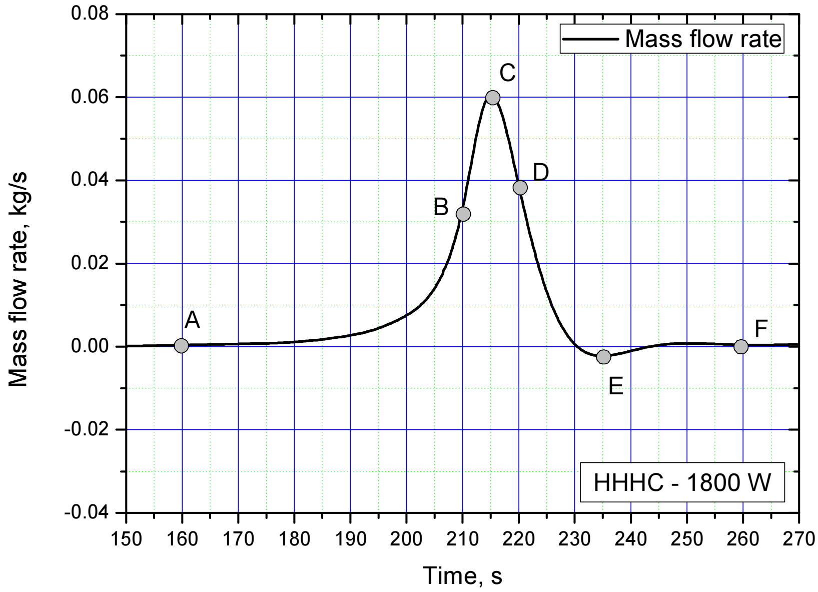

Figure 6.14: Enlarged portion of transient variation of mass flow rate for 1800 W HHHC configuration

During the flow initiation transients, once the heater is switched ON, heat is transferred from the heater to the fluid in the loop. Initially flow is almost stagnant. But due to heating, at first, secondary flow in heater section gets established. Due to surface heating, the fluid near surface rises and it comes down from centre. Due to continuous heating all along heater surface, hot plug (pocket of hot fluid) is formed in the heater section and rest of the fluid in the loop (except at cooler) will be at the initial temperature i.e. 300^{o}C. This hot plug diffuses axially on both sides of heater. Finally it covers the entire bottom horizontal leg as shown in Fig. 6.15(A). After that, the hot plug will try to move into one of the vertical legs. At the same time, due to continuous cooling, cold plug (pocket of cold fluid) is formed at the cooler. After this, entry of the hot plug into left vertical leg takes place as shown in Fig. 6.15(B). Simultaneously, cold plug is entering right vertical leg from top. After this, hot plug rises through the left vertical leg and cold plug descends through right vertical leg. The flow accelerates during this phase. The maximum flow rate is observed, when the entire hot plug is in the left vertical leg (which is much longer than the hot plug length) and the entire cold plug is in the right vertical leg. This is shown Fig. 6.15(C). As the head of the hot plug enters the top horizontal section, the buoyancy force reduces and due to wall friction/elbow resistance, the flow tends to decelerate (Fig. 6.15(D)). Entry of cold plug into bottom horizontal leg also leads to flow retardation. However, due to flow inertia, hot and cold plugs travel through cooler and heater sections respectively. Although, the hot plug passes through the cooler, it does not get sufficiently cooled due to the high velocity while passing through the cooler. The hot and cold plugs enter into right and left vertical legs respectively, as shown in Fig. 6.15(E). Hot plug descends along the right vertical leg in rapidly decelerating flow conditions. The deceleration is due to presence of cold fluid in right vertical leg below hot plug and also due to continuous frictional resistance offered by wall and right top elbow. Hot plug comes to halt and eventually reverses back due to buoyancy leading to small reverse flow. During the reverse flow (very short duration), the hot plug in the right vertical leg returns back to the cooler. Cold plug returns to heater section. Then the flow becomes forward flow i.e. clockwise direction but flow rate is very small. During this time, hot fluid in the top horizontal pipe gets cooled and becomes a cold plug (cold pocket). At the same time cold fluid in the bottom horizontal pipe gets heated and becomes a hot plug (hot pocket). This is shown in Fig. 6.15(F). Subsequently, next hot plug is formed and it enters left vertical leg again due to small anti-clockwise flow existing in the loop and whole cycle gets repeated leading to uni-directional oscillatory flow.

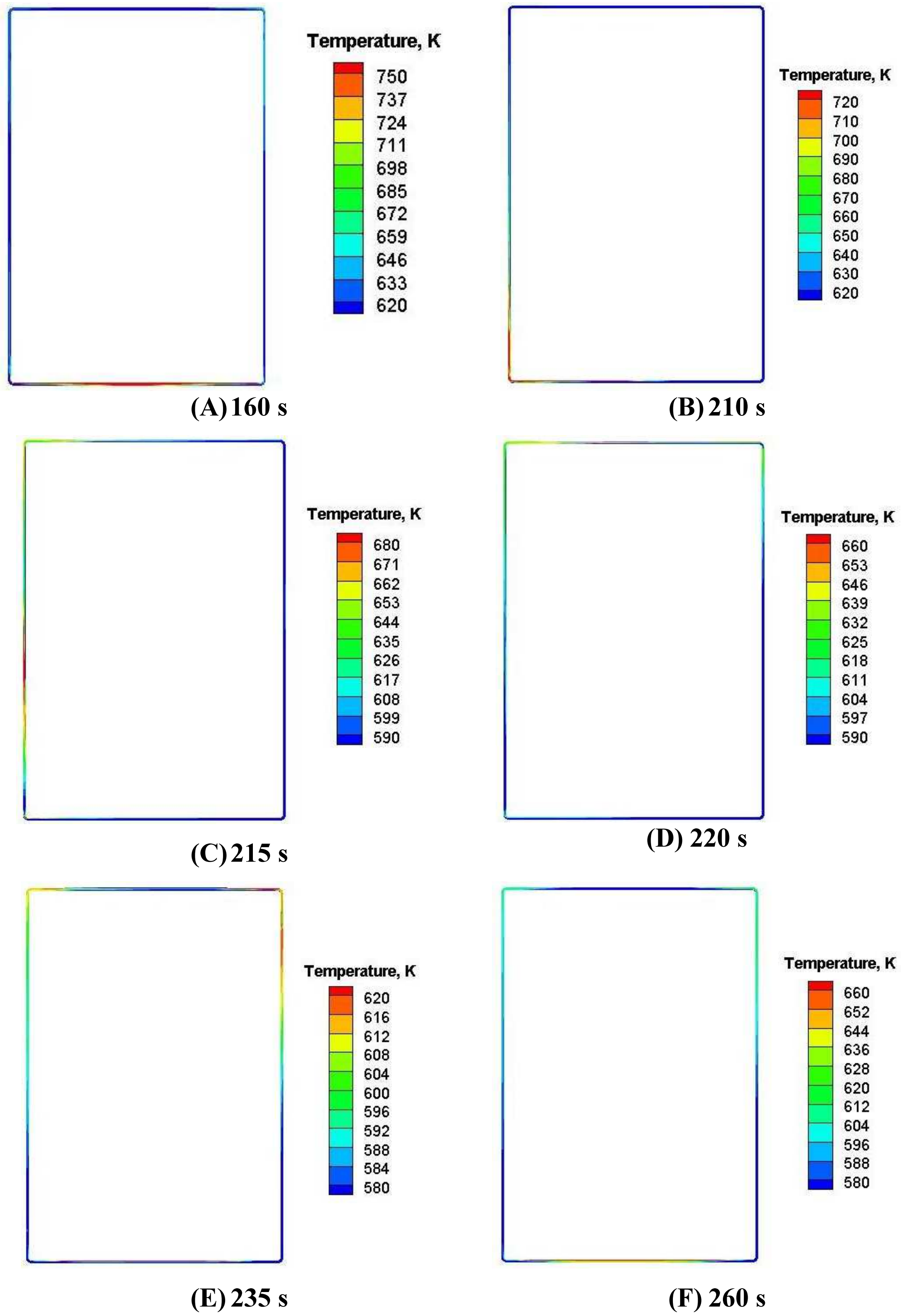

Figure 6.15: Temperature contours of central vertical plane of 1800 W HHHC configuration at different time instants

The oscillating flow field influences heat transfer characteristics in the HHHC configuration. The same has been studied using the temperature field in the cross-sectional plane at the middle of the horizontal heater section. Cross-sectional plane chosen is situated at middle of the heater in Y-Z plane, whereas the loop is kept in X-Z plane as shown in Fig. 6.16.

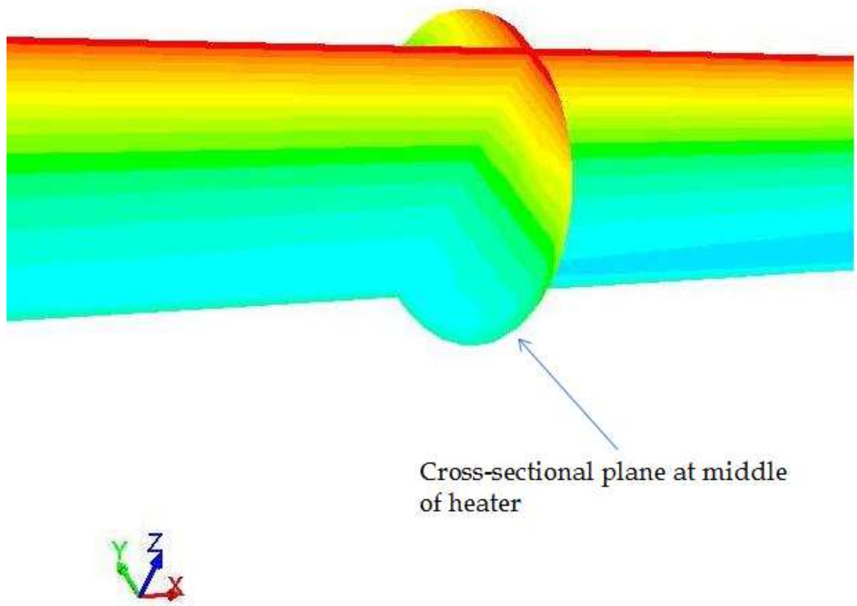

Figure 6.16: Cross-sectional plane situated at the middle of the heater

The transient variation of wall temperature and the bulk temperature across the above mentioned cross-sectional plane is obtained from 3D CFD simulations. Fig. 6.17 shows the temperature fields at different time instants. From these temperature fields, wall temperature as well as area weighted mean fluid temperature is obtained from FLUENT post-processor and the same is used for Nusselt number calculation.

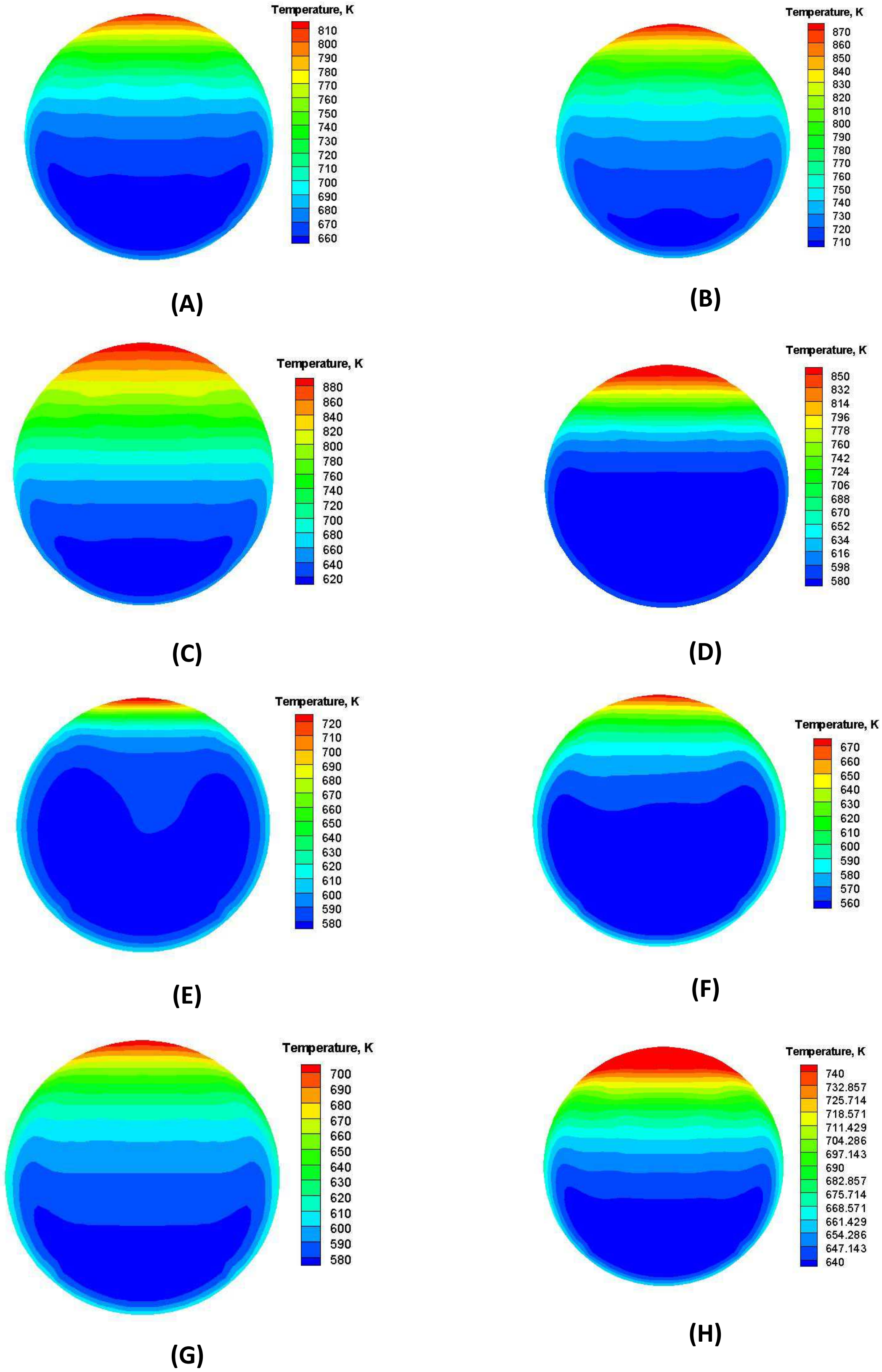

Figure 6.17: Temperature contours of the cross-sectional plane at (a) 160 s, (B) 190 s,(C) 205 s, (D) 210 s, (E) 215 s, (F) 220 s, (G) 235 s, and (H) 260 s.

Figure 6.18 shows the transient variation of mass flow rate in the loop and that of local Nusselt number in the cross-sectional plane situated at the middle of the heater section. Applied heat flux is constant. Maximum value of Nusselt number in a cycle is observed when mass flow rate is minimum and vice-versa. Generally, from well known steady state characteristics of a heat transfer in a pipe, with rise in mass flow rate, Nu should rise and with fall in mass flow rate, Nu should reduce. But in this particular case, opposite trend is observed. This phenomenon is explained in following manner. Figure 6.19 shows the comparison of transient variation of mass flow rate, surface temperature, cross-section averaged mean fluid temperature (T_m), ΔT i.e. (T_{wall}-T_m) and Nusselt number for one cycle of oscillation.

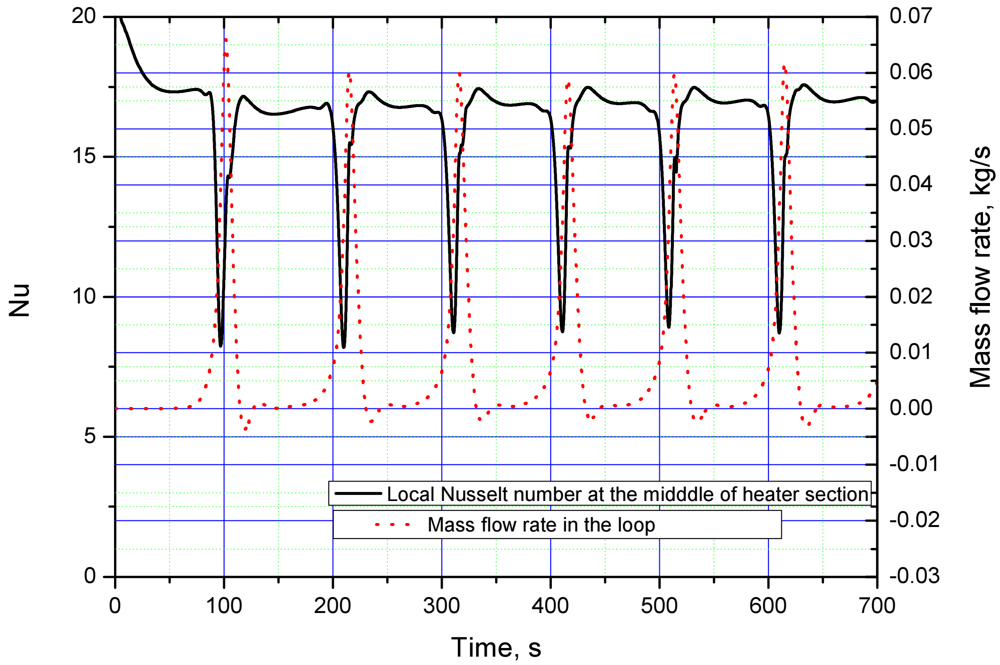

Figure 6.18: Transient variation of mass flow rate in the loop and local Nu in the cross-sectional plane at the middle of the heater section

During stagnant flow condition from 150 s to 190 s, continuous increase in the surface temperature and mean cross sectional temperature (T_m) takes place due to continuous heating. The difference between T_{wall} and T_m is almost constant. After 190 s, there is rise in mass flow rate. The hot plug formed in heater moves to left side. Hence heater gets filled with cold fluid coming from its right side. Hence the bulk temperature drops. Due to convective cooling by this cold fluid, wall temperature also drops even though there is continuous heating. This reduction in T_{wall} and T_m continues from 190 s to 220 s. This period (from 190 s to 220s) can be divided into two periods i.e. 1st period from 190 s to 210 s and then from 210 s to 220 s. In the first period, even though T_{wall} and T_m are falling, their difference is rising. This means, the reduction in T_m is faster and T_{wall} reduces slower. This is obvious because in convective cooling, T_{wall} reduction will follow the T_m reduction. But from 210 s to 220 s, T_{wall} reduces faster than $T_{mean.}$ Hence T_{wall}-T_m decreases.

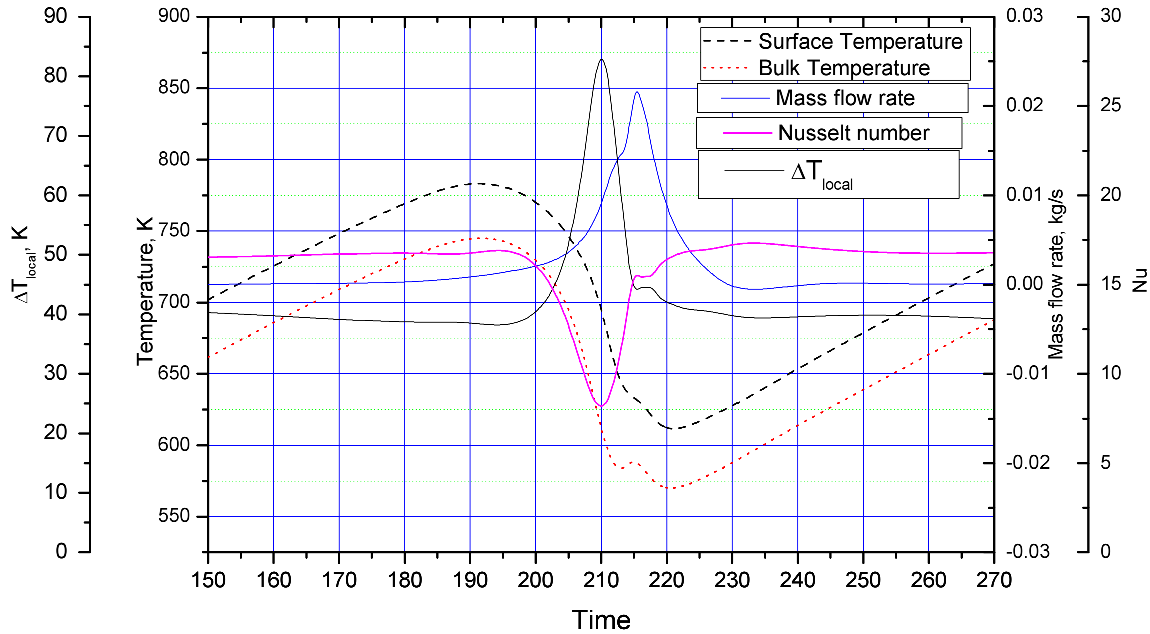

Figure 6.19: Comparison of transient variation of loop mass flow rate, local Nu, local surface temperature, local bulk temperature and local temperature difference

Nusselt number is inversely proportional to (T_{wall}-T_m). Hence from 190 s to 210 s, the Nusselt number reduces even though mass flow rate is increasing. From 210 s to 220 s, Nusselt number rises.

6.7 Closure

The heat transfer characteristics of molten salt in a natural circulation loop are studied by using 3D CFD simulation. Following are the conclusions made from the heat transfer study on molten salt natural circulation loop:

- Heat transfer studies for vide range Reynolds number have been performed. The effect of gravity on heat transfer is also been studied. It is found that, for vertical heater, effect of gravity was significant at low Reynolds number. This shows that in the loop mixed convection phenomena exists at low Reynolds number. The results are compared with Boelter correlation for mixed convection and found in good agreement.
- In high Reynolds number it is found that effect of gravity is negligible. The results obtained in CFD simulation are compared with available forced convection correlations in heat transfer literature.
- The heat transfer characteristics of MSNCL are matching well with those predicted by Boelter correlation for mixed convection. The heat transfer characteristics at high Re, as obtained from open half loop simulation and comparison with various correlation shows that, it is important to account for effect of wall temperature. The Dittus-Boelter correlation, which does not account for T_{wall} shows deviation from CFD simulation results while Sieder-Tate and Liu correlation match well.
- In HHHC configuration of molten salt natural circulation loop, oscillatory flow is obtained at a given power. This affects heat transfer characteristics. It is found that local Nusselt number varies in oscillatory flow. Nusselt number is high when axial mass flow rate is nearly zero in the loop and it reduces when mass flow rate rises

CHAPTER 7

SUMMARY, CONCLUSIONS AND SCOPE FOR FUTURE WORK

7.1 Introduction

The work accomplished during the research project can be summarized in following three subjects :

a) Computational studies on natural circulation loop (NCL) working with water in light of existing experimental work published on the same.

b) Experimental and computational studies on natural circulation loop working with molten salt (MSNCL).

c) Heat transfer characteristics of molten salt natural circulation loop.

The summary and conclusions drawn from obtained result for each of the above topics are given below.

7.2 Studies on NCL working with water

CFD simulations of NCL working with water are performed for predicting steady state characteristics as well as various transients. For NCL working with water reliable experimental data is available. The objective of this work was to assess the capability of CFD simulations to predict steady state/transient characteristics of natural circulation loops. The CFD model included primary and secondary sides of the loop with pipe thickness. Multi-block structured mesh was used which generally gives best accuracy. Required mesh size and time step size were decided from mesh and time step independence studies. Steady state characteristics were obtained for VHVC and VHHC configurations and they were compared with correlations by Vijayan, Swapnalee, Wang and Naveen Kumar and also experimental data. It was observed that the 3D CFD simulation results were matching well with experimental data over a wide range of heater power for VHVC as well as VHHC configurations.

Flow initiation transients for VHHC configuration were performed. The experimental steady state Reynolds number (Re_{ss}) indicates the flow should be laminar but Rayleigh number calculated based on heater parameters indicate that flow is turbulent. Hence CFD simulation for computing flow initiation transient in VHHC configuration was performed with laminar as well as turbulent models and both results were compared with experimental data. It was found that qualitatively both models predict similar trend but quantitatively laminar model gives much better match with experimental data. The reason for the same is explained in the thesis.

The flow initiation transient for HHHC configuration was performed for various powers. Initial simulations were performed with standard k-ε turbulence model. It was found that flow pattern (i.e uni/bi-directional oscillating flow) was adequately computed by standard k-ε turbulence model but frequency and amplitude of oscillations were not exactly matching with experimental data. Results with laminar model showed random oscillations and flow pattern was not matching with experimental data. Launder and Sharma low-Re k-ε turbulence model showed very good match with experimental data. The reason for better accuracy of low-Re turbulence model compared to high Re turbulence model and laminar model is explained in the thesis in detail.

Instabilities occurring in the HHHC configuration of natural circulation loop are predicted well using 3D CFD simulation and explanation of formation of uni-directional/bi-directional oscillation is explained with the help of temperature fields at different time instances. Flow initiation transient for HHVC configuration was performed with standard and low-Re k-ε turbulence models and here also low-Re k-ε turbulence model gave exact match with experimental data.

7.3 Studies on molten salt natural circulation loop

Experimental and computational studies were performed for molten salt natural circulation loop. Experiments were performed on VHHC configuration of molten salt natural circulation loop. The experimental facility and experimental procedure is explained in detail in Chapter 3 of thesis. Steady state characteristics over a range of heater powers were obtained through experiment. Experimental data was also obtained for various transients like power step up/power step down, power trip and loss of heat sink transients. 3D CFD simulations were performed to obtain steady state characteristics for VHHC configuration and results were found to match well with experimental data. Steady state characteristics were also computed for VHVC and HHVC configurations and results were compared with correlations by Vijayan, Naveen Kumar and Wang. In molten salt natural circulation loop, there is some heat loss to ambient which cannot be modeled in correlations. Hence there is slight deviation of CFD results from correlations.

Using the CFD model, it was predicted that the experimental loop should be operated at a power more than 1000 W otherwise molten salt temperature drop to less than its solidification temperature. Similarly heater power should not be more than 2500 W; otherwise molten salt temperature will be more than 600^{o}C which is maximum allowable temperature for molten nitrate salt.

Flow initiation transients were computed for all the four configurations of molten salt natural circulation loop. Except HHHC configuration, flow initiation transient induces initial oscillations in the loop but these oscillations die out and steady state is reached. On the other hand in HHHC configuration, sustaining oscillations were observed. At low power in HHHC configuration of MSNCL as well as NCL working with water, uni-directional sustaining oscillations are obtained. But at high power in MSNCL uni-directional oscillations are obtained unlike NCL where bi-directional oscillations are obtained.

Power step-up and power step-down transients do not show evidence of instability in molten salt natural circulation loop. The studies covered sudden change in power by 200 W. It is observed that, for modeling molten salt natural circulation loop with large power change, e.g. power trip at 2000 W, for getting better results from CFD simulations, it was necessary to model expansion tank. This simulation gives the time within which the molten salt in the loop will reach its lower permissible limit, i.e crystallization temperature. The molten salt should be dumped within this time or power should be restored.

The loss of heat sink is considered in the safety analysis of reactors. The loss of heat sink experiment was carried out at 1200 W and 1500 W heater powers. In the loss of heat sink transient study at 1500 W heater power, the loop was started and steady state was established. After achieving steady state, secondary flow in the cooler duct (i.e. air flow) was stopped completely in experimental study. In CFD simulation also the similar procedure was used. The comparison of computational results with experimental data shows good match with experimental data. For loop operating at 1200 W, the time taken for the heater outlet temperature to rise from 342^{o}C to 368^{o}C is around 3000 s. Hence it will take another 27000 s to reach 600^{o}C, which is the maximum limit of stable liquid state of the nitrate salt. Thus around 9 hours time is available to restore cooling at this power. For loop operating at 1500 W, the time taken for the heater outlet temperature to rise from 359^{o}C to 410^{o}C is around 3500 s. Hence it will take another 14000 s to reach 600^{o}C, which is the maximum limit of stable liquid state of the nitrate salt. Thus around 5 hours time is available to restore cooling at this power.

The following conclusions were made from the heat transfer studies on molten salt natural circulation loop.

- Heat transfer characteristics in the molten salt natural circulation loop are obtained in terms of variation of Nusselt number with power. The computed results were compared with Boelter correlation for mixed convection flow. Good agreement was found between the two results.

- Turbulent convective heat transfer characteristics of the molten salt natural circulation loop were obtained from the half loop simulation. The computed result shows good match with the turbulent forced convection heat transfer correlations.

The transient variation of local Nusselt number in the oscillatory flow formed in HHHC configuration has been studied. The unique characteristic of local Nusselt number in oscillatory flow is explained with the help of temperature fields obtained at different time instants.

7.4 Scope for future work

Experimental data need to be generated for VHVC, VHHC and HHHC configurations of MSNCL. Instabilities occurring in the natural circulation loop (especially in the HHHC configuration) may be computed with advanced turbulence models like RSM, LES and results may be compared with experimental data.

REFERENCES

Acosta, R., Sen, M., Romos, E., 1987, Single-phase natural circulation in a tilted square loop, Wärme-und Stoffübertragung, 21, 269-275.

Alstad, C. D., Isbin, H. S., Amundson, N. R., 1955, Transient behavior of single phase natural circulation systems, A. I. Ch. E. Journal, 1(4), 417-425.

Ambrosini, W., Ferreri, J. C., 1998, The effect of truncation error on numerical prediction of stability boundaries in a natural circulation loop. Nuclear Engineering Design, 183, 53-76.

Ambrosini, W., Forgione, N., Ferreri, J. C., Bucci, M., 2004, The effect of wall friction in Single-phase natural circulation stability at the transition between laminar and turbulent flow, Annals of Nuclear Energy, 31, 1833-1865.

Bejan, A., 2013, Convective Heat Transfer, Third Edition, Wiley, India.

Bernier, M. A., Baliga, B. R., 1992, A 1D/2D model and experimental results for a closed loop thermosyphon with vertical heat transfer sections, International Journal of Heat Mass Transfer, 35(11), 2669-2982.

Bin, L., Yu-ting, W., Chong-fang, M., Meng, Y., Hang, G., 2009, Turbulent convective heat transfer with molten salt in a circular pipe, Int. Comm. Heat and Mass Transfer, 36, 912-916.

Boelter, L. M. K., 1948, Heat transfer notes, University of California press, Berkely.

Borgohain, A., Jaiswal, B. K., Maheshwari, N. K., Vijayan, P. K., Saha, D., Sinha, R. K., 2011, Natural circulation studies in a lead bismuth eutectic loop, Progress in Nucl. Energy, 53, 308-319.

Borgohain, A., Srivstava, A. K., Srivastava, A. K., Gupta, A., Maheshwari, N. K., Krishnani, P. D., Vijayan, P. K., 2015, Conceptual design of a pool type molten salt breeder reactor, In the proceedings of Thorium Energy Conference, Oct 12-15, 2015, BARC, Mumbai, India.

Cengel, Y. A., Ghajar, A. J., 2011, Heat and Mass Transfer, Fourth edition, Mc Graw Hill special Indian Edition, New Delhi.

Chen, K., 1985, On the oscillatory instability of closed-loop thermosyphons, Trans. ASME J. Heat transfer 107, 826-832.

Churchill, S. W., Ozoe, H., 1973, Correlations for forced convection with uniform heating in flow over a plate and in developing and fully developed flow in a tube, Journal of Heat Transfer, 95, 78-84.

Creveling, H. F., De Paz, J. F., Baladi, J. Y., Schoenhals, R. J., 1975, Stability characteristics of a single-phase free convection loop, J. Fluid Mechanics, 67, 65-84.

Damerell, P. S., Schoenhals, R. J., 1979, Flow in a toroidal thermosyphon with angular displacement of heated and cooled sections, J. Heat Transfer, 101, 672-676.

Devia, F., Misale, M., 2012, Analysis of the effects of heat sink temperature on single-phase natural circulation loops behavior, International Journal of Thermal Sciences, 59, 195-202.

Dittus, F. W., Boelter, L. M. K., 1930, Heat transfer in automobile radiators of the tubular type, Univ. California Publ. Eng. 2, 443-461.

Dulera, I. V., Sinha, R. K., 2008, High temperature reactos, Journal of Nuclear Materials, 383, 183-188.

Farmer M. T., Sienicki J. J., 2004, Analysis of transient coolant void formation during a Guilltone-Type tube rupture event in the STAR-LM system employing a supercritical CO2 Brayton cycle, in: 12th International Conference on Nuclear Engineering (ICONE12), Arlington, VA, April 25-29, 2004, Paper ICONE12-49227.

Ferng, Y. M., Kun-Yueh Lin, Chen-Wei Chi, 2012, CFD investigating thermal-hydraulic characteristics of FLiNaK salt as a heat exchange fluid, Applied Thermal Engineering, 37, 235-240.

Ferri, R, Cammi, A, Mazzei, D, 2008, Molten salt mixture properties in RELAP5 code for Thermodynamic solar applications, International Journal of Thermal Sciences, 47, 1676-1687.

Forsberg, C. W., Peterson, P. F., Zhao, H., 2004, An advanced Molten Salt Reactor Using High-Temperature Reactor Technology, International Congress on Advances in Nuclear Power Plants (ICAPP ’04), June 13-17, 2004.

Forsberg, C. W., 2004, Reactors with molten salts: Options and missions. Proc. Frederic Joliot & Otto Han Summer School on Nuclear Reactors: Physics, Fuels, and Systems, Cadarache, France, August 25-September 3.

Forsberg, C., 2005, The advanced High-Temperature Reactor: High-temperature fuel, liquid salt coolant, liquid- metal- reactor plant, Progress in Nuclear Energy, 47(1-4), 32-43.

Grele, M. D., Gedeon, L., 1954, Forced-convection Heat-transfer Characteristics of Molten FLiNaK Flowing in an Inconnel X system, Research Memorandom Report Number NACA RM E53L18.

Gorman, M., Widmann, P., Robbins, K., 1984, Chaotic flow regimes in a convection loop, Phys. Rev. Lett. 52, 2241-2244.

Hearmann U., Kearney D. W., 2002, Survey of thermal energy storage for parabolic trough power plants, Journal of Solar Energy Engineering, 124, 145-152.

Hoffman, H. W., Lones, J., 1955, Fused Salt Heat Transfer Part II: Forced Convection Heat Transfer in Circular Tubes Containing NaF-KF-LiF Eutectic, Oak Ridge National Laboratory, Report Number ORNL 1777.

Huang, B. J., Zelaya, R., 1988, Heat transfer behavior of a rectangular Thermosyphon loop, Journal of Heat Transfer, 110, 487-493.

Ignat'ev, V. V., Keronovskii, S. V., Surenkov, A. I., Shcherbanyuk, O. P., Manchkha, S. P., Smirnov, Y. B., 1984, Heat exchange during the flow of a melt of LiF-NaF-KF fluoride salts in a circular tube, At. Energiya, 57, 123-124.

Ingersoll D. T, Forsberg C. W, Ott L. J, Williams D. F, Renier J. P, Wilson D. F, Ball S. J, Reid L, Corwin W. R, Del Cul G. D, Peterson P. F, Zhao H., Pickard P. S., Parma E. J., Vernon M., Status of preconceptual design of the advanced high-temperature reactor, ORNL/TM-2004/104, Oak Ridge National Laboratory, Oak Riedge, TN, USA, 2004, 1-86.

Jackson, J. D., Cotton, M. A., Axcell, B. P., 1989, Review Studies of mixed convection in vertical tubes, International Journal of Heat and Fluid Flow, 10(1), 2-15.

Jaiswal, B. K., Pal, A. K., Vijayan, P. K., 2011, Heliostat Field Layout Optimization in Solar Power Tower System, In proceedings of International conference on Advances in Energy Research (ICAER-2011), Paper No. MS#CAER11/131.

Kearney, D., Kelly, B., Herrmann, U., Cable, R., Pacheco, J., Mahoney, J,; Price, H., Blake, D., Nava, P., Potrovitza, N., 2004, Engineering aspects of a molten salt heat transfer fluid in a trough solar field, Energy, 29, 861-870.

Keller J., 1966, Periodic oscillations in a model of thermal convection, J. Fluid Mechanics, 26, 599-606.

Kiran Kumar. K., Ram Gopal. M., 2011, Experimental studies on CO_2 based single and two-phase natural circulation loops, Applied Thermal Engineering, 31, 3437-3443.

Kostin V. I., Samoilov O. B., Valvilkin V. N., Panov Yu. K., Kurachenkov A. V., Bolshukhin M.A., Alekeev V. I., Shmelev I. V., Baranaev Yu. D, Pekanov A. A., 2004, Small floating nuclear power plants with ABV reactors for electric power generation, heat production and seawater desalination, in: Fifteenth Annual Conference of Indian Nuclear Society, INSAC-November 15-17, 2004, Mumbai, India.

Kurvi, S., Jamie Trahan, Yogi Goswami, D., Rahman, M. M., Stefanakos, E. K., 2013, Thermal energy storage technologies and systems for concentrating solar power plants, Progress in Energy and Combustion Science, 39, 285-319.

Launder, B. E., Sharma, B. L., 1974, Application of energy-dissipation model of turbulence to the calculation of flow near spinning disc, Lett. Heat Mass Transfer, 1, 131-138.

Lavine, A. S., Greif, R. J., Humphrey, A. C., 1987, A three-dimensional analysis of natural convection in a toroidal loop-the effect of Grashof number. International Journal of Heat Mass Transfer, 30, 251-262.

Louisos, W. F., Hitt, D. L., Danforth, C. M., 2013, Chaotic flow in a 2D natural convection loop with heat flux boundaries, International Journal of Heat and Mass Transfer, 61, 565-576.

Mazzi, R., CAREM: an innovative integrated PWR, in: 18th International Conference on Structural Mechanics in Reactor Technology (SMiRT-18), Beijing, China, August 7-12, 2005, SMiRT18-S01-2.

Misale, M., Frogheri, M., D'Auria, F., Fontani, E., Garcia, A., 1999, Analysis of Single-phase natural circulation experiments by system codes, International Journal of Thermal Sciences, 38, 977-943.

Misale, M., Ruffino, P., Frogheri, M., 2000, The influence of the wall thermal capacity and axial conduction over a single-phase natural circulation loop: 2-D numerical study, Heat and Mass Transfer, 36(6), pp. 533-539. (Special Issue for the Eurotherm seminar No. 63, Single and Two-Phase Natural Circulation, 6-8 September, Genoa, Italy).

Misale, M., Garibaldi, P., Passos, J. C., Ghisi de Bitencourt, G., 2007, Experiments in a single-phase natural circulation mini-loop, Experimental Thermal and Fluid Science, 31, 1111-1120.

Misale, M., Garibaldi, P., Tarozzi, L., Barozzi, G. S., 2011, Influence of thermal boundary conditions on the dynamic behaviour of a rectangular single-phase natural circulation loop, International Journal of Heat and Fluid Flow, 32, 413-423.

Modro S. M., Fisher J., Weaver K., Babka P., Reyes J., Groome J., Wilson G, 2002, Generation-IV Multi-Application Small Light Water Reactor (MASLWR), In: Proceeding of ICONE-10, Tenth International conference on Nuclear Energy, April 14-18, 2002, Arlington, Virginia, USA.

Moir R. W., 2008, Recommendations for a restart of molten salt reactor development, Energy Conversion and Management, 49, 18-49.

Moriyama H., Sagara A., Tanaka S., Moir R. W., Sze D. K., 1998, Molten salts in fusion nuclear technology, Fusion Engineering Design, 627, 39-40.

Mousavian, S. K., Misale, M., D'Auria, F., and Salehi, M.A., 2004, Transient and stability analysis in single-phase natural circulation loop, Annals of Nuclear Energy, 31, 1177-1198.

Naphade, P., Borgohain, A., ThundilKaruppa Raj, R., Maheshwari, N. K., 2013, Experimental and CFD study on Natural Circulation Phenomenon in Lead Bismuth Eutectic Loop, Procedia Engineering, 64, 936-945.

Naveen Kumar, Doshi, J. B., Vijayan, P. K., 2011, Investigation on the role of mixed convection and wall friction factor in single-phase natural circulation loop dynamics, Annals of Nuclear Energy, 38, 2247-2270.

Naveen Kumar, Doshi, J. B., Vijayan, P. K., 2014, Investigations on the role of secondary convection currents in single-phase natural circulation loop dynamics Part 1: Model for simulating Start-up from rest, Progress in Nuclear Energy, 76, 148-159.

Naveen Kumar, Iyer, K., Doshi, J. B., Vijayan, P. K., 2015, Investigation on single-phase natural circulation loop dynamics part 3: Role of expansion tank, Progress in Nuclear Energy, 78, 63-79.

Nayak, A. K., Gartia, M. R., Vijayan, P. K., 2008, An experimental investigation of single-phase natural circulation behaviour in a rectangular loop with Al_2O_3 nanofluids, Experimental Thermal Fluid Science, 33, 184-189.

Nissan, D. A., 1982, Thermophysical Properties of the Equimolar Mixture $NaNO_3$-KNO_3 from 300 to 600^{o}C, Journal of Chemical Engineering Data, 27, 269-273.

NITI Ayog Report, 2015, A Report on Energy Efficiency and Energy Mix in the Indian Energy System (2030) Using India Energy Security Scenarios, 2047, NITI Ayog, April 2015.

Patankar, S. V., 1980, Numerical Heat Transfer and Fluid Flow, Hemisphere Publishing Corporation, Washington, D. C.

Pilkhwal, D. S., Ambrosini, W., Forgione, N., Vijayan, P. K., Saha, D., Ferreri, J. C., 2007, Analysis of the unstable behavior of a single-phase natural circulation loop with one-dimensional and computational fluid-dynamic models, Annals of Nuclear Energy, 34, 339-355.

Sieder, E. N., Tate, G. E., 1936, Heat transfer and pressure drop in liquids in tubes, Ind. Eng. Chem., 28, 1429-1435.

Shah, R. K., Bhatti, M. S., 1987, Laminar convective heat transfer in ducts, in S. Kakac, R. K. Shah, and W. Aung, eds., Handbook of single-phase convective heat transfer, Wiley, New York, chapter 3.

Sharma M., Vijayan P. K., Pilkhwal D. S., Yutaka Asako, 2013, Steady state and stability characteristics of natural circulation loops operating with carbon dioxide at supercritical pressures for open and closed loop boundary conditions, Nuclear Engineering Design, 265, 737-754.

Samuel D., 2009, Molten salt coolants for high temperature reactors, A literature summary of key R & D activities and challenges, IAEA Internship Report, NENP-TDS/INPRO, IAEA.

Smith C. F., Halsey W. G., Brown N. W., Sienicki J. J., Moisseytsev A., Wade D. C., 2008, SSTAR: The US-lead-cooled fast reactor (LFR), J. Nucl. Mater. 376, 255-259.

Sona, C. S., Khanwale, M. A., Mathpati, C. S., Borgohain, A., Maheshwari, N. K., 2014, Investigation of flow and heat characteristics and structure identification of FLiNaK in pipe using CFD simulations, Applied Thermal Engineering, 70, 451-461.

Srivastava, A. K., Vaidya, A. M., Maheshwari, N. K., Vijayan, P. K., 2013, Heat transfer and pressure drop characteristics of molten fluoride salt in circular pipe, Applied Thermal Engineering, 61, 198-205.

Stern C. H., Grief R., Humphrey J. A., 1988, An experimental study of natural convection in a toroidal loop, J. Heat Transfer, 110, 877-884.

Swapnalee, B. T., Vijayan, P. K., 2011, A generalized flow equation for single phase natural circulation loops obeying multiple friction laws, International Journal of Heat and Mass transfer, 54, 2618-2629.

Swapnalee, B. T., Vijayan, P. K., Sharma, M., Pilkhwal, D. S., 2012, Steady state flow and static instability of supercritical natural circulation loops, Nuclear Engineering Design, 245, 99-112.

Tyner C., Wasyluk D., 2013, eSolar's modular, scalable molten salt power tower reference plant design, SolarPACES 2013, Energy Procedia, 2013.

Vijayan, P. K., Austregesilo, H., 1994, Scaling laws for single-phase natural circulation loops, Nuclear Engineering Design, 152, 331-347.

Vijayan, P. K., Austregesilo, H., Teschendorff, V., 1995, Simulation of the unstable oscillatory behavior of single-phase natural circulation with repetitive flow reversals in a rectangular loop using computer code ATHLET, Nuclear Engineering Design, 155, 623-641.

Vijayan, P. K., Bhojwani, V. K., Bade, M. H., Sharma, M., Nayak, A. K, Saha, D., Sinha, R. K., 2001, Investigations on the effect of heater and cooler orientation on the steady state, transient and stability behavior single-phase natural circulation in a rectangular loop. Bhabha Atomic Research Centre, Report BARC/2001/E/034 (2001).

Vijayan, P. K., 2002, Experimental observations on general trends of the steady state and stability behavior of single-phase natural circulation loops, Nuclear Engineering Design, 215, 139-152.

Vijayan P. K., Sharma M., Saha D., 2007, Steady state and stability characteristics of single-phase natural circulation in a rectangular loop with different heater and cooler orientations. Experimental Thermal Fluid Science, 31, 925-945.

Vijayan P. K., Nayak A. K., Saha D., Gartia M. R., 2008, Effect of loop diameter on the steady state and stability behavior of single-phase and two-phase natural circulation loops, Science and Technology of Nucl. Installations, volume 2008, Article ID 672704, 17 pages, DOI: 10.1155/2008/672704.

Vriesema, B., 1979, Aspects of Molten Flourides as Heat Transfer Agents for Power Generation, WTHD No. 112, Delft Institute of Technology.

Wacholder, E., Kaizerman, S., Elias, E., 1982, Numerical analysis of the stability and transient behaviour of natural circulation loops, International Journal of Engineering Science, 20, 1235-1254.

Wang, J. Y., Chuang, T. J., Ferng, Y. M., 2013, CFD investigating flow and heat transfer characteristics in a natural circulation loop, Annals of Nuclear Energy, 58, 65-71.

Welander P., 1967, On the oscillatory instability of a differentially heated loop, Journal of Fluid Mechanics, 29, 17-30.

Williams D. F., 2006, Assessment of candidate molten salt coolants for the NGNP/NHI heat transfer loop, ORNL/TM-2006/69.